The redshift distribution and dust properties of dusty star-forming galaxies at high redshift

Dissertation

zur

Erlangung des Doktorgrades (*Dr. rer. nat.*)

der

Mathematisch-Naturwissenschaftlichen Fakultät

der

Rheinischen Friedrich–Wilhelms–Universität, Bonn

vorgelegt von

Maria Louise Strandet Jensen

aus

Hvidovre, Dänemark

Bonn December 2017

Angefertigt mit Genehmigung der Mathematisch-Naturwissenschaftlichen Fakultät
der Rheinischen Friedrich–Wilhelms–Universität Bonn

1. Referent: Prof. Dr. Karl M. Menten
2. Referent: Prof. Dr. Cristiano Porciani
Tag der Promotion: 08.03.2018
Erscheinungsjahr: 2018

RHEINISCHE FRIEDRICH–WILHELMS–UNIVERSITÄT BONN

Abstract

by Maria Louise Strandet

for the degree of

Doctor rerum naturalium

Millimeter (mm) and submillimeter (submm) continuum observations brought about a radical shift with the discovery that luminous, dusty galaxies were a thousand times more abundant in the early Universe than they are at present day. The first submm/mm detected high redshift dusty star-forming galaxies (DSFGs) were discovered in 1998, and surveys of these suggested that the peak of dust enshrouded star formation occurred at $z \sim 2$, simultaneous with the peak of black hole accretion and cosmic star formation. While the history of star formation has now been measured out to $z \sim 8$ in rest-frame UV surveys, little progress has been made until recently to quantify the amount of highly obscured star formation at $z > 3.5$ in the mm/submm regime mainly because of the difficulties in obtaining robust redshifts for DSFGs.

In this thesis I explore the redshifts of a sample of DSFGs selected from the South Pole Telescope (SPT) Survey. The survey covers an impressive $2500\,\mathrm{deg}^2$ at the wavelengths of 1.4 mm, 2.2 mm and 3.0 mm. The large area of the survey made it possible to assemble a large sample of rare and bright sources. The sources are mostly gravitationally lensed and at high redshifts. Here, we explore the high redshift nature of the SPT-DSFGs through ALMA redshift scans of 42 sources. We combine these observations with previously published and new mm/submm line and photometric data of the SPT-DSFGs to study their redshift distribution. This yields a sample of 62 sources with reliable redshifts based on either two spectral lines or one spectral line combined with photometric observations, and a median redshift is $z = 4.1 \pm 0.2$. The redshift distribution of the SPT-DSFGs is affected by strong gravitational lensing and when correcting for the effect of gravitational lensing we find a median redshift of $z = 3.5 \pm 0.3$. Comparing to redshift distributions selected at shorter wavelengths from the literature, we show that selection wavelength affects the shape of the redshift distribution.

To complete the redshift distribution for the full sample of 91 SPT-DSFGs, we take advantage of the well sampled photometry for the full sample. We investigate different ways on finding photometric redshifts, settling on fitting spectral energy distributions. We use the sources with spectroscopic redshifts to construct a dust temperature distribution that is used as input for the spectral energy distributions. By combining the redshift distribution presented above

with photometric redshifts of the remaining 29 sources without spectroscopic redshifts, we find a median redshift of $z = 3.7 \pm 0.1$. A study of the dust temperature as a function of redshift (for the sources with spectroscopic redshifts) shows that the dust temperature is increasing with redshift, consistent with what is seen for lower redshift samples.

The highest redshift galaxy found in the entire SPT-DSFG sample, SPT0311-58 at $z = 6.900 \pm 0.002$, is also the highest-redshift millimeter-selected DSFG discovered to date. We constrain the properties of the ISM in SPT0311-58 with a radiative transfer analysis of the dust continuum photometry and the CO and [C I] line emission. This allows us to determine the gas content without ad hoc assumptions about gas mass scaling factors. SPT0311-58 is extremely massive, with an intrinsic gas mass of $M_{\rm gas} = 3.3 \pm 1.9 \times 10^{11} M_{\odot}$. Its large mass and intense star formation is very rare for a source well into the Epoch of Reionization.

To my parents who always support me

Acknowledgements

I would like to express my gratitude to Prof. Dr. Karl M. Menten for giving me the chance to do my PhD with him and for welcoming me as a student of the group. I have enjoyed working here, and I am grateful for the opportunities I have been given, e.g. in form of funding for travels to conferences, meetings and observatories. I would also like to acknowledge financial support from IMPRS in Bonn. My biggest thanks goes to my day-to-day supervisor Dr. Axel Weiss, for the patient guidance, encouragement and advice he has provided throughout my time as his student. I feel lucky to have had a supervisor who always made time for me, who cared about my work and who stood up for me when needed.

During my PhD I have worked within the SPT-SMG collaboration, which has provided me with exciting science projects and has allowed and helped me to pursue new ideas. I have met many great colleagues here, who have included me in their projects and scientific discussions which has helped me grow as scientist. It is also from this collaboration most of my co-authors come, and I would like to thank you for your contributions and feedback to my work. I would especially like to thank Dr. Carlos De Breuck who helped me with my scientific work, and supported me when the work load became large. He stood up for me when I needed to be heard, and it meant the world to me.

A special thanks goes to my colleague and friend Dr. Benjamin Magnelli who has supported me both scientifically and morally throughout my full PhD. I knew that his door was always open to me, whether it was for help on my thesis or for advice on how to get through my PhD. I know that he occasionally doubt his supervising abilities, but my experience tells me that he is and will be an amazing supervisor. Besides that he has been a great friend through it all and I am very thankful for that.

I have greatly appreciated the opportunity to travel to and observe with the Atacama Pathfinder Experiment (APEX) telescope. A very big thank you goes to the APEX staff who has managed to create a friendly and including atmosphere that is focused around science and the telescope. I always looked forward to and enjoyed these trips, that were both fun and educational.

I am grateful to my colleagues in the submillimeter group and International Max-Planck Research School (IMPRS) for their support and encouragement as well as the stimulating research atmosphere and friendly work place that they created. I would also like to thank my office mates through the time I have spend here for a good and friendly climate in the office. The first office mate I met was Katharina Immer and she grew to become one of my best friends. I am very thankful for both her friendship and the guidance she has provided me with throughout my PhD.

I would like to offer my special thanks to the people who proof-read my dissertation and gave constructive comments and feedback: Axel Weiß, Christian Henkel, Eva Bøgelund, and Mathilde Lindhart.

I thank Prof. Dr. Cristiano Porciani for being on my thesis committee and for

advice during my thesis committee meeting. I would also like to thank Prof. Dr. Ian C. Brock and Prof. Dr. Christiane Dahl for joining the PhD examination committee.

I want to thank my danish girls Ann-Katrine, Bitten, Eva, Mathilde, Mette, Simone, and Turi for their support and welcome distractions. I am so grateful that we still talk almost everyday. You are all so amazing and I am so proud of each you. I regularly brag about your newest achievements to anyone who will listen. A special thanks to Mette for listening and advising when things got frustrating and for providing me with fun and interesting things to read and watch. It has been a welcome distraction that has helped lift my mood so many times. I would also like to specially thank Eva, who is the sweetest and most optimistic person I know. I cannot be in her company without smiling. Her visits here, with endless cups of tea has allowed us to talk through everything. A very special thanks goes to Mathilde, who has supported me in many ways, but the many long skype conversations when I needed it, and the help and advice given when everything seemed bleak were invaluable. She is the bravest and coolest person I know and there is no way I would have made it this far without her.

I also want to thank all the friends i have made during my time in Bonn. Some left while I was here, some arrived later, and some have been here through it all, but they all have in common that we have had a great time together. Thanks for the weekly Sunday brunch at Mademoiselles (an additional thanks to Sarah for the yummy food), fun evening out on the town, dinners, Christmas markets, carnivals, bouldering sessions and good times spend together. During my time spend in Munich I became friends with a great group of people who got me hooked on geocaching through long and dark, but very fun, nights in the forest. Thank you for your great company.

I also want to express my gratitude to Calum Anderson who helped me pick myself up and get through the last part of the PhD.

I also want to thank my family and the people closest to me. First Florian, for all his support. I know I have not always been easy to be around, but he has always been there with a hug and a joke to make everything a bit better. He and Fauli can always make me laugh and we have had so many great experiences. He is my rock!

The biggest thanks goes to my parent without whom I would have surely not made it so far and to whom this thesis is dedicated. They raised me to believe that I can do anything I want and support me in getting there. It has not been easy living so far away from them, but luckily they are good at skyping, have travelled here, and have helped me with tickets to get to Denmark. I love them very much. I also want to thank my sister and grandparents for their support.

Contents

Chapter 1

Introduction

1.1 Galaxy Formation and Evolution

When the Universe was created 13.8 billion years ago it looked significantly different than it does today. In its original state it was made up of a hot and dense ionized plasma soup. As it expanded it cooled down, and after $\sim 380\,000$ years (redshift of $z \sim 1089$) it reached temperatures at which neutral Hydrogen could form. This neutralization made it transparent, marking the end of what has been named the Dark Ages. Between 150 million and one billion years after the Big Bang ($6 \lesssim z \lesssim 20$) the first stars and galaxies were formed, initiating the Epoch of Reionization (EoR) (Ryden, 2003). In this thesis I investigate how star formation evolves over cosmic time by studying some of the most intensely star forming galaxies in the Universe (Chapter 4 and 5). In particular, the exploration of galaxies in the EoR is the theme of Chapter 6.

The first studies of the star formation history of the Universe were based on sources identified at ultraviolet (UV) wavelengths (Madau et al., 1996). UV light is emitted by the most massive and hot stars (O-stars) which only live short lives of ~ 0.5 billion years (in contrast to low mass stars, like the Sun, that live for ~ 10 billion years), and UV light therefore traces newly-formed or very young stellar populations (Stahler & Palla, 2004). Using UV light to trace star formation unfortunately misses the star formation happening enshrouded in dust clouds. Here, the ongoing star formation heats the surrounding dust and gas clouds. This heat is emitted as thermal radiation in the millimeter (mm), submillimeter (submm) and far infrared (FIR) regime and can be used to trace dust enshrouded star formation both in our own and distant galaxies.

In the last two decades, mm and submm surveys have transformed our understanding of galaxy formation and evolution by revealing that luminous, dusty galaxies were a thousand times more abundant in the early Universe than they are at the present day (e.g., see review by Casey et al., 2014).

1.2 Dusty Star-Forming Galaxies

Dusty Star Forming Galaxies (DSFGs) are galaxies found or selected at wavelengths where the emission is dominated by dust, i.e. their thermal dust peak. To investigate star formation across cosmic time, the effect of redshift must be considered. When DSFGs are redshifted the observed frequency changes as $\nu_{\rm obs} = \nu_{\rm emit}/(1+z)$ and the flux is dimmed by the redshift as $S_{\rm obs} \propto S_{\rm emit}(1+z)/D_{\rm L}^2$. The change in observing frequency and flux with redshift, shifts the thermal dust peak parallel to the Rayleigh-Jeans slope, resulting in a constant flux density over a large redshift interval

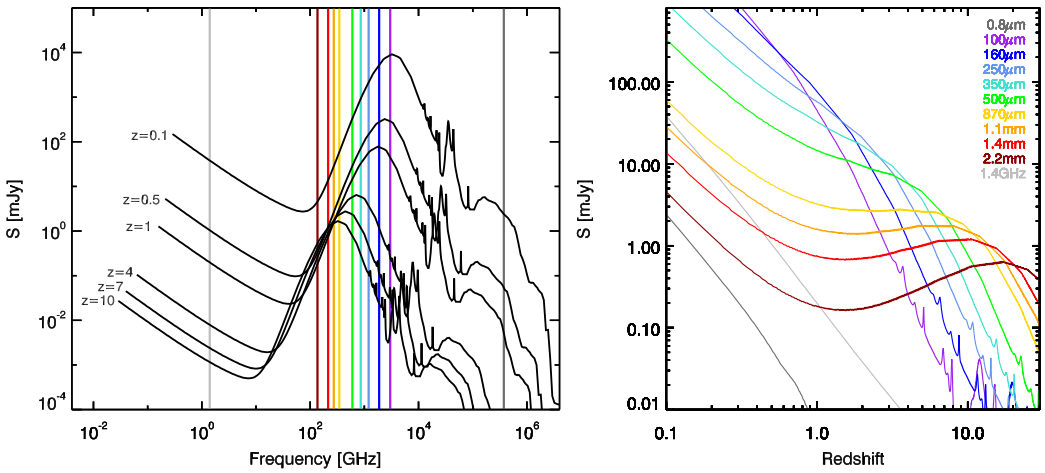

Figure 1.1: *Left*: The Arp220 SED template as it would appear from an observers perspective at different redshifts. The top SED is at the redshift of Arp220, $z = 0.1$. The SEDs below have been redshifted as indicated. *Right*: The flux density as a function of redshift for Arp220. Each line illustrates how the flux density changes with redshift at a certain observed wavelength. The color coding of the observed wavelength is given in the right panel and illustrated by vertical lines in the left panel.

for certain wavelengths. This effect is called negative K-correction and it is illustrated in Figure 1.1. In the left panel the template of the nearby ($z \sim 0.1$) star forming galaxy Arp220 (Silva et al., 1998) is plotted at different redshifts. The right side of the panel shows how the flux density of Arp220 changes with redshift at selected wavelengths. The wavelengths are chosen from typical surveys and instruments and are differentiated by color, given in the right panel and illustrated as vertical lines in the left panel. At optical and radio wavelengths (*dark gray* and *gray*) a fast drop of flux density with redshift is seen. At $\sim 250\,\mu$m (*light blue*) a flattening of the slope over a small redshift range is seen. At $870\,\mu$m (*yellow*) there is hardly any change in flux density in the redshift range $1 \lesssim z \lesssim 10$. This means that at $870\,\mu$m it is as easy to identify a star forming galaxy at $z \sim 10$ as at $z \sim 1$, assuming that these galaxies have the same intrinsic specific luminosity (luminosity at a given frequency). To study the distribution of galaxies throughout the full history of the Universe, we need to select galaxies at wavelengths where the flux density remains constant over as large a redshift range as possible. This effectively means selecting at around or longer than $870\,\mu$m.

The first mm/submm detected DSFGs were discovered in 1998, by Smail et al. (1997), Hughes et al. (1998) and Barger et al. (1998) using the newly installed Submillimeter Common User Bolometer Array (SCUBA) at the James Clerk Maxwell Telescope (JCMT). SCUBA, observing at $850\,\mu$m, was the first instrument to observe at submm wavelengths. The sources were named submm galaxies (SMGs) as they were discovered at submm wavelengths. Nowadays these sources are referred to as DSFGs as detection wavelengths has extended beyond the submm range and into the mm range and the term SMG was therefore no longer appropriate. It was clear that these sources

are members of a new galaxy population, and efforts to determine their redshifts and learn more about them were undertaken. The extra-galactic surveys were performed with single-dish submm telescopes, like the JCMT, which have a poor spatial resolution of ~ 20 arcsec($''$) (in contrast to an angular resolution of $\sim 0.05''$ of Hubble). This halted immediate counterpart identification at optical wavelengths. Furthermore, as seen from Figure 1.1 DSFGs are weak at optical wavelengths making them difficult or impossible to detect.

Counterpart identification was at this time essential because the only way to spectroscopically identify the redshift was through optical spectroscopy. The problem with identifying counterparts meant that when Barger et al. (1999) attempted to gather redshifts of the DSFGs identified in the first SCUBA map, only 25 % of the bright sources were assigned redshifts and counterparts of most of the weaker sources remained unidentified.

Even with high spatial resolution data taken at radio (e.g., Ivison et al., 2002) and/or mid-infrared (MIR) (e.g., Ashby et al., 2006; Pope et al., 2006) wavelengths, the K-correction made the counterpart identification difficult or impossible (See Figure 1.1). Thus, 50% of DSFGs typically lack robust counterparts at other wavelengths (e.g., Biggs et al., 2011), although the exact fraction depends on the depth of the radio/MIR observations. This mismatch in sensitivity at different wavelengths has potentially left the highest-redshift sources ($z > 3$) unidentified, which would bias the observed redshift distribution of DSFGs towards lower redshifts.

Using high-resolution observations from the Very Large Array (VLA, a radio telescope composed of 27 radio antennas located in New Mexico) Chapman et al. (2005) identified counterparts of 60 % of 150 sources detected in the original SCUBA maps. For 73 sources (75 % of the targeted sample), spectroscopic redshifts were obtained from deep optical spectroscopy. The median redshift of $z_{\rm median,Chapman} = 2.2$ found for the sample, indicated that the peak of star formation for DSFGs were coeval with the peak of black hole accretion and cosmic star formation (e.g., Hopkins & Beacom, 2006). This suggested that a significant fraction of star formation activity in the universe at $z = 2 - 3$ is taking place in DSFGs brighter than $\rm S_{850\mu m} \approx 1$ mJy, and could be hidden from the view of optical/UV observations owing to the large dust obscuration (e.g., Wardlow et al., 2011).

Theoretical models suggest that the contribution of DSFGs to the total star formation rate density at $z = 2-4$ is of order 10% (for sources with $S_{870\mu m} > 1$ mJy; González et al., 2011). While the history of star formation has now been measured out to $z \sim 8$ through rest-frame UV surveys (see review by Madau & Dickinson, 2014), progress in measuring highly obscured star formation as a function of look-back time has been much slower, mainly because of the difficulties in obtaining robust redshifts for DSFGs.

Mm interferometry provides a more reliable and complete method to obtain secure multi-wavelength identifications of DSFGs discovered in single-dish surveys. Dannerbauer et al. (2002) first published counterpart identifications based on high spatial resolution data for three 1.2 mm-selected DSFGs observed with the IRAM Plateau de Bure Interferometer (PdBI), and Younger et al. (2007) used the Submillimeter Array (SMA) to identify counterparts of seven 1.1 mm-detected sources. In spite of the accu-

rate and reliable positions, neither study successfully obtained redshifts for the DSFGs, although one of the sources was eventually determined to be at a record-breaking (for DSFGs) $z = 5.3$, assigned using rest frame UV spectroscopy (Riechers et al., 2010; Capak et al., 2011). Smolčić et al. (2012) used PdBI to follow up a sample of 1.1 mm selected DSFGs, leading to optical spectroscopic redshifts for roughly half the sample and photometric redshift estimates for the remaining half. This study found a mean redshift of $\bar{z}$=3.1 suggesting that the previous spectroscopically determined redshift distributions of DSFGs (e.g., Chapman et al., 2005) were biased towards lower values. Other follow-up efforts have led to different conclusions. For example, Simpson et al. (2014) and more recently da Cunha et al. (2015) use the 17-band optical to MIR photometry of the Extended Chandra Deep Field South (ECDFS) to study the photometric redshift distribution of DSFGs with counterpart identification based on high resolution Atacama Large Mm/submm Array (ALMA) 870μm observations (Hodge et al., 2013). Simpson et al. (2014) derive a median redshift of $\bar{z} = 2.5$, albeit with a significant tail of DSFGs at $z > 4$. This result is consistent with the early findings of Chapman et al. (2005) under the assumption that Chapman et al. (2005) did not detect the high-redshift tail since that study only targeted radio-confirmed DSFGs.

In the past few years, new instruments with larger bandwidths have enabled a more direct and unbiased way to derive redshifts of DSFGs via observations of molecular emission lines at mm wavelengths. The molecular line emission, typically from CO, or [C II], can be related unambiguously to the mm/submm dust continuum, eliminating the need for high-resolution imaging, counterpart identification, and optical spectroscopy (Weiß et al., 2009; Harris et al., 2012; Lupu et al., 2012; Walter et al., 2012; Chapman et al., 2015). The first redshift distribution based on molecular emission lines detected via blind spectral scans in the 3 mm window using ALMA was published by Weiß et al. (2013) for 26 strongly lensed sources selected from the 2500 degree^2 South Pole Telescope (SPT) survey. Performing a redshift search for such a big sample in the early stage of ALMA operations was only possible due to the strongly lensed nature of the sources which makes them extraordinarily bright. The redshift distribution of the SPT sample showed a higher mean ($\bar{z} = 3.5$) than observed for any other sample of DSFGs and has stimulated an on-going discussion on the redshift distribution of DSFGs in the literature (e.g., Koprowski et al., 2014; Miettinen et al., 2015; Béthermin et al., 2015). In this thesis we study a larger sample of the SPT selected sources and investigate the redshift distribution further.

Progress has also been made towards a theoretical understanding of the differences seen in observed redshift distributions. Recently Béthermin et al. (2015) modeled the expected DSFG redshift distribution based on a phenomenological model of galaxy evolution. They conclude the difference can be understood in terms of survey selection wavelengths and, to a minor degree, the survey depth. In addition, they investigate the effect of gravitational lensing on the redshift distribution. At wavelengths shorter than 1.1 mm the lensed redshift distribution always tends to show a higher median redshift than the unlensed distribution. At longer selection wavelengths, as investigated here, the effect of gravitational lensing on the redshift distribution vanishes unless only extremely luminous sources are selected (e.g., $S_{1.4\mathrm{mm}} > 25$ mJy).

1.3 DSFGs in the Epoch of Reionization

Searches for the most distant galaxies have now reached as far back as the first billion years in the history of the Universe, and are peeking into the Epoch of Reionization (EoR). Some of the most important questions in observational cosmology concern the time scale over which the reionization of the Universe took place, the identification of the objects providing the ionizing photons and the enrichment of galaxies with metals. It is expected that star-forming galaxies play a major role in the reionization, so to understand the evolution of the Universe from its neutral phase to its present ionized state we must study the galaxies in the EoR (see reviews by Stark, 2016; Bouwens, 2016). Galaxies in the EoR are currently being identified from rest-frame UV surveys (e.g. Ouchi et al., 2010). Most of these systems, however, are low-mass star-forming galaxies for which the enrichment of the cold interstellar medium (ISM) is difficult to study even in long integrations with the ALMA (Bouwens et al., 2016, b).

Massive DSFGs are not expected to be found in the EoR as it is theoretically difficult to produce their large dust masses within a few hundred Myr of the Big Bang (Ferrara, 2010; Mattsson, 2015). Recent wide-area *Herschel* and optical Quasi-stellar object (QSO) surveys, however, have revealed dusty galaxies out to $z \sim 6$ - 7 (e.g., Venemans et al., 2012; Riechers et al., 2013; Strandet et al., 2017). These systems offer the unique opportunity to study extreme cases of metal/dust enrichment of the ISM within the EoR in the most massive over-densities at these redshifts.

1.4 Atmospheric Transmission

A major challenge when studying DSFGs is the poor transmission at the mm/submm wavelengths caused by water in earth's atmosphere. Water in the atmosphere decreases the percentage of the signal that gets through, increases the noise by radiating thermally, and inhomogeneities in the water vapor distribution degrade the sensitivity and resolution of the images produced. Figure 1.2 shows the atmospheric transmission between 10 and 1000 GHz (30 - 0.3 mm) for different water vapor contents at 5000 m. The atmospheric transmission degrades with frequency and is broken up into small windows by emission lines from water in the atmosphere. The different colors show how the precipital water vapor (pwv) content of the atmosphere affects the transmission. The effect of the pwv on the transmission is largest at high frequencies and near atmospheric water emission lines. Low transmission will lead to long observing times and poor calibration. Observations performed at frequencies with poor transmission therefore need very good weather conditions. Only a few places on earth are dry enough to reach pwv < 0.5 mm, and even here sufficient weather conditions might only occur a small percentage of the time. Chajnantor, at an altitude of 5000 m, in the Atacama desert is the host of the Atacama Pathfinder EXperiment (APEX) and ALMA, and is famous for its exceptional atmospheric conditions for mm and submm observations. From Figure 1.2 we see that close to atmospheric water lines and above $\nu_{\rm obs} \gtrsim 500$ GHz, a pwv of < 0.5 is needed to obtain a reasonable transmission. Unfortunately pwv < 0.5 only occurs around 25% of the time in just the five best months of the year (For more information on the weather

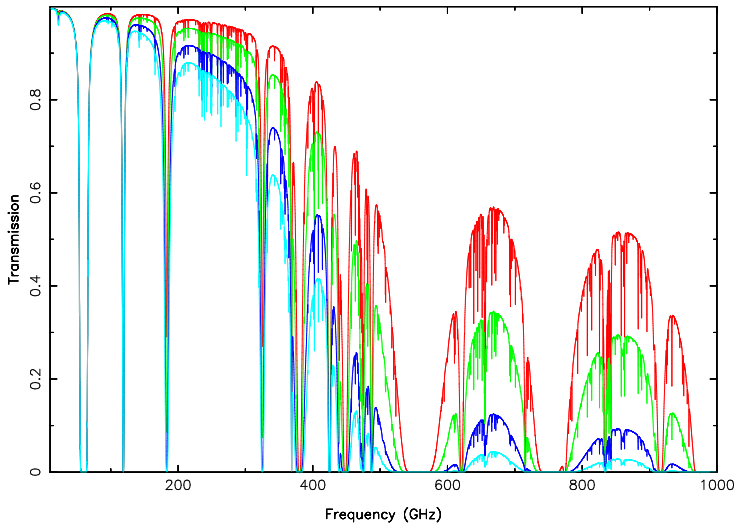

Figure 1.2: Atmospheric transmission in the mm/submm wavelength regime as modeled for Chajnantor at 5000 m height in the Atacama dessert. The different colors illustrate different atmospheric precipital water vapor (pwv) levels showing very good conditions in *red* (pwv = 0.5), good conditions in *green* (pwv = 1.0) and mediocre condition in *blue* (pwv = 2.0) and *light blue* (pwv = 3.0). The figure is made using the atmospheric calculator from the APEX webpage (http://www.apex-telescope.org/sites/chajnantor/atmosphere/transpwv/).

conditions at Chajnantor see https://almascience.nrao.edu/about-alma/weather).

Figure 1.2 shows that frequencies below $\nu_{\rm obs} < 230\,{\rm GHz}$ are advantageous for performing surveys.

1.5 Gravitational lensing

Gravitational lensing amplifies the light from distant sources on the sky and can help us detect these. Gravitational lensing is a consequence of Einstein's theory of general relativity, where mass can bend light, and occurs when two objects align along a line of sight. The light from the background source is deflected by the foreground source (lens) and is seen as multiple images, arcs or Einstein rings. When the lensing produces multiple images or a ring of the background source it is defined as strong gravitational lensing. In these cases the lens is typically a galaxy or a galaxy cluster.

The magnification occurs as the apparent solid angle of the source is increased while the surface brightness of the source is preserved. The magnification is given by the ratio of the observed and intrinsic size of a source. The more massive the foreground source, the larger the apparent solid angle and thereby magnification. The magnification of the source flux density makes it possible to find and observe sources, that would otherwise have been to faint to observe.

When the source and lens are perfectly aligned the source will appear as a ring, also known as an Einstein ring. Perfect Einstein rings are created only at perfect alignment and when the foreground object is gravitationally symmetric along the line of sight

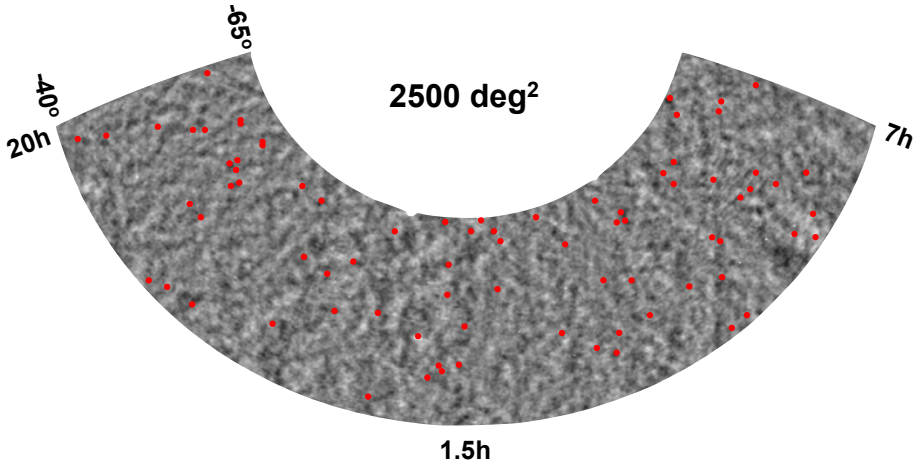

Figure 1.3: A map of the full 2500 degree^2 SPT-survey. The *red* dots show the positions of the SPT sources.

(like an elliptical galaxy). When the alignment is not perfect or the foreground object is not gravitationally symmetric (like a galaxy cluster) arcs or multiple source images are seen.

Unfortunately such alignments of two sources in our line of sight are rare and a very large survey is needed to build a sample of gravitationally lensed sources.

For more details on gravitational lensing, see the review by Wambsganss (1998).

1.6 The South Pole Telescope sources

The SPT (Carlstrom et al., 2011) has systematically identified a population of high-redshift, strongly gravitationally lensed systems by selecting extremely mm-bright objects from the largest mm-wavelength survey of the extragalactic sky (Vieira et al., 2010; Mocanu et al., 2013).

The SPT survey covers an impressive 2500 degree^2 at 1.4 mm, 2.2 mm and 3.0 mm, see Figure 1.3. The aim of the survey is to study the cosmic microwave background (CMB) structure and the Sunyav-Zel'dovich signal from Galaxy clusters and was the first of its kind in size. Due to its large extent it became possible to assemble a large sample of rare and bright sources in the mm regime.

Point sources are identified from a detection at 1.4 mm which typically means $S_{1.4\mathrm{mm}} > 15$ mJy. The dusty sources are selected based on their spectral index, calculated as the ratio $S_{1.4\mathrm{mm}}/S_{2.2\mathrm{mm}}$. Figure 1.4 shows the distribution of the spectral index for all point sources in the SPT survey, which splits into two populations: A synchrotron dominated population ($S_{1.4\mathrm{mm}}/S_{2.2\mathrm{mm}} \lesssim 1.5$) and a dust dominated population ($S_{1.4\mathrm{mm}}/S_{2.2\mathrm{mm}} \gtrsim 1.5$). Sources with a spectral index above $S_{1.4\mathrm{mm}}/S_{2.2\mathrm{mm}} > 1.66$ are selected. To isolate the high-redshift DSFG population, sources with counterparts in the IRAS Faint Source Catalog and the 843 MHz Sydney University Molonglo Sky

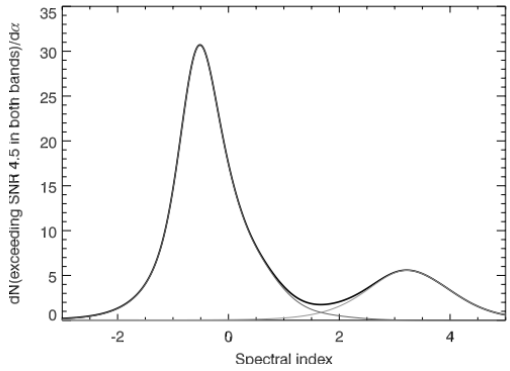

Figure 1.4: Distribution of the sources detected in the SPT survey as a function of their spectral index ($S_{1.4\mathrm{mm}}/S_{2.2\mathrm{mm}}$). This plot was published by Vieira et al. (2010).

Survey were removed as these are most likely very low redshift sources. With these vetoes ~ 150 sources remained. These sources were observed with LABOCA and when possible SPIRE and the sample was narrowed down to 91 high redshift DSFGs. The process of confirming the sources is described in more detail in Section 3.2. Given the brightness and rarity of the sources they were good candidates for gravitationally lensed high redshift objects.

High resolution ALMA imaging at 870 μm (see Figure 1.5) showed gravitational lensing features (rings, arcs, and multiple source images) and demonstrated that the SPT-DSFGs are indeed mostly gravitationally lensed (Hezaveh et al., 2013). The SPT sample also contains a few unlensed sources and recently high resolution imaging revealed that, for at least one of these sources, the submm emission arises from a dozen unlensed galaxies in a compact protocluster at $z = 4.3$ (Miller et al. submitted).

The high redshift nature of the sources was first investigated photometrically (see Chapter 2.1) for 11 SPT-DSFGs by Greve et al. (2012) where a median redshift of $z_{\mathrm{photometric,median}} = 3.0$ was found. The redshifts were determined through spectral energy distribution (SED) fitting of photometric measurements at 2.0 and 1.4 mm from SPT and at 870 and 350 μm from LABOCA/SABOCA at APEX. Weiß et al. (2013) published a spectroscopic survey of 26 SPT-DSFGs using ALMA. Based on the unambiguous redshifts and the best possible redshift identification for the sources with a single line, a median redshift of $z_{\mathrm{spectroscopic,median}} = 3.5$ was found.

The SPT-DSFG sample is the largest sample of gravitationally lensed high redshift galaxies, available today. They do not represent the most common galaxies in the Universe, but with star formation rates (SFRs) reaching a few thousand solar masses per year they do represent the most intense star formation (Casey et al., 2014). The SPT-DSFGs are therefore a good tool for studying the most intense stellar mass build up in the cosmic history.

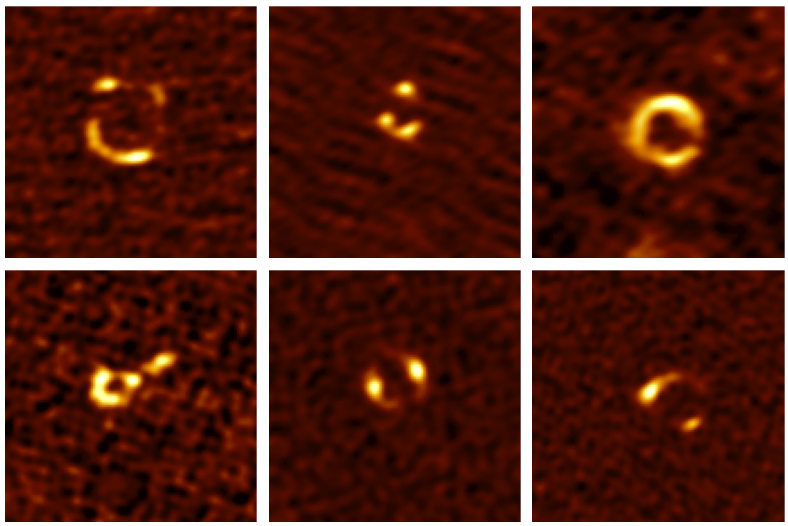

Figure 1.5: High resolution ALMA 870 μm imaging of six SPT-DSFGs. The maps are 10″ × 10″. The sources are from left to right in the top row SPT0113-46, SPT0346-52, and SPT0418-47 and in the bottom row SPT2103-60, SPT2146-55, and SPT2147-50. These high resolution images show that the SPT-DSFGs are mostly gravitationally lensed. These maps were published by Hezaveh et al. (2013) and Vieira et al. (2013).

1.7 This thesis

This thesis focuses on determining redshifts of the SPT-DSFGs. Since the SPT-DSFGs are selected at 1.4 mm, their flux density is constant over a very broad redshift range ($z = 1-10$, see Figure 1.1). As such it is of prime importance to determine their redshift to put the sources into a cosmological context and to derive their intrinsic properties such as their baryonic mass and the star formation rates for comparison to other galaxy samples.

The methods to find both spectroscopic and photometric redshifts are described in Chapter 2. Chapter 3 presents the observations on which the thesis is build. It is split into two sections, one presenting the spectroscopic observations and one presenting the photometric observations. Chapter 4 presents spectroscopic redshift scans for a total of 42 sources, extending the original sample of 26 DSFG studied by Weiß et al. (2013) to 68 galaxies. Together with previously determined spectroscopic redshifts we determine the redshift distribution of the SPT-DSFGs. In Chapter 5 we discuss the photometric properties of the full SPT-DSFG sample of 91 galaxies. We investigate the redshift distribution of the full sample and study the dust in these sources by deriving dust temperatures, infrared (IR) luminosities, star formation rates and dust masses. Chapter 6 focuses on SPT0311-58 which is the highest redshift source in the SPT-DSFG sample and the highest redshift DSFG currently known. Its spectroscopic redshift was derived from the redshift scans at 3 mm described in Chapter 4 and we investigate the ISM properties in this unique object by analyzing the dust continuum as well as the CO, CI and CII line emission.

Chapter 2

Methods

2.1 Spectral Energy Distributions

Spectral Energy Distributions (SEDs) from submm/mm data are used to fit the photometric data of a source to obtain parameters as redshift, dust temperature, dust mass, IR and FIR luminosity, and SFR. A good photometric coverage from optical through MIR to mm or even radio wavelengths gives the best constraints on the photometric redshift. Unfortunately this is where the gravitationally lensed nature of the SPT-DSFGs becomes a disadvantage. The lensing galaxies are typically massive elliptical galaxies containing only little gas, which means that they do not emit strong mm and FIR emission, but are instead optically bright. Emission from the lensing galaxy at submm and mm wavelengths is therefore not a worry, but at optical and MIR and NIR wavelengths the lensing galaxy is much brighter than the DSFG and thereby contaminates the observations. Ma et al. (2015) decomposed high spatial resolution imaging data for six SPT-DSFGs from *Hubble Space Telescope* and *Spitzer*. This required tremendous efforts, and the uncertainties of the fluxes are large. High quality photometric data for the SPT-DSFGs is therefore limited to submm/mm and IR wavelengths, covering the dust peak.

The simplest way of fitting the thermal dust emission is with a Planck distribution where the flux density, B_ν, is described as a function of frequency, ν, by

$$B_\nu(T_{\rm dust}) = \frac{2h\nu^3}{c^2}\frac{1}{e^{\frac{h\nu}{k_{\rm B}T_{\rm dust}}}-1}, \tag{2.1}$$

where $T_{\rm dust}$ is the dust temperature, h is the Planck constant ($6.62607004 \times 10^{-34}\,{\rm m^2\,kg\,s^{-1}}$), c is the speed of light ($299\,792\,458\,{\rm m\,s^{-1}}$), and $k_{\rm B}$ is the Boltzmann constant ($1.38064852 \times 10^{-23}\,{\rm m^2\,kg\,s^{-2}\,K^{-1}}$). The Planck law is valid when the dust opacity is $\tau_\nu \gg 1$, which does not hold for dusty galaxies, as the emission is not optically thick over the full frequency range of the SED. To correct for this, a dust opacity (τ_ν) that is dependent on frequency is adopted and the flux density is given by

$$S_\nu = B_\nu(T_{\rm dust})\big(1-{\rm e}^{-\tau_\nu}\big)\Omega_{\rm s}, \tag{2.2}$$

where $\Omega_{\rm s}$ is the source solid angle which is incorporated to take the source size into account. The dust opacity is calculated as

$$\tau_\nu = \kappa_{\rm dust}(\nu)M_{\rm dust}/(D_A^2\Omega_{\rm s}), \tag{2.3}$$

where $\kappa_{\rm dust}$ is the dust absorption coefficient, $M_{\rm dust}$ is the dust mass and D_A is the angular size distance that relates to the luminosity distance as $D_L = (1+z)^2 D_A$. The

dust absorption coefficient can be expressed as ν^{β}, where β is the spectral index of the emissivity. As the source solid angle is typically unknown we cannot securely derive the dust column density ($M_{\rm dust}/(D_A^2\Omega_{\rm s})$), and we therefore use a simplified version of Equation 2.3 where the normalization of the opacity is done by assuming a critical frequency ν_c where the dust opacity becomes unity. That gives the following expression for the optical depth

$$\tau_\nu = \left(\frac{\nu}{\nu_c}\right)^{\beta}. \tag{2.4}$$

Incorporating this into Equation 2.2 gives the expression

$$S_\nu = \Omega_{\rm s} B_\nu(T_{\rm dust}) \left(1 - {\rm e}^{\left(\frac{\nu}{\nu_c}\right)^{\beta}}\right). \tag{2.5}$$

This equation is in the restframe of the source, but as we are investigating high redshift sources, the redshift dependence also needs to be implemented. The observed frequency depends on redshift as $\nu_{\rm obs} = \nu_{\rm rest}(z+1)^{-1}$ and the flux as $S_{\rm obs} = S_\nu(z+1)^{-3}$. The source solid angle is also redshift dependent and can be expressed as $\Omega_{\rm s} = (1+z)^4 A/D_L^2$, where A is the area of the source. Another aspect that becomes increasingly important with redshift is the effect of the CMB temperature which is dependent on redshift as $T_{\rm CMB}(z) = (z+1)T_{\rm CMB}^{z=0}$. Implementing all this into Equation 2.5 gives the expression

$$S_{\nu_{\rm obs}} = \frac{(z+1)A}{D_L^2}\Big(B_{\nu_{\rm rest}}(T_{\rm dust}) - B_{\nu_{\rm rest}}(T_{\rm CMB}[z])\Big)\left(1 - {\rm e}^{\left(\frac{\nu_{\rm rest}}{\nu_c}\right)^{\beta}}\right). \tag{2.6}$$

As the observed frequency has to be transformed into a restframe frequency, the exponential of the blackbody will carry the redshift as $\propto (z+1)T_{\rm dust}^{-1}$. The redshift and dust temperature are therefore degenerate and one cannot be determined without knowledge or assumption of the other.

2.1.1 Dust masses

To calculate dust masses we use an optically thin approximation of Equation 2.2, where $1 - e^{-\tau_\nu} \rightarrow \tau_\nu$, which applies at the Rayleigh Jeans side of the peak, so the exponential becomes very small. We include the CMB in the same manner as Equation 2.6. The expression of the observed flux becomes

$$S_{\nu_{\rm obs}} = \Omega_{\rm s}\tau_{\nu_{\rm rest}}\big(B_{\nu_{\rm rest}}(T_{\rm dust}) - B_{\nu_{\rm rest}}(T_{\rm CMB})\big). \tag{2.7}$$

Inserting the expression for τ_ν defined in Equation 2.3 and isolating the dust mass gives the expression

$$M_{\rm dust} = \frac{S_{\nu_{\rm obs}} D_{\rm L}^2}{\kappa_{\rm dust}(\nu_{\rm rest})}\big(B_{\nu_{\rm rest}}(T_{\rm dust}) - B_{\nu_{\rm rest}}(T_{\rm CMB})\big)^{-1}. \tag{2.8}$$

This expression holds at wavelengths were the emission is optically thin, which is at the Rayleigh Jeans side of the SED, and typically considered to be above 100 μm at the restframe of the source. This means that the SPT sources is represented by the 870 μm flux density.

2.1.2 Infra red luminosity and Star Formation Rates

The IR or FIR luminosity is an indicator of the amount of obscured star formation in the galaxy. The IR luminosity $L_{\rm IR}$ is calculated as the integral between 8 and 1000 μm and the FIR luminosity $L_{\rm FIR}$ is calculated as the integral of the SED between 40 and 120 μm at the restframe of the studied galaxies (these definitions can vary in the literature).

The IR luminosity scaling relations can be used to determine the SFR of the sources. The SFR is calculated as through this relation presented by Kennicutt (1998):

$$SFR(M_{\odot}\mathrm{yr}^{-1}) = 4.5 \times 10^{-44} L_{\rm IR}(\mathrm{erg\ s}^{-1}) = 1.71 \times 10^{-10} L_{\rm IR}(L_{\odot}). \qquad (2.9)$$

2.2 Finding redshifts

Redshifts can be determined either photometrically or spectroscopically. Spectroscopic redshifts are more precise, but as they require deep integrations, they usually need significantly longer observing times and/or better facilities. Photometric redshifts are calculated from photometric measurements of the source. These measurements are faster, but the uncertainty on the redshift is larger.

2.2.1 Spectroscopic redshifts

The most precise and secure way to determine redshifts of galaxies is through spectroscopic observations. To avoid problems with counterpart identification it is advantageous to observe lines from the molecular gas, which originates from the same component that is responsible for the thermal dust peak used for the source identification. The brightest lines and best probes for redshift identification are CO lines and fine structure lines (FSLs) like [C II] and [O III]. Figure 2.1 shows redshift coverage as a function of observing frequency for the strongest emission lines arising from the ISM of a galaxy which is actively forming stars.

Figure 2.2 shows the submm to FIR spectrum (450–1500 GHz) of Mrk231, a nearby Ultra Luminous IR Galaxy (ULIRG), observed by SPIRE/*Herschel*. The spectrum shows strong emission from CO transitions between CO(5–4) and CO(13–12) (the CO ladder), both fine structure lines of atomic carbon, several water transitions as well as the [N II] fine structure line. All these lines have been shown to be strong also in high redshift galaxies (e.g. Riechers et al., 2013) and may serve as probes for determining the redshift of a source. Of particular importance for determining spectroscopic redshifts is the CO ladder because its rest-frequencies are evenly distributed over the entire submm to FIR regime with a spacing of 115 GHz $\times J_{\rm up}$, and scaling with redshift as $(1+z)^{-1}$. Surveying a sufficiently large frequency range of the spectrum will therefore yield detections of two lines at most redshifts. Taking into account the transmission shown in Figure 1.2, the transmission window around 3 mm (85 GHz to 115 GHz) is the most optimal for carrying out a spectral survey for CO lines. By scanning this window using ALMA we are sensitive to CO lines between the CO(1–0) and CO(7–6) transition, which gives a redshift coverage of $0.0 < z < 0.4$ and $1.0 < z < 8.6$ with a narrow redshift

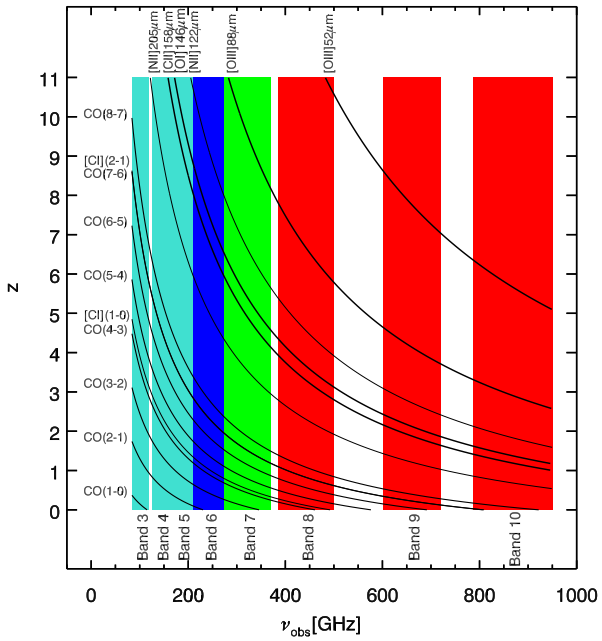

Figure 2.1: Lines to identify redshifts as a function of frequencies. The colored areas show the ALMA bands and the colors represent the average estimated water vapor needed to observe in the band, and are as in Figure 1.2: pwv = 3.0 is *turquoise*, pwv = 2.0 is *blue*, pwv = 1 is *green* and pwv = 0.5 is *red*.

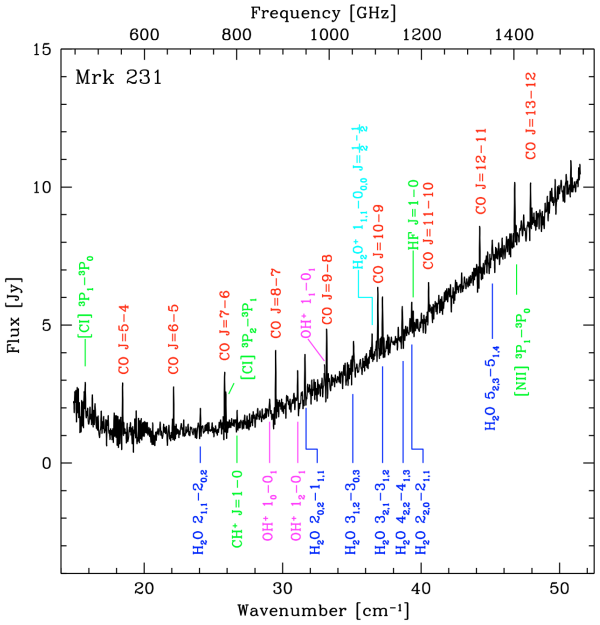

Figure 2.2: *Herschel*/SPIRE spectrum of the nearby ULIRG Mrk 231 illustrating the bright emission lines arising from the ISM of this star-forming galaxy. The spectrum is published by van der Werf et al. (2010).

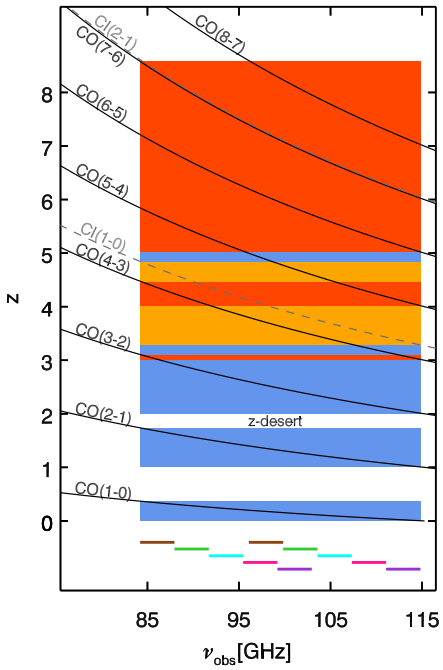

Figure 2.3: Redshift as a function of the ALMA 3 mm spectral scan coverage, where the *black* lines show the CO transitions and the *gray* lines show the [C I] transitions. The *red* areas show redshift ranges where we have two CO lines, the *orange* areas show the redshift ranges where the second line is the weaker [C I] line and the *blue* areas show the redshift ranges where we will see a single line. At the bottom of the plot the placement of the five tunings are shown.

desert at $1.74 < z < 2.00$, see Figure 2.3. Above $z > 3.3$ two or more lines are seen in this frequency range, except for a small window at $4.8 < z < 5.0$.

FSLs are typically the brightest lines, with lines like [C II] capable of carrying up to 1% of the bolometric flux of a source. [C II] is emitted in photon dominated regions tracing ongoing star formation. Unfortunately FSLs are not optimal for a spectral search as they are further apart in the spectrum meaning that to get two lines in one spectral scan a very large frequency range must be searched. Furthermore the high frequency of [C II] ($\nu_{[\mathrm{CII}]} = 1900.54\,\mathrm{GHz}$) means that for sources at redshift $z \lesssim 4$ these lines need very good weather conditions (see Figure 2.1). Instead these bright lines are optimal for targeted follow-up observations to confirm redshifts, when only one spectral line is detected in a source.

2.2.2 Photometric redshifts

As spectroscopic redshifts can be hard to achieve due to long observation times or the need for large telescope facilities (like ALMA), an approximate redshift can be determined using photometry. Photometry used for fitting photometric redshifts typically extends into the optical regime, but as high-redshift DSFGs are weak at optical wavelengths, and the lensing source usually is bright at optical wavelengths, it is difficult

or impossible to extract a flux density for the SPT-DSFGs here. For the SPT-DSFGs this means that only submm, mm and FIR photometry is fitted. The FIR photometry is very difficult to observe from earth, and fitting photometric redshifts without optical data only really took off after the launch of *Herschel*. The fitting of the photometry can be done either with an SED or with galaxy templates.

2.2.2.1 Fitting SEDs

We fit the SEDs using Equation 2.6. Unfortunately this equation has a degeneracy between the redshift and dust temperature, so to determine the redshift we need to assume an appropriate dust temperature. By fitting SEDs to the subsample of the SPT-DSFGs with spectroscopic redshifts a probability distribution of dust temperatures can be created. This distribution is used to create a probability distribution of the photometric redshift for each source. The details of this will be described in Section 5.2.1. As this method relies on determining the frequency at which the dust peak occurs, it is important to have photometry that shows the fall off on both sides, and is well sampled around the peak.

2.2.2.2 Fitting library templates

Theoretical or emiprical galaxy templates can be used to fit photometric redshifts. However, it is crucial to select templates that are appropriate for the studied sources. Some templates are based purely on radiative transfer modeling (e.g. Siebenmorgen & Krügel, 2007; Siebenmorgen et al., 2014); some are based on empirical data calibrated by either local studies of the ISM (e.g. Draine & Li, 2007), local galaxies (e.g. Chary & Elbaz, 2001; Dale & Helou, 2002), while some choose to split the templates into different types of galaxies separately (e.g. 'normal' star forming galaxies and starburst galaxies) (e.g. Lagache et al., 2003). The biggest challenge for the SPT-DSFGs is the missing observational coverage at the optical, MIR, and NIR wavelengths, that is usually very well described for the templates due to the high number of spectral tracers here (e.g. Polycyclic Aromatic Hydrocarbon (PAH) features) which is valuable for obtaining a good estimate of the photometric redshift. The simplest way of creating an appropriate library of templates for the SPT-DSFG sample is to use the SPT-DSFGs for which a spectroscopic redshift is known. The details of the library is described in Section 5.2.3.

2.2.3 Single line redshifts

As mentioned in Section 2.2.1 two spectroscopic lines are needed to make an unambiguous redshift identification. In the event that only one CO line is detected in a redshift scan we combine this information with that gained from a photometric redshift estimation. A single line will yield concrete redshift options as the line has a limited number of CO-line identifications given the frequency and the possible redshift range. In the typical ALMA CO-redshift scans a single line will be either CO(2–1), CO(3–2), CO(4–3) or CO(5–4) as higher-J CO lines typically will come with a second line. A detailed description of the redshift scans can be found in Section 3.1.2. With the probability

distribution of the photometric redshift we can calculate a probability of each of the redshift options presented by the single line. When possible we confirm the most likely redshift option through spectroscopic observations of e.g. the bright [C II] line. The details of this procedure is described in Section 4.1.

Chapter 3

Observations

This chapter presents the observations that are the basis of this thesis. The first part of the chapter describes the spectroscopic observations, with ALMA redshift scans of 42 SPT-DSFGs, and follow up observations used for redshift confirmations. These observations are the basis of Chapter 4 and part of them are published in **Strandet et al. 2016, The Astrophysical Journal, Volume 822, Issue 2**, which presents ALMA Cycle 1 scans of 15 sources. In this thesis we add spectral scans of an additional 27 sources from ALMA Cycle 3. The second part of the chapter describes the photometric observations, which cover all 91 SPT-DSFGs, and are analyzed in Chapter 5. Some of the photometric measurements have been published in studies of smaller samples. Table 3.2 lists which flux densities are published and where. Chapter 6 presents an in-depth study of the ISM properties of the highest redshift SPT source SPT0311-58 at $z = 6.900(2)$. The redshift is based on a spectral scan presented in this chapter, but additional observations on this source are presented in Chapter 6.

3.1 Spectroscopic Observations

Spectroscopic observations presented in this thesis include ALMA Cycle 1 observations in the 3 mm and 1 mm bands, ALMA Cycle 3 observations in the 3 mm band, as well as observations from APEX using the First Light APEX Submillimeter Heterodyne (FLASH) receiver, the Swedish-ESO PI receiver for APEX (SEPIA), and the Z-spec camera, installed at APEX in 2012 as a guest instrument.

In ALMA Cycle 0, Weiß et al. (2013) set out to determine redshifts for 26 SPT-selected DSFGs using CO lines in the ALMA 3 mm band. Unambiguous redshifts (from multiple CO lines) were determined for twelve sources, while 11 sources showed only a single line. Using the same strategy we searched for CO in the 3 mm band in 15 sources in Cycle 1 and in 27 additional sources in Cycle 3. The observation strategy is presented in Section 3.1.2.

For sources with only one detected line in the 3 mm redshift scans, we use well-sampled photometry to determine a photometric redshift and thereby the most probable line identification and redshift (see Section 2.2.3). We use this information to perform targeted redshift confirmation observations, either in different ALMA bands or using heterodyne receivers on APEX. For eight sources with single line detections in the ALMA Cycle 0 redshift scans, we obtained ALMA Cycle 1 data in band 6 (1 mm) to detect a second CO line or the 205 μm [N II] line; we present these observations in Section 3.1.1. For eight sources (including one source observed in ALMA band 6 and some single-line detections in the Cycle 1 and 3 redshift scans), we followed up the

most probable redshift options with APEX/FLASH targeting [C II] (Section 3.1.3) and APEX/SEPIA targeting higher-J CO transitions (Section 3.1.4). For an additional source a redshift scan was performed in 2012 with APEX/Z-Spec (Section 3.1.5). An overview of these observations is found in Table 3.1.

Table 3.1: Summary of spectroscopic observations presented in this chapter, with ALMA 3 mm continuum positions

Short name	Source	RA	Dec
ALMA 1 mm band 6, redshift confirmation (Figure 4.1)			
SPT0125-50[a]	SPT−S J012506-4723.7	01:25:07.08	-50:38:20.9
SPT0300-46[a]	SPT−S J030003-4621.3	03:00:04.37	-46:21:24.3
SPT0319-47[a]	SPT−S J031931-4724.6	03:19:31.88	-47:24:33.7
SPT0441-46[a]	SPT−S J044143-4605.3	04:41:44.08	-46:05:25.5
SPT0459-58[a]	SPT−S J045859-5805.1	04:58:59.80	-58:05:14.0
SPT0512-59[a]	SPT−S J051258-5935.6	05:12:57.98	-59:35:41.9
SPT0550-53[a]	SPT−S J055001-5356.5	05:50:00.56	-53:56:41.7
SPT2132-58[a]	SPT−S J213242-5802.9	21:32:43.23	-58:02:46.2
ALMA Cycle 1 3 mm band 3, (Figure 4.2)			
SPT0002-52	SPT−S J000223-5232.1	00:02:23.24	-52:31:52.5
SPT2307-50	SPT−S J230726-5003.8	23:07:24.71	-50:03:35.6
SPT2311-54	SPT−S J231125-5450.5	23:11:23.94	-54:50:30.0
SPT2319-55	SPT−S J231922-5557.9	23:19:21.67	-55:57:57.8
SPT2335-53	SPT−S J233513-5324.0	23:35:13.15	-53:24:29.9
SPT2340-59[b]	SPT−S J234009-5943.1	23:40:09.36	-59:43:32.8
		23:40:08.95	-59:43:32.0
SPT2349-50	SPT−S J234942-5053.5	23:49:42.16	-50:53:30.7
SPT2349-56[b]	SPT−S J234944-5638.3	23:49:42.68	-56:38:19.4
		23:49:42.79	-56:38:23.9
		23:49:42.84	-56:38:25.0
SPT2351-57	SPT−S J235149-5722.2	23:51:50.79	-57:22:18.3
SPT2353-50	SPT−S J235339-5010.1	23:53:39.22	-50:10:08.2
SPT2354-58	SPT−S J235434-5815.1	23:54:34.27	-58:15:08.4
SPT2357-51	SPT−S J235718-5153.6	23:57:16.84	-51:53:52.9
ALMA Cycle 3 3 mm band 3, redshift search (Figure 4.3)			
SPT0020-51	SPT−S J002023-5146.3	00:20:23.58	-51:46:39.1
SPT0027-50	SPT−S J002706-5007.3	00:27:06.54	-50:07:19.1
SPT0106-64	SPT−S J010623-6412.9	01:06:23.86	-64:12:50.7
SPT0109-47	SPT−S J010950-4702.1	01:09:49.66	-47:02:12.0
SPT0112-55	SPT−S J011207-5516.2	01:12:09.03	-55:16:41.3
SPT0114-59	SPT−S J011409-5909.2	01:14:08.32	-59:09:27.2
SPT0136-63	SPT−S J013652-6307.3	01:36:50.28	-63:07:24.6
SPT0147-64	SPT−S J014707-6458.9	01:47:07.07	-64:58:53.0
SPT0150-59	SPT−S J015012-5924.0	01:50:09.26	-59:23:59.2
SPT0155-62	SPT−S J015548-6250.8	01:55:47.75	-62:50:54.2
SPT0202-61	SPT−S J020257-6121.1	02:02:58.75	-61:21:10.8
SPT0245-63	SPT−S J024542-6320.6	02:45:44.08	-63:20:38.7
SPT0311-58	SPT−S J031132-5823.4	03:11:33.14	-58:23:33.3
SPT0348-62	SPT−S J034840-6220.8	03:48:42.10	-62:20:51.3
SPT0516-59	SPT−S J051639-5920.4	05:16:37.98	-59:20:29.7

continued

Table 3.1: Summary of spectroscopic observations presented in this chapter, with ALMA 3 mm continuum positions

Short name	Source	RA	Dec
SPT0544-40	SPT−S J054401-4036.3	05:44:01.12	-40:36:30.0
SPT0552-42	SPT−S J055227-4244.0	05:52:26.52	-42:44:20.3
SPT0553-50	SPT−S J055320-5007.2	05:53:20.39	-50:07:15.3
SPT0555-62	SPT−S J055517-6218.9	05:55:16.00	-62:18:50.7
SPT0604-64	SPT−S J060458-6447.3	06:04:57.57	-64:47:22.3
SPT0611-58	SPT−S J061155-5514.2	06:11:57.21	-55:14:07.7
SPT0625-58	SPT−S J062524-5835.3	06:25:22.18	-58:35:19.7
SPT2008-60	SPT−S J200758-5848.3	20:07:58.78	-58:48:22.3
SPT2037-65	SPT−S J203729-6513.3	20:37:31.98	-65:13:17.3
SPT2048-55	SPT−S J204823-5520.5	20:48:22.87	-55:20:40.8
SPT2052-56[b]	SPT−S J205239-5611.6	20:52:41.47	-56:11:57.1
		20:52:41.28	-56:11:43.5
SPT2101-60	SPT−S J210112-6048.8	21:01:13.77	-60:48:54.1
APEX/FLASH, redshift confirmation (Figure A.1 and B.2)			
SPT0106-64	see above		
SPT0202-61	see above		
SPT0319-47[a]	see above		
SPT0516-59	see above		
SPT0551-50[a]	SPT−S J055138-5058.0	05:51:39.42	-50:58:02.1
SPT2335-53	see above		
SPT2349-56	see above		
SPT2353-50	see above		
APEX/SEPIA, redshift confirmation (Figure B.2)			
SPT0002-52	see above		
SPT2349-50	see above		
APEX/Z-Spec, redshift search (Figure B.3)			
SPT0551-48[d]	SPT−S J055156-4825.1	05:51:54.65	-48:25:01.8

a These sources and their positions are from Weiß et al. (2013).
b These sources split into multiple counterparts at 3 mm; we here give the 870 μm positions of all counterparts.
c These sources split into multiple counterparts at 3 mm; we here give the 3 mm positions of all counterparts.
d Position from APEX/LABOCA; No ALMA data.

3.1.1 ALMA 1 mm follow up observations

In the ALMA 3 mm spectral scans presented in Weiß et al. (2013), ten sources showed a single CO line detection (plus one source, SPT0319-47, which showed a line feature not significant enough for detection). In these cases photometric measurements were used to validate possible line assignments and to find the most likely redshift option (this approach is described in more detail in Section 4.1.3.3). Using this method the redshifts of three sources were quickly secured by APEX/FLASH follow-up observations in [C II] (Gullberg et al., 2015). For the eight remaining sources, we were awarded observing

time with ALMA in the Cycle 1 early science compact array configuration, to search for a second CO line (CO(6–5) - CO(12–11)) or a [N II] line in ALMA band 6 (211 GHz - 275 GHz) (project ID 2012.1.00994.S). These eight sources are listed in Table 3.1.

The sources were grouped into five science blocks based on their sky position and tuning frequencies of possible redshifted molecular emission lines (mainly CO). The sidebands were placed such that these five science blocks would yield at least one line for each source. One source (SPT0441-46) is observed in two tunings since it had two likely redshift options.

The observations were carried out from 2013 December to 2014 December. The flux density calibration was based on observations of the Solar System objects Uranus, Neptune and Ganymede and the quasars J0334-401 and J0519-454. The bandpass and phase calibration were determined using nearby quasars. The number of antennas used during the observations ranged from 25 to 40, with baselines less than 500 m resulting in a synthesized beam size of $1.5\times0.8''$. In band 6 the primary beam is $29'' - 23''$. The observing time for each science block ranged from 8 to 20 minutes on-source, excluding overheads. Typical single-sideband (SSB) system temperatures for the observations were $T_{\rm sys} = 80$–100 K. The data were processed using the Common Astronomy Software Application package (CASA McMullin et al., 2007; Petry & CASA Development Team, 2012). We used natural weighting and constructed the spectra with a channel width of 19.5 MHz ($18-22\,{\rm km\,s^{-1}}$ for the highest and lowest observing frequency). The typical noise per channel is 0.9–1.9 mJy beam^{-1}. The spectra are shown in Figure 4.1. Continuum images were cleaned and generated from the full bandwidth and have typical noise levels of 50 μJy beam^{-1}.

3.1.2 ALMA 3 mm scans

In ALMA Cycle 1 and 3, we extended the Cycle 0 redshift search from Weiß et al. (2013) to 42 additional SPT-DSFGs (project ID 2012.1.00844.S and 2015.1.00504.S). As in the Cycle 0 observations, we searched for CO lines in the 3 mm atmospheric transmission window (ALMA band 3). As described in Section 2.2.1 the CO lines were chosen as they are the brightest lines that are observable over a large redshift range at wavelengths not demanding very low water vapor in the atmosphere.

The sub-samples in Cycle 1 and 3 were selected rather differently. The sources observed in Cycle 1 are in the SPT Deep Field that has full coverage from both *Herschel*/SPIRE and *Spitzer*/IRAC. The sources form a complete, flux-density-limited sample with raw (not corrected for the boosting due to sources below the detection limit) $S_{1.4{\rm mm}} > 16$ mJy within a 10×10 square-deg field (12 sources). This selection and limitation is a consequence of ALMA Cycle 1 target restrictions requiring that all sources be within 10 deg of each other to share a phase calibrator. In addition we included three fainter sources from the same field (raw $S_{1.4{\rm mm}} \sim 15$ mJy) to reach the maximum number of 15 science targets allowed in this observing setup in Cycle 1. The sources observed in Cycle 3 are distributed over the entire sky covered by the SPT survey and were selected to have $S_{1.4{\rm mm}} > 20$ mJy and were grouped as efficiently as possible to maximize the number of sources observed with a minimum number of

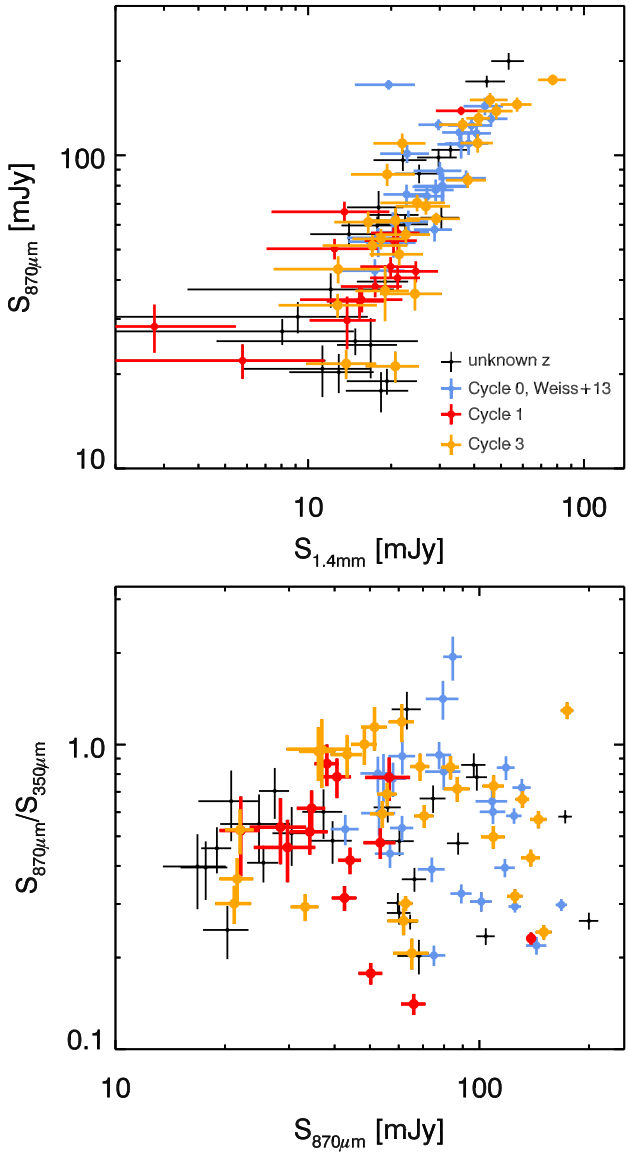

Figure 3.1: Flux density and color plots for all sources in the SPT-DSFG sample (*black*), with the 28 sources from Weiß et al. (2013) (*blue*) and the new DSFGs from Cycle 1 (*red*) and Cycle 3 (*orange*). Together these samples constitute a representative subset of the overall SPT-DSFG sample. *Top:* APEX/LABOCA 870 μm flux density as a function of SPT 1.4 mm flux density. *Bottom:* The ratio of *Herschel*/SPIRE 350 μm flux density to APEX/LABOCA 870 μm flux density as a function of APEX/LABOCA 870 μm flux density. This color indicates the redness and thereby redshift of the sample.

ALMA pointings.

Weiß et al. (2013) studied a subset of the SPT-DSFG population selected using a higher raw flux density cut of $S_{1.4\mathrm{mm}} > 25\,\mathrm{mJy}$, and thereby picking out the brightest sources of the SPT-DSFG population from a large area of the sky ($1300\,\mathrm{deg}^2$ in Cycle 0 compared to $100\,\mathrm{deg}^2$ in Cycle 1). In Figure 3.1 we show 1.4 mm vs 870 μm color-color as well as 870 μm /350 μm color ratio diagrams for the entire SPT sample as well as for the sub-samples targeted in ALMA Cycle 0 (*blue*), 1 (*red*) and 3 (*orange*). Note that the 1.4 mm SPT flux densities shown here are deboosted flux densities and not raw flux densities from which the original selection was made. The top panel shows that the Cycle 1 sample populates the fainter part of the SPT-DSFG sample at both 1.4 mm and 870 μm, which is expected based on the selection method. The Cycle 3 sample populates both the lower and higher flux end of the top panel, covering both the area of the Cycle 0 and Cycle 1 sample. The redshift of the sources can be inferred from the 870 μm to 350 μm flux density ratio shown in the bottom panel (where sources with a higher 870 μm/350 μm flux density ratio typically are at higher redshifts). This plot shows that the sample studied here is expected to have a similar redshift distribution as the full SPT-DSFG sample. Together with the Weiß et al. (2013) sample it is a representative sample of the full SPT-DSFG population.

The observations were set up as spectral scans using five tunings to cover the 3 mm atmospheric transmission window (See Figure 2.3). Each tuning consists of two 3.75 GHz wide sidebands covered by two 1.875 GHz spectral windows in the ALMA correlator, which in total gives 7.5 GHz coverage. This setup spans 84.2−114.9 GHz, where the range 96.1−103.0 GHz is covered twice. Over this frequency range the FWHM of ALMA's primary beam is $61''-45''$. The Cycle 1 ALMA 3 mm spectral scans were carried out in 2013 July and 2013 December in the Cycle 1 early science compact array configuration, with the number of antennas ranging from 28 to 40. Each source was observed for 120 seconds, in each tuning, which amounts to roughly 10 minutes per source in total, with typical system temperatures of $T_{\mathrm{sys}} = 60$–$90\,\mathrm{K}$ (SSB). The Cycle 3 ALMA 3 mm spectral scans were carried out in the period 2015 December - 2016 March in the compact array configuration, with the number of antennas ranging from 34 to 41. Each tuning for each source was observed for 61-91 seconds which adds up to 5.5 - 6.5 minutes on-source per source, with typical system temperatures for the observations of $T_{\mathrm{sys}} = 50 - 80\,\mathrm{K}$. Flux calibration was performed on Uranus, Neptune, Ganymede, J0519-4546, and J0538-4405 and passband and phase calibration were determined from nearby quasars. The typical synthesized beams for the observations are $3.7'' \times 2.4''$ to $3.0'' \times 1.8''$ from the low to high-frequency ends of the band.

We used the CASA package to process the data. The cubes were created using natural weighting to optimize the sensitivity and constructed with a channel width of 19.5 MHz (50–65 kms^{-1}). The typical noise per channel is 1.5–2 $\mathrm{mJy\,beam}^{-1}$. The spectra are shown in Figure 4.2 for the Cycle 1 sources and in Figure 4.3 for the Cycle 3 sources. The continuum images were also created and cleaned using natural weighting and were generated from the full bandwidth. For these we have typical noise levels of 50 $\mu\mathrm{Jy\,beam}^{-1}$.

3.1.3 APEX/FLASH [C II] follow-up

The main spectroscopic line used for redshift confirmation is [C II] due to its brightness as described in Section 2.2.1. For a subset of sources with only one line in the ALMA 3 mm data (from either Cycle 0, 1, or 3), we have performed APEX/FLASH (Klein et al., 2014) observations in the 345 GHz and 460 GHz transmission window (see Table 3.1 for a list of targets). The data were obtained using Max Planck Society observing time in the period 2015 March to August and 2016 April to September. All observations were done in good weather conditions with an average precipitable water vapor of pwv < 1.5 mm, yielding typical system temperatures of $T_{\rm sys} = 240$ K. The observations were performed and the data processed in the same manner as described in Gullberg et al. (2015). Further details on the sources targeted in these observations can be found along with the [C II] spectra in Appendix A and B.

3.1.4 APEX/SEPIA CO follow-up

For two sources (SPT0002-52 and SPT2349-50) we see a single bright line in the 3 mm ALMA spectrum both with the most probable identification being CO(3–2). We have obtained APEX/SEPIA 158 – 211 GHz (Billade et al., 2012) observations confirming the redshifts of these sources by observing the CO(5–4) and CO(7–6) line for SPT0002-52 and SPT2349-50, respectively. The observations were carried out in 2015 September - November during ESO time (E-096.A-0939A-2015) under good weather conditions with an average precipitable water vapor pwv < 1.0 mm yielding typical system temperatures of $T_{\rm sys} = 150$ K. The data were reduced in the same manner as the APEX/FLASH [C II] observations described above. Details on the sources along with the spectrum can be found in Appendix B.

3.1.5 APEX/Z-Spec spectrum

For one source in the sample presented here (SPT0551-48), we used APEX/Z-Spec (Naylor et al., 2003; Bradford et al., 2009) to search for high-J CO lines in the frequency range 190 – 310 GHz and thereby identify the redshift of the source. The observations were obtained in November 2012 in good weather conditions. The reduction of the data was done in the same manner as described in Bothwell et al. (2013). The resulting spectrum showed several lines identifying the redshift as $z = 2.5833(2)$ and it can be found in Appendix B along with a description of the source.

3.1.6 Ancillary spectroscopic observations

In addition to the primary data presented here, we also make use of spectroscopic data taken at radio and optical wavelengths.

Simultaneously with the ALMA and APEX redshift confirmation observations, we carried out follow-up observations with the Australia Telescope Compact Array (ATCA) targeting low-J CO transitions. These data are presented in Spilker et al. (2014), Aravena et al. (2013) and Aravena et al. (2016) and helped to secure some of the redshifts before the delivery of the 1 mm ALMA data. Results from these observations are discussed in Section 4.1.2 and included in Table 4.1.

Optical spectroscopy was performed for SPT2357-51 on the night of 2013 October 16 with the X-shooter echelon spectrograph (Vernet et al., 2011) on the ESO VLT-UT2 (Kueyen) as part of program E-092.A-0503(A), with near-continuous spectroscopy from 0.3 μm to 2.48 μm with a 1.″2-wide and 11″-long slit. Seeing conditions were $\sim 0.8''$, taken at low average airmass of 1.2. The resolving power attained for our IR-channel observations was $R = 5000$. The resolving power for the optical channel was $R = 6700$. We used the ESO pipeline (Modigliani et al., 2010) to reduce our data. This pipeline applied spatial and spectral rectification to the spectra, and the data were flat-fielded and cosmic rays were identified and masked. The two dither positions were subtracted to remove the sky to first order, and the different echelle orders were combined together into a continuous spectrum (taking into account the variation in throughput with wavelength in different overlapping echelle orders) before spatially registering and combining the data taken at the two dither positions, and removing any residual sky background. The spectrum can be found in Appendix B in Figure B.7.

3.2 Photometric Observations

The SPT-DSFGs have a good photometric coverage, with flux densities measured at 2 mm, 1.4 mm (SPT), 870 μm (APEX/LABOCA), and 500 μm, 350 μm, and 250 μm (*Herschel*/SPIRE) for all sources. This means that even with the large redshift span of the SPT-DSFGs ($1.9 < z < 6.9$), the thermal dust peak is covered. For sources in our ALMA 3 mm redshift scans we have added the 3 mm flux density and for sources where the peak of the SED was not already well covered, we added *Herschel*/PACS 160 μm and 100 μm observations. In this Section we first describe the sample in more detail and then the photometric observations from longest to shortest wavelength. All flux densities are given in Table 3.2. The last part of this Section deals with the counterpart identification across the photometric maps.

3.2.1 The sample

SPT has a very large beamsize, which means that a point source in the SPT maps can easily be a blend of several sources, in extreme cases, even a compact object in the galactic cirrus. To confirm the high redshift nature of the targets we followed all sources up at 870 μm using APEX/LABOCA. The much smaller beam size of APEX/LABOCA combined with its large wavelength allows us to discard sources that do not appear to be high redshift galaxies. Furthermore, sources where the APEX/LABOCA or *Herschel*/SPIRE position were clearly coincident with a nearby galaxy or galactic object

were discarded. The final sample consists of **91** high redshift DSFGs. Table C.1 gives the full name, short name and position of all the sources.

3.2.2 ALMA/Band 3 at 3 mm

We performed scans for CO in ALMA band 3 in Cycle 0, 1 and 3 covering the frequency range 84.2 – 114.9 GHz using five tunings for a total of 68 sources (project ID's:2011.0.00957.S, 2012.1.00844.S and 2015.1.00504.S).

The continuum images were created using the CASA (McMullin et al., 2007; Petry & CASA Development Team, 2012) CLEAN procedure with natural weighting and were generated from the full bandwidth. The ALMA 3 mm flux densities were extracted as the peak flux density of the point sources on the cleaned continuum map and the uncertainty was determined from the noise level near the source.

3.2.3 SPT at 2.0 mm and 1.4 mm

The SPT 1.4 mm and 2.0 mm flux densities were extracted and deboosted as described by Mocanu et al. (2013). The deboosting is performed to adjust for the boost in signal that the source receives from confusion noise, due to sources below the detection threshold that are contributing to the source flux (Casey et al., 2014). This is relevant for the SPT maps due to the large applied beam size ($\sim 1'$).

3.2.4 APEX/LABOCA at 870 μm

We used APEX/LABOCA (Siringo et al., 2009) to obtain 870 μm fluxes for all sources. The observations were done as raster-spirals using the planetary calibrators Uranus, Mars and Neptune and almost all other listed APEX/LABOCA calibrators. Focus was checked every few hours on a planet if possible or otherwise a bright calibrator. Pointing corrections were done just before 'on source' observations on a calibrator or a nearby quasar. The atmospheric attenuation was mostly obtained from the APEX radiometer and when this was not available skydips were used. The observations were performed during the period September 2010 - October 2013 (project ID's: M-085.F-0008-2010, M-087.F-0015-2011, E-087.A-0968B-2011, M-089.F-0009-2012, E-089.A-0906A-2012, M-091.F-0031-2013, E-091.A-0835B-2013, M-092.F-0021-2013), and were carried out under mediocre or good weather conditions with typical pwv < 1.5 mm. For more details on how the observations were conducted see Greve et al. (2012).

We created a map for each source using the Bolometer Array analysis software (BoA) varying the spatial resolution (20.4 - 26.3″) by using a smoothing kernel (7 to 18″) to investigate the signal-to-noise ratio (SNR) as a function of the spatial resolution. For each source the best map was selected based on the SNR and resolution. The data reduction was basically done as in Greve et al. (2012) though we here attempt to improve it slightly, by carefully generating a catalogue of calibrators and then interpolating the calibration for each observing session and when possible use more than one calibrator per observing block.

The fluxes are extracted by fitting a Gaussian point spread function (PSF) and assuming the peak flux as the source flux density. The noise was estimated from the RMS in the area around the source.

3.2.5 *Herschel*/SPIRE at 500 μm, 350 μm, and 250 μm

With *Herschel*/SPIRE we obtained 500 μm, 350 μm, and 250 μm photometry simultaneously for all sources in our sample. The observations were performed in the period 2012 March – 2013 March (project ID's: OT1_jvieira_4, OT2_jvieira_5, DDT_tgreve_2 and DDT_mstrande_1). The *Herschel*/SPIRE data consist of triple repetition maps, with coverage complete to a radius of 5 arcmins ($'$) from the nominal SPT position. The maps were produced via the standard reduction pipeline HIPE v9.0, and co-added, weighted by noise. The flux densities were extracted by fitting a Gaussian shaped PSF to the source and adopting the peak as the flux density. The flux densities have been corrected for pixelation, by dividing the fluxes by 0.951,0.931, and 0.902 for 250 μm, 350 μm, and 500 μm, respectively, as described in the *Herschel*/SPIRE Observers Manual. The noise was estimated by taking the RMS in the central few arcmins of the map and the uncertainty from pixelation was added in quadrature.

3.2.6 *Herschel*/PACS at 160 μm and 100 μm

For a subsample of 66 sources we obtained *Herschel*/PACS maps at 100 and 160 μm (project ID's: OT1_jvieira_4, OT1_dmarrone_1, OT2_jvieira_5 and DDT_mstrande_1). Both wavelengths were observed simultaneously. Each scan comprises ten separate 3$'$ strips, each offset orthogonally by 4$''$. The scans were co-added, weighted by coverage. The aperture sizes were fixed to 7$''$ for the 100 μm map and 10$''$ for the 160 μm map as this is the radius where the highest percentage of the source emission is inside the aperture with the least confusion noise. The apertures were determined from Figure 17 of the *Herschel*/PACS Photometer - Point-Source Flux Calibration document released from *Herschel*.[1]. From here we also obtained the aperture correction based on Table 15. The uncertainty was obtained by random aperture photometry in the few central arcmins.

3.2.7 Identifying the DSFG across wavelengths

As described above, the DSFGs are identified in the SPT survey, but given the large beam size of the SPT it can be a challenge to identify the correct counterpart in the shorter wavelength maps. Thumbnails of the maps are shown in Appendix D, and a few selected ones in Figure 3.2. For the cross-identification the APEX/LABOCA 870 μm maps are invaluable. The wavelength is long enough (or close enough to that of the SPT) that emission in the APEX/LABOCA and SPT maps can be assumed to originate from the same source. However, the resolution of the APEX/LABOCA maps ($\sim$18.7$''$) is significantly better than that of the SPT maps ($\sim$1.0 - 1.7 $'$). In

[1] http://herschel.esac.esa.int/twiki/pub/Public/PacsCalibrationWeb/pacs_bolo_fluxcal_report_v1.pdf

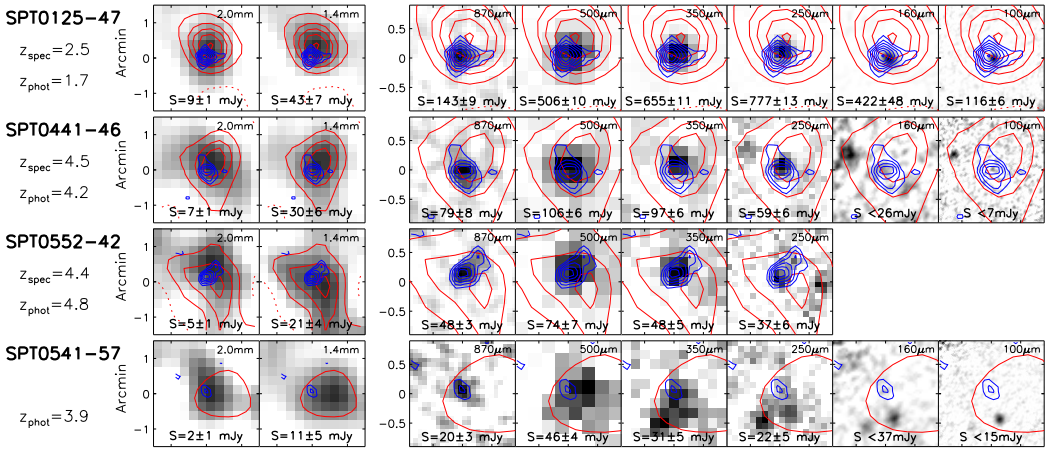

Figure 3.2: Thumbnails of the maps available for the sources SPT0125-47, SPT0441-46, SPT0552-42, and SPT0541-57. The color scale is adjusted each panel, based on the peak flux at the given wavelength. SPT contours are given in *red* and APEX/LABOCA contours are given in *blue*.

Table C.1 the source position is given along with the origin of the position, which is APEX/LABOCA maps or when available, ALMA 3 mm maps. In the *Herschel* maps we often see several counterparts. These can stem from the SPT discovered source or nearby galaxies. By using the improved position and contours from APEX/LABOCA it becomes possible to distinguish the counterparts and select the appropriate counterpart of the the SPT-DSFG. In most cases identifying the correct counterpart of the DSFG is straightforward with all the available photometry. This is the case for the sources in the three upper panels of Figure 3.2. The top row is an example of a bright source (SPT0125-47) where the flux densities are rising towards 250 μm, and *Herschel*/PACS maps were therefore obtained. With detections at both wavelengths the peak is now well described. The second row of panels shows a source (SPT0441-46) where we obtained *Herschel*/PACS maps, but did not detect the source. Whether the sources are detected in the *Herschel*/PACS maps is highly dependent on their redshift. For sources at low redshifts, e.g. SPT0125-47, the peak of the thermal dust emission is close to $\sim 100\,\mu$m (see Sect 5.2.2). At higher redshift the thermal dust peak occurs at longer wavelengths and at the *Herschel*/PACS wavelengths the source becomes hard to detect. The third row of panels show a source (SPT0552-42) that peaks around $\sim 500\,\mu$m and where *Herschel*/PACS observations have not been undertaken as the peak is already well sampled. For sources where the peak was found to be at long wavelengths, detections at the *Herschel*/PACS wavelengths were not expected and observations with this instrument were not undertaken. The fourth row of panels shows a source (SPT0541-57) where the are several counterparts within the SPT beam in the *Herschel* maps, and where the brightest of these are not associated with the SPT-DSFG. However with the APEX/LABOCA contours we can select the counterpart associated with the SPT-DSFG. In a few cases though, it is not so straight forward, which is especially true when the counterparts are blended. In Appendix E the source

extraction of the cluster lens SPT2332-53 is described. For this source we see several lens images and these are blended with other sources. A few sources appear slightly extended at 870 μm or 500 μm, but the fluxes have been extracted in the same way as the other sources, using the peak flux, for consistency. These sources may be candidates for protoclusters, where the flux is spread over several counterparts and therefore does not appear as a point source.

Table 3.2: Photometry of all SPT-DSFGs

Source	$S_{3.0mm}$ [mJy]	$S_{2.0mm}$ [mJy]	$S_{1.4mm}$ [mJy]	$S_{870\mu m}$ [mJy]	$S_{500\mu m}$ [mJy]	$S_{350\mu m}$ [mJy]	$S_{250\mu m}$ [mJy]	$S_{160\mu m}$ [mJy]	$S_{100\mu m}$ [mJy]
SPT0002-52[e]	0.44 ± 0.05	2.9 ± 1.3	12.5 ± 5.4	50.3 ± 3.8	202 ± 10	283.5 ± 8.9	332 ± 10	234 ± 21	93.9 ± 5.4
SPT0020-51[f]	1.29 ± 0.03	7.5 ± 1.4	24.8 ± 6.5	70.5 ± 4.3	144.1 ± 8.6	120.9 ± 7.4	71.5 ± 7.5	<26	<8.1
SPT0027-50[f]	1.39 ± 0.03	9.7 ± 1.4	48.1 ± 7.0	138.4 ± 8.2	316.1 ± 8.1	325.7 ± 7.2	232.9 ± 6.8	85 ± 13	15.8 ± 2.3
SPT0054-41		9.5 ± 1.2	29.7 ± 4.9	98.4 ± 6.5	174 ± 10	125.9 ± 8.9	79.0 ± 9.3		
SPT0103-45[b]	1.46 ± 0.23	8.8 ± 1.4	39.1 ± 7.0	124.5 ± 6.1	231.6 ± 7.6	213.3 ± 6.8	133 ± 10	<47	<13.2
SPT0106-64	2.20 ± 0.03	12.6 ± 1.4	57.2 ± 7.4	145.3 ± 7.6	237.3 ± 8.7	255 ± 10	151.9 ± 8.0	64 ± 13	<12.3
SPT0109-47[f]	1.10 ± 0.03	8.2 ± 1.6	21.9 ± 4.7	109.2 ± 8.2	213.9 ± 8.4	219.4 ± 9.1	166.4 ± 8.8	57.3 ± 9.5	<8.4
SPT0112-55	0.18 ± 0.03	5.2 ± 1.1	24.4 ± 6.2	36.1 ± 4.1	37.0 ± 7.3	38.0 ± 6.3	<18.9		
SPT0113-46[b]	1.28 ± 0.20	9.5 ± 1.6	30.8 ± 6.9	79.4 ± 8.2	89.1 ± 6.4	56.2 ± 5.8	24.9 ± 5.6	<22	<6.6
SPT0114-59	0.17 ± 0.03	5.8 ± 1.4	20.7 ± 4.5	21.2 ± 2.4	61.8 ± 7.9	70.5 ± 6.2	38.7 ± 6.0		
SPT0125-47[b]	1.88 ± 0.29	9.2 ± 1.3	43.7 ± 7.1	143.5 ± 9.3	506 ± 10	655 ± 11	777 ± 13	422 ± 48	116.3 ± 6.0
SPT0125-50[b]	1.51 ± 0.24	8.5 ± 1.3	38.2 ± 6.8	109.0 ± 8.8	162.4 ± 7.1	181.1 ± 6.5	155.7 ± 8.0	65 ± 13	13.1 ± 2.8
SPT0128-51[b]	0.41 ± 0.09	4.3 ± 1.5	19.3 ± 5.5	†19.0 ± 1.8	†51.1 ± 7.2	41.6 ± 6.0	38.2 ± 8.0	<23	<7.5
SPT0136-63	1.13 ± 0.03	7.6 ± 1.4	26.7 ± 6.0	68.7 ± 4.1	122.1 ± 6.3	81.1 ± 6.8	42.1 ± 5.2		
SPT0147-64	1.90 ± 0.04	10.1 ± 1.4	37.9 ± 6.2	†83.3 ± 4.6	122.4 ± 6.7	98.8 ± 6.8	49.4 ± 6.2		
SPT0150-59	1.03 ± 0.03	7.7 ± 1.5	29.1 ± 6.4	62.7 ± 2.8	170.1 ± 8.7	208.2 ± 7.3	173.9 ± 7.9		
SPT0155-62	4.18 ± 0.04	25.5 ± 1.6	77.1 ± 8.9	174.2 ± 6.9	199.9 ± 7.3	134.6 ± 6.6	58.1 ± 4.3	<25	<11.4
SPT0202-61[f]	2.75 ± 0.04	14.2 ± 1.4	41.2 ± 5.5	109.4 ± 7.4	145.7 ± 6.9	149.6 ± 7.6	128.3 ± 7.7	44 ± 11	10.1 ± 2.7
SPT0226-45				66.3 ± 5.1	172 ± 14	183.5 ± 8.6	184 ± 10		
SPT0243-49[b]	3.16 ± 0.48	11.5 ± 1.5	37.4 ± 6.7	†84.5 ± 5.0	57.5 ± 6.9	43.5 ± 6.7	24.9 ± 5.6	<31	<10.2
SPT0245-63[f]	1.39 ± 0.04	6.0 ± 1.4	16.5 ± 4.1	61.2 ± 4.9	59.3 ± 6.7	51.5 ± 6.1	49.7 ± 6.2	49.3 ± 7.8	31.2 ± 2.6
SPT0300-46[b]	1.01 ± 0.16	6.3 ± 1.4	22.8 ± 4.6	†56.8 ± 5.2	†153.2 ± 7.2	129.5 ± 6.1	84.6 ± 7.8	<37	<9.6
SPT0311-58[g]	1.30 ± 0.04	7.5 ± 1.3	19.0 ± 4.2	36.9 ± 7.4	51.8 ± 8.2	38.2 ± 6.0	28.8 ± 8.0		
SPT0314-44		9.1 ± 1.3	32.8 ± 4.8	†104.1 ± 6.1	390 ± 11	443 ± 10	337 ± 10	117 ± 14	<12.0
SPT0319-47[b]	1.20 ± 0.20	6.5 ± 1.3	27.9 ± 6.0	67.1 ± 6.3	103.4 ± 6.6	101.9 ± 6.1	69.4 ± 6.8	33.0 ± 8.0	<7.2
SPT0345-47[b]	1.48 ± 0.24	6.0 ± 1.2	30.0 ± 5.9	†89.2 ± 6.0	214.9 ± 7.7	275.0 ± 7.4	233.2 ± 6.2	84 ± 12	12.5 ± 2.4
SPT0346-52[b]	2.82 ± 0.43	11.6 ± 1.3	46.0 ± 6.8	†130.8 ± 7.6	†203.7 ± 8.3	181.0 ± 6.5	122.1 ± 6.9	32.6 ± 8.6	<6.3

continued

Table 3.2: Photometry of all SPT-DSFGs

Source	$S_{3.0mm}$ [mJy]	$S_{2.0mm}$ [mJy]	$S_{1.4mm}$ [mJy]	$S_{870\mu m}$ [mJy]	$S_{500\mu m}$ [mJy]	$S_{350\mu m}$ [mJy]	$S_{250\mu m}$ [mJy]	$S_{160\mu m}$ [mJy]	$S_{100\mu m}$ [mJy]
SPT0348-62[f]	0.83 ± 0.04	4.1 ± 1.4	17.1 ± 5.8	†51.5 ± 4.2	†55.0 ± 6.8	45.1 ± 6.4	29.1 ± 6.1	<26	<5.7
SPT0402-45		11.6 ± 1.3	53.3 ± 7.2	†199 ± 12	554 ± 12	757 ± 13	796 ± 15		
SPT0403-58[f]		4.4 ± 1.1	19.0 ± 4.0	39.5 ± 5.1	86.8 ± 8.0	81.7 ± 7.7	55.6 ± 7.2	<32	<10.2
SPT0404-59[f]		5.0 ± 1.2	16.9 ± 4.1	24.8 ± 5.4	53.0 ± 6.6	45.2 ± 5.6	38.5 ± 6.2	<28	<7.5
SPT0418-47[b]	0.79 ± 0.13	7.5 ± 1.2	35.9 ± 6.4	†108 ± 10	†174.6 ± 7.3	166.4 ± 6.2	113.5 ± 6.4	45.3 ± 8.2	<6.9
SPT0425-40				†60.3 ± 5.7	†116.6 ± 7.7	125.1 ± 6.2	70.5 ± 6.4		
SPT0433-59		4.1 ± 1.0	18.0 ± 4.2	†68.2 ± 8.7	228.4 ± 9.9	337.1 ± 8.4	371.6 ± 9.3		
SPT0436-40				74.6 ± 6.1	118.0 ± 8.8	112.1 ± 7.1	71.0 ± 7.2		
SPT0441-46[b]	1.26 ± 0.20	7.3 ± 1.3	30.6 ± 6.3	79.8 ± 8.9	106.4 ± 6.5	97.9 ± 6.3	59.5 ± 6.8	<26	<7.2
SPT0452-50[b]	0.67 ± 0.11	4.9 ± 0.8	17.4 ± 4.9	42.8 ± 3.8	93.9 ± 7.4	81.1 ± 5.9	54.4 ± 5.4	<29	<6.6
SPT0457-49[b]		4.0 ± 2.2	14.8 ± 10.2	25.5 ± 2.5	70.5 ± 6.4	62.3 ± 6.1	40.0 ± 4.0	<25	<6.9
SPT0459-58[b]	0.96 ± 0.16	4.6 ± 1.0	20.4 ± 4.2	†52.6 ± 5.5	79.9 ± 6.6	65.4 ± 5.6	44.1 ± 5.9	<28	<6.9
SPT0459-59[b]	1.19 ± 0.19	6.2 ± 1.3	23.1 ± 4.2	†61.4 ± 5.2	†74.5 ± 7.8	67.0 ± 6.6	54.3 ± 7.9	<27	<11.1
SPT0509-53		3.3 ± 1.2	12.9 ± 4.4	†20.3 ± 2.9	†62 ± 12	82 ± 11	47 ± 11	<39	<7.5
SPT0512-59[a]	0.98 ± 0.16	5.5 ± 1.2	22.7 ± 4.0	75.0 ± 5.6	257.3 ± 8.1	369.0 ± 7.3	305.2 ± 7.1	138 ± 17	33.1 ± 3.8
SPT0516-59	0.39 ± 0.03	2.6 ± 1.0	12.8 ± 5.0	33.2 ± 2.9	88.8 ± 7.0	113.2 ± 5.9	89.4 ± 5.8	51 ± 10	19.7 ± 2.7
SPT0520-53		4.1 ± 1.4	14.1 ± 3.9	56.0 ± 4.8	96.6 ± 6.8	90.0 ± 5.9	55.7 ± 6.0	<21	<7.5
SPT0528-53		1.6 ± 1.2	8.1 ± 6.6	27.4 ± 2.6	41.0 ± 6.3	38.9 ± 6.4	27.4 ± 7.9		
SPT0529-54[a]	1.51 ± 0.23	9.2 ± 1.3	35.4 ± 4.8	†118.3 ± 6.7	†174.2 ± 9.8	140.8 ± 9.9	87.8 ± 7.0	<67	<27.3
SPT0532-50[a]	3.04 ± 0.47	13.3 ± 1.4	40.8 ± 5.2	117.5 ± 7.6	290.1 ± 7.6	298.0 ± 7.5	215.6 ± 6.9	69 ± 12	<8.1
SPT0538-50[a]		8.5 ± 1.4	29.7 ± 4.6	125.2 ± 5.0	360.4 ± 9.1	425.8 ± 8.5	343.5 ± 7.9	141 ± 15	31.3 ± 1.8
SPT0541-57		2.4 ± 1.2	11.3 ± 5.5	20.8 ± 3.9	46.2 ± 4.5	31.9 ± 5.8	22.9 ± 5.1	<37	<15.3
SPT0544-40	1.53 ± 0.04	4.9 ± 1.3	19.3 ± 5.0	86.9 ± 7.1	132.0 ± 8.4	121.4 ± 5.6	68.0 ± 5.6	<39	<10.2
SPT0550-53	0.61 ± 0.12	3.7 ± 1.0	17.9 ± 4.0	53.0 ± 5.7	97 ± 10	89 ± 10	68.7 ± 9.8	28.1 ± 8.9	7.9 ± 2.3
SPT0551-48		10.5 ± 1.6	35.9 ± 6.8	138.7 ± 4.4	420 ± 11	600 ± 19	632 ± 11	408 ± 50	132.0 ± 9.3
SPT0551-50[a]	1.04 ± 0.17	5.0 ± 0.9	27.0 ± 4.2	†74.0 ± 6.3	†196.9 ± 7.5	189.9 ± 7.3	148.8 ± 7.1	63 ± 13	13.3 ± 2.5
SPT0552-42	1.20 ± 0.03	5.0 ± 1.6	21.4 ± 4.7	48.3 ± 3.9	74.2 ± 7.5	48.2 ± 5.8	37.2 ± 6.3		

continued

Table 3.2: Photometry of all SPT-DSFGs

Source	$S_{3.0mm}$ [mJy]	$S_{2.0mm}$ [mJy]	$S_{1.4mm}$ [mJy]	$S_{870\mu m}$ [mJy]	$S_{500\mu m}$ [mJy]	$S_{350\mu m}$ [mJy]	$S_{250\mu m}$ [mJy]	$S_{160\mu m}$ [mJy]	$S_{100\mu m}$ [mJy]
SPT0553-50	1.13 ± 0.03	3.0 ± 1.3	12.8 ± 5.3	43.3 ± 4.3	66.6 ± 8.6	46.7 ± 5.9	27.2 ± 6.6	<38	<7.8
SPT0555-62	1.00 ± 0.03	5.5 ± 1.1	22.6 ± 5.0	55.8 ± 3.4	86.8 ± 6.9	81.1 ± 5.3	78.9 ± 5.7	56 ± 16	22.6 ± 4.2
SPT0604-64	1.33 ± 0.03	11.4 ± 1.4	45.6 ± 7.1	150.3 ± 7.6	440 ± 11	620 ± 12	509 ± 12	206 ± 24	51.2 ± 4.4
SPT0611-55	0.47 ± 0.03	0.6 ± 1.9		†65.2 ± 7.3	†249 ± 10	315.5 ± 9.5	260 ± 10		
SPT0625-58	1.70 ± 0.03	9.7 ± 1.5	36.3 ± 6.5	125.2 ± 6.1	320.7 ± 8.8	393.9 ± 8.7	323.8 ± 7.4	149 ± 17	25.7 ± 4.6
SPT0652-55		15.2 ± 1.6	44.4 ± 7.3	172.1 ± 7.4	325.4 ± 7.9	296.6 ± 7.6	186.2 ± 7.7	<36	<12.0
SPT2008-58	0.26 ± 0.04	3.1 ± 0.9	13.7 ± 3.9	21.6 ± 2.3	55 ± 10	59.6 ± 8.0	67.5 ± 9.8		
SPT2031-51[f]		4.4 ± 1.1	20.8 ± 4.3	64.5 ± 3.1	225.1 ± 7.2	246.3 ± 7.1	227.0 ± 7.8	91 ± 12	21.9 ± 4.4
SPT2037-65	9.45 ± 0.05	19.6 ± 1.2	41.5 ± 4.1	131.3 ± 5.6	237 ± 11	198.5 ± 9.3	129 ± 10		
SPT2048-55[f]	1.97 ± 0.04	6.8 ± 1.3	18.4 ± 3.9	54.1 ± 4.1	80.3 ± 8.7	91.3 ± 6.2	47.9 ± 8.7	<24	<6.9
SPT2052-56[f]	0.25 ± 0.04		16.0 ± 3.4	†22.0 ± 2.0	54.9 ± 7.5	41.9 ± 6.0	24.1 ± 6.3	<18	<7.8
SPT2101-60	0.92 ± 0.04	6.0 ± 1.2	20.7 ± 4.6	61.9 ± 6.0	185.8 ± 7.0	234.5 ± 8.3	170.2 ± 7.8		
SPT2103-60[b]	0.99 ± 0.16	8.8 ± 1.1	29.0 ± 4.7	77.5 ± 6.2	111.0 ± 6.7	83.8 ± 5.4	47.9 ± 5.4	<22	<6.6
SPT2129-57		6.3 ± 1.2	25.2 ± 4.6	87.4 ± 6.0	148.3 ± 7.9	184.2 ± 8.6	154.8 ± 6.1	91 ± 15	34.3 ± 3.1
SPT2132-58[b]	1.42 ± 0.23	6.1 ± 0.9	28.7 ± 4.5	57.9 ± 4.9	80.0 ± 7.4	74.9 ± 7.1	57 ± 11	<36	<9.0
SPT2134-50[b]	1.13 ± 0.18	6.0 ± 1.3	22.8 ± 4.6	†101.2 ± 6.8	268.8 ± 9.2	331.5 ± 9.0	349.7 ± 8.8	196 ± 21	49.3 ± 3.0
SPT2146-55[b]	1.18 ± 0.19	5.2 ± 1.3	17.8 ± 4.0	54.5 ± 3.7	83.3 ± 8.8	69 ± 11	64 ± 11	<28	<7.5
SPT2147-50[b]	0.76 ± 0.12	5.8 ± 1.3	20.3 ± 4.6	61.3 ± 4.5	121.4 ± 7.8	115.1 ± 7.0	71.7 ± 7.3	<28	8.6 ± 2.3
SPT2152-40		7.1 ± 1.6	22.1 ± 4.8	†96.5 ± 7.4	113.0 ± 6.9	112.5 ± 5.5	84.5 ± 7.1	37 ± 10	<11.7
SPT2203-41		6.9 ± 1.3	30.4 ± 4.9	63.2 ± 5.8	78.6 ± 6.7	48.4 ± 5.2	37.7 ± 4.4		
SPT2219-42		4.3 ± 1.4	18.4 ± 4.7	†17.7 ± 2.6	†54.7 ± 7.4	44.8 ± 7.2	34.5 ± 7.8		
SPT2232-61		6.0 ± 1.2	22.4 ± 4.7	60.2 ± 4.5	210.3 ± 7.5	214.9 ± 8.2	168.0 ± 8.7		
SPT2307-50[e]	0.26 ± 0.05	1.2 ± 1.4	5.8 ± 6.7	22.1 ± 2.8	37 ± 10	42 ± 11	50 ± 12		
SPT2311-45		4.0 ± 1.0	17.8 ± 4.6	59.7 ± 4.0	154.5 ± 7.7	197.6 ± 8.0	163.8 ± 6.1	89 ± 12	11.8 ± 3.6
SPT2311-54[e]	0.55 ± 0.05	5.4 ± 1.2	19.9 ± 4.5	44.1 ± 3.2	95.1 ± 6.6	105.7 ± 7.3	85 ± 10	<32	11.6 ± 2.5
SPT2316-50		1.9 ± 1.3	9.2 ± 7.3	30.5 ± 3.5	65 ± 10	59 ± 11	38 ± 10		
SPT2319-55[a]	0.82 ± 0.05	5.4 ± 1.2	17.5 ± 4.4	38.1 ± 2.9	49.0 ± 6.6	44.0 ± 6.0	32.8 ± 6.4	<25	<7.5

continued

Table 3.2: Photometry of all SPT-DSFGs

Source	$S_{3.0mm}$ [mJy]	$S_{2.0mm}$ [mJy]	$S_{1.4mm}$ [mJy]	$S_{870\mu m}$ [mJy]	$S_{500\mu m}$ [mJy]	$S_{350\mu m}$ [mJy]	$S_{250\mu m}$ [mJy]	$S_{160\mu m}$ [mJy]	$S_{100\mu m}$ [mJy]
SPT2332-53[a]		3.3 ± 0.7	19.6 ± 4.8	168.0 ± 6.0	304.0 ± 5.0	564 ± 16	585 ± 37	233 ± 37	57.0 ± 7.0
SPT2335-53[e]	0.30 ± 0.04	4.9 ± 1.3	13.8 ± 3.7	35.6 ± 4.9	78.6 ± 9.9	64.6 ± 8.4	42.7 ± 9.0		
SPT2340-59[e]	0.49 ± 0.05	3.6 ± 1.0	15.3 ± 3.7	34.2 ± 4.1	71.1 ± 8.7	66.1 ± 6.9	41.6 ± 8.5	<29	<8.1
SPT2349-50[e]	0.51 ± 0.05	5.2 ± 1.1	24.6 ± 5.0	42.6 ± 3.3	127.8 ± 7.6	135.8 ± 7.1	129.2 ± 8.6	<76	<38
SPT2349-52		2.5 ± 1.7	12.1 ± 8.4	37.3 ± 4.7	72.6 ± 9.7	62.0 ± 8.4	45.2 ± 8.6		
SPT2349-56[a]	0.40 ± 0.05	4.7 ± 1.2	21.1 ± 4.2	56.5 ± 8.0	85.4 ± 6.4	72.4 ± 5.9	36.8 ± 6.4	<32	<12.0
SPT2351-57[e]	0.83 ± 0.05	5.6 ± 1.3	15.7 ± 6.3	†34.6 ± 3.1	73.8 ± 5.7	56.0 ± 6.4	44.3 ± 5.3	<43	<9.6
SPT2353-50[a]	0.89 ± 0.05	5.4 ± 1.4	21.1 ± 4.3	40.6 ± 3.8	56.2 ± 7.1	51.8 ± 6.0	29.9 ± 7.4	<41	<11.7
SPT2354-58[e]	0.61 ± 0.08	2.7 ± 1.2	13.5 ± 6.2	†66.0 ± 5.1	†277.7 ± 7.9	469.0 ± 9.0	613 ± 10	531 ± 58	238 ± 10
SPT2357-51[a]	0.42 ± 0.04	4.1 ± 0.9	20.4 ± 4.4	53.4 ± 5.4	122.9 ± 7.5	112.1 ± 6.2	70.9 ± 5.1	<33	<7.5

When fitting to the SEDs we have added in quadrature an absolute calibration uncertainty of 7% for *Herschel*/PACS and 10% for all other wavelengths. For SPT2332-53, the flux is derived in Appendix E based on a decomposition of the source.

† These fluxes are potentially underestimated as the sources appear extended.

a APEX/LABOCA fluxes were published by Greve et al. (2012)

b Fluxes were published by Weiß et al. (2013)

c Fluxes were published by Bothwell et al. (2013)

d Fluxes were published by Ma et al. (2015)

e Fluxes were published by Strandet et al. (2016)

f APEX/LABOCA fluxes were published by Spilker et al. (2016)

g Fluxes were published by Strandet et al. (2017)

Chapter 4

The spectroscopic redshift distribution of Dusty Star Forming Galaxies from the SPT survey

In this chapter we investigate the spectroscopic redshift distribution of the SPT-DSFGs. The chapter is based on the publication: **Strandet et al. 2016, The Astrophysical Journal, Volume 822, Issue 2**. This publication presents the analysis of spectral scans of 15 sources from ALMA Cycle 1. In this thesis we add spectral scans of an additional 27 sources from ALMA Cycle 3 to the analysis. We combine these observations with previously published and new mm/submm line and photometric data of the SPT-selected DSFGs to study their redshift distribution.

The analysis in this chapter is based on the observations presented in Section 3.1 containing spectral surveys of in total 42 galaxies and redshift confirmation observations using a variety of facilities. In Section 4.1, we show the spectra derived from these observations and present redshifts determined from those spectra. In Section 4.2, we present the redshift distribution of DSFGs selected from the SPT survey and discuss how the sample is affected by gravitational lensing and selection wavelength.

We adopt a flat ΛCDM cosmology, with $\Omega_\Lambda = 0.696$ and $H_0 = 68.1\,\mathrm{km\ s^{-1}\,Mpc^{-1}}$ (Planck Collaboration et al., 2014).

4.1 Results

4.1.1 Targeted ALMA 1 mm observations

In the 1 mm continuum images all sources but one are spatially unresolved, which is expected given the $\sim 1''$ resolution of the maps. The continuum emission is detected with high SNR (25 - 100) in all cases. For the spatially resolved source (SPT0512-59, see Figure A.3), the brightest component is detected with a SNR of 9, and we extract the source spectrum from this component. All 1 mm spectra are shown in Figure 4.1 (smoothed to lower velocity resolution for better visualization of the lines).

We detect spectral line features in all sources, including emission lines from various CO transitions, [N II] and several H_2O transitions and absorption lines from H_2O^+ and NH_3. More details on the lines/transitions can be found in the description of the individual sources in Appendix A.

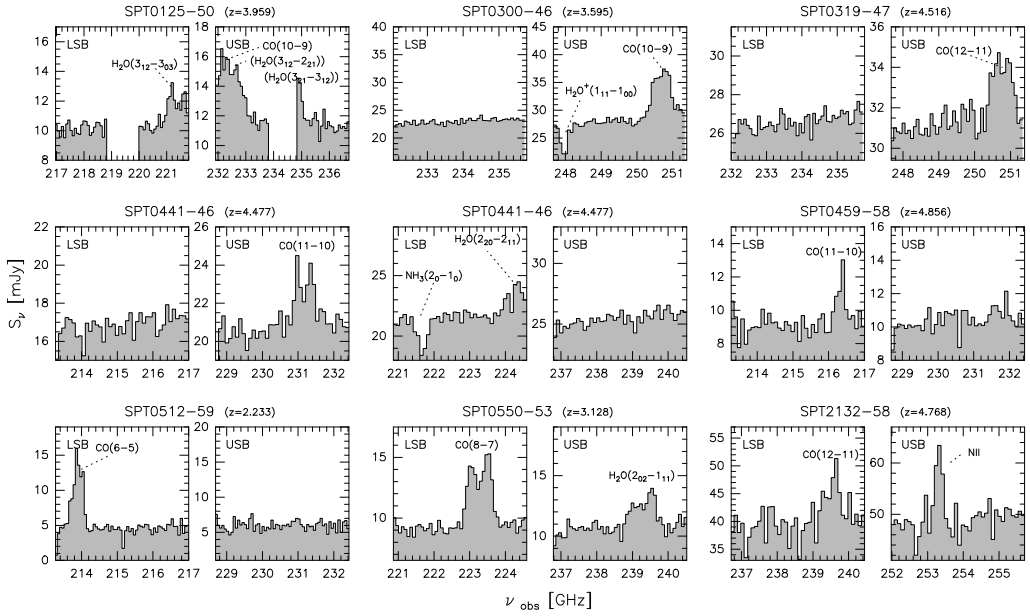

Figure 4.1: ALMA 1 mm spectra for sources with redshifts based on a single submm emission line from Weiß et al. (2013) (see Section 4.1.1). For each source we show the LSB and USB spectra in the left and right panel, respectively. Each sideband has a total bandwidth of 3.9 GHz.

The most important result from our ALMA 1 mm observations, with respect to the source redshifts, is that they confirm the most probable redshifts as given in Weiß et al. (2013) for all except one source (see Table 4.1). The one exception had two almost equally likely redshift options and the source turned out to be at the slightly less likely redshift. As such, our 1 mm follow-up observations demonstrate that reliable redshifts for DSFGs can be obtained when only a single line is detected in the 3 mm redshift scan, provided that the dust continuum spectral energy distribution (SED) of the source is well sampled.

One of the sources included in our 1 mm follow-up program (SPT0319-47) was presented as having no lines detected in its ALMA 3 mm scan in Weiß et al. (2013). The 3 mm spectrum, however, did show a very broad (FWHM ~ 1700 km s^{-1}), faint line feature at 104.4 GHz. In our 1 mm follow-up observations we now detect a highly significant line at 250.76 GHz in this source. This detection identifies the 3 mm and 1 mm lines as CO(5–4) and CO(12–11) placing SPT0319-47 at $z = 4.516(4)$. This source was also detected in [C II] with APEX/FLASH cementing the redshift (see Appendix A).

4.1.2 A misidentified redshift: The discovery and solution

SPT0551-50 was identified in Weiß et al. (2013) as a secure redshift at $z = 2.1232(2)$ based on a single CO line detection (identified as CO(3–2)) in conjunction with a detection of the CIV line from the Very Large Telescope (VLT). We afterwards failed to detect [C II] with APEX (Gullberg et al., 2015) and CO(1–0) with ATCA at this

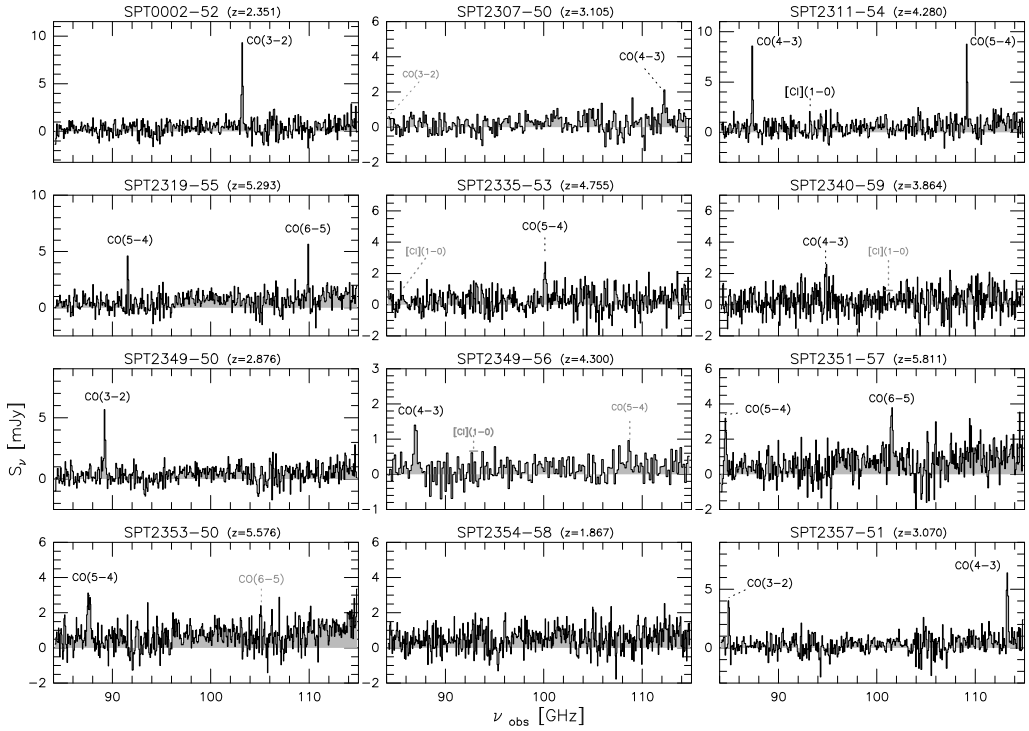

Figure 4.2: The 3 mm Cycle 1 ALMA spectra (spanning 84.2 – 114.9 GHz) of the 12 sources detected in continuum. Dashed *gray* lines indicate the frequencies of lines that are expected but not detected in the spectrum. SPT2340-59 has multiple counterparts and the spectrum is extracted from counterpart B (see Appendix B). SPT2349-56 likewise has multiple components and the spectrum shown here is a stack of the spectra extracted from components B and C.

redshift. In particular the non-detection of the ATCA line is very significant with $L'_{\mathrm{CO(3-2)}}/L'_{\mathrm{CO(1-0)}} > 6$ compared to $L'_{\mathrm{CO(3-2)}}/L'_{\mathrm{CO(1-0)}} \sim 1.2$ for sources with secure redshifts (Spilker et al., 2014), where L' is the line luminosity (in $\mathrm{K\,km\,s^{-1}\,pc^2}$, see Solomon et al. 1997), and rules out the earlier redshift determination by Weiß et al. (2013). Based on this we re-visited the other redshift options. The favored option based on the dust continuum SED is $z = 3.163(3)$ with the line in the ALMA 3 mm spectrum being CO(4–3). This redshift was confirmed by new [C II] observations with APEX/FLASH. The line observed with the VLT and interpreted as CIV most likely originates from an unrelated lensing arc. For a more detailed description on the source and a presentation of the above mentioned data see Appendix A.

4.1.3 New ALMA Cycle 1 and 3 3 mm scans

4.1.3.1 Continuum results and morphology

In Cycle 1 we detect the 3 mm continuum in 12 out of 15 sources at SNRs of 5 - 18. For two sources the non-detection in ALMA was expected after a careful analysis of all photometric data (only available to us after ALMA's Cycle 1 deadline) showed that

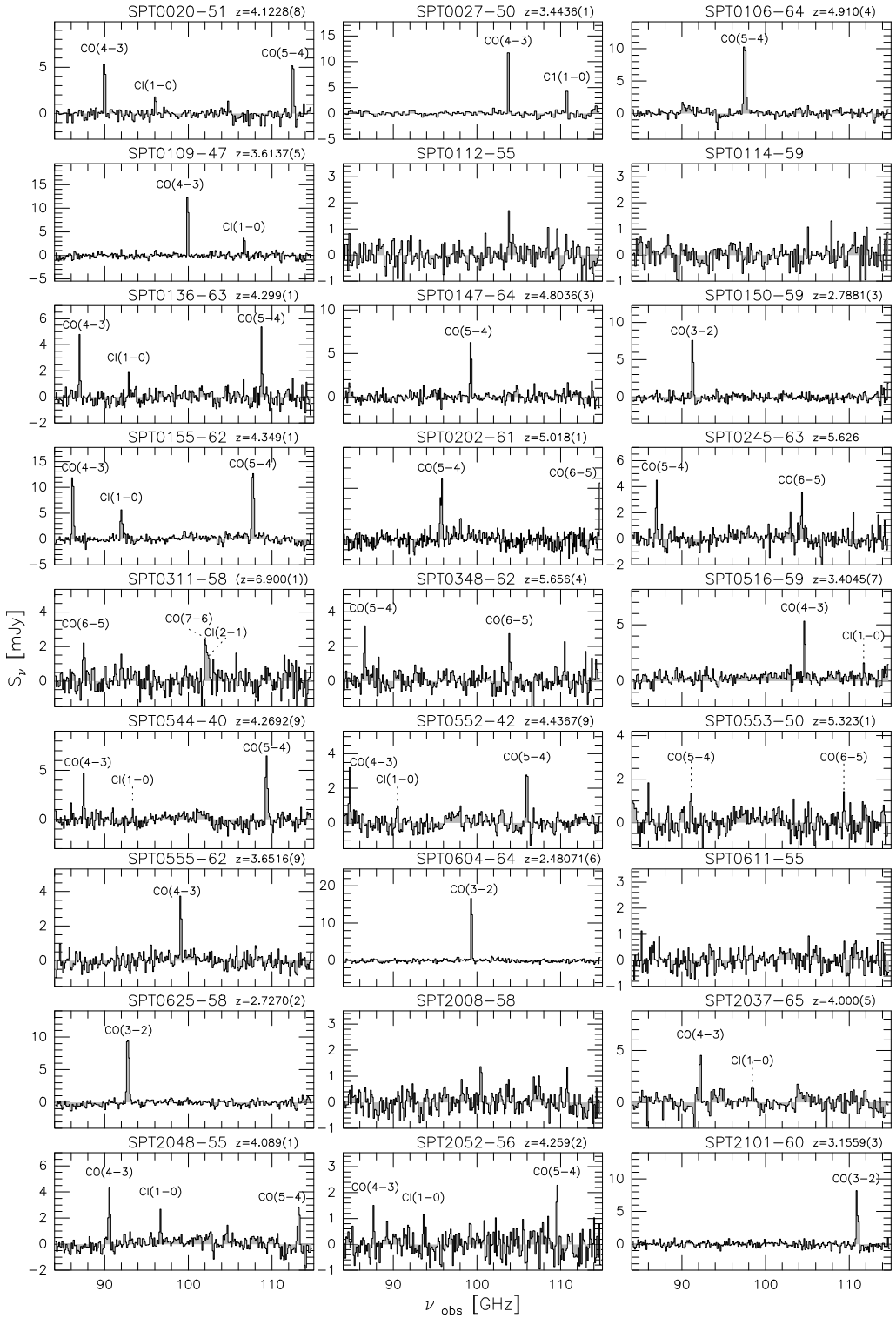

Figure 4.3: The 3 mm Cycle 3 ALMA spectra (spanning 84.2 – 114.9 GHz) of all 27 sources. SPT2052-56 has two counterparts and the spectrum is extracted from counterpart A (see Appendix B).

both sources are likely due to extended galactic foreground.[1] These two sources have low SNRs in the SPT maps and are ignored in the following. For the third source, the 3 mm ALMA non-detection is consistent with the overall photometry of the source. In Cycle 3 we detect all 27 sources in continuum with SNRs of 6–190.

Table 3.1 lists the ALMA 3 mm continuum position of the detected sources. Their 3 mm continuum flux densities are given in Section 3.2.

In total 36 sources appear as point sources, and three sources (SPT2052-56, SPT2340-59 and SPT2349-56) split into multiple components (see Figure B.4). Given the compactness of the lensed images this is expected at the coarse resolution of the maps ($\sim 3''$). To spatially resolve the lensed source distribution typically a much higher spatial resolution of $\sim 0.5''$ is required as demonstrated by our high resolution 870 μm imaging (Spilker et al., 2016).

Multiple components at the resolution of the 3 mm maps can be explained in two ways: We either see multiple individual sources or multiple gravitationally lensed images of the lensed source. For SPT2052-56 and SPT2340-59 we see two components (listed in Table 3.1, and named A and B respectively, see Appendix B for the continuum image). We extract spectra at both positions, but only see a line in component A, which we then use in the further analysis. For SPT2349-56 we see two components, one point source and one more extended component. For this source we take advantage of also having high resolution ALMA 870 μm imaging, which shows three counterparts (Spilker et al., 2016). In this image the extended 3 mm component breaks up into two point sources and we use the three 870 μm positions to define the three components A, B, and C listed in Table 3.1 and shown in Appendix B. We see a hint of a line at the same frequency in all components (with small shifts between the line frequency), with component B and C showing stronger lines. Deeper 870 μm data with $\sim 0.5''$ spatial resolution show, that these 3 components of SPT2349-56 are only the brightest galaxies of a protocluster with 14 detected members (Miller et al. 2017, submitted). Given the discovery of the nature of SPT2349-56 the two other sources showing several components (SPT2052-56 and SPT2340-59) are now considered candidates for protoclusters.

4.1.3.2 Spectroscopy results

The ALMA spectra of the 12 sources from Cycle 1 are presented in Figure 4.2. The spectrum for SPT2344-51 is not shown, since without the ALMA 3 mm continuum detection, we do not know the source position with sufficient accuracy to be able to extract the spectrum. We verified, however, that the data cube for this source does not contain any strong lines. The spectra from the 27 sources from Cycle 3 are shown in Figure 4.3. In total we see 59 lines (16 lines in the 12 Cycle 1 spectra and 43 lines in the 27 Cycle 3 spectra), which we identify as ^{12}CO and [C I] emission lines. We have marked the CO and [C I] lines that we do not detect in *gray*, where the horizontal line represents the expected flux density based on the SPT-DSFG line luminosities from Spilker et al. (2014).

[1] We submitted a source change request for these two sources to ALMA but the request was rejected.

Table 4.1: Redshifts and line identifications

Source	**case**	z	$T_{\rm dust}$ **[K]**	$\lambda_{\rm peak}\star$ **[μm]**	**lines from 3 mm scans †**	**new lines & comments**
SPT2354-58	II	1.867(1)	42.8±1.9	77±6	no 3 mm line	$z_{\rm phot} = 1.2 \pm 0.2$, OH^+ from ALMA
SPT0452-50	III	**2.0104(2)**	22.0±0.9	151±7	CO(3–2)[a]	CO(1–0)[g] from ATCA
SPT0512-59	III	**2.2331(2)**	32.7±1.4	102±4	CO(3–2)[a]	CO(6–5) from ALMA; [C II][d] from SPIRE FTS
SPT0002-52	II	**2.3513(4)**	42.3±2.1	72±6	CO(3–2)	CO(5–4) from APEX
SPT0604-64	I	2.48071(6)	36.9±1.2	96±3	CO(3–2)	$z_{\rm phot} = 2.4 \pm 0.3$
SPT0125-47	III	**2.51480(7)**	38.6±1.6	70±4	CO(3–2)[a] & CO(1–0)[a]	
SPT0551-48	II	**2.5833(2)**	38.6±1.9	78±7	CO(7–6), CO(8–7) & [C I](2–1)	lines from Z-Spec; CO(1–0)[e] from ATCA; no ALMA data.
SPT2332-53	III	**2.7256(2)**	47.4±2.8	78±4	CO(7–6)[a], Lyα[a] & C IV 1549Å[a]	lines from Z-Spec; CO(1–0)[e] from ATCA; no ALMA data
SPT0625-58	I	2.7270(2)	34.6±1.2	101±	CO(3–2)	$z_{\rm phot} = 2.9 \pm 0.5$
SPT2134-50	III	**2.7799(2)**	39.0±1.6	70±8	CO(3–2)[a], CO(7–6)[a] & CO(8–7)[a]	
SPT0538-50	III	**2.7855(1)**	36.5±1.4	96±7	CO(7–6)[a], CO(8–7)[a] & Si IV 1400Å[a]	lines from Z-Spec; CO(1–0)[e] and CO(3–2)[f] from ATCA; no ALMA data
SPT0150-59	I	2.7881(3)	34.8±1.2	93±7	CO(3–2)	$z_{\rm phot} = 3.1 \pm 0.6$
SPT2349-50	II	**2.877(1)**	37.9±1.6	106±16	CO(3–2)	CO(7–6) from SEPIA
SPT2357-51	II	**3.0703(6)**	37.2±1.2	107±5	CO(3–2) & CO(4–3)	Lyman-α and $OII_{3727Å}$ from VLT/X-shooter
SPT0103-45	III	**3.0917(3)**	32.3±1.2	109±7	CO(3–2)[a] & CO(4–3)[a]	
SPT2307-50	II	3.108(1)	35.8±3.3	61±16	CO(4–3)	$z_{\rm phot} = 3.4 \pm 0.7$
SPT0550-53	III	**3.1280(7)**	33.2±1.9	110±10	CO(4–3)[a]	CO(8–7) from ALMA; [C II][d] from APEX
SPT2101-60	I	3.1559(3)	40.7±1.4	85±5	CO(4–3)	$z_{\rm phot} = 3.0 \pm 0.5$
SPT0551-50	III	**3.164(1)**	37.4±1.4	104±5	CO(4–3)[b]	[C II] and CO(8–7) from APEX
SPT0529-54	III	**3.3689(1)**	31.8±1.2	119±9	CO(4-3)[a], [C I](1–0)[a] & ^{13}CO(4–3)[a]	
SPT0532-50	III	**3.3988(1)**	37.6±1.4	93±6	CO(4-3)[a], [C I](1–0)[a] & ^{13}CO(4–3)[a]	
SPT0516-59	I	**3.4045(7)**	45.8±1.9	79±5	CO(4–3)	[C II] from APEX
SPT0027-50	I	**3.4436(1)**	41.8±1.4	93±6	CO(4–3), [C I](1–0)	
SPT0300-46	III	**3.5954(7)**	38.6±1.6	99±3	CO(4–3)[a] & [C I](1–0)[a]	CO(10–9) from ALMA; [C II][d] from APEX
SPT0109-47	I	**3.6137(5)**	43.2±1.4	88±8	CO(4–3), [C I](1–0)	

continued

Table 4.1: Redshifts and line identifications

Source	**case**	z	$T_{\rm dust}$ **[K]**	$\lambda_{\rm peak}\star$ **[μm]**	**lines from 3 mm scans †**	**new lines & comments**
SPT0555-62	I	3.6516(9)	35.1±1.4	100±19	CO(4–3)	$z_{\rm phot} = 4.0 \pm 0.6$
SPT2147-50	III	**3.7602(3)**	40.2±1.6	91±6	CO(4–3)[a] & [C I](1–0)[a]	
SPT2340-59	II	3.864(1)	40.2±1.9	91±7	CO(4–3)	$z_{\rm phot} = 3.8 \pm 0.6$
SPT0125-50	III	**3.959(3)**	43.7±2.3	68±9	CO(4–3)[a] & [C I](1–0)[a]	CO(10–9) and H_2O[c] abs line from ALMA
SPT2037-65	I	**4.000(5)**	35.1±1.4	95±4	CO(4–3), [C I](1-0)	
SPT2048-55	I	**4.089(1)**	32.0±1.6	71±6	CO(4–3), [C I](1-0)	
SPT0020-51	I	**4.1228(8)**	38.3±1.4	90±3	CO(4–3), CO(5–4)	
SPT0418-47	III	**4.2248(7)**	45.3±2.3	84±8	CO(4–3)[a] & CO(5–4)[a]	
SPT0113-46	III	**4.2328(5)**	31.3±1.4	119±9	CO(4–3)[a], [C I](1-0)[a] & CO(5–4)[a]	
SPT2052-56	I	**4.259(2)**	46.0±28	88±3	CO(4–3), [C I](1-0), CO(5–4)	
SPT0544-40	I	**4.2692(9)**	38.6±1.4	92±13	CO(4–3), CO(5–4)	
SPT2311-54	II	**4.2795(4)**	47.7±2.8	72±7	CO(4–3), [C I](1–0) & CO(5–4)	
SPT0345-47	III	**4.2958(2)**	50.2±2.8	63±4	CO(4–3)[a] & CO(5–4)[a]	
SPT0136-63	I	**4.299(1)**	37.4±1.4	94±2	CO(4–3), CO(5–4), [C I](1–0)	
SPT2349-56	II	**4.304(2)**	46.7±2.8	91±9	CO(4–3)	[C II] from APEX/FLASH
SPT0155-62	I	**4.349(1)**	30.4±0.9	113±8	CO(4–3), CO(5–4), [C I](1–0)	
SPT2103-60	III	**4.4357(6)**	37.4±1.6	96±7	CO(4–3)[a] & CO(5–4)[a]	
SPT0552-42	I	**4.4367(9)**	33.9±1.4	94±4	CO(4–3), CO(5–4)	
SPT0441-46	III	**4.4771(6)**	38.1±1.9	91±15	[C I](1–0)[a], CO(5–4)[a] & [C II][a]	CO(11–10) & NH_3 from ALMA
SPT0319-47	III	**4.510(4)**	39.9±2.1	77±8	CO(5–4)	CO(12–11) from ALMA; [C II] from APEX
SPT2146-55	III	**4.5672(2)**	37.4±2.1	91±11	[C I](1–0)[a] & CO(5–4)[a]	
SPT2335-53	II	**4.757(2)**	57.0±4.2	80±4	CO(5–4)	[C II] from APEX
SPT2132-58	III	**4.7677(2)**	37.9±1.9	79±11	CO(5–4)[a] & [C II][a]	CO(12–11) and [N II] from ALMA
SPT0459-59	III	**4.7993(5)**	38.1±1.9	102±16	[C I](1–0)[a] & CO(5–4)[a]	
SPT0147-64	I	4.8036(3)	38.3±1.4	84±6	CO(5–4)	$z_{\rm phot} = 4.6 \pm 0.7$
SPT0459-58	III	**4.856(4)**	41.6±1.9	84±7	CO(5–4)[a]	CO(11–10) from ALMA
SPT0106-64	I	**4.910(4)**	47.4±1.9	64±5	CO(5–4)	[C II] from APEX
SPT0202-61	I	**5.018(1)**	39.3±1.6	60±15	CO(5–4)	[C II] from APEX
SPT2319-55	II	**5.2929(5)**	42.1±2.1	81±14	CO(5–4) & CO(6–5)	
SPT0553-50	I	**5.323(1)**	42.5±1.9	83±6	CO(5–4), CO(6–5)	

continued

Table 4.1: Redshifts and line identifications

Source	**case**	z	$T_{\rm dust}$ **[K]**	$\lambda_{\rm peak}\star$ **[μm]**	**lines from 3 mm scans †**	**new lines & comments**
SPT2353-50	II	**5.576(3)**	46.3±2.3	63±9	CO(5-4)	[C II] from APEX
SPT0245-63	I	**5.626(1)**	41.4±2.1	103±4	CO(5–4), CO(6–5)	
SPT0346-52	III	**5.6559(4)**	50.5±2.3	71±6	CO(5–4)^a, CO(6–5)^a, H_2O^a & H_2O^{+a}	
SPT0348-62	I	**5.656(4)**	46.5±2.3	98±8	CO(5–4), CO(6–5)	
SPT0243-49	III	**5.699(1)**	32.7±1.6	113±3	CO(5–4)^a & CO(6–5)^a	
SPT2351-57	II	**5.811(2)**	53.5±2.8	70±2	CO(5–4) & CO(6–5)	
SPT0311-58	I	**6.900(1)**	45.6±3.5	65±7	CO(6–5)^h, CO(7–6)^h, [C I](2–1)^h	[C II]^h from APEX and ALMA; CO(3–2)^h from ATCA
SPT0128-51	IV				no lines^a	$z_{\rm phot} = 3.6 \pm 0.9$
SPT0457-49	IV				no lines^a	$z_{\rm phot} = 3.4 \pm 0.6$
SPT2344-51	IV				no lines	$z_{\rm phot} = 3.5 \pm 0.7$
SPT0112-55	IV				no lines	$z_{\rm phot} = 3.6 \pm 0.7$
SPT0114-59	IV				no lines	$z_{\rm phot} = 3.0 \pm 0.5$
SPT0611-58	IV				no lines	$z_{\rm phot} = 2.3 \pm 0.4$
SPT2008-60	IV				no lines	$z_{\rm phot} = 3.0 \pm 0.6$

The parenthesis at the end of the redshift gives the uncertainty on the last digit presented. The unbolded redshifts show the single line redshifts. The numbers in the column named 'case' refers to the following cases: **I** New Cycle 3 redshifts **II** New Cycle 1 redshifts. **III** Sources presented in Weiß et al. (2013). Comments in the right column indicates observations added since then; **IV** Sources showing no lines.

† This column shows the lines from the 3 mm line scan from this work and lines presented in Weiß et al. (2013)

⋆ The rest frame SED peak wavelength, found from fitting a spline. See more details in Section 5.2.2.

a Published by Weiß et al. (2013)

b Published by Weiß et al. (2013) as CO(3–2)

c Published by Spilker et al. (2014)

d Published by Gullberg et al. (2015)

e Published by Aravena et al. (2013)

f Published by Spilker et al. (2015)

g Published by Aravena et al. (2016)

h Published by Strandet et al. (2017)

The lines are distributed over the sources in the following manner:
• 18 sources (four in Cycle 1 and 14 in Cycle 3) show two or more lines, yielding an unambiguous redshift from the 3 mm data alone (see Table 4.1 top).
• 16 sources (seven in Cycle 1 and nine in Cycle 3) show a single line in the 3 mm spectra. For six sources (SPT0106-64, SPT0202-61, SPT0516-59, SPT2335-53, SPT2349-56 and SPT2353-50) we have detected [C II] with APEX/FLASH, and for two sources (SPT0002-52 and SPT2349-50) we have detected CO using APEX/SEPIA. These additional lines secure the redshifts of eight sources. For the remaining eight sources we use the dust SEDs to obtain the line identification and the redshift (see Section 4.1.3.3).
• Five sources (one in Cycle 1 and four in Cycle 3) show no lines. For one source in Cycle 1 (SPT2354-58) we find an absorption line in our 870 μm high resolution ALMA imaging cube determining the redshift, and placing the source in the redshift desert (see Section 4.1.3.4).

4.1.3.3 Sources with one detected line

For the eight sources where only a single line is detected in the 3 mm spectrum, the first step in determining their redshift is to establish the possible line identifications. In all spectra with multiple lines, the brightest line always turns out to be a transition of CO and we therefore assume that the single line detections are from CO as well. For an overview of which lines are detectable in our 3 mm spectral scans from sources at a given redshift, see Figure 2.3 and Spilker et al. (2014). The most likely line identifications are either CO(2–1) or CO(3–2), as these lines appear in the observed band without any other lines present for a large redshift interval ($1.0 < z < 3.0$ with a narrow redshift desert at $1.7 < z < 2.0$). At most redshifts CO(4–3) and CO(5–4) come with a [C I] line, and will only appear as single lines in very small redshift intervals or when the fainter [C I] line remains undetected. We rule out $J = 6$–5 and higher transitions as they will always come with another CO line in the observed band.

In the analysis of the dust SEDs, the redshift and the dust temperature are degenerate when the dust spectrum is fit by a single component modified grey body. From a fit to all sources with unambiguous redshifts (53 targets) we know the distribution of dust temperatures of the SPT-DSFGs (see Figure 4.4). For sources with a single line we calculate the implied dust temperature for each of the 4 redshift options (see Section 2.2.3). The likelihood of each redshift option is obtained by comparing the resulting four dust temperatures to their occurrence in the SPT-DSFG sample. The process is described in more detail in Section 5.2.1.

We use this technique to test the redshift options for all eight sources with a single line identification (see sources with redshifts given in *blue* in Figure 4.5). We calculate the probability of each redshift option by reading off the probability of each option from the photometric redshift probability distribution and normalizing the total probability to unity.

In Figure 4.5 we show the redshift options of all sources with a single line in their ALMA 3 mm spectrum from both Weiß et al. (2013) and this work. We use the current dust temperature distribution (*green* distribution in Figure 4.4) to calculate the

probabilities for the line identifications for all the sources in the Figure. We show the spectroscopic redshift of each source in *green* and where the prediction does not correspond to the spectroscopic redshift we have highlighted the redshift in *red*. For the sources which do not have a spectroscopic redshift the most probable redshift is highlighted in *blue*. In a sample of 18 sources with a single line in their ALMA spectrum we correctly predict the redshift for 13 sources (70% success rate). This seems to be a reliable but not perfect method so to be certain of the redshifts presented we continue our observing campaigns to obtain an additional line. All sources from Weiß et al. (2013) which previously only had a single line observed now have a second line observed and thereby have secure redshifts. The redshifts for the sources with single line detections are listed unbolded in Table 4.1.

In two of the cases where we find one line in the ALMA spectrum we would expect to detect a second CO line given their most probable or confirmed redshift. For SPT2353-50 the ALMA 3 mm line is found to be CO(5–4) based on the detection of [C II] but we do not detect the CO(6–5) line that is expected to also be in the spectral scan. It may be associated with a SNR ~ 1.5 feature in the spectrum at the position of the line. Using the stacked spectrum of the SPT-DSFGs (Spilker et al., 2014) we calculate the line luminosity ratio $L'_{\mathrm{CO(6–5)}}/L'_{\mathrm{CO(5–4)}} \sim 0.7$ for the SPT-DSFGs presented in Weiß et al. (2013). The SNR ~ 1.5 feature gives a line luminosity ratio of $L'_{\mathrm{CO(6–5)}}/L'_{\mathrm{CO(5–4)}} \sim 0.3$. For SPT2349-56, the ALMA 3 mm line is found to be CO(4–3) based on the detection of [C II] but we do not detect the CO(5–4) line, though it can be associated with a SNR ~ 1.5 feature in the spectrum at the predicted frequency of the CO(5–4) line. From Spilker et al. (2014) the line luminosity ratio is $L'_{\mathrm{CO(5–4)}}/L'_{\mathrm{CO(4–3)}} \sim 1.1$. The SNR ~ 1.5 feature gives a line luminosity ratio of $L'_{\mathrm{CO(5–4)}}/L'_{\mathrm{CO(4–3)}} \sim 0.7$. In both cases the second line have lower than expected line luminosity ratios but are not inconsistent with typical line ratios found in high redshift sources (e.g. see review by Carilli & Walter, 2013).

4.1.3.4 Sources without ALMA line detections

In total there are six sources in Cycle 1 and 3 not showing any lines in their 3 mm spectra. We here go over each of the sources to assess why no lines are detected. A summary of the sources for which we do not detect any lines is presented at the bottom of Table 4.1.

As mentioned above, we searched for emission lines in the ALMA data cube of SPT2344-51 (which remained undetected in the 3 mm continuum data), but did not find evidence for any strong lines despite its photometric redshift of $z_{\mathrm{phot}} = 3.5 \pm 0.7$. Given the faintness of this source in the continuum, the most likely interpretation is that the source is simply too faint to detect its CO lines at the sensitivity limit of our observations.

This most likely also holds for SPT0114-59, SPT2008-58 and the two remaining sources without line detections from Weiß et al. (2013) (SPT0128-51 & SPT0457-49). Their 1.4 mm and 870 μm continuum flux densities are comparable to those of SPT2344-51, which place them at the faint end of the SPT sources targeted with ALMA though

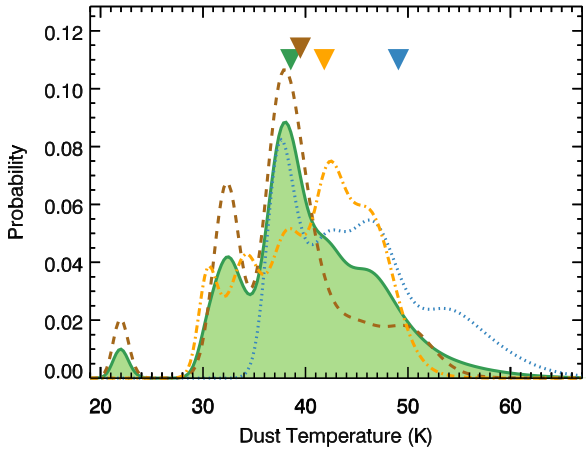

Figure 4.4: The probability distribution of the dust temperature based on all 53 sources in the SPT-DSFG sample with unambiguous redshifts (*green*). Overlaid is the dust temperature distribution for all sources with unambiguous redshifts observed in ALMA Cycle 0 (Weiß et al., 2013) in *brown*, ALMA Cycle 1 in *blue*, and ALMA Cy 3 in *orange*. The triangles in the top of the plot show the median of the distributions.

we do detect these sources in continuum. For SPT0457-49 we searched the redshift desert with ATCA looking for CO(1–0) without success (see Appendix A).

SPT0112-55 is not as weak at 1.4 mm and 870 μm as the sources described above, but it is in the fainter end of the SPT-DSFG population. The spectrum shows some potential line features, but they are not significantly detected, and cannot be combined into a single redshift identification. The photometric redshift of this source is $z_{\mathrm{phot}} = 3.5 \pm 0.7$ which indicates that the redshift of this source doesn't fall in the redshift desert, but that it, as the above described sources, and has too weak lines for detection.

The reason that these sources are not detected, even though their photometric redshifts indicate that they are in the right redshift range, might be that they break up into multiple sources at 3 mm. In that case the continuum and lines are distributed across multiple positions which may cause them to remain undetected. This was almost the case for SPT2349-56, which is detected but is split into multiple components in the 3 mm ALMA spectrum showing weak lines despite being bright at both 1.4 mm and 870 μm.

SPT0611-58 is bright at 1.4 mm and 870 μm and it cannot be assumed, as for the above sources, that it is too faint for detection. With a low photometric redshift of $z_{\mathrm{phot}} = 2.3 \pm 0.4$, it is possible however that the redshift of this source falls within the redshift desert or even below $z < 1$.

Without more or deeper observations we cannot determine the redshifts of these seven sources and we drop them in the analysis of the redshift distribution.

SPT2354-58 does not show indications for CO lines in the ALMA Cycle 1 3 mm spectrum and the continuum flux densities (see Section 3.2) are such that we should have detected CO lines based on the line to continuum ratio of the SPT sources where

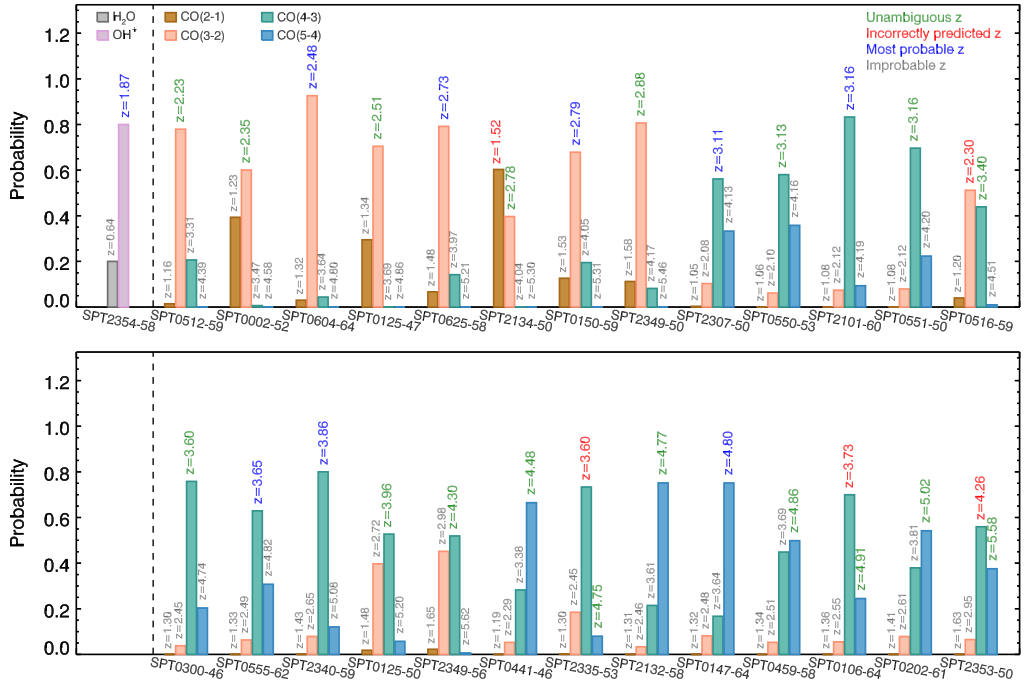

Figure 4.5: Histograms showing the probability of the redshift options for each source with a single line detection in the ALMA 3 mm spectrum based on the dust temperature distribution shown in Figure 4.4. To the far left we show a similar analysis for the line identifications for the absorption line in the 870 μm data for SPT2354-58. The sources are sorted by redshift (spectroscopic if available and otherwise most probable). The bars represent the possible line identification and their probability. Sources where the most probable redshift is identical to the spectroscopic redshift are highlighted in *green*; sources where the most probable redshift is not the spectroscopic redshift are highlighted in *red*. Sources for which we do not yet have a confirmed spectroscopic redshift with at least two lines are highlighted in *blue*.

we detect lines (like SPT0611-58). For this source we find an absorption line in our 870 μm high resolution imaging data cube. This absorption line has two line identifications that fall outside the redshift range probed by the 3 mm redshift scan: $OH^+(1_{22} - 0_{11})$ at $z = 1.867(1)$ (in the redshift desert) and $H_2O(1_{10} - 1_{01})$ at $z = 0.6431(3)$ (below our searched redshift range). There could possibly be more molecules which may show up in absorption, but we limit the discussion to the most likely ones. $OH^+(1_{22} - 0_{11})$, unlike $H_2O(1_{10} - 1_{01})$, has been detected in the local ultra luminous galaxy Arp220 (Rangwala et al., 2011). Furthermore, for the second option we should have seen CO(5–4) in the same cube but we did not. The first redshift option is also much more likely based on the photometry (see Figure 4.5) and it is thus the most likely redshift and we have added this source to our list of sources with single-line redshifts (see Table 4.1). The ALMA 870 μm spectra are shown along with a more detailed description of the source in Appendix B.

Table 4.2: Measured redshift distribution for SPT sources

z	$\mathbf{N}^a$	$\mathbf{d}n/\mathbf{d}z$	**lens-cor**^{b} $\mathbf{d}n/\mathbf{d}z$
$1.5-2.0$	1	0.02 ± 0.02	0.05 ± 0.05
$2.0-2.5$	4	0.06 ± 0.03	0.13 ± 0.06
$2.5-3.0$	8	0.13 ± 0.05	0.18 ± 0.06
$3.0-3.5$	10	0.16 ± 0.05	0.18 ± 0.06
$3.5-4.0$	6	0.10 ± 0.04	0.09 ± 0.04
$4.0-4.5$	15	0.24 ± 0.06	0.20 ± 0.05
$4.5-5.0$	8	0.13 ± 0.05	0.09 ± 0.03
$5.0-5.5$	3	0.05 ± 0.03	0.03 ± 0.02
$5.5-6.0$	6	0.10 ± 0.04	0.06 ± 0.02
$6.0-6.5$	0	0.0 ± 0.0	0.0 ± 0.0
$6.5-7.0$	1	0.02 ± 0.02	0.01 ± 0.01

4.2 Discussion

4.2.1 The redshift distribution

Our sample is composed of 62 sources with reliable redshifts (three from APEX/Z-Spec and 59 from ALMA 3 mm scans), meaning that they show at least one spectral line along with well-sampled photometry. This translates into a success rate for our ALMA 3 mm scan technique of $>85\,\%$ (59 out of 69 targeted). Two or more lines have been identified in 53 of the 62 sources ($\sim 85\%$). For 35 sources the redshifts were identified directly from the ALMA 3 mm spectrum, for 3 sources the redshifts were found using Z-Spec/APEX, and for the remaining 15 sources the redshift was secured with observations of a second molecular line from ALMA, APEX, ATCA or *Herschel*/SPIRE. The highest redshift source in the sample is SPT0311-58 at $z = 6.900(2)$, which is the highest redshift DSFG discovered so far. Chapter 6 (Strandet et al., 2017) describes this source in more detail and investigate the ISM conditions in the source. The redshift survey of the SPT-DSFGs is by far the largest and most complete redshift survey of DSFGs so far.

The redshift distribution of this sample is shown in *orange* in Figure 4.6 and listed in Table 4.2. The median redshift is $z_{\rm median} = 4.1 \pm 0.2$ (indicated by an *orange* triangle above the distribution), compared to $z = 3.9 \pm 0.4$ when only including the Cycle 1 redshifts (Strandet et al., 2016). The errors on the median were determined using a bootstrap method, where we randomly sampled 62 sources from the redshift distribution 1000 times and took the standard deviation of the median values.

The distribution peaks between $z = 2.5$ and $z = 5.0$ with a large fraction (75%) of the sample at $z > 3$. We see no sources at $z < 1.5$ as the probability of a source undergoing strong gravitational lensing drops significantly below a redshift of $z \sim 2$.

In the top panel of Figure 4.6 we overlay the distribution from Weiß et al. (2013) (dashed *red* line). As the sample in Weiß et al. (2013) was selected from 1300 square-degrees with $S_{1.4\rm mm} > 20\,$mJy, it is representative of the brightest sources from the SPT-DSFG sample (the difference between the SPT sub-samples observed in the ALMA

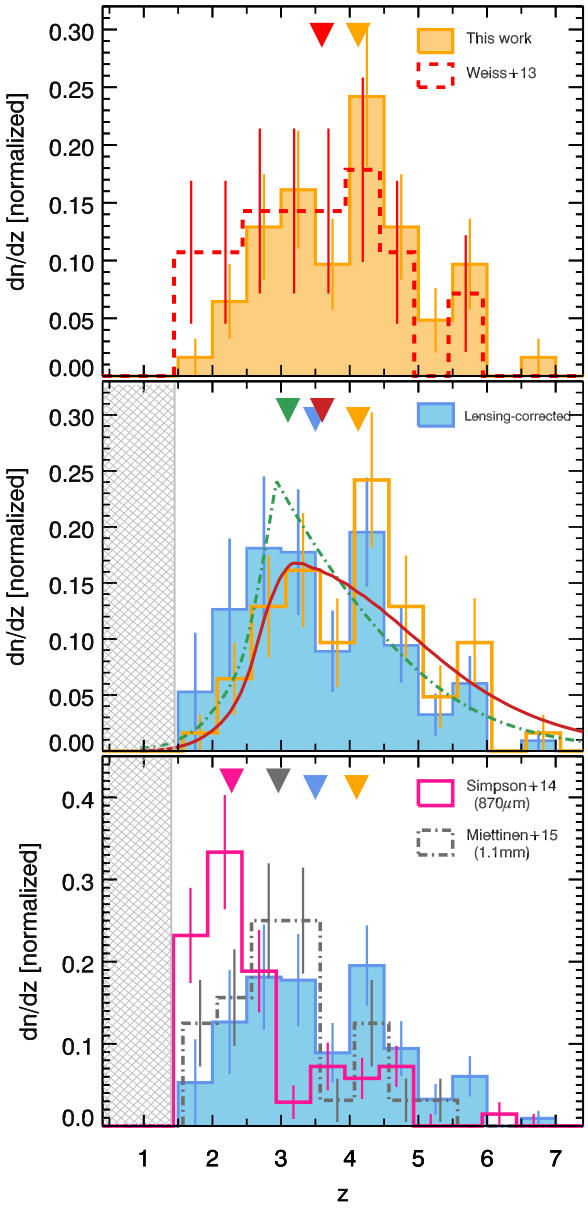

Figure 4.6: Redshift distributions for various samples described in Section 4.2. The filled triangles in the top of the plots show the median redshifts of the samples with the corresponding colors. *Top*: The *orange* histogram shows the redshift distribution of the sources in our sample including the sources from Weiß et al. (2013). It is compared to the original redshift distribution from Weiß et al. (2013) (*red* dashed line). *Middle*: The lensing-corrected redshift distribution of our sample (*blue*) compared to the original redshift distribution (*orange*, identical to the *orange* distribution in the top panel). The *gray* hatched region indicates the region we do not include in our analysis due to the low probability of finding lensed sources (see Figure 4.7). Also shown are model predictions from Béthermin et al. (2015) of a sample of lensed sources selected in the same way as the SPT-DSFGs (*red*) and a sample of unlensed sources selected in the same way as the SPT-DSFGs (*green*). *Bottom*: The lensing-corrected redshift distribution compared to redshift distributions from Simpson et al. (2014, *pink*) and Miettinen et al. (2015, *gray*), where sources below $z < 1.5$ have been removed for a fair comparison.

3 mm scans has been discussed in Section 3.1.2 and is shown in Figure 3.1). Models from Béthermin et al. (2015) predict that the difference between these two samples based on the change in flux cut are negligible. The only redshift bins in which we see a significant difference between this sample and that of Weiß et al. (2013), are those in the range $1.5 < z < 2.5$. In Weiß et al. (2013), all three sources without line detections were placed in the $1.5 < z < 2.5$ bin assuming they fell into the CO redshift desert ($1.74 < z < 2.00$). As discussed in Section 4.1.3.4, we do not follow this approach, but ignore sources without any detected lines. Removing these sources from the distribution of Weiß et al. (2013) (except for SPT0319-47 which now enters with an unambiguous redshift of $z = 4.510(4)$) and correcting the one misidentified redshift (SPT0551-50, see Section 4.1.2) changes the median from $z = 3.6$ to $z = 3.8$, which is consistent with what we find in this work. A Kolmogorov-Smirnov (K-S) test shows that the probability that these two distributions originate from a common sample is $p = 0.41$ (and when only the Cycle 1 redshifts are added $p = 0.81$ Strandet et al., 2016).

4.2.2 Selection effects

This section describes the influence of our selection methods on the redshift distribution. The two main effects come from our high flux cut that selects almost exclusively gravitationally lensed sources and our long selection wavelength.

As discussed in Blain et al. (2002), da Cunha et al. (2013), and Staguhn et al. (2014) the CMB could make cold DSFGs at high redshifts difficult to detect. As SPT-DSFGs have a median dust temperature of $T_{\rm dust} = 39 \pm 6$ K, and are thus quite warm, this effect only becomes relevant at very high redshifts ($z > 10$). For the sources presented in this work, the effect of the CMB is negligible.

In the two following sections we describe the two main selection effects, gravitational lensing and wavelength selection, which complicate a direct comparison between the redshift distributions of DSFGs in the literature.

4.2.2.1 Lensing effects and lensing-correction

Based on models of the high-redshift DSFG population (e.g. Baugh et al., 2005; Lacey et al., 2010; Béthermin et al., 2012; Hayward et al., 2013), we would expect very few sources intrinsically bright enough to exceed our adopted flux density threshold at 1.4 mm (> 16 mJy), and we thus expect the SPT-DSFG sample to consist almost solely of gravitationally lensed sources (Blain, 1996; Negrello et al., 2007). This expectation was confirmed by ALMA 870 μm high resolution observations showing that our sources resolve into arcs, multiple images, and Einstein rings, characteristic of lensed objects (Vieira et al., 2013; Hezaveh et al., 2013; Spilker et al., 2014). We have found a few examples where the source splits into multiple, ultra luminous galaxies (e.g., SPT2349-56; see Appendix B) but these are rare in our sample.

Gravitational lensing is what enables us to study these high redshift sources in detail but also hampers a direct comparison of our results to unlensed samples. Figure 4.7, based on the model presented in Hezaveh & Holder (2011), shows the probability

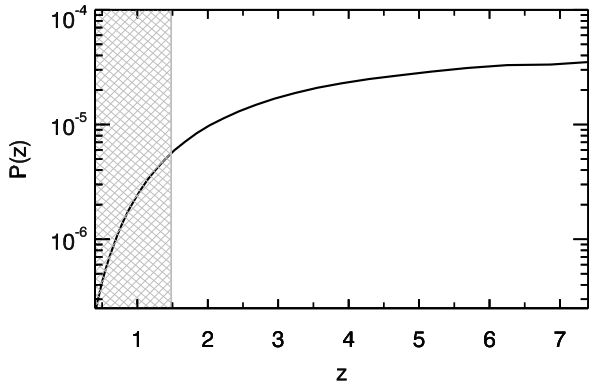

Figure 4.7: The assumed probability of gravitational lensing as a function of redshift for a source magnification of $\mu = 10$ (Hezaveh & Holder, 2011). Because of the drastically falling probability of lensing below $z < 1.5$ (*gray* hatched region) we do not conclude anything about the redshift distributions in this range.

of a source undergoing strong gravitational lensing between a given source redshift and the observer. The probability of sources at $z \lesssim 1.5$ undergoing strong lensing is heavily suppressed relative to sources at higher redshifts ($z > 4$), where the probability of lensing is flat. The lensing probability at $z \sim 2$ is suppressed by a factor of three compared to at high redshifts, while at $z \sim 3$ this is reduced to a factor of less than two. All of these findings assume that DSFGs do not undergo a systematic size evolution with increasing redshift. The size evolution matters as more compact emission regions are preferentially identified from gravitational lensing, and more compact sources will give a higher chance of strong lensing. For the size evolution to be the explanation of the higher redshifts seen in our sample compared to other samples there would need to be a decrease in source size with redshift. Whether DSFGs undergo a systematic size evolution is still under debate. A few studies suggest a decrease in size with redshift (Fathi et al., 2012; Greve et al., 2012, based on QSO host galaxies at high redshift, and thereby not necessarily representative for DSFGs). Other studies do not support an evolution in size with redshift (Tacconi et al., 2008; Engel et al., 2010; Rujopakarn et al., 2011; Ikarashi et al., 2015; Smolčić et al., 2015; Simpson et al., 2015), although there are not enough measurements at high redshift ($z > 4$) to exclude the possibility of size evolution entirely. For a thorough discussion of the influence of size evolution of DSFGs with redshift on the redshift distribution see Weiß et al. (2013).

To compare our sample to other samples from the literature, we correct our redshift distribution for the effect of gravitational lensing. We do this by dividing the redshift distribution by the probability for strong gravitational lensing as a function of redshift using the average magnification of our sample of $\mu \sim 10$ (see Figure 4.7). This yields the *blue* redshift distribution shown in the middle panel of Figure 4.6, and the median of our distribution decreases from $z_{\rm median} = 4.1 \pm 0.2$ to $z_{\rm median} = 3.5 \pm 0.3$ after the lensing-correction ($z_{\rm median} = 3.1 \pm 0.3$ for the lensing corrected sample when only adding the Cycle 1 redshifts Strandet et al., 2016). To be able to calculate the error on the median

of the lensing-corrected sample we randomly sample 62 sources 1000 times from the lensing-corrected redshift distribution. For each sample we find the standard deviation of the median and we use the mean of these as the error. A K-S comparison of the observed and lensing-corrected distributions gives a value of $p = 0.04$ ($p = 0.23$ when only adding Cycle 1 redshifts Strandet et al., 2016). In other words, gravitational lensing appears to have some impact on our measurement of the redshift distribution of DFSGs.

We use a single magnification to produce our lensing-corrected redshift distribution, which is a simplified approximation. The observed range of magnifications from the SPT DSFGs is $1 < \mu < 33$ with $< \mu > \approx 9$ (see Hezaveh et al., 2013; Spilker et al., 2016). The relative shape of the lensing probability kernel (Figure 4.7) for different magnifications is identical, but offset vertically for higher or lower magnifications. It is not obvious, *a priori*, that using a single magnification factor to lensing-correct our redshift distribution is a valid assumption. To test this assumption, we compare our lensed and lensing-corrected redshift distributions to a lensed and unlensed model population from Béthermin et al. (2015) in Figure 4.6 (middle panel). As discussed above, we have ignored sources in the model with $z < 1.5$. The lensed model population is created using the same selection criterion as the SPT-DSFGs i.e. $S_{1.4\mathrm{mm}} > 16\,\mathrm{mJy}$ (*dark red*) with an analytic model which includes gravitational lensing as in Hezaveh & Holder (2011). The model agrees well with our observed redshift distribution (Sum of squared residuals, weighted by the inverse square of the errors $\chi^2 = 8.9$ over 9 bins, median redshift $= 3.6/4.1$ for model/observed distributions). The good agreement also holds if we use a slightly higher flux cut of $S_{1.4\mathrm{mm}} > 25\,\mathrm{mJy}$ as in Weiß et al. (2013). The unlensed model population is selected from the same model by "demagnifying" the SPT DSFG flux cut by a factor of $\mu = 10$, i.e. $S_{1.4\mathrm{mm}} > 1.6\,\mathrm{mJy}$ (*green*). With such a low flux cut, the number counts of unlensed sources completely dominates the lensed source counts. The model prediction for this sample has a median of $z = 3.1$, in agreement with our lensing-corrected redshift distribution, with $\chi^2 = 9.7$ over 9 bins. The good agreement between the redshift distributions indicates that our simple method of lensing-correcting using a single magnification is a satisfactory approximation.

4.2.2.2 The influence of the selection wavelength

The other major influence on our redshift distribution is the selection wavelength. As discussed in Blain et al. (2002), Zavala et al. (2014), and Casey et al. (2014), the source selection function of mm and submm surveys varies with redshift, which affects the observed redshift distribution. In general, for surveys down to mJy depths, a selecting sources at longer wavelengths will lead to a higher observed redshift distribution.

In the bottom panel of Figure 4.6, we compare our lensing-corrected redshift distribution to redshift distributions from the literature selected at different wavelengths. To make the distributions comparable to ours, we have removed sources with redshifts below $z < 1.5$, because the probability of strong gravitational lensing as a function of source redshift strongly disfavors the presence of these sources in our SPT-DSFG sample (see Figure 4.7). We focus on the redshift distributions published since Weiß et al.

(2013). As these distributions were selected from a small area ($< 1\,\mathrm{deg}^2$) on the sky using a lower flux cut and are therefore made up of mostly unlensed sources, we compare them to our lensing-corrected redshift distribution.

Using a selection wavelength of 1.1 mm, Miettinen et al. (2015) presented redshifts for 15 galaxies from the COSMOS field, discovered with JCMT/AzTEC and followed up with high-resolution PdBI imaging. They add these new 15 sources to the 1.1 mm selected sources from Smolčić et al. (2012), also found using JCMT/AzTEC, and updated the redshifts where better data was available. The final sample consists of 30 sources selected at 1.1 mm with a mix of photometric and spectroscopic redshifts (see Figure 4.6, *gray*). (Note that the distribution looks slightly different from the one shown by Miettinen et al. (2015) as they use probability functions for their redshifts and we use the redshifts given in their Table 4.) The median of this distribution is $z = 3.0$, similar to ours, with a K-S comparison probability of $p = 0.19$ which means that these two distribution could be from the same common distribution.

Simpson et al. (2014) created a sample of 97 870 μm-selected sources, using high resolution ALMA data to identify the counterparts. They present a photometric redshift distribution containing 77 sources (where a fraction has spectroscopic redshifts) from the ALESS catalogue (Hodge et al., 2013; Karim et al., 2013), which is a sample of ALMA 870 μm-confirmed sources from the ECDF-S. The redshift distribution is shown in the bottom panel of Figure 4.6 (*pink*). The photometric redshifts are based on a combination of radio, submm and NIR-optical data, and only sources with four or more data points are considered. Their median photometric redshift of $z = 2.3$ is consistent with what was found by Chapman et al. (2005), though the redshift distribution of Simpson et al. (2014) shows an excess of high-redshift sources over the earlier work, which relied on radio-wavelength counterpart identification. Their distribution differs significantly from ours with a K-S comparison probability $p = 0.01$. In the paper they present another 19 sources with less than four photometry points. The redshifts for these are not given, but we tried to add 19 sources randomly in the redshift range $2.5 < z < 6.0$ which also gives a K-S comparison probability of $p = 0.01$. Both these values are below $p < 0.05$, indicating they are not drawn from the same distribution.

In addition to studying the effect of gravitational lensing on the redshift distribution of DSFGs, Béthermin et al. (2015) studied how their model predicts the shape and median of redshift distributions for samples selected at different wavelengths. They found that the difference in redshift distributions seen in Figure 4.6 can be reasonably explained by the wavelength selection. Both the distribution of Simpson et al. (2014) and Miettinen et al. (2015) follow these predictions, although the distributions selected around 850 μm put some strain on the models, as they are peaking at slightly lower redshifts than predicted. While there may remain some questions as to the redshift completeness and reliability of photometric redshifts in the two comparison samples, we interpret the selection wavelength as the main driver for the difference in redshift distributions seen in the bottom panel of Figure 4.6.

4.3 Summary and Conclusion

We have used ALMA in Cycle 1 and Cycle 3 to determine spectroscopic redshifts for strongly lensed DSFGs selected from the SPT survey. With this data, we confirmed the redshifts of six sources with single-line redshifts from Cycle 0 presented in Weiß et al. (2013) and performed a redshift search for 42 additional SPT-DSFGs.

Observing in Band 6 for 8–20 minutes per source, we have measured mid- to high-J CO lines to confirm previously reported single-line redshifts from Weiß et al. (2013). In addition to detecting lines originating from transitions in CO, we also detected [N II], H_2O, H_2O^+ and NH_3. The most probable redshifts (based on one line plus well sampled photometry) for all but one source were confirmed to be correct, demonstrating a robust method to estimate redshifts from a single line and a well measured dust temperature. This method will be useful for future blind surveys with ALMA.

In Cycle 1 we sought redshift identification for 15 new sources selected from a 100 deg^2 field of the SPT survey with $S_{1.4\mathrm{mm}} > 16\,\mathrm{mJy}$, by searching for emission lines in ALMA Band 3. In Cycle 3 we used the same technique towards 27 additional sources from the full 2500 deg^2 SPT survey. We covered the frequency range 84.2–114.9 GHz which in Cycle 1 was done in five tunings of 2 minutes each, adding up to 10 minutes of integration per source and in Cycle 3 was done in 61-91 seconds per tuning which adds up to a total of 5.5-6.5 minutes per source. 12 sources in Cycle 1 and all 27 sources in Cycle 3 are detected in continuum and their spectra are extracted. In 18 sources, we find two or more lines and unambiguously determine their redshift. In 16 sources we find one single line and calculate the most probable redshift for each of them using their dust temperature. For six of these sources we detect [C II] with APEX/FLASH and for two sources we detect CO with APEX/SEPIA, securing their redshift. In one source we do not see any lines in the 3 mm ALMA spectrum, but we determine the redshift from an absorption line detected in our ALMA Cycle 0 870 μm high resolution imaging cube.

In total, we determine reliable redshifts for 34 sources targeted in our ALMA 3 mm scans, present a redshift found using APEX/Z-Spec, and confirm six single-line redshifts from Weiß et al. (2013) with our targeted 1 mm scans. Adding this to the already established redshifts of SPT-DSFGs gives a final sample of 62 sources with spectroscopic redshifts. The median of the sample is $z = 4.1 \pm 0.2$ with a slightly lower mean of $\bar{z} = 4.0$.

Assuming no size evolution with redshift, we lensing-correct the redshift distribution by taking into account the probability of gravitational lensing occurring as a function of redshift. After correction for lensing, we recover the redshift distribution of DSFGs above $z > 1.5$ and we find a median of $z = 3.5 \pm 0.3$ for DSFGs selected at 1.4 mm. The redshift distribution and the lensing-corrected redshift distribution are consistent with the prediction made by the models of Béthermin et al. (2015).

By comparing to redshift distributions from the literature, we show that the selection wavelength is an important variable to the shape of the redshift distribution. The long selection wavelength (1.4 mm) of the SPT DSFGs provides a promising way of studying the $z > 3$ tail of DSFGs, including their most distant ($z > 5$) counterparts.

This sample of SPT-DSFGs is the most complete spectroscopic sample of DSFGs

in the literature. Besides studying the redshift distribution of DSFGs, spectroscopic redshifts are an important first step for future detailed studies of the ISM at high redshifts (e.g., Aravena et al., 2013; Bothwell et al., 2013; Gullberg et al., 2015; Spilker et al., 2015). In the future, we will work towards our goal of obtaining redshifts for the complete sample of 100 SPT-DSFGs, which will enable detailed studies of the ISM over cosmic time.

4.4 Acknowledgments

M.L.S. was supported for this research through a stipend from the International Max Planck Research School (IMPRS) for Astronomy and Astrophysics at the Universities of Bonn and Cologne. M.A. acknowledges partial support from FONDECYT through grant 1140099. J.D.V., K.C.L., D.P.M., and J.S.S. acknowledge support from the U.S. National Science Foundation under grant No. AST-1312950. This chapter makes use of the following ALMA data: ADS/JAO.ALMA# 2015.1.00504.S, 2012.1.00844.S, 2012.1.00994.S, 2011.0.00957.S and 2011.0.00958.S. ALMA is a partnership of ESO (representing its member states), NSF (USA) and NINS (Japan), together with NRC (Canada) and NSC and ASIAA (Taiwan), in cooperation with the Republic of Chile. The Joint ALMA Observatory is operated by ESO, AUI/NRAO and NAOJ. This work is based in part on observations made with *Herschel* under program ID's OT1_jvieira_4 and DDT_mstrande_1. *Herschel* is a European Space Agency Cornerstone Mission with significant participation by NASA. We also use data from the Atacama Pathfinder Experiment under program IDs E-086.A-0793A-2010, M-085.F-0008-2010, M-087.F-0015-2011, M-091.F-0031-2013, E-094.A-0712A-2014, M-095.F-0028-2015, E-096.A-0939A-2015. APEX is a collaboration between the Max-Planck-Institut für Radioastronomie, the European Southern Observatory, and the Onsala Space Observatory. The Australia Telescope is funded by the Commonwealth of Australia for operation as a National Facility managed by CSIRO. We have also used data from VLT/X-Shooter under the ESO project ID E-092.A-0503(A). The SPT is supported by the National Science Foundation through grant PLR-1248097, with partial support through PHY-1125897, the Kavli Foundation and the Gordon and Betty Moore Foundation grant GBMF 947.

Chapter 5

Investigating the full sample of SPT selected Dusty Star-Forming Galaxies discovered through photometric observations

This chapter presents the first analysis of the full sample of 91 SPT-DSFGs. Using photometric observations we determine redshifts, and construct a redshift distribution for the full SPT-DSFG sample. The observations also enable a study of the dust in these sources through their dust temperature, dust mass, infra red luminosity and star formation rate.

First, a short presentation of the results of the observations is given in Section 5.1. In Section 5.2 several methods are employed to obtain photometric redshifts. Using sources with spectroscopic redshift we test these methods to select the method that yields the best results. The redshift distribution of the full sample is presented in Section 5.3 and it is compared to photometric redshift distributions from recent literature. An analysis of the dust properties is presented in Section 5.4.

We adopt a flat ΛCDM cosmology, with $\Omega_\Lambda = 0.696$ and $H_0 = 68.1 \dot{\text{km}}\ \text{s}^{-1}\,\text{Mpc}^{-1}$ (Planck Collaboration et al., 2014).

5.1 Results from photometry

Here, we present a brief summary of the observations (Section 3.2) that form the basis for this chapter. Flux densities are listed in Table 3.2 and the thumbnail images can be found in Appendix D.

The 91 sources were selected in the raw SPT maps at 1.4 mm and 2.0 mm. The deboosted fluxes at 2.0 mm range between 0.6 - 25 mJy with a median flux of ∼ 6.0 mJy and SNRs of 0.3 - 16 and at 1.4 mm they range between 6 - 77 mJy with a median flux of ∼ 22 mJy and SNRs of 0.9 - 10. This means that the fluxes are not all significantly detected when deboosted, but LABOCA observations have confirmed that these sources are real.

With APEX/LABOCA we observed the sources until they were detected, which means the observing time and noise varies from source to source. The fluxes range

between 18 and 199 mJy with a median of $\sim$62 mJy and SNRs ranging from 4.6 to 32.

All sources were observed with *Herschel*/SPIRE with similar integration times. At 500 μm the fluxes are in the range 37 - 554 mJy with a median flux of 118 mJy and SNRs in the range 3.6 - 61. At 350 μm the fluxes are in the range 32 - 757 mJy with a median flux of 112 mJy and SNRs in the range 3.8 - 59. At 250 μm 90 out of 91 sources (98 %) are detected with fluxes in the range 23 - 796 mJy, a median flux of 71 mJy, and SNRs of 3.5 - 58 for the detected sources.

With *Herschel*/PACS 66 sources (72 %) were observed. These sources were selected as their *Herschel*/SPIRE observations indicated that they were bright enough to be detected by *Herschel*/PACS. 30 of these sources are detected (45 % of the observed sources and 32 % of the full sample) at 160 μm with fluxes in the range 28 - 531 mJy with a median of 86 mJy and SNRs of 3.2 - 11. At 100 μm 24 sources are detected (36 % of the observed sources and 26 % of the full sample) with fluxes in the range 7.9 - 238 mJy, a median flux of 26 mJy, and SNRs of 3.3 - 22.

5.2 Finding redshifts

In Chapter 4 we present 53 unambiguous redshifts and a further 9 sources with redshifts based on one spectral line + photometry. The SPT-DSFG sample, however, is larger than this with a total of 91 sources. To create a redshift distribution including all SPT-DSFGs, we find the photometric redshift of all sources. As described in Section 2.2 this can be done in several different ways. The focus here is on the three methods that yielded the best results: 1) Fitting an SED, 2) Using the wavelength of the thermal dust peak, and 3) Fitting a library of templates.

We first explain how each of these methods work in Sections 5.2.1, 5.2.2, and 5.2.3 and then test and compare them in Section 5.2.4.

5.2.1 Fitting SEDs

The SEDs are fitted using Equation 2.5, with a spectral slope of $\beta = 2$, and the optically thin/thick transition wavelength set to 100 μm, similar to Greve et al. (2012). We attempted fitting β instead of fixing it, but it didn't make a big difference in the photometric redshifts. We ignore data shortwards of restframe 50 μm in order to only fit the cold component of the thermal dust emission, since a single temperature SED is usually not reproducing the entire spectral energy distribution. The free parameters for the fit are dust temperature, redshift and the area of the source. Due to the degeneracy between dust temperature and redshift we have to assume a dust temperature to find the redshift. We investigate the dust temperature of our sample by fitting SEDs to all sources with an unabiguous redshift and create a probability distribution for $T_{\rm dust}$ for each source. We co-add these to create a probability distribution of the dust temperature for the full sample of sources with unambiguous redshifts. Figure 4.4 shows the probability distribution of the dust temperature (*green*), and the triangle marks the median temperature of $T_{\rm dust} = 39 \pm 10$ K. The outlier in this distribution is SPT0452-50 which has an extremely low dust temperature of 22 K. The photometry for this source

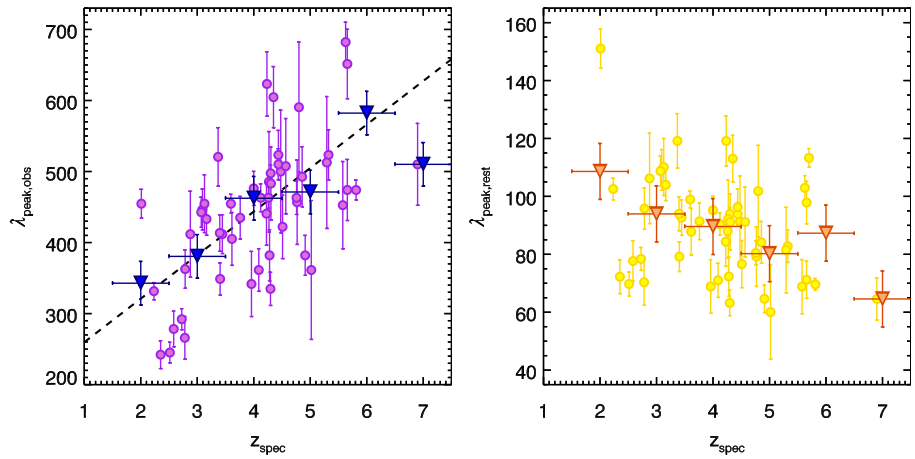

Figure 5.1: Peak wavelength vs redshift for sources with spectroscopic redshifts. The circles show the individual sources and the triangles show the medians of the bins shown by the horizontal bars. *Left panel*: The *purple* circles show the observed peak wavelength, and the *blue* triangles show the median. *Right panel*: The *yellow* circles show the restframe peak wavelength, and the *orange* triangles show the medians.

is well fitted (see the SED in Appendix F) and the redshift is well established from CO(1–0) and CO(3–2) line detections, so the source simply appears to be significantly colder than the rest of the SPT-DSFG sample. We use this dust temperature distribution to derive the photometric redshifts for all sources in the sample that do not have spectroscopic redshifts (29 sources).

For each of these sources, we create a photometric redshift probability distribution by randomly sampling 10^3 dust temperatures from the SPT-DSFG $T_{\rm dust}$ distribution and fitting SEDs, leaving the redshift as a free parameter. The peak of this distribution is then used as the photometric redshift with its errors reflected by the $1\,\sigma$ confidence interval around the peak. This produces asymmetric errors, and we choose the largest of the two values in order to be conservative.

5.2.2 Using $\lambda_{\rm peak}$

An SED identifies the redshift by fitting the position of the thermal dust peak and assuming a dust temperature. A simpler approach would be to directly use the measured wavelength of the dust peak to identify the source redshift. By using the sources with spectroscopic redshifts we can determine an empirical relation between the peak wavelength and the redshift.

The peak of the thermal dust emission is determined by fitting a continuous spline to the photometry and the error on the peak wavelength is determined by varying the fluxes within their errors and refitting the spline 10^3 times and using the standard deviation. The observed peak wavelengths are listed in Table 5.2. Using the spectroscopic

redshifts, we calculate the restframe peak wavelengths, which are listed in Table 4.1. The median restframe peak wavelength is $\lambda_{\text{rest, median}} = 91 \pm 18\,\mu$m, where the error is the standard deviation. The median is well constrained, which shows that it can be used as a redshift indicator.

Figure 5.1 (left panel) shows the relation between peak wavelength and spectroscopic redshift. Fitting the observed peak wavelength and redshift with a linear relation we find the expression

$$z = (6.4 \pm 1.1) \times 10^{-3} \cdot \lambda_{\text{peak}} + 1.2 \pm 0.5. \tag{5.1}$$

With this expression we transform the observed peak wavelength for all sources into a photometric redshift. The errors on the photometric redshift are calculated by adding (in quadrature) the error on the relation between redshift and λ_{peak}, due to the spread of the sources and the error from varying λ_{peak} within the errors, and the error from recalculating the photometric redshift 10^3 times using the standard deviation of the distribution as the error. The derived redshifts are listed in Table 5.2. Figure 5.1 also shows the restframe peak wavelength as a function of redshift. It is clear that there is an evolution of the restframe peak wavelength with redshift, which means we might be underestimating the redshifts of high redshift sources or overestimating redshift of low redshift sources when using this method.

5.2.3 Fitting a library of SPT-DSFG templates

Another way to estimate photometric redshifts is by fitting templates or libraries of templates to the photometric data. For this method to work well the library needs to reflect the nature of the sources investigated. We find that the best and simplest way to do this is by creating our own library from the large number of SPT-DSFGs with a spectroscopic redshift based on two or more lines (we also tested finding photometric redshifts using a single template from a star forming galaxy like Arp220, but the results were not nearly as good as when using the SPT-DSFG library). The advantage of this is that it is model independent and estimating a dust temperature is not necessary.

When creating the library of templates it is important to fit the photometry well. We tested fitting a spline, a continuous spline, and a two component SED (see description in Section 5.4.3), and found similar results for all methods but the continuous fitting with a physical motivation (the two component SED) gave the best results when comparing to the spectroscopic redshifts. We limit the frequency range of the templates by the lowest and highest frequency data point. The library of templates is shown in Figure 5.2, where all sources are placed at redshift zero and the peak fluxes are shifted for a better view of the individual templates. To determine the redshift of a source, the full library of templates is fitted to the photometry of the source. Each template is shifted over a fine grid of the wavelength range, fitting the amplitude at every position to determine the quality of the fit by calculating the reduced chi square. This is transformed into a probability distribution for each template, and the results from all templates are combined into a redshift probability distribution for each source. The

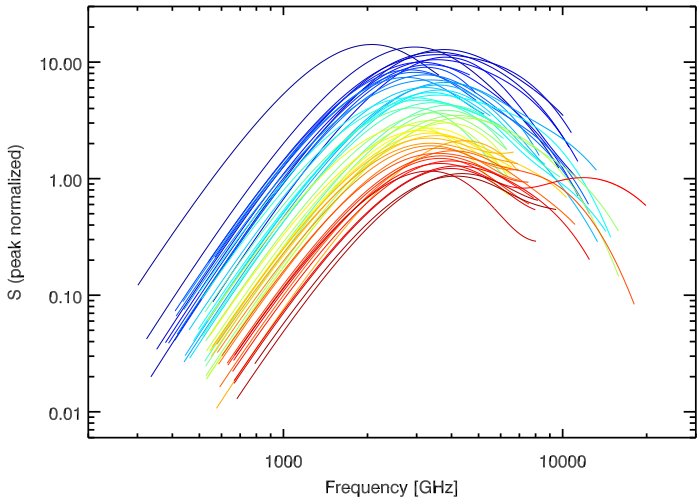

Figure 5.2: The library of templates created from the 53 sources in the SPT-DSFG sample with a spectroscopic redshift. The templates are shown in their rest-frame and the peak flux is shifted to better show the different templates. The colors vary from the lowest redshift source in *dark blue* to the highest redshift source in *dark red.*

peak of this distribution is used as the photometric redshift and the errors are taken as the one sigma confidence limit.

5.2.4 Testing and comparing the methods

To test the prediction power of the three methods we use the sample of SPT-DSFGs with unambiguous redshifts and compare the photometric redshifts to the spectroscopic redshifts. Figure 5.3 shows the comparison, with the SED based photometric redshifts as *red* squares, the $\lambda_{\rm peak}$ based photometric redshifts as *purple* triangles, and the template based photometric redshifts as *green* circles. The left panel shows $z_{\rm phot}$ vs $z_{\rm spec}$ and the right panel $z_{\rm phot}/z_{\rm spec}$ vs $z_{\rm spec}$. For the methods using the peak wavelength and the library we have removed the source under investigation. This was also tested for the SED fitting method, but this only made a small difference in the error, and not in the calculated value, so the full dust temperature distribution was used.

For the SED fitting method we find a reduced chi square of the one-to-one line of $\chi^2 = 0.76$ and the mean of the ratio $z_{\rm phot,Tdust}/z_{\rm spec} = 0.98 \pm 0.21$ (illustrated by the *red* dotted line).

For the method using the peak wavelength we find a reduced chi square of the one-to-one line of $\chi^2 = 1.16$ and the mean of the ratio $z_{\rm phot,\lambda peak}/z_{\rm spec} = 1.05 \pm 0.24$ (illustrated by the *purple* dotted line). We found the peak of the thermal dust emission by fitting a continuous spline. We also attempted using a single component SED to

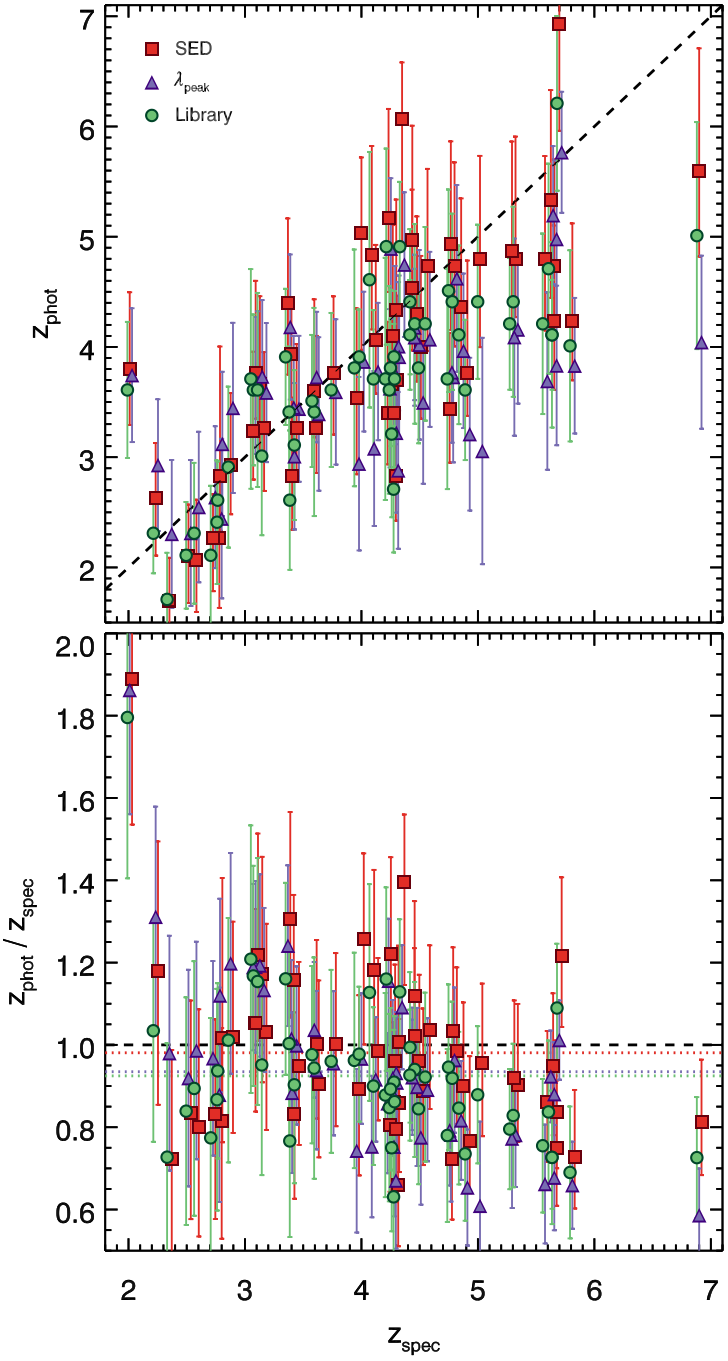

Figure 5.3: A comparison of photometric and spectroscopic redshifts to test the three methods of obtaining photometric redshifts. The *black* dashed line shows $z_{\rm phot}/z_{\rm spec} = 1$. *Top*: squares show photometric redshifts obtained from fitting an SED, *purple* triangles show the photometric redshift from $\lambda_{\rm peak}$, and *green* circles show photometric redshifts obtained from fitting a library of SPT-DSFG templates. *Bottom*: The photometric vs spectroscopic redshifts for all sources in the SPT-DSFG sample with spectroscopic redshifts. *Right*: The ratio of $z_{\rm phot}/z_{\rm spec}$ vs $z_{\rm spec}$. The dotted lines show the median redshift of the sample shown in the same color.

find the peak redshift, which gives results closer to that of the SED fitting method, though not superior to this.

For the method using the library we find a chi square of $\chi^2 = 0.66$, though the mean of the redshift ratio is slightly lower $z_{\rm phot,library}/z_{\rm spec} = 0.95 \pm 0.18$ (illustrated by the *green* dotted line).

The three methods give very similar photometric redshifts which is encouraging and perhaps also not so surprising. All methods give an uncertainty of only $\sim 20\%$ over the full sample. The χ^2 and spread of the template method is smallest, but the mean of the redshift ratio for the SED fitting method is closer to one than for the two other methods. Given the slightly closer to one mean of the $z_{\rm phot,\lambda peak}/z_{\rm spec}$ ratio of the SED method, we use the photometric redshifts derived using this method.

5.3 The redshift distribution

The best redshift distribution of the SPT-DSFGs is created using the spectroscopic redshifts from Chapter 4 (53 unambiguous redshifts and 9 redshifts based on one spectroscopic line and photometry) and photometric redshifts for the remaining 29 sources. The distribution is shown in *orange* in the top panel of Figure 5.4. We find a median redshift of $z_{\rm best,median} = 3.7 \pm 0.1$ for this sample. The median of the combined sample is in full agreement with the $z_{\rm median} = 3.9 \pm 0.4$ presented in Strandet et al. (2016).

In the Chapter 4 we compared the SPT-DSFG sample to, mainly, spectroscopic redshift distributions from the literature. Since including photometric redshifts have not significantly changed the shape of the redshift distribution of the SPT-DSFGs, we here compare to the latest photometric redshift distributions in the literature.

Su et al. (2017) presented the redshift distribution of the ACT sources which, like the SPT-DSFGs, consists mainly of lensed galaxies. This makes a one-to-one comparison between the samples possible without having to correct for the effects of gravitational lensing. The ACT sources are selected at 1.4 mm with a spectral slope, similar to that of the SPT-DSFGs, with $S_{\rm 2mm}/S_{\rm 1.4mm} > 2$ in a field of 120 deg^2, where the ACT survey and a deep *Herschel*/SPIRE scan overlap. They find nine sources, of which two have a spectroscopic redshift. For the remaining seven sources the photometric redshift is found based on flux densities from ACT at 2.0, 1.4 and 1.1 mm and from *Herschel*/SPIRE at 500, 350 and 250 μm. The available data is similar to that of the SPT-DSFGs, though the fitting is done with a modified black body model with a power-law temperature distribution. The redshift distribution is plotted in *green* in the top panel of Figure 5.4. It agrees well with the SPT-DSFG distribution, but given the low number of ACT sources the uncertainty is quite high. The median redshift of the ACT sample is $z_{\rm median,Su} = 3.9 \pm 0.2$ which is consistent with that of the SPT-DSFGs.

To compare to samples that are not gravitationally lensed, we correct the SPT-DSFG sample for gravitational lensing as done in Section 4.2.2.1. The lensing corrected distribution is shown in *blue* in the bottom panel of Figure 5.4. The median redshift of this is $z_{\rm lens\text{-}cor,median} = 3.0 \pm 0.1$ consistent with the lensing corrected redshift distri-

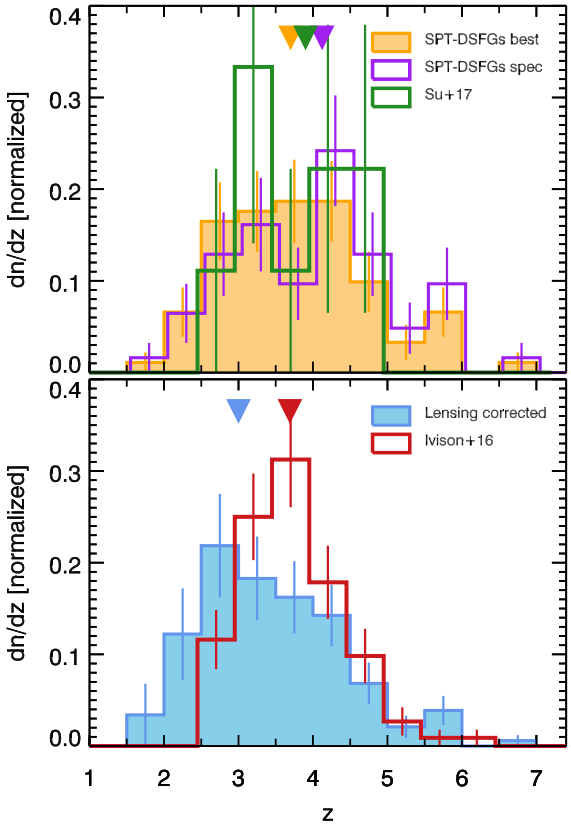

Figure 5.4: The redshift distribution of the SPT-DSFGs. The triangles in the top of the plots show the median of the sample with the corresponding color. *Top*: The *orange* histogram show the full sample of 91 SPT-DSFGs, with spectroscopic redshift for 53 sources, redshifts based on one spectroscopic line and photometry for 9 sources and photometric redshifts of the remaining 29 sources. The spectroscopic distribution from Chapter 4 is shown in *purple*. The redshift distribution of the ACT sample from Su et al. (2017) is shown in *green*. *Bottom*: The *blue* histogram shows the lensing corrected version of the *orange* distribution above. The redshift distribution of the *Herschel* sample from Ivison et al. (2016) is shown in *red*.

Table 5.1: Measured redshift distribution for SPT-DSFGs

z	$z_{\rm best}$ $\mathrm{d}n/\mathrm{d}z$	lens-cor[b] $\mathrm{d}n/\mathrm{d}z$
1.0 - 1.5	0.01 ± 0.01	0
1.5 - 2.0	0	0
2.0 - 2.5	0.07 ± 0.03	0.13 ± 0.05
2.5 - 3.0	0.15 ± 0.04	0.21 ± 0.06
3.0 - 3.5	0.19 ± 0.05	0.20 ± 0.05
3.5 - 4.0	0.18 ± 0.04	0.16 ± 0.04
4.0 - 4.5	0.20 ± 0.05	0.16 ± 0.04
4.5 - 5.0	0.10 ± 0.03	0.07 ± 0.02
5.0 - 5.5	0.03 ± 0.02	0.02 ± 0.01
5.5 - 6.0	0.07 ± 0.03	0.04 ± 0.02
6.0 - 6.5	0	0
6.5 - 7.0	0.01 ± 0.01	0.01 ± 0.01

bution from Strandet et al. (2016) ($z_{\text{lens-cor,median}} = 3.1 \pm 0.3$). It is worth noting that this distribution is very similar to what we saw in Chapter 4 for the lensing corrected redshift distribution of the spectroscopically confirmed sources.

In the large *Herschel*-ATLAS imaging survey at 250, 350, and 500μm a large number of potential DSFGs was discovered. These sources are expected to be largely unlensed (based on their faint 350- and 500-μm fluxes). Ivison et al. (2016) published a photometric redshift distribution of a sub-sample of these sources. The sources were selected from different fields covering in total $\sim 600\,\mathrm{deg}^2$, following a few criteria. The first criterium is a 3σ detection at 500 μm, then the two color criteria $S_{500\mu\mathrm{m}}/S_{250\mu\mathrm{m}} \geq 1.5$ and $S_{500\mu\mathrm{m}}/S_{350\mu\mathrm{m}} \geq 0.85$ are applied to select $z > 4$ sources. To select a reliable sample for 870 μm follow up with LABOCA and SCUBA-2 five members of the team went over the photometry of the sources. In total 109 sources were followed up with LABOCA or SCUBA and included in the photometric redshift distribution. The redshift distribution is shown in *red* in the bottom panel of Figure 5.4. The median redshift of the sample is $z_{\text{median,Ivison}} = 3.7 \pm 0.1$. The criteria for the *Herschel* sources were put in place to ensure a high redshift sample, and the redshift distribution is therefore biased towards high redshifts. The distribution for the *Herschel* sources is at higher redshifts than the lensing corrected SPT-DSFG distribution, with a higher median. It is fairly similar to the SPT-DSFG distribution without lensing correction, with an identical median. It is clear that the selection used by Ivison et al. (2016) is efficient in selecting high redshift sources. Using the same selection criteria as Ivison et al. (2016) for the SPT-DSFGs, 44 sources remain ($\sim 50\,\%$ of the sample) and the median of these sources is $z_{\mathrm{SPT-DSFGs\,as\,Ivison}} = 4.2 \pm 0.3$.

Table 5.2: Parameters obtained from photometry fitting

Source	$z_{\rm spec}$	$\lambda_{\rm peak}$	$z_{\rm phot}^{\rm SED}$	$z_{\rm phot}^{\lambda}$	$z_{\rm phot}^{\rm library}$	$T_{\rm dust}$ [K]	$M_{\rm dust}^{870\mu m}$ $\times10^9$ $[M_\odot]$	$M_{\rm dust}^{3000\mu m}$ $\times10^9$ $[M_\odot]$	$L_{\rm FIR}$ $\times10^{13}$ $[L_\odot]$	$L_{\rm IR}$ $\times10^{13}$ $[L_\odot]$	SFR $[M_\odot\,{\rm yr}^{-1}]$
SPT0002-52	2.3513(4)	242 ± 19	1.5 ± 0.6	2.8 ± 0.6	1.7 ± 0.6	42.3 ± 1.6	6.7 ± 0.4	5.3 ± 0.4	$4.8^{+0.2}_{-0.3}$	$7.9^{+0.8}_{-1.0}$	14000^{+1000}_{-2000}
SPT0020-51	4.1228(8)	463 ± 17	3.9 ± 0.6	4.2 ± 0.6	3.7 ± 0.9	38.3 ± 1.4	8.6 ± 0.6	10.2 ± 0.4	$4.4^{+0.2}_{-0.2}$	$7.6^{+7.0}_{-2.1}$	13000^{+12000}_{-4000}
SPT0027-50	3.4436(1)	411 ± 27	3.1 ± 0.5	3.9 ± 0.5	3.1 ± 0.7	41.8 ± 0.9	15.1 ± 0.7	11.8 ± 0.3	$8.2^{+0.3}_{-0.3}$	$11.6^{+1.2}_{-1.2}$	20000^{+2000}_{-2000}
SPT0054-41		497 ± 15	4.3 ± 0.8	4.4 ± 0.8	4.2 ± 1.0	41.8 ± 0.9	11.3 ± 5.4		$5.4^{+0.3}_{-0.2}$	$8.2^{+5.2}_{-1.0}$	14000^{+9000}_{-2000}
SPT0103-45	3.0917(2)	446 ± 29	3.7 ± 0.6	4.1 ± 0.6	3.6 ± 0.7	32.3 ± 0.9	25.8 ± 1.3	20.6 ± 1.9	$3.5^{+0.3}_{-0.2}$	$4.9^{+2.0}_{-0.5}$	8000^{+3000}_{-900}
SPT0106-64	4.910(4)	381 ± 27	3.8 ± 0.8	3.7 ± 0.8	3.6 ± 0.8	47.4 ± 1.9	9.5 ± 0.6	10.0 ± 0.4	$12.7^{+0.5}_{-0.5}$	$23.7^{+2.8}_{-4.4}$	41000^{+5000}_{-7000}
SPT0109-47	3.6137(5)	405 ± 37	3.2 ± 0.6	3.8 ± 0.6	3.4 ± 0.9	43.2 ± 1.4	10.8 ± 0.6	8.4 ± 0.3	$6.3^{+0.3}_{-0.3}$	$9.9^{+1.8}_{-1.7}$	17000^{+3000}_{-3000}
SPT0112-55		350 ± 234	3.5 ± 0.7	3.5 ± 0.7	3.8 ± 0.9	43.2 ± 1.4	4.6 ± 1.9	1.7 ± 0.5	$0.7^{+0.2}_{-0.1}$	$1.1^{+0.2}_{-0.2}$	1900^{+400}_{-300}
SPT0113-46	4.2328(5)	623 ± 45	5.0 ± 0.8	5.2 ± 0.8	4.9 ± 0.9	31.3 ± 1.4	16.8 ± 1.7	14.2 ± 1.5	$2.3^{+0.1}_{-0.1}$	$6.8^{+0.7}_{-3.6}$	12000^{+1000}_{-6000}
SPT0114-59		393 ± 24	2.9 ± 0.6	3.8 ± 0.6	3.1 ± 0.6	31.3 ± 1.4	2.9 ± 1.1	1.9 ± 0.5	$0.9^{+0.1}_{-0.1}$	$1.3^{+0.1}_{-0.2}$	2100^{+200}_{-300}
SPT0125-47	2.51480(6)	245 ± 13	1.7 ± 0.7	2.8 ± 0.7	2.1 ± 0.6	38.6 ± 1.6	21.9 ± 1.3	24.5 ± 2.3	$12.0^{+0.5}_{-0.5}$	$18.8^{+1.9}_{-2.4}$	32000^{+3000}_{-4000}
SPT0125-50	3.959(3)	341 ± 45	3.4 ± 0.7	3.4 ± 0.7	3.8 ± 1.1	43.7 ± 2.1	9.9 ± 0.8	10.2 ± 1.0	$6.9^{+0.6}_{-0.6}$	$10.5^{+1.1}_{-1.1}$	18000^{+2000}_{-2000}
SPT0128-51		454 ± 22	3.7 ± 0.8	4.1 ± 0.8	3.3 ± 0.8	43.7 ± 2.1	2.3 ± 1.0	3.6 ± 1.2	$1.5^{+0.1}_{-0.3}$	$7.9^{+1.2}_{-6.3}$	13000^{+2000}_{-11000}
SPT0136-63	4.299(1)	497 ± 11	4.3 ± 0.6	4.4 ± 0.6	3.9 ± 0.9	37.4 ± 1.4	8.8 ± 0.6	8.9 ± 0.4	$3.5^{+0.1}_{-0.2}$	$10.5^{+1.1}_{-6.1}$	18000^{+2000}_{-10000}
SPT0147-64		490 ± 31	4.6 ± 0.7	4.4 ± 0.7	4.4 ± 0.9	37.4 ± 1.4	9.7 ± 0.7	13.2 ± 1.5	$5.1^{+0.3}_{-0.2}$	$12.8^{+1.7}_{-6.2}$	22000^{+3000}_{-11000}
SPT0150-59		353 ± 26	3.1 ± 0.6	3.5 ± 0.6	2.7 ± 0.7	37.4 ± 1.4	10.8 ± 0.7	12.8 ± 1.4	$3.0^{+1.1}_{-1.1}$	$4.0^{+15.5}_{-0.4}$	6800^{+27000}_{-700}
SPT0155-62	4.349(1)	604 ± 42	5.1 ± 1.7	5.1 ± 1.7	4.9 ± 1.3	30.4 ± 0.9	40.6 ± 2.4	48.1 ± 1.8	$6.0^{+0.1}_{-0.3}$	$8.0^{+3.3}_{-0.8}$	14000^{+6000}_{-1000}
SPT0202-61	5.018(1)	361 ± 92	4.6 ± 1.1	3.5 ± 1.1	4.4 ± 1.0	39.3 ± 1.6	11.6 ± 0.9	16.7 ± 0.8	$8.6^{+0.3}_{-0.4}$	$15.5^{+1.7}_{-1.7}$	27000^{+3000}_{-3000}
SPT0226-45		400 ± 79	2.9 ± 0.6	3.8 ± 0.6	2.8 ± 0.7	39.3 ± 1.6	9.2 ± 3.5		$5.0^{+0.3}_{-0.8}$	$30.2^{+4.5}_{-23.4}$	52000^{+8000}_{-40000}
SPT0243-49	5.699(1)	758 ± 22	6.5 ± 1.1	6.1 ± 1.1	6.2 ± 1.4	32.7 ± 1.6	16.3 ± 1.8	24.8 ± 2.8	$3.7^{+0.2}_{-0.2}$	$7.8^{+2.4}_{-1.8}$	13000^{+4000}_{-3000}
SPT0245-63	5.626(1)	682 ± 28	5.1 ± 1.0	5.6 ± 1.0	4.7 ± 0.9	41.4 ± 1.6	5.4 ± 0.4	6.7 ± 0.3	$4.0^{+0.2}_{-0.2}$	$15.5^{+1.7}_{-1.6}$	27000^{+3000}_{-3000}
SPT0300-46	3.5954(7)	454 ± 13	3.6 ± 0.6	4.1 ± 0.6	3.5 ± 0.7	38.6 ± 1.4	7.3 ± 0.5	9.2 ± 0.9	$3.3^{+0.4}_{-0.4}$	$4.3^{+10.0}_{-0.4}$	7300^{+17000}_{-800}
SPT0311-58	6.900(1)	510 ± 54	5.4 ± 1.1	4.5 ± 1.1	5.0 ± 1.0	45.6 ± 3.3	2.3 ± 0.4	4.1 ± 0.4	$4.4^{+0.4}_{-0.3}$	$11.5^{+3.0}_{-4.8}$	20000^{+5000}_{-8000}
SPT0314-44		389 ± 23	2.7 ± 0.5	3.7 ± 0.5	2.6 ± 0.8	45.6 ± 3.3	14.9 ± 5.3		$6.3^{+0.3}_{-0.2}$	$11.1^{+1.5}_{-2.8}$	19000^{+3000}_{-5000}
SPT0319-47	4.510(4)	422 ± 44	3.8 ± 0.8	3.9 ± 0.8	3.8 ± 0.9	40.0 ± 1.9	7.1 ± 0.6	8.0 ± 0.8	$4.5^{+0.2}_{-0.2}$	$7.9^{+1.1}_{-1.0}$	14000^{+2000}_{-2000}
SPT0345-47	4.2958(2)	334 ± 23	2.8 ± 0.6	3.4 ± 0.6	2.7 ± 0.8	50.2 ± 2.8	5.7 ± 0.5	7.3 ± 0.8	$11.4^{+0.2}_{-0.6}$	$17.7^{+1.8}_{-1.9}$	30000^{+3000}_{-3000}
SPT0346-52	5.6559(4)	474 ± 42	4.0 ± 0.8	4.3 ± 0.8	4.1 ± 0.8	50.5 ± 1.9	6.7 ± 0.4	9.6 ± 0.9	$13.1^{+0.3}_{-0.6}$	$19.6^{+3.0}_{-2.0}$	34000^{+5000}_{-3000}
SPT0348-62	5.656(1)	651 ± 51	4.7 ± 0.7	5.4 ± 0.7	4.1 ± 0.9	46.5 ± 2.1	3.3 ± 0.3	3.2 ± 0.2	$3.4^{+0.2}_{-0.2}$	$7.0^{+2.3}_{-2.4}$	12000^{+4000}_{-4000}

continued

Table 5.2: Parameters obtained from photometry fitting

Source	$z_{\rm spec}$	$\lambda_{\rm peak}$	$z^{\rm SED}_{\rm phot}$	$z^{\lambda}_{\rm phot}$	$z^{\rm library}_{\rm phot}$	$T_{\rm dust}$ [K]	$M^{870\mu m}_{\rm dust}$ $\times10^9$ $[M_\odot]$	$M^{3000\mu m}_{\rm dust}$ $\times10^9$ $[M_\odot]$	$L_{\rm FIR}$ $\times10^{13}$ $[L_\odot]$	$L_{\rm IR}$ $\times10^{13}$ $[L_\odot]$	SFR $[M_\odot\,{\rm yr}^{-1}]$
SPT0402-45		273 ± 27	2.7 ± 0.4	3.0 ± 0.4	2.4 ± 0.7	46.5 ± 2.1	28.9 ± 10.5		$12.9^{+1.4}_{-0.7}$	$16.8^{+3.7}_{-1.9}$	29000^{+6000}_{-3000}
SPT0403-58		436 ± 26	3.7 ± 0.7	4.0 ± 0.7	3.8 ± 0.8	46.5 ± 2.1	4.9 ± 2.2		$2.3^{+0.2}_{-0.1}$	$3.0^{+2.6}_{-0.3}$	5000^{+5000}_{-500}
SPT0404-59		456 ± 22	3.8 ± 0.9	4.2 ± 0.9	3.9 ± 1.2	46.5 ± 2.1	3.0 ± 1.4		$1.6^{+0.1}_{-0.2}$	$7.8^{+1.6}_{-5.6}$	13000^{+3000}_{-10000}
SPT0418-47	4.2248(7)	440 ± 44	3.3 ± 0.6	4.0 ± 0.6	3.7 ± 1.1	45.3 ± 1.9	8.7 ± 0.7	4.7 ± 0.5	$6.8^{+0.2}_{-0.3}$	$8.9^{+1.2}_{-0.9}$	15000^{+2000}_{-2000}
SPT0425-40		390 ± 27	3.5 ± 0.6	3.7 ± 0.6	3.7 ± 0.8	45.3 ± 1.9	7.7 ± 3.1		$2.7^{+0.2}_{-0.1}$	$3.6^{+0.5}_{-0.4}$	6200^{+900}_{-700}
SPT0433-59		250 ± 22	2.4 ± 0.4	2.8 ± 0.4	2.0 ± 0.5	45.3 ± 1.9	10.5 ± 3.4		$4.3^{+1.6}_{-0.2}$	$5.6^{+22.8}_{-0.6}$	10000^{+39000}_{-1000}
SPT0436-40		436 ± 34	3.7 ± 1.3	4.0 ± 1.3	3.7 ± 1.1	45.3 ± 1.9	9.2 ± 4.0		$3.0^{+0.2}_{-0.1}$	$3.9^{+1.2}_{-0.4}$	7000^{+2000}_{-800}
SPT0441-46	4.4771(5)	500 ± 83	4.2 ± 0.7	4.4 ± 0.7	4.2 ± 0.9	38.1 ± 1.6	9.6 ± 0.9	9.2 ± 0.9	$4.3^{+0.2}_{-0.2}$	$6.8^{+5.4}_{-1.5}$	12000^{+9000}_{-2000}
SPT0452-50	2.0104(2)	454 ± 20	3.8 ± 0.7	4.1 ± 0.7	3.6 ± 0.8	22.0 ± 0.9	23.8 ± 2.0	23.8 ± 2.5	$0.5^{+0.4}_{-0.1}$	$0.8^{+4.5}_{-0.2}$	1000^{+8000}_{-300}
SPT0457-49		444 ± 18	3.4 ± 0.6	4.1 ± 0.6	3.3 ± 0.9	22.0 ± 0.9	3.3 ± 1.4		$1.5^{+0.1}_{-0.1}$	$2.1^{+0.4}_{-0.3}$	3500^{+700}_{-600}
SPT0459-58	4.856(4)	492 ± 41	4.2 ± 0.7	4.4 ± 0.7	4.1 ± 0.8	41.6 ± 1.9	4.8 ± 0.4	5.5 ± 0.6	$3.6^{+0.2}_{-0.2}$	$6.0^{+5.2}_{-1.3}$	10000^{+9000}_{-2000}
SPT0459-59	4.7993(5)	590 ± 93	4.5 ± 0.9	5.0 ± 0.9	4.4 ± 0.9	38.1 ± 1.9	7.2 ± 0.7	8.0 ± 0.9	$3.7^{+0.2}_{-0.2}$	$15.1^{+1.5}_{-9.1}$	26000^{+3000}_{-16000}
SPT0509-53		358 ± 25	3.1 ± 0.6	3.5 ± 0.6	2.9 ± 0.8	38.1 ± 1.9	2.7 ± 1.1		$1.3^{+0.1}_{-0.1}$	$1.7^{+0.2}_{-0.3}$	3000^{+400}_{-400}
SPT0512-59	2.2331(2)	331 ± 11	2.4 ± 0.6	3.4 ± 0.6	2.3 ± 0.8	32.7 ± 0.9	16.7 ± 0.9	17.7 ± 1.8	$3.5^{+0.5}_{-0.1}$	$5.1^{+0.6}_{-0.5}$	8700^{+1000}_{-900}
SPT0516-59	3.4045(7)	348 ± 22	2.8 ± 0.6	3.5 ± 0.6	2.6 ± 0.6	45.8 ± 1.6	3.0 ± 0.2	2.9 ± 0.2	$2.9^{+0.1}_{-0.1}$	$5.2^{+0.6}_{-0.6}$	8900^{+1000}_{-1000}
SPT0520-53		450 ± 45	3.7 ± 0.6	4.1 ± 0.6	3.8 ± 0.8	45.8 ± 1.6	6.8 ± 2.9		$2.5^{+0.2}_{-0.1}$	$3.3^{+1.5}_{-0.3}$	6000^{+2000}_{-600}
SPT0528-53		458 ± 87	4.1 ± 0.9	4.2 ± 0.9	3.9 ± 0.8	45.8 ± 1.6	3.2 ± 1.5		$1.4^{+0.2}_{-0.1}$	$1.8^{+1.7}_{-0.2}$	3000^{+3000}_{-300}
SPT0529-54	3.3689(1)	520 ± 40	4.1 ± 0.9	4.6 ± 0.9	3.9 ± 0.8	31.8 ± 0.9	24.9 ± 1.4	20.2 ± 1.9	$3.1^{+0.2}_{-0.1}$	$4.3^{+0.5}_{-0.5}$	7300^{+900}_{-800}
SPT0532-50	3.3988(1)	413 ± 26	3.4 ± 0.6	3.9 ± 0.6	3.4 ± 0.9	37.6 ± 1.4	16.3 ± 1.0	30.6 ± 3.0	$7.3^{+0.1}_{-0.4}$	$9.6^{+3.7}_{-1.0}$	16000^{+6000}_{-2000}
SPT0538-50	2.7855(1)	362 ± 26	2.9 ± 0.6	3.5 ± 0.6	2.6 ± 0.8	36.5 ± 1.2	20.5 ± 0.9		$6.9^{+0.3}_{-0.2}$	$10.0^{+1.1}_{-1.0}$	17000^{+2000}_{-2000}
SPT0541-57		478 ± 13	3.9 ± 0.8	4.3 ± 0.8	3.9 ± 0.9	36.5 ± 1.2	2.5 ± 1.2		$1.2^{+0.1}_{-0.1}$	$3.2^{+1.9}_{-1.8}$	6000^{+3000}_{-3000}
SPT0544-40	4.269(0)	485 ± 70	4.0 ± 0.7	4.3 ± 0.7	3.8 ± 0.8	38.6 ± 1.4	10.3 ± 0.7	11.5 ± 0.5	$4.6^{+0.2}_{-0.2}$	$6.3^{+2.9}_{-0.7}$	11000^{+5000}_{-1000}
SPT0550-53	3.1280(7)	454 ± 39	3.5 ± 0.7	4.1 ± 0.7	3.6 ± 0.9	33.2 ± 1.4	10.2 ± 0.9	8.1 ± 1.0	$1.9^{+0.1}_{-0.1}$	$3.0^{+0.3}_{-0.3}$	5200^{+600}_{-600}
SPT0551-48	2.5833(2)	278 ± 25	2.2 ± 0.6	3.0 ± 0.6	2.3 ± 0.6	38.6 ± 1.6	20.9 ± 1.1		$11.1^{+0.3}_{-0.7}$	$18.4^{+1.8}_{-2.3}$	31000^{+3000}_{-4000}
SPT0551-50	3.164(1)	433 ± 22	3.2 ± 0.6	4.0 ± 0.6	3.0 ± 0.7	37.4 ± 1.4	10.8 ± 0.7	11.4 ± 1.1	$4.5^{+0.5}_{-0.5}$	$5.9^{+0.8}_{-0.6}$	10000^{+1000}_{-1000}
SPT0552-42	4.437(0)	510 ± 21	4.8 ± 0.7	4.5 ± 0.7	4.4 ± 1.1	33.9 ± 1.2	8.1 ± 0.6	10.9 ± 0.4	$2.5^{+0.1}_{-0.1}$	$6.2^{+5.0}_{-2.7}$	11000^{+9000}_{-5000}
SPT0553-50	5.323(1)	523 ± 35	4.8 ± 0.8	4.6 ± 0.8	4.4 ± 0.9	42.5 ± 1.9	3.6 ± 0.3	5.6 ± 0.3	$3.3^{+0.2}_{-0.2}$	$5.2^{+0.9}_{-0.9}$	9000^{+1000}_{-2000}
SPT0555-62		465 ± 86	4.0 ± 0.7	4.2 ± 0.7	3.8 ± 0.7	42.5 ± 1.9	8.7 ± 0.7	9.5 ± 1.1	$2.8^{+0.1}_{-0.1}$	$5.9^{+0.6}_{-0.7}$	10000^{+1000}_{-1000}
SPT0604-64		332 ± 11	2.4 ± 0.6	3.4 ± 0.6	2.3 ± 0.9	42.5 ± 1.9	25.5 ± 1.5	19.1 ± 1.3	$7.4^{+0.7}_{-0.2}$	$10.8^{+1.2}_{-1.1}$	18000^{+2000}_{-2000}

continued

Table 5.2: Parameters obtained from photometry fitting

Source	$z_{\rm spec}$	$\lambda_{\rm peak}$	$z^{\rm SED}_{\rm phot}$	$z^{\lambda}_{\rm phot}$	$z^{\rm library}_{\rm phot}$	$T_{\rm dust}$ [K]	$M^{870\mu m}_{\rm dust}$ $\times10^9$ $[M_\odot]$	$M^{3000\mu m}_{\rm dust}$ $\times10^9$ $[M_\odot]$	$L_{\rm FIR}$ $\times10^{13}$ $[L_\odot]$	$L_{\rm IR}$ $\times10^{13}$ $[L_\odot]$	SFR $[M_\odot\,{\rm yr}^{-1}]$
SPT0611-55		350 ± 22	2.3 ± 0.3	3.5 ± 0.3	2.2 ± 0.6	42.5 ± 1.9	10.2 ± 3.4	6.5 ± 1.5	$2.6^{+1.4}_{-0.1}$	$3.6^{+14.4}_{-0.4}$	6100^{+25000}_{-600}
SPT0625-58		347 ± 24	2.9 ± 0.5	3.5 ± 0.5	2.7 ± 0.7	42.5 ± 1.9	22.3 ± 1.4	22.8 ± 2.2	$6.3^{+0.3}_{-0.2}$	$8.9^{+0.9}_{-0.9}$	15000^{+2000}_{-2000}
SPT0652-55		452 ± 28	3.8 ± 0.6	4.1 ± 0.6	3.8 ± 0.8	42.5 ± 1.9	21.0 ± 8.7		$8.7^{+0.3}_{-0.4}$	$12.6^{+3.6}_{-1.9}$	22000^{+6000}_{-3000}
SPT2008-58		250 ± 71	3.1 ± 0.6	2.8 ± 0.6	3.0 ± 0.8	42.5 ± 1.9	$2.9\ \pm1.1$	2.8 ± 0.8	$1.3^{+0.8}_{-0.8}$	$1.6^{+12.1}_{-0.2}$	2800^{+21000}_{-400}
SPT2031-51		401 ± 50	2.6 ± 0.5	3.8 ± 0.5	2.5 ± 0.7	42.5 ± 1.9	$9.6\ \pm3.3$		$3.5^{+0.2}_{-0.1}$	$5.1^{+0.5}_{-0.6}$	8800^{+900}_{-1000}
SPT2037-65	4.000(5)	476 ± 22	4.4 ± 1.2	4.3 ± 1.2	3.9 ± 1.3	35.1 ± 1.4	20.4 ± 1.4	90.1 ± 3.6	$6.8^{+0.3}_{-0.3}$	$9.3^{+7.5}_{-1.0}$	16000^{+12800}_{-2000}
SPT2048-55	4.089(1)	361 ± 28	4.6 ± 0.8	3.5 ± 0.8	4.6 ± 1.2	32.0 ± 1.6	10.8 ± 1.0	21.6 ± 1.2	$2.9^{+0.2}_{-0.1}$	$3.8^{+0.5}_{-0.4}$	6500^{+900}_{-700}
SPT2052-56	4.259(2)	463 ± 15	3.6 ± 0.6	4.2 ± 0.6	3.6 ± 0.9	46.0 ± 2.8	$1.7\ \pm0.2$	1.4 ± 0.2	$1.6^{+0.2}_{-0.1}$	$2.1^{+3.1}_{-0.2}$	4000^{+5000}_{-400}
SPT2101-60		354 ± 18	3.0 ± 0.6	3.5 ± 0.6	2.7 ± 0.6	46.0 ± 2.8	$7.8\ \pm0.7$	9.4 ± 1.1	$4.4^{+0.5}_{-0.2}$	$5.5^{+3.4}_{-0.6}$	9000^{+6000}_{-1000}
SPT2103-60	4.4357(5)	523 ± 36	4.3 ± 0.7	4.6 ± 0.7	4.1 ± 1.0	37.4 ± 1.4	$9.8\ \pm0.8$	7.6 ± 0.8	$3.8^{+0.2}_{-0.2}$	$11.1^{+1.4}_{-6.3}$	19000^{+2000}_{-10800}
SPT2129-57		333 ± 19	3.0 ± 0.7	3.4 ± 0.7	3.3 ± 0.8	37.4 ± 1.4	12.0 ± 4.6		$3.7^{+0.2}_{-0.2}$	$6.4^{+0.7}_{-0.7}$	11000^{+1000}_{-1000}
SPT2132-58	4.7677(2)	456 ± 60	4.7 ± 0.9	4.2 ± 0.9	4.5 ± 0.9	37.9 ± 1.9	$6.9\ \pm0.6$	9.8 ± 1.0	$3.9^{+0.2}_{-0.2}$	$9.0^{+6.1}_{-3.7}$	15000^{+10000}_{-6000}
SPT2134-50	2.7799(2)	265 ± 29	1.8 ± 0.6	2.9 ± 0.6	2.4 ± 0.6	39.0 ± 1.6	14.4 ± 0.9	13.2 ± 1.3	$6.9^{+0.3}_{-0.3}$	$10.6^{+1.1}_{-1.1}$	18000^{+2000}_{-2000}
SPT2146-55	4.5672(2)	507 ± 66	4.4 ± 0.9	4.5 ± 0.9	4.2 ± 0.9	37.4 ± 1.9	$6.8\ \pm0.6$	8.7 ± 1.0	$3.7^{+0.2}_{-0.2}$	$17.1^{+1.8}_{-10.7}$	29000^{+3000}_{-18000}
SPT2147-50	3.7602(2)	434 ± 30	3.6 ± 0.7	4.0 ± 0.7	3.6 ± 0.7	40.2 ± 1.4	$7.0\ \pm0.4$	6.2 ± 0.6	$3.4^{+0.2}_{-0.1}$	$5.3^{+0.7}_{-0.5}$	9000^{+1000}_{-900}
SPT2152-40		639 ± 111	3.7 ± 0.8	5.3 ± 0.8	4.2 ± 1.0	40.2 ± 1.4	11.8 ± 5.2		$3.5^{+0.2}_{-0.2}$	$5.7^{+1.0}_{-0.7}$	10000^{+2000}_{-1000}
SPT2203-41		557 ± 43	5.0 ± 0.8	4.8 ± 0.8	5.2 ± 1.0	40.2 ± 1.4	$6.9\ \pm3.8$		$3.3^{+0.1}_{-0.1}$	$9.4^{+3.1}_{-3.5}$	16000^{+5000}_{-6000}
SPT2219-42		452 ± 16	3.4 ± 0.7	4.1 ± 0.7	3.4 ± 0.8	40.2 ± 1.4	$2.3\ \pm1.0$		$1.2^{+0.1}_{-0.1}$	$1.6^{+2.1}_{-0.2}$	3000^{+4000}_{-400}
SPT2232-61		420 ± 22	3.1 ± 0.6	3.9 ± 0.6	2.8 ± 0.6	40.2 ± 1.4	$8.2\ \pm3.1$		$1.0^{+3.6}_{-3.6}$	$2.0^{+7.9}_{-3.3}$	3000^{+14000}_{-6000}
SPT2307-50		250 ± 63	3.4 ± 0.8	2.8 ± 0.8	3.0 ± 0.8	40.2 ± 1.4	$2.8\ \pm1.2$	2.5 ± 0.8	$1.1^{+0.5}_{-0.1}$	$1.4^{+9.1}_{-0.2}$	2500^{+16000}_{-400}
SPT2311-45		341 ± 23	2.7 ± 0.6	3.4 ± 0.6	2.6 ± 0.7	40.2 ± 1.4	$8.7\ \pm3.1$		$3.1^{+0.1}_{-0.1}$	$4.3^{+0.5}_{-0.5}$	7400^{+800}_{-800}
SPT2311-54	4.2795(4)	381 ± 34	3.3 ± 0.6	3.7 ± 0.6	3.2 ± 0.8	47.7 ± 2.3	$3.1\ \pm0.2$	3.0 ± 0.2	$4.3^{+0.2}_{-0.2}$	$7.9^{+0.9}_{-0.9}$	14000^{+2000}_{-2000}
SPT2316-50		446 ± 40	3.6 ± 0.7	4.1 ± 0.7	3.5 ± 0.9	47.7 ± 2.3	$3.8\ \pm1.7$		$1.5^{+0.3}_{-0.1}$	$2.0^{+2.9}_{-0.2}$	3000^{+5000}_{-400}
SPT2319-55	5.2929(5)	512 ± 86	4.7 ± 0.9	4.5 ± 0.9	4.2 ± 0.9	42.1 ± 2.1	$3.3\ \pm0.3$	4.1 ± 0.3	$2.9^{+0.1}_{-0.2}$	$3.9^{+4.9}_{-0.4}$	7000^{+8000}_{-700}
SPT2332-53	2.7256(2)	292 ± 14	2.0 ± 0.5	3.1 ± 0.5	2.1 ± 0.6	47.4 ± 2.6	16.7 ± 1.0		$9.7^{+0.6}_{-0.3}$	$13.8^{+2.2}_{-1.4}$	24000^{+4000}_{-2000}
SPT2335-53	4.757(2)	463 ± 24	3.4 ± 0.6	4.2 ± 0.6	3.7 ± 1.0	57.0 ± 3.5	$1.6\ \pm0.2$	1.1 ± 0.1	$3.3^{+0.2}_{-0.2}$	$4.1^{+6.3}_{-0.4}$	7000^{+11000}_{-700}
SPT2340-59		440 ± 31	3.8 ± 0.6	4.0 ± 0.6	3.6 ± 0.7	57.0 ± 3.5	$4.2\ \pm1.8$	4.2 ± 1.3	$2.1^{+0.1}_{-0.2}$	$3.0^{+0.5}_{-0.6}$	5000^{+800}_{-1000}
SPT2349-50	2.877(1)	411 ± 61	2.9 ± 0.6	3.9 ± 0.6	2.9 ± 0.7	37.9 ± 1.6	$6.3\ \pm0.4$	6.0 ± 0.4	$2.3^{+0.8}_{-0.1}$	$2.9^{+10.6}_{-0.3}$	5000^{+18100}_{-500}
SPT2349-52		467 ± 35	3.8 ± 0.8	4.2 ± 0.8	3.8 ± 0.8	37.9 ± 1.6	$4.5\ \pm2.1$		$2.0^{+0.1}_{-0.2}$	$3.2^{+2.7}_{-0.9}$	5000^{+5000}_{-1000}

continued

Table 5.2: Parameters obtained from photometry fitting

Source	$z_{\mathbf{spec}}$	$\lambda_{\mathbf{peak}}$	$z^{\mathbf{SED}}_{\mathbf{phot}}$	$z^{\lambda}_{\mathbf{phot}}$	$z^{\mathbf{library}}_{\mathbf{phot}}$	$T_{\mathbf{dust}}$	$M^{870\mu m}_{\mathbf{dust}}$ $\times 10^9$	$M^{3000\mu m}_{\mathbf{dust}}$ $\times 10^9$	$L_{\mathbf{FIR}}$ $\times 10^{13}$	$L_{\mathbf{IR}}$ $\times 10^{13}$	**SFR**
						[K]	$[M_\odot]$	$[M_\odot]$	$[L_\odot]$	$[L_\odot]$	$[M_\odot\,\mathrm{yr}^{-1}]$
SPT2349-56	4.304(2)	483 ± 47	3.6 ± 0.6	4.3 ± 0.6	3.7 ± 0.8	46.7 ± 2.3	4.2 ± 0.5	2.2 ± 0.2	$2.8\ ^{+0.2}_{-0.1}$	$3.4\ ^{+4.8}_{-0.3}$	$6000\ ^{+8000}_{-600}$
SPT2351-57	5.811(2)	474 ± 13	4.1 ± 0.8	4.3 ± 0.8	4.0 ± 0.9	53.5 ± 2.6	1.5 ± 0.1	2.5 ± 0.1	$4.6\ ^{+0.2}_{-0.3}$	$6.8\ ^{+1.0}_{-0.7}$	12000^{+2000}_{-1000}
SPT2353-50	5.576(3)	452 ± 58	4.7 ± 0.9	4.1 ± 0.9	4.2 ± 0.8	46.3 ± 2.3	2.6 ± 0.2	3.6 ± 0.2	$3.5\ ^{+0.2}_{-0.2}$	$5.9\ ^{+1.1}_{-1.3}$	10000^{+2000}_{-2000}
SPT2354-58		221 ± 16	1.2 ± 0.6	2.6 ± 0.6	1.3 ± 0.5	46.3 ± 2.3	10.4 ± 0.6	10.3 ± 0.9	$5.8\ ^{+1.2}_{-0.2}$	$9.5\ ^{+1.1}_{-1.0}$	16000^{+2000}_{-2000}
SPT2357-51	3.0703(5)	442 ± 22	3.2 ± 0.7	4.1 ± 0.7	3.7 ± 1.0	37.2 ± 1.2	8.0 ± 0.6	4.8 ± 0.3	$1.8\ ^{+0.5}_{-0.5}$	$2.4\ ^{+8.2}_{-0.3}$	$4100\ ^{+14000}_{-400}$

All parameters are given as observed. The intrinsic M_{dust}, L_{FIR}, L_{IR}, and SFR is found by dividing by the average sample magnification $\mu = 5.5$.

5.4 Dust properties

Through SED fitting we can obtain more than the photometric redshift. In Section 4.1.3.3 we have already briefly discussed the dust temperature, when creating a dust temperature distribution to use find photometric redshifts. We will discuss the dust temperature in more detail in Section 5.4.1. We furthermore present dust masses, infra red luminosities, and star formation rates of the sample.

5.4.1 The dust temperature

To find dust temperatures of the SPT-DSFGs we employ the same method as for finding photometric redshifts (see Section 4.1.3.3), but instead of fixing the dust temperature and varying the redshift, the redshift is fixed to the spectroscopic redshift and the dust temperature is varied. This creates a probability distribution for the dust temperature of each source. In Figure 4.4 the combined dust temperature distribution for the 53 sources with unambiguous spectroscopic redshifts is shown. The calculated dust temperatures are listed in Table 5.2.

Figure 5.5 shows the dust temperature as a function of redshift for the 53 sources with spectroscopic redshift (*orange* circles). The scatter in the dust temperature is large, so to investigate whether the dust temperature evolves with redshift the sources are sorted into redshift bins of one and the medians of these bins are shown with *red* triangles, where the horizontal error bars show the bin size and the vertical error bars show the spread. The medians are increasing with redshift, and a linear fit to the sources yields a slope of $2.7 \pm 0.8\,\mathrm{K}$, which means that the slope is detected with an $\mathrm{SNR} \sim 3$, confirming the existence of a trend.

To see how the SPT-DSFGs compare to the large, but lower redshift samples in the literature, we plot dust temperatures derived from SED fitting of star forming galaxies from Béthermin et al. (2015) and trends of the evolution seen by Magnelli et al. (2014). The sample of Béthermin et al. (2015) consists of star forming galaxies in the COSMOS field with redshifts up to $z = 4$. The sample is mass-selected from the UltraVISTA sample (Ilbert et al., 2013), with criteria in place to select only star forming galaxies. The sources are split into two groups, star forming galaxies on the main sequence and starburst galaxies. Each group is split into 11 redshift bins for which a median flux densities are calculated. Dust temperatures are not derived for the Béthermin et al. (2015) samples, but by fitting the median photometry in the same way as for the SPT-DSFGs we find a dust temperature for each of the redshift bins. The median SEDs are broader than that of the typical SPT-DSFG, which is most likely due to the stacking of the SEDs, as shifts in the peaks of the SEDs within each redshift bin will translate into a broad peak. For the SPT-DSFG sample we see a large spread in dust temperatures, also within the redshift bins defined by Béthermin et al. (2015) (see Figure 5.2 and 5.5). With the broad SEDs it is hard to identify the peak of the cold dust, which could lead to an over estimation of the dust temperature. The samples are plotted in Figure 5.5 in *blue* for the main sequence galaxies and *turquoise* for the starburst galaxies. Both groups show an evolution of dust temperature with

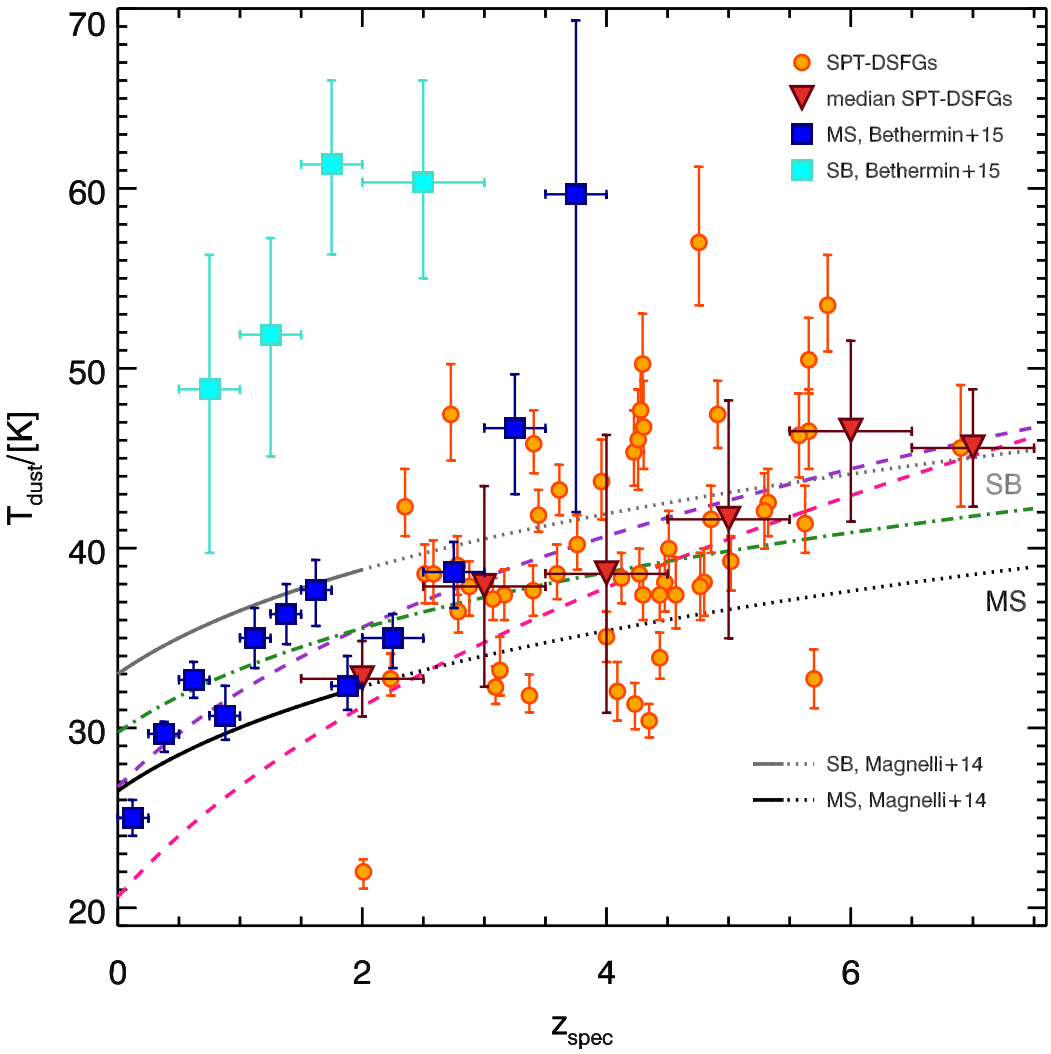

Figure 5.5: Dust temperatures as a function of redshift. The *orange* circles show the individual sources and the *red* triangles show the mean dust temperature of the bin shown by the horizontal error bar. The *blue* squares show main sequence star forming galaxies (Béthermin et al., 2015) and the *turquoise* squares show starburst galaxies (Béthermin et al., 2015). The pink dashed line is a power-law fit to the SPT-DSFGs and the *purple* dashed line shows a power-law fit to the combined sample of main sequence galaxies from Béthermin et al. (2015) and the SPT-DSFGs. The solid *black* line shows the relation between dust temperature and redshift found by Magnelli et al. (2014) for main sequence galaxies, and the dotted *black* line is the extension of this. The *gray* line is the same relation for starburst galaxies.

redshift. The starburst galaxies appear warmer than both the main sequence sample and the SPT-DSFGs. However, the SPT-DFSGs seem to be an extension of the trend of main sequence galaxies. We note that the slope of the main sequence galaxies from Béthermin et al. (2015) is steeper (6.9 ± 1.2 K, or 3.9 ± 1.1 K ignoring sources above $z < 3$).

Magnelli et al. (2014) studied the relation between dust temperature and redshift for star-forming galaxies up to $z < 2$ from deep PACS and SPIRE observations. They derived this relation between the dust temperature and redshift, that also depends on the specific star formation rate (sSFR $=$ SFR$/M_*$)

$$T_{\rm dust} = 26.5(1+z)^{0.18} + 6.5 \times \Delta\log(sSFR)_{\rm MS}{\rm K}. \tag{5.2}$$

$\Delta\log(sSFR)_{\rm MS}$ represents the distance from the main sequence. This relation is plotted in Figure 5.5 for main sequence galaxies (*black*) and for starburst galaxies (*gray*, $10 \times$ sSFR). The solid lines represent the redshift range for which this relation was fitted, and the dotted line is the extension. The *pink* line shows a power-law fit to the SPT-DSFGs, which has a power of 0.38 ± 0.03. As the redshifts of SPT-DSFGs are all higher than seen for the Magnelli et al. (2014) sample, we combine it with the main-sequence sample from Béthermin et al. (2015), giving us a sample with a large redshift range of $0.1 < z < 6.9$. A power-law fit to this sample gives the expression

$$T_{\rm dust} = (26.7 \pm 13.6)(1+z)^{0.26 \pm 0.33}{\rm K} \tag{5.3}$$

and is shown by a *purple* line in Figure 5.5. There is a large error on this parameter, but it is close to that found for the Magnelli et al. (2014) sample. Fitting the SPT-DSFGs to a power-law using the constants found by Magnelli et al. (2014) we find that the sample lies 3.2 K above the main sequence.

With the large SPT-DSFG sample with spectroscopic redshifts, it is possible to extend the relation between dust temperature and redshift to higher redshifts than previously seen. The trend observed for the SPT-DSFGs is similar to that of lower redshift sources, and they seem to follow the power-law suggested by Magnelli et al. (2014) well.

Whether the relation between redshift and dust temperature could be a result of the selection effect for the SPT-DSFGs is not fully clear and an in-depth study would require detailed numerical simulations based on galaxy evolution models. Sources with higher redshift will be selected at shorter intrinsic wavelengths, which means closer to the peak of the thermal dust emission. As the position of the peak shifts as a function of dust temperature, there could be a selection bias, but it is difficult to predict exactly which effect this would have.

5.4.2 Dust masses

We use Equation 2.8 to determine dust masses of the full SPT-DSFG sample, based on the 870 μm fluxes, using $\kappa[{\rm m^2 kg^{-1}}] = 0.045(\nu_{\rm rest}/250\,{\rm GHz})^{\beta}$, where $\beta = 2$ as Greve et al. (2012). We tested varying β, but only when using $\beta = 2$ we find similar values when

comparing the dust mass calculated based on the 870 μm flux density with that based on the 3.0 mm flux density. The median dust mass of the sample is $M_{\rm dust,median} = (4.1 \pm 3.4) \times 10^9 M_\odot$, and when correcting for the average magnification of the sample ($\mu = 5.5$ Spilker et al., 2016) we find $M_{\rm dust,median}/\mu = (6.4 \pm 5.4) \times 10^8 M_\odot$. This is consistent with what is found for the 99 ALESS DSFGs investigated by da Cunha et al. (2015), with a median dust mass of $M_{\rm dust} = (5.6 \pm 1.0) \times 10^8 M_\odot$.

Using a gas-to-dust-mass ratio of 150 (Weiß et al., 2008) we find a demagnified gas mass for the SPT-DSFGs of $M_{\rm gas,median}/\mu = (9.5 \pm 8.0) \times 10^{10} M_\odot$. This is slightly higher than what is observed for the DSFGs presented by Bothwell et al. (2013), where a mean gas mass of $M_{\rm gas} = (5.3 \pm 1.0) \times 10^{10} M_\odot$ was found, based on CO observations.

This comparison shows, that the 1.4 mm selected, bright SPT-DSFGs probe similarly gas rich systems as 850 μm selected samples, albeit at higher redshift.

5.4.3 Far Infra Red luminosity and Infra Red luminosity

To estimate the amount of dust obscured star formation in the SPT-DSFGs we calculate their FIR and IR luminosities. The FIR luminosity $L_{\rm FIR}$ is defined as the integral of the thermal dust peak between 40 and 120 μm and the IR luminosity $L_{\rm IR}$ is integrated between 8 and 1000 μm. The data we currently have for the SPT-DSFGs does not cover the full wavelength range of the $L_{\rm IR}$ and for sources with $z < 5.2$ and no PACS data the full $L_{\rm FIR}$ range is not covered. This means we need to extrapolate the SED fit for a few sources to determine $L_{\rm FIR}$ and for all sources to determine the $L_{\rm IR}$. When we want to characterize the full SED a single modified black body does not describe the data sufficiently. There are several ways to fit all the data points, and we describe four here. Figure 5.6 shows the different fits for four different sources to demonstrate the strengths and weaknesses of the different methods. The methods are:

Spline: Connecting the photometric data by a continuous spline is the simplest way of describing the data without assuming anything about the source. The disadvantage of this method is that it is impossible to extrapolate as there is no physics in the spline to base it on. As stated above this will give problems when calculating the $L_{\rm FIR}$ for a few sources and the $L_{\rm IR}$ for all sources. Figure 5.6 shows the spline fits as the *green* dot-dashed lines. SPT0113-46 (upper right panel) is an example of a source where the data does not cover the frequency range for the $L_{\rm FIR}$.

Single component SED fit: Fitting a single component SED is one of the simplest way to fit the data. From Figure 5.6 it is clear that this method does not fit the data well enough, especially at short wavelengths, to give an infrared luminosity. This method is sometimes used for an easy comparison between many samples like done by e.g. Gullberg et al. (2015).

Two component SED fit: To fit SEDs with two dust components we use Equation 2.5 but add an extra Planck function ($B_\nu(T_{\rm dust2})$). In principle we could fit more than two components but given the limited data we have, this will not improve the fit significantly. The two component SEDs are shown in Figure 5.6 as the solid *blue* line with each component shown as a dotted *blue* line. This method generally fits the data well and offers a reasonable extrapolation towards shorter wavelengths.

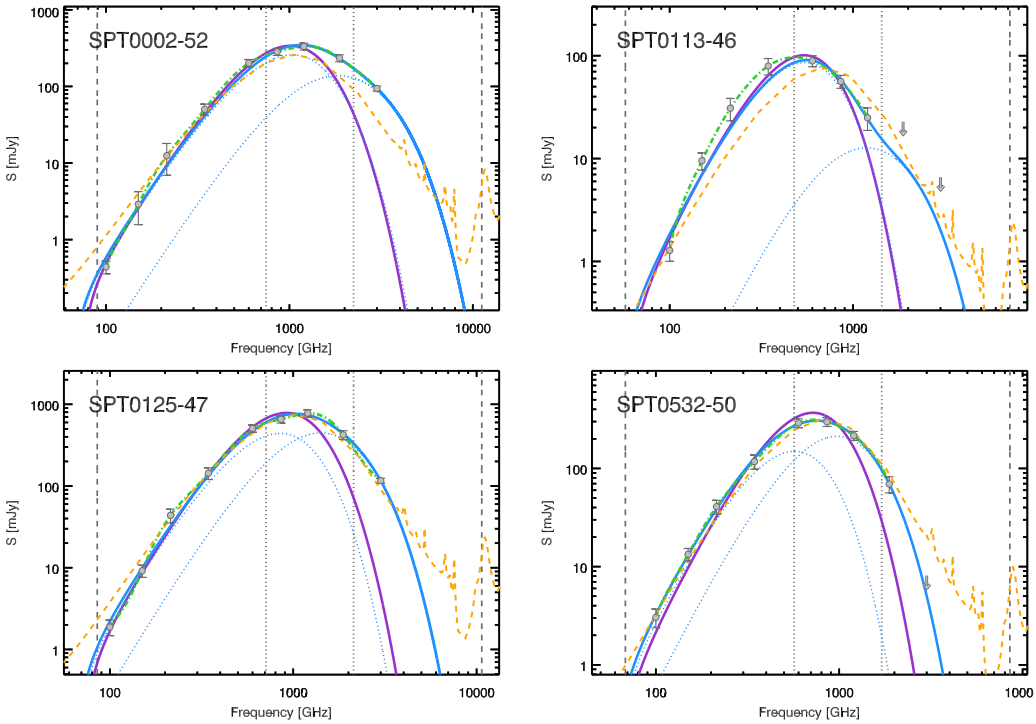

Figure 5.6: SEDs for the four sources: SPT0002-52, SPT0113-46, SPT0125-47, and SPT0532-50 shown at the observed frequency. The vertical lines show the integration limits for the FIR (dotted, 120 – 40 μm rest) and IR luminosity regime (dashed, 1200 – 8 μm rest) The *purple* solid lines show the single modified black body, the *orange* dashed line is the Arp220 template, the *blue* solid line shows the two component modified black bodies with the *blue* dotted lines showing the two individual components, and the *green* dash-dotted line shows the spline.

Fitting a template: Unfortunately we cannot use the library of templates we created from the SPT-DSFGs as these are cut off at the last data point and they will therefore have the same issue as the spline when it comes to integrating $L_{\rm FIR}$ and $L_{\rm IR}$. Instead, we use the template of the prototypical low redshift ($z = 0.1$) ULIRG Arp220 (Silva et al., 1998). This template is shown with an *orange* dashed line in Figure 5.6. To fit the template we shift it to the spectroscopic redshift of the source and fit the amplitude to the data. The advantage of using a well described template as the one of Arp220 is that it gives a good idea of how the extrapolation at the high frequency side could look like. The disadvantage is that the SPT-DSFGs have many different SED shapes and the SED of Arp220 does not always follow the data very well (e.g. SPT0002-52 and SPT0113-46). The difference in the fit of the high frequency regimes of SPT0113-46 and SPT0125-47 are good examples of why we should be careful with the extrapolation.

We find that the two component SED fitting is the best method to ensure both a good fit to the data and a reasonable extrapolation, and we use this method to determine the $L_{\rm FIR}$ and $L_{\rm IR}$. Both infrared luminosities are given in Table 5.2 for all sources. As seen from Figure 5.6 we might be underestimating the $L_{\rm IR}$ at the highest frequencies compared to what we see in Arp220. This difference is up to $\sim 10\%$ of the infrared luminosity which we add in quadrature to the error.

Figure 5.7 shows the far infrared luminosity plotted as a function of redshift for all sources (*orange* circles). The *red* triangles indicate the median of redshift bins given by the horizontal bar, showing that there is no change in redshift.

The median $L_{\rm FIR}$ of the sample is $L_{\rm FIR,med} = (3.5 \pm 2.9) \times 10^{13} L_\odot$. When corrected for the average magnification of the sample, the median $L_{\rm FIR}$ is $L_{\rm FIR,med}/\mu = (6.4 \pm 5.3) \times 10^{12} L_\odot$

The median $L_{\rm IR}$ of the sample is $L_{\rm IR,med} = (6.3 \pm 5.4) \times 10^{13} L_\odot$ which demagnified becomes $L_{\rm IR,med}/\mu = (1.2 \pm 1.0) \times 10^{13} L_\odot$. This places the samples on the border between being Ultra luminous galaxies (ULIRGs, $10^{12} < L_{\rm IR}/L_\odot < 10^{13}$) and Hyper luminous galaxies (HyLIRGs, $10^{13} < L_{\rm IR}/L_\odot < 10^{14}$) (Casey et al., 2014).

Based on the infrared luminosity we can estimate an SFR based on Equation 2.9. The calculated apparent SFRs for the SPT-DSFG sample are given in Table 5.2. The median SFR of the full sample is $SFR_{\rm median} = 10800 \pm 9300$, which demagnified is $SFR_{\rm median}/\mu = 2000 \pm 1700$.

5.5 Conclusion

Photometric observations are used to, for the first time, study the full SPT-DSFG sample of 91 sources. All the sources has well-sampled photometric coverage with observed flux densities at 2.2 and 1.4 mm (SPT), 870 μm (APEX/LABOCA), and 500 350, and 250 μm (*Herschel*/SPIRE). For a subsample of 66 sources, where the thermal dust peak was not completely covered, *Herschel*/PACS observations at 100 and 160 μm were conducted. We test different methods of obtaining photometric redshift, and use SPT-DSFGs with spectroscopic redshifts to compare the methods. We find that the

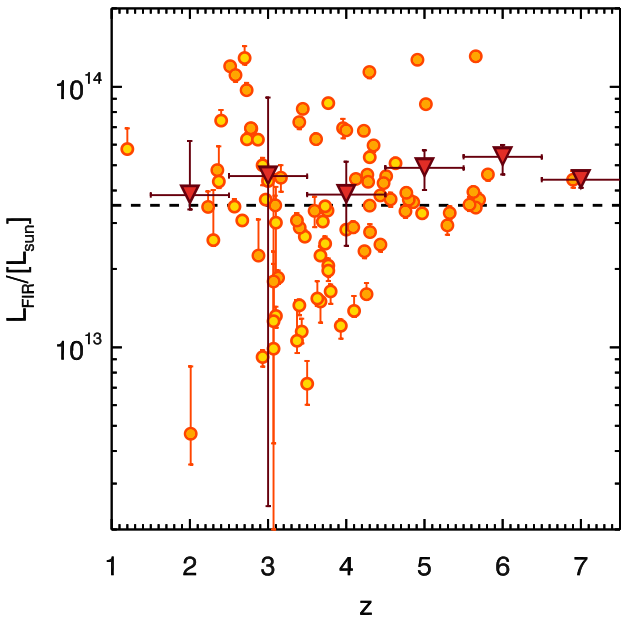

Figure 5.7: FIR luminosity as a function of redshift. The *orange* circles show the SPT-DSFGs, where the darker filling indicates the sources with spectroscopic redshifts and the lighter filling illustrates the sources with photometric redshift. The *red* triangles show the medians of the redshift bins illustrated by the horizontal bars.

best method is fitting a single component SED, using a dust temperature distribution based on SPT-DSFGs with spectroscopic redshifts. We create a redshift distribution for the full sample by combining the redshifts of the 62 sources with spectroscopic redshifts (unambiguous and one line redshifts) with the photometric redshifts of the remaining 29. By replacing the redshifts of the 53 sources with spectroscopic redshifts, with these, we create the best possible redshift distribution of the sample, which shows a very consistent median of $z_{\rm phot} = 3.7 \pm 0.1$. The spectroscopic redshift distribution has a much flatter peak than the photometric redshift distribution though.

For the first time the SPT-DSFG sample could be directly compared to a gravitationally lensed sample, like that of the ACT sources from Su et al. (2017). The distributions of the two samples are very similar, with a similar medians, though the number of sources in the SPT-DSFG distribution is 10 times as large as that of the ACT sources.

A comparison is also made to the photometric redshift distribution of a selection of high redshift likely unlensed *Herschel* DSFGs presented by Ivison et al. (2016). The selection is specifically created to select high redshift sources, and can therefore not be interpreted as unbiased. The two samples are very similar, with similar medians. When the SPT-DSFG sample is lensing corrected (as it should be for this comparison) we find a median of $z_{\rm lens-cor} = 3.0 \pm 0.1$, and this distribution peaks at lower redshifts than that of Ivison et al. (2016).

The SPT-DSFG redshift distribution, after correcting for biases from gravitational

lensing, allows us to study the high redshift tail of DSFGs in a statistically robust manner.

The median dust temperature of the SPT-DSFGs with spectroscopic redshifts is $T_{\rm dust} = 39 \pm 6\,{\rm K}$, and we find that the dust temperature increases with redshift following a trend seen for lower redshift sources. We show that this evolution can be described by the expression $T_{\rm dust} = (26.7 \pm 13.6)(1+z)^{(0.26\pm0.33)}\,{\rm K}$.

We use the $870\,\mu$m flux density to determine an intrinsic (correcting for lensing using the average magnification of the sample of $\mu = 5.5$) median dust mass of the full sample of $M_{\rm dust} = (6.4 \pm 5.4) \times 10^8 M_\odot$. Using a gas-to-dust-mass-ratio of 150 we convert this into an intrinsic gas mass of $M_{\rm gas} = (9.5 \pm 8.0) \times 10^{10} M_\odot$.

By fitting a two component SED to the flux densities we find an intrinsic FIR luminosity of $L_{\rm FIR} = (6.4 \pm 5.3) \times 10^{12} L_\odot$ and we find that there is no evolution with redshift. This translates into an intrinsic SFR of $2000 \pm 1700\,M_\odot\,{\rm yr}^{-1}$.

This is one of the largest and most uniform photometric databases of DSFGs known to date.

5.6 Acknowledgments

M.L.S. was supported for this research through a stipend from the International Max Planck Research School (IMPRS) for Astronomy and Astrophysics at the Universities of Bonn and Cologne. This chapter makes use of the following ALMA data: ADS/JAO.ALMA# 2015.1.00504.S, 2012.1.00844.S, 2011.0.00957.S, and 2011.0.00958.S. ALMA is a partnership of ESO (representing its member states), NSF (USA) and NINS (Japan), together with NRC (Canada) and NSC and ASIAA (Taiwan), in cooperation with the Republic of Chile. The Joint ALMA Observatory is operated by ESO, AUI/NRAO and NAOJ. This work is based in part on observations made with *Herschel* under program ID's OT1_jvieira_4, OT2_jvieira_5, DDT_tgreve_2, and DDT_mstrande_1. *Herschel* is a European Space Agency Cornerstone Mission with significant participation by NASA. We also use data from the Atacama Pathfinder Experiment under program IDs M-085.F-0008- 2010, M-087.F-0015-2011, E-087.A-0968B-2011, M-089.F-0009-2012, E-089.A-0906A- 2012, M-091.F-0031-2013, E-091.A-0835B-2013, M-092.F-0021-2013. APEX is a collaboration between the Max-Planck-Institut für Radioastronomie, the European Southern Observatory, and the Onsala Space Observatory. The SPT is supported by the National Science Foundation through grant PLR-1248097, with partial support through PHY-1125897, the Kavli Foundation and the Gordon and Betty Moore Foundation grant GBMF 947.

Chapter 6

ISM properties of a Massive Dusty Star-Forming Galaxy discovered at $z \sim 7$

In this chapter we report the discovery and constrain the physical conditions of the interstellar medium of the highest-redshift millimeter-selected dusty star-forming galaxy (DSFG) to date, SPT0311-58, at $z = 6.900 \pm 0.002$. The content of this chapter is published in Strandet et al. (2017) **Strandet et al. 2017, The Astrophysical Journal Letters, Volume 842, Issue 15**. We constrain the properties of the ISM in SPT0311-58 with a radiative transfer analysis of the dust continuum photometry and the CO and [C I] line emission. This model was created and run for SPT0311-58 by Dr. Axel Weiß . We also observe [C II] for this source and use this to put the source into the context of other star forming galaxies.

6.1 Introduction

Here we present the DSFG SPT−S J031132−5823.4 (hereafter SPT0311-58) discovered in the SPT-SZ survey (Carlstrom et al., 2011; Vieira et al., 2013). SPT0311-58 is the highest redshift millimeter-selected DSFG known to-date, located well into the EoR at a redshift of $z = 6.900 \pm 0.002$. With this source, we take a step of almost 100 Myr closer to the Big Bang than the previously most distant DSFG at $z = 6.34$ found by Riechers et al. (2013), bringing us ~ 760 Myr away from Big Bang. Throughout this chapter, we assume a ΛCDM cosmology with $H_0 = 70$ km s^{-1} Mpc^{-1}, $\Omega_\Lambda = 0.7$ and $\Omega_M = 0.3$.

6.2 Observational Results

6.2.1 Determining the redshift

The redshift scan for SPT0311-58 was performed in ALMA band 3 by combining five tunings covering 84.2 – 114.9 GHz (project ID: 2015.1.00504.S; see Weiß et al., 2013; Strandet et al., 2016, for further details on the observing setup). The observations were carried out on 2015 December 28 and 2016 January 2 in the Cycle 3 compact array configuration. The number of antennas varied from 34 to 41, with baselines up to 300 m yielding a synthesized beam size of $2\farcs2 - 3\farcs0$. Typical system temperatures for the observations were $T_{sys} = 50$ – 80 K (SSB). Flux calibration was done with Uranus,

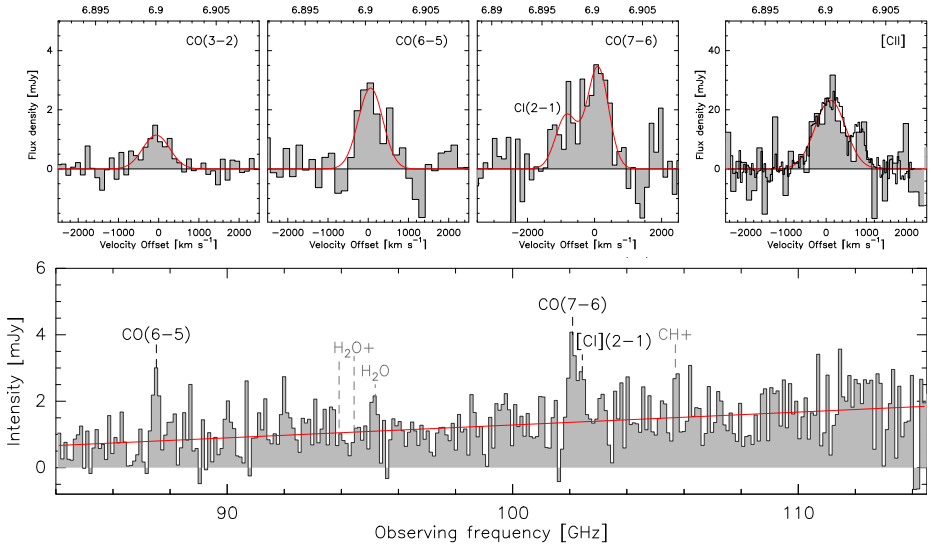

Figure 6.1: The lower part of the figure shows the ALMA 3 mm spectrum of SPT0311-58 spanning 84.2 – 114.9 GHz. The spectrum has been binned to best show the lines. Transitions labeled in *black* are detected and *gray* labels indicate where other transitions should be. The *red* line indicate the zeroth order baseline. The sub-panels above the spectrum show, from left to right, the continuum-subtracted spectra of: ATCA CO(3–2), ALMA CO(6–5), ALMA CO(7–6) and CI(2–1), and APEX [C II] with ALMA [C II] overlaid as a solid *black* histogram. Gaussian fits to the spectra are shown in *red*.

bandpass calibration with J0334−4008, and phase calibration with J0303−6211 and J0309−6058. The on-source time varied between 60 seconds and 91 seconds per tuning, accounting for a total of 6 minutes and 10 seconds. The data were processed using the CASA package (McMullin et al., 2007).

We created a cleaned 3 mm continuum image by combining all 5 tunings. This yields a high SNR of $\sim$35. We also generated a spectral cube using natural weighting with a channel width of 19.5 MHz (50 – 65 kms^{-1} for the highest and lowest observing frequency, respectively), which gives a typical noise per channel of 0.9 –1.7 mJy beam^{-1}.

The ALMA 3 mm spectrum of SPT0311-58 was extracted at the centroid of the 3 mm continuum emission (α: $03^{\rm h}11^{\rm m}33\overset{\prime\prime}{.}142$ δ: $-58^{\circ}23'33\overset{\prime\prime}{.}37$ (J2000)) and is shown in Figure 6.1. We detect emission in the CO $J = 6$ – 5 and 7 – 6 lines and the [C I] $^3P_2 - ^3P_1$ line (in the following $2 - -1$) and their noise-weighted line frequencies yield a redshift of $z = 6.900 \pm 0.002$. We also see hints of $H_2O(2_{11} - 2_{02})$ and $CH^+(1–0)$, but these are not formally detected in this short integration.

The line and continuum properties are given in Table 6.1. For the fit to the CO(7–6) and [C I](2–1) lines we fix the line width to the mean value derived from the unblended lines. Their uncertainties include the variations of the line intensities for a fit where the line width is a free parameter.

Table 6.1: Observed properties of SPT0311-58

Line properties					Continuum properties	
Transition	$\int SdV$ **[Jy km/s]**	dV^a **[km/s]**	$L' \times 10^{11}$ **[K km/s/pc^2]**	$L \times 10^8$ **[$L_\odot$]**	λ **[μm]**	S_ν **[mJy]**
CO(3–2)	0.96 ± 0.15	790 ± 150	1.52 ± 0.24	2.01 ± 0.32	3000	1.30 ± 0.05
CO(6–5)	2.10 ± 0.33	720 ± 140	0.83 ± 0.13	8.8 ± 1.4	2000	7.5 ± 1.3
CO(7–6)	2.78 ± 0.80	750^b	0.81 ± 0.11	13.6 ± 1.8	1400	19.0 ± 4.2
[C I](2–1)	1.29 ± 0.80	750^b	0.37 ± 0.10	6.4 ± 1.8	870	32.0 ± 5.0
[C II]$_{\rm APEX}$	22.1 ± 5.1	890 ± 260	1.16 ± 0.27	254 ± 59	500	52.0 ± 8.0
[C II]$_{\rm ALMA}$	25.88 ± 0.65		1.36 ± 0.03	298.1 ± 7.5	350	38.0 ± 6.0
					250	29.0 ± 8.0

a FWHM
b fixed from CO(3–2) and CO(6–5).

6.2.2 Observations of CO(3–2) and [C II]

We used the 7 mm receivers of the Australia Telescope Compact Array (ATCA) to observe the CO(3–2) line (project ID: CX352). Observations were carried out with the hybrid H214 array, which yields a beam size of 5-6″ at the observing frequency of 43.77 GHz. The line is detected with a SNR of 5.0 at a frequency and line width consistent with the ALMA derived redshift and line profiles.

In addition, we used the Atacama Pathfinder Experiment (APEX) to observe [C II] at 240.57 GHz. The observations were carried out in 2016 April–May in good weather conditions with a precipitable water vapor content < 1.5 mm (project IDs E-296.A-5041B-2016 and M-097.F-0019-2016). The observations were performed and the data processed as described by Gullberg et al. (2015). The [C II] line is detected with a SNR of 4.3. From ALMA high spatial resolution observations of the [C II] line (Marrone et al. in submitted; project ID: 2016.1.01293.S), we extract a [C II] spectrum and flux, which are in good agreement with the APEX data. We adopt the ALMA [C II] flux hereafter.

The line parameters derived from Gaussian fits to the data are given for both transitions in Table 6.1; the spectra are shown in Figure 6.1.

6.2.3 FIR dust continuum

Table 6.1 (right) summarizes the dust continuum observations of SPT0311-58. With seven broadband continuum detections between 3 mm to 250 μm, the far-infrared spectral energy distribution (SED) of SPT0311-58 is thoroughly covered.

The SPT 1.4 and 2.0 mm flux densities were extracted and deboosted as described by Mocanu et al. (2013). We obtained a 870 μm map with APEX/LABOCA (project ID: M-091.F-0031-2013). The data were obtained, reduced, and the flux extracted following Greve et al. (2012). Using *Herschel*/SPIRE, we obtained maps at 250 μm, 350 μm and 500 μm (project ID: DDT_mstrande_1). The data were obtained and reduced as described by Strandet et al. (2016).

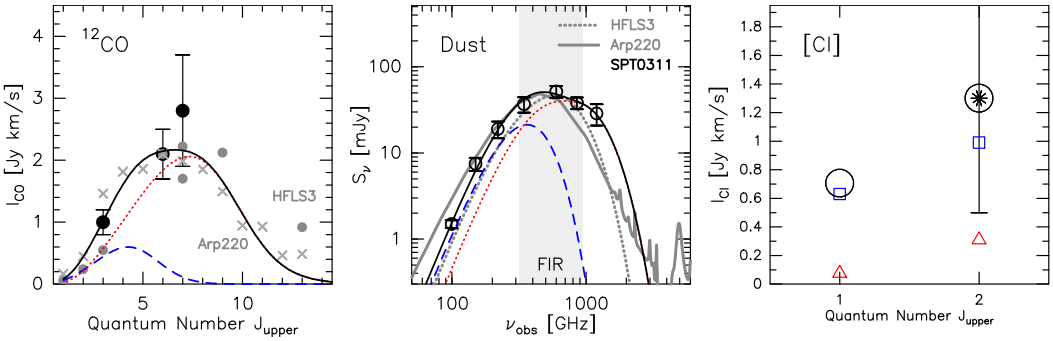

Figure 6.2: Results of simultaneous fitting of the CO SLED (*left*), SED (*middle*) and [C I] (*right*) line flux. The CO line intensities are plotted as filled circles, the continuum fluxes as open circles and the [C I]flux as an asterisk. The *blue* dashed line and squares show the cold component, the *red* dotted line and triangles show the warm component, the *black* solid line and circles (in right panel) show the combination of the two components. In *gray* is shown similar data for HFLS3 (dots and dotted line) and Arp220 (crosses and solid line), normalized to the CO(6–5) flux of SPT0311-58 for the CO-SLED and to the peak of the continuum SED of SPT0311-58 for the SED. The line fluxes and continuum properties fitted are listed in Table 6.2. *Left*: Two component CO-SLED. *Middle*: Two component SED fitting based. *Right*: The contribution of each of the two components to the [C I](2–1) line and predictions for the [C I](1–0) line.

From our photometry, we derive an apparent far-infrared (FIR) luminosity (integrated between 40–120 μm rest) of $L_{FIR} = 4.1 \pm 0.7 \times 10^{13}\, L_\odot$ (see Figure 6.2).

6.3 Characterizing the ISM in SPT0311-58

6.3.1 Source properties from high resolution imaging

ALMA high spatial resolution imaging (angular resolution of $0.3 \times 0.5''$) of the [C II] line in SPT0311-58 shows that the system consists of two galaxies in close proximity (Marrone et al. in submitted). Only the western source is significantly gravitationally magnified and this source dominates the apparent continuum luminosity ($> 90\%$ of the restframe 160 μm continuum flux density is emitted by the western source). In the following, we assume that the contribution from the eastern source is negligible and model the system as a single object, using the system magnification of $\mu = 1.9$ (Marrone et al. in submitted).

6.3.2 Radiative Transfer Models

We use the FIR photometry and the line luminosities from Table 6.1 to simultaneously model the dust continuum, CO spectral line energy distribution (SLED), and the [C I](2–1) line following the radiative transfer calculation presented in Weiß et al. (2007). In this model, the background radiation field is set to the cosmic microwave background (CMB) for the dust and to the CMB plus the dust radiation field for the

Table 6.2: ISM parameters of SPT0311-58 from the radiative transfer calculation

Parameter	unit	overall	cold component	warm component
r_0 [a]	pc	$(4000 \pm 1700)\,\mu^{-1/2}$	$(3700 \pm 1300)\,\mu^{-1/2}$	$(1500 \pm 1200)\,\mu^{-1/2}$
$T_{\rm dust}$	K		36 ± 7	115 ± 54
$T_{\rm kin}$	K		58 ± 23	180 ± 51
$\log(n(\mathrm{H_2}))$	$\mathrm{cm^{-3}}$		3.7 ± 0.4	5.1 ± 1.9
$dv_{\rm turb}$	$\mathrm{km\,s^{-1}}$		130 ± 17	100 ± 4
$\kappa_{\rm vir}$ [b]			1.9 ± 1.9	3.1 ± 2.5
GDMR			110 ± 15 [d]	
β			1.91 ± 0.05 [d]	
[C I]/[H_2]			$(6.0 \pm 1.4)\times10^{-5}$	$(1.7 \pm 2.3)\times10^{-5}$
$M_{\rm dust}$	$M_\odot$	$(5.7 \pm 0.8)\times10^{9}\,\mu^{-1}$	$(5.2 \pm 0.7)\times10^{9}\,\mu^{-1}$	$(4.8 \pm 0.7)\times10^{8}\,\mu^{-1}$
$M_{\rm gas}$	$M_\odot$	$(6.3 \pm 3.7)\times10^{11}\,\mu^{-1}$	$(5.7 \pm 3.8)\times10^{11}\,\mu^{-1}$	$(5.3 \pm 3.8)\times10^{10}\,\mu^{-1}$
$\alpha_{\rm CO}$	$M_\odot/\mathrm{K\,km\,s^{-1}\,pc^2}$	4.8 ± 2.9	5.5 ± 4.0	3.1 ± 2.5
$L_{\rm FIR}$	$L_\odot$	$(4.1 \pm 0.7)\times10^{13}\,\mu^{-1}$	$(1.2 \pm 1.1)\times10^{13}\,\mu^{-1}$	$(2.9 \pm 0.7)\times10^{13}\,\mu^{-1}$
SFR [c]	$M_\odot\,\mathrm{yr^{-1}}$	$(4100 \pm 700)\,\mu^{-1}$		
$t_{\rm dep}$	Myr	150 ± 90		

lines. The line and dust continuum emission are further linked via the gas column density in each component that introduces the turbulence line width as a free parameter in the calculation (see Eq. 7 in Weiß et al., 2007). The gas column density calculated from the line emission together with the gas to dust mass ratio (GDMR) then determines the optical depth of the dust.

The calculations treat the dust and the kinetic temperature as independent parameters, but with the prior that the kinetic gas temperature has to be equal to or higher than the dust temperature. Physically, this allows for additional sources of mechanical energy (e.g. shocks) in the ISM in addition to photo-electric heating.

The chemical parameters in our model are the CO and [C I] abundances relative to H_2 and the GDMR. We use a fixed CO abundance of 8×10^{-5} relative to H_2 (Frerking et al., 1982), but keep the [C I] abundance and the GDMR as free parameters. For the frequency dependence of the dust absorption coefficient we adopt $\kappa_{\rm d}(\nu) = 0.04\,(\nu/250\,\mathrm{GHz})^{\beta}$ [$\mathrm{m^2\,kg^{-1}}$] (Kruegel & Siebenmorgen, 1994), which is in good agreement with $\kappa_{870\mu m} = 0.077\,\mathrm{m^2\,kg^{-1}}$ used in other work (see Spilker et al., 2015, and references therein), for our best-fitting β.

Model solutions are calculated employing a Monte-Carlo Bees (Pham & Castellani, 2009) algorithm which randomly samples the parameter space and gives finer sampling for good solutions (as evaluated from a χ^2 analysis for each model). In total, we sample $\sim 10^7$ models. Parameter values and uncertainties were calculated using the probability-weighted mean of all solutions and the standard deviations.

6.3.3 Model results

Figure 6.2 shows the CO SLED, the continuum SED, and [C I] flux density. From the figure, it is apparent that the dust continuum SED cannot be modeled with a single temperature modified black body, so we instead fit two components. Since we have no information on the high-J CO transition, we use the shape of the CO SLED of Arp220 (Rosenberg et al., 2015) and HFLS3 (Riechers et al., 2013) as priors. With this choice, we compare the moderately excited CO SLED of Arp220 (see Rosenberg et al. (2015) for a comparison of Arp220 to other local ULIRGs) to the more extreme case of HFLS3 where the CO SLED stays high up to the $J_{\rm up} = 9$ level (see Figure 6.2). The use of the priors mainly affects the parameters of the warm gas and therefore only has a small effect on our derived gas mass (see below). Table 6.2 lists the parameters obtained from the radiative transfer calculations for the Arp220 prior, not corrected for magnification.

For both priors, the warm dust component dominates the peak of the CO SLED and the short wavelength part of the dust spectrum and therefore the FIR luminosity. Its size is small compared to the cold gas with an area ratio of ~ 6 ($r_0 = 1.7 \pm 1.4$ kpc where r_0 is the equivalent radius defined as $\rm r_0 = D_A \sqrt{\Omega_s/\pi}$ (Weiß et al., 2007)) for HFLS3 and slightly smaller for Arp220) which implies that the region of intense FIR continuum emission is significantly smaller than the overall gas distribution. Due to a lack of observations of CO transitions beyond (7–6), its properties are mainly driven by the assumed shape of the CO SLED for the high-J transitions. But the models for both priors indicated consistently that the warm gas has a substantial density (of order $10^5\,\rm cm^{-3}$), a dust temperature of ~ 100 K and a kinetic temperature in excess (but consistent within the errors) of the dust temperature ($T_{\rm kin} = 180 \pm 50$ K when using Arp220 priors).

The cold dust component is required to fit the CO(3–2) and [C I] line emission, and the long wavelength part of the dust SED. Due to its large extent and relatively high density ($\rm r_0 = 3.7 \pm 1.3$ kpc, $\rm \log(n(H_2) = 3.7 \pm 0.4)$), it carries $\approx 90\%$ of the gas mass. The abundance of neutral carbon in this gas phase is $\rm [C\,I]/[H_2] = 6.0 \pm 1.4 \times 10^{-5}$ in agreement with other estimates at high redshift and in nearby galaxies (e.g. Weiß et al., 2005, and references therein). For both priors, the cold gas dominates the CO(1–0) line luminosity. As for the warm gas, we find that the kinetic temperature is above the dust temperature ($\rm T_{dust} = 36 \pm 7$ K, $T_{\rm kin} = 58 \pm 23$ K), which may suggest that the ISM in SPT0311-58 experiences additional mechanical energy input e.g., via feedback from stellar winds or AGN driven outflows. This is also supported by the large turbulent line width of order 100 $\rm km\,s^{-1}$ and super-virial velocity gradients ($\kappa_{\rm vir} > 1$, see note b in Table 6.2) we find for both components and priors.

We use the kinematic parameters ($\rm dv_{turb}$ and $\kappa_{\rm vir}$) together with the source size and the H_2 density for each component (see Eq. 8 in Weiß et al., 2007) to derive a total apparent gas mass of $\rm M_{gas} = (6.3 \pm 3.7) \times 10^{11} M_\odot$ (including a 36% correction to account for the cosmic He abundance). For the HFLS3 prior, the gas mass is $\sim 30\%$ higher.

6.4 Discussion

6.4.1 Gas mass conversion factor

With the independent gas mass estimate from the radiative transfer models in-hand we can also derive the gas-to-dust mass ratio (GDMR) and the CO-to-H_2 conversion factor ($\alpha_{\rm CO}$) for SPT0311-58. Since the CO(1–0) transition has not been observed, we use the flux density from the radiative transfer model which predicts $I_{\rm CO(1-0)} = 0.10 \pm 0.03$ Jy km/s. In our models, we assume that each gas component has the same GDMR and we find GDMR $= 110 \pm 15$. Due to the different physical conditions in each gas component, there is a specific $\alpha_{\rm CO}$ value for each component. For the cold dust component, we find $\alpha_{\rm CO} = 5.5 \pm 4.0\, M_\odot (\mathrm{K\,km\,s^{-1}\,pc^2})^{-1}$ and for the warm dust component $\alpha_{\rm CO} = 3.1 \pm 2.5\, M_\odot (\mathrm{K\,km\,s^{-1}\,pc^2})^{-1}$. Combining both gas components we find for SPT0311-58 $\alpha_{\rm CO} = 4.8 \pm 2.9\, M_\odot (\mathrm{K\,km\,s^{-1}\,pc^2})^{-1}$.

When calculating gas masses for ULIRGs, a factor of $\alpha_{\rm CO} = 0.8\, M_\odot (\mathrm{K\,km\,s^{-1}\,pc^2})^{-1}$ is typically assumed (Downes & Solomon, 1998), significantly below our estimate. The difference can easily be explained by the much higher densities we find in both components compared to the models from Downes & Solomon (1998) in which most of the CO(1–0) luminosity arise from a diffuse inter-cloud medium. Since the bulk of the gas mass of this source is in the dense component, it is vital to include the higher-J CO transitions in the calculation of $\alpha_{\rm CO}$.

A similar two-component analysis was done for the broad absorption line quasar APM08279+5255 at $z = 3.9$ (Weiß et al., 2007), where the dense component was found to dominate the CO(1–0) line by 70%. They find a high conversion factor of $\alpha_{\rm CO} \sim 6\, M_\odot (\mathrm{K\,km\,s^{-1}\,pc^2})^{-1}$, similar to what we find in the dense gas component. A similar reasoning for higher CO conversion factors owing to the presence of dense gas was put forward by Papadopoulos et al. (2012) based on the CO SLED in local (U)LIRGs.

6.4.2 [C II]

From our [C II] detection, we derive a $L_{\rm [CII]}/L_{\rm FIR}$ ratio of $(7.3 \pm 0.1) \times 10^{-4}$. Figure 6.3 shows that this puts SPT0311-58 into the lower region of the $L_{\rm [CII]}/L_{\rm FIR}$ ratio observed in a larger sample of SPT-DSFGs (Gullberg et al., 2015). Similarly, low $L_{\rm [CII]}/L_{\rm FIR}$ ratios are found for the $z = 6.3$ star-forming galaxy HFLS3 (Riechers et al., 2013) and for the $z = 7.1$ QSO host galaxy J1120+0641(Venemans et al., 2012).

The $L_{\rm [CII]}/L_{\rm CO(1-0)}$ ratio in SPT0311-58 is similar to what is observed in the SPT sample (4300 ± 1300 compared to 5200 ± 1800 Gullberg et al., 2015), and HFLS3 (~ 3000, Riechers et al., 2013). This is consistent with the picture in which the [C II] emission stems from the surface of dense clouds exposed to the strong UV field from the intense starburst in SPT0311-58 (Stacey et al., 2010; Gullberg et al., 2015; Spilker et al., 2016).

The larger [C II] deficit together with the decreasing $L_{\rm [CII]}/L_{\rm CO(1-0)}$ ratio of SPT0311-58 and other high redshift sources compared to local galaxies may be understood as a consequence of an increasing gas surface density (Narayanan & Krumholz,

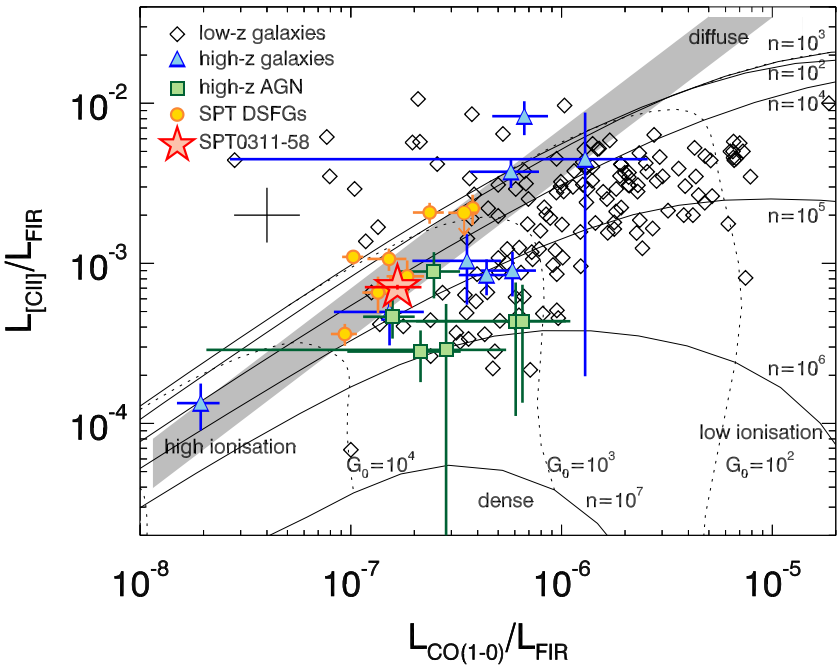

Figure 6.3: $L_{[\mathrm{CII}]}/L_{\mathrm{FIR}}$ vs $L_{[\mathrm{CII}]}/L_{\mathrm{CO(1–0)}}$ with PDR models and samples adapted from Gullberg et al. (2015). The *red* star shows how SPT0311-58 falls within the larger SPT DSFG sample. The typical error bar for the low redshift sample is presented by the *black* cross.

2017): the higher molecular gas surface density pushes the $\mathrm{H_I}$ + $\mathrm{H_2}$ mass budget towards higher $\mathrm{H_2}$ fractions. Since [C II] mainly arises from the PDR zone associated with $\mathrm{H_I}$ and the outer $\mathrm{H_2}$ layer, this effect reduces the size of the [C II] emitting region and therefore the [C II] line intensity. At the same time, the ratio of $L_{[\mathrm{CII}]}/L_{\mathrm{CO(1–0)}}$ will decrease due to an increase in the fraction of carbon locked in CO compared to [C II].

6.4.3 Concluding remarks

Both our radiative transfer model and fine structure line results indicate that SPT0311-58 resembles typical DSFGs, just at $z \sim 7$. This is also supported by its extreme SFR surface density of $\Sigma_{\mathrm{SFR}} \sim 600\,\mathrm{M_\odot yr^{-1}kpc^{-2}}$ (derived using the size of the warm gas component that dominates the FIR luminosity) which approaches the modeled values for radiation pressure limited starbursts ($10^3\,\mathrm{M_\odot yr^{-1}kpc^{-2}}$ Thompson et al., 2005) and is comparable to what is found in other starburst like Arp220, HFLS3 and other SPT-DSFGs (Scoville, 2003; Riechers et al., 2013; Spilker et al., 2016). Future observations of this source will explore its spatial structure, physical conditions, formation history, and chemical evolution in great detail as it is one of very few massive galaxies known at $z \sim 7$.

6.5 Acknowledgments

M.L.S. was supported for this research through a stipend from the International Max Planck Research School (IMPRS) for Astronomy and Astrophysics at the Universities of Bonn and Cologne. M.A. acknowledges partial support from FONDECYT through grant 1140099. J.D.V., D.P.M., K.C.L., J.S.S. and S.J. acknowledge support from the U.S. National Science Foundation under grant No. AST-1312950. B.G. acknowledges support from the ERC Advanced Investigator programme DUSTYGAL 321334. The Flatiron Institute is supported by the Simons Foundation. Partial support for D.N. was provided by NSF AST-1009452, AST-1445357, NASA HST AR-13906.001 from the Space Telescope Science Institute, which is operated by the Association of University for Research in Astronomy, Incorporated, under NASA Contract NAS5-26555, and a Cottrell College Science Award, awarded by the Research Corporation for Science Advancement. ALMA is a partnership of ESO (representing its member states), NSF (USA) and NINS (Japan), together with NRC (Canada) and NSC and ASIAA (Taiwan), in cooperation with the Republic of Chile. The Joint ALMA Observatory is operated by ESO, AUI/NRAO and NAOJ. The National Radio Astronomy Observatory is a facility of the National Science Foundation operated under cooperative agreement by Associated Universities, Inc. *Herschel* is a European Space Agency Cornerstone Mission with significant participation by NASA. APEX is a collaboration between the Max-Planck-Institut für Radioastronomie, the European Southern Observatory, and the Onsala Space Observatory. The Australia Telescope is funded by the Commonwealth of Australia for operation as a National Facility managed by CSIRO. The SPT is supported by the National Science Foundation through grant PLR-1248097, with partial support through PHY-1125897, the Kavli Foundation and the Gordon and Betty Moore Foundation grant GBMF 947.

Chapter 7

Summary and Future outlook

The SPT-DSFGs are selected from the large 2500 degree^2 SPT survey at 1.4 mm and 2.2 mm, and consist of mostly strongly lensed galaxies at high redshifts.

To investigate the high redshift nature of the sources, we create a **spectroscopic** redshift distribution of the SPT-DSFGs by combining spectral scans of 42 SPT-DSFGs with already published redshifts from Weiß et al. (2013), along with redshift confirmation observations for sources with ambiguous redshift. This sample of SPT-DSFGs is the most complete spectroscopic sample of DSFGs in the literature.

The redshift scans are set up to observe a large frequency range in ALMA Band 3 (84.2–114.9 GHz) searching for CO and [C I] lines. In ALMA proposal cycles 1 and 3 a total of 42 sources were targeted. 39 of these sources are detected in continuum, and spectra were extracted. We find: 18 sources showing two or more lines, yielding unambiguous redshifts based on the ALMA spectra alone; 16 sources showing a single line, six of which have been detected in [C II] using APEX/FLASH and two of which has been detected in CO with APEX/SEPIA; and in one source no lines are found, but we determine the redshift from an absorption line detected in our ALMA Cycle 0 870 μm high resolution imaging cube.

For eight sources from Weiß et al. (2013) with ambiguous redshift, ALMA Band 6 observations were performed, to detect mid- to high-J CO lines. The observations confirmed the most probable redshift option for all but one source, demonstrating that finding redshifts from a single line and a well measured dust temperature provides a reliable measurement of the redshift. This may prove useful for similar studies in the future.

Combining these redshifts gives a total sample of 62 sources with a median of $z_{\mathrm{median}} = 4.1 \pm 0.2$. In order to compare to unlensed samples, we lensing-correct this distribution. This is done by taking the probability of gravitational lensing as a function of redshift into account, yielding a median redshift of $z = 3.5 \pm 0.3$, which is still significantly larger than the $z \sim 2.5$ commonly adopted for DSFGs based on 870 μm work. Both redshifts distributions are consistent with model predictions from Béthermin et al. (2015).

We compare these redshift distributions to the literature, and show that selection wavelength has a major influence on the shape of the redshift distribution. The long selection wavelength (1.4 mm) of the SPT DSFGs provides a promising way of studying the $z > 3$ tail of DSFGs, out to the highest redshifts where these systems have formed.

Using **photometric** observations we present the first analysis of the redshift dis-

tribution based on the full SPT-DSFG sample. An exquisite photometric coverage has been acquired for all SPT-DSFGs, with flux densities measured at 2 and 1.4 mm (SPT), 870 μm (APEX/LABOCA), and 500, 350, and 250 μm (*Herschel*/SPIRE). Furthermore, 100 and 160 μm (*Herschel*/PACS) were added for a subsample of 66 sources. This is one of the largest and most uniform photometric databases of DSFGs known to date.

We test different methods of finding photometric redshifts based on mm to IR observations, and find that using a single component SED assuming a dust temperature determined from the SPT-DSFG sample, best reconstructs the spectroscopic redshifts of the sources.

We create a redshift distribution of the entire SPT-DSFG sample by using spectroscopic redshifts of the 62 sources with one or more spectral lines detected and photometric redshifts for the remaining 29 sources. The median redshift of this sample is $z_{\rm phot} = 3.7 \pm 0.1$.

From the SPT-DSFGs with spectroscopic redshifts, we find a median dust temperature of $T_{\rm dust} = 39 \pm 6$ K. The dust temperature appears to rise with redshift in a manner consistent with previous observations in lower redshift samples, and we show that the evolution can be described by the equation $T_{\rm dust} = (26.7 \pm 13.6)(1+z)^{0.26\pm0.33}$.

From the 870 μm flux density we find an intrinsic dust mass of $M_{\rm dust} = (6.4 \pm 5.4) \times 10^8 M_\odot$ for the full sample (corrected for lensing using the average magnification of the sample of $\mu = 5.5$), consistent with what is found for DSFGs in the literature. We translate this into a median intrinsic gas mass of $M_{\rm gas} = (9.5 \pm 8.0) \times 10^{10} M_\odot$.

The median intrinsic FIR luminosity of the sample is $L_{\rm FIR} = (6.4 \pm 5.3) \times 10^{12} L_\odot$, and does not evolve with redshift. From this an intrinsic star formation rate for the SPT-DSFGs is estimated to SFR $= 2000 \pm 1700\, M_\odot\, {\rm yr}^-1$, showing that the DSFGs are among the most extremely star forming galaxies known throughoutÊcosmic time.

Among the sources with spectroscopic redshifts, we found SPT0311−58 at $z = 6.900(2)$, which makes it the **highest-redshift millimeter-selected dusty star-forming galaxy** to date. The spectroscopic redshift was determined through an ALMA 3 mm frequency scan that detected CO(6−5), CO(7−6), and [C I](2−1), and subsequently was confirmed by detections of CO(3−2) with ATCA and [C II] with APEX. We constrain the properties of the ISM in SPT0311−58 with a radiative transfer analysis of the dust continuum photometry and the CO and [C I] line emission. SPT0311−58 is extremely massive, with an intrinsic gas mass of $M_{\rm gas} = 3.3 \pm 1.9 \times 10^{11} M_\odot$. Both our radiative transfer model and observed fine structure line ratios indicated that the ISM properties of SPT0311-58 at $z \sim 7$ already resembles those of typical DSFGs observed at lower redshift. Its large mass and intense star formation is very rare for a source well into the epoch of reionization.

The large sample of spectroscopic redshifts is an important step for **future** detailed studies of the ISM at high redshifts as carried out in the studies by Aravena et al. (2013); Bothwell et al. (2013); Gullberg et al. (2015); Spilker et al. (2015) and the case study of SPT0311-58 (Chapter 6).

In the near future we will continue to work towards our goal of obtaining redshifts for the complete sample of 91 SPT-DSFGs using ALMA. Furthermore, we have systematically observed [C II] for SPT-DSFGs $z > 3$ (i.e. $\sim 75\%$ of our sample), where [C II] falls within an observable band at APEX. [C II] observations, combined with low- and mid-J CO lines (typically obtained using ATCA) provides a great fundament to study the ISM through PDR models and estimate the cooling budget and the ionising radiation field. We have now more than doubled the large sample presented in Gullberg et al. (2015), making it the largest survey of [C II] emission at $z < 3$ available today.

On a slightly longer timescale we can combine the APEX observed [C II] lines with ALMA observed [N II] lines which, through the [N II]/[C II]ratio, will teach us about the metallicity and ionizing radiation field of the SPT-DSFGs along with the UV-radiation field. Similar observations exist for local galaxies, enabling a direct comparison to these. The high spectral resolution from ALMA will give us detailed line profiles from which we can learn about the internal kinematics of the sources.

Future observations of our high-redshift source SPT0311-58 will explore its spatial structure, physical conditions, formation history, and chemical evolution in great detail as it is one of very few massive galaxies known at $z \sim 7$. Through already existing ALMA [C II] and [O III] and future [O I] and [N II] observations we hope to resolve the structure of the source and better diagnose its physical conditions. This will help us learn how such massive galaxies have formed in the EoR and how the intergalactic medium is enriched by the metals formed in these galaxies. There are further nine sources in the SPT-DSFG sample above $z > 5$ for which similar observations would be very interesting.

We have long had the theory that a small subsample of the SPT-DSFGs is not lensed, but instead unlensed Hyper luminous IR galaxies. High resolution ALMA observations show that SPT2349-56 splits up into several components, forming a protocluster at $z = 4.3$, making it the most over-dense active structure known in the distant Universe. Further ALMA observations of this extraordinary source will uncover the full protocluster environment, characterize the protocluster galaxies, and probe stellar masses. We furthermore started a campaign to follow up sources showing clear signs of being unlensed. Initial results of a few of these DSFGs show that they also split up into multiple sources. We now plan to expand this survey to cover all sources showing any signs of being unlensed.

One of our greatest challenges in the study of the SPT-DSFGs is estimating the stellar content of the sources. Stellar masses are poorly constrained for the SPT-DSFGs due to the dominating emission from the foreground lens object. With the resolution of *Spitzer*/IRAC it is exceedingly difficult to decompose the lens and background source (Ma et al., 2015). With the upcoming launch of the James Webb Space Telescope (JWST) this will change as the resolution is significantly better than at current facilities. In this work we have mainly discussed massive DSFGs and only touched upon the more common, less obscured galaxies like Lyman Break Galaxies (LBGs). Both galaxy types are important to the cosmic history of star formation, but they do not have much data in common, which means only few comparisons of the two groups have been made. JWST will be able to obtain a common set of spectral diagnostics for galaxies that span

the full range of dust extinction. With the sensitivity of JWST at mid-IR wavelengths we will be able to unveil dust-enshrouded star formation, and with the IFU we will be able to study large-scale galaxy kinematics and physical conditions. The gravitationally lensed SPT-DSFGs will play a key role in these studies as they will make it possible for JWST to probe scales of $\sim 100\,\mathrm{pc}$ in the distant universe, which will remain impossible for unlensed galaxies at similar redshift. This resolution is comparable to current IR observations of galaxies in the local Universe, making direct comparisons feasible.

There are many captivating, unanswered questions about early star formation and its role in the evolution of the Universe. It is our hope that with the SPT-DSFG sample, we can contribute to broadening our understanding of this fundamental subject.

Bibliography

Aravena, M., Murphy, E. J., Aguirre, J. E., et al. 2013, MNRAS, 433, 498 (Cited on pages 26, 42, 54, 88 and 127.)

Aravena, M., Spilker, J. S., Bethermin, M., et al. 2016, MNRAS, 457, 4406 (Cited on pages 26, 42 and 108.)

Ashby, M. L. N., Dye, S., Huang, J.-S., et al. 2006, ApJ, 644, 778 (Cited on page 3.)

Barger, A. J., Cowie, L. L., Sanders, D. B., et al. 1998, Nature, 394, 248 (Cited on page 2.)

Barger, A. J., Cowie, L. L., Smail, I., et al. 1999, AJ, 117, 2656 (Cited on page 3.)

Baugh, C. M., Lacey, C. G., Frenk, C. S., et al. 2005, MNRAS, 356, 1191 (Cited on page 49.)

Béthermin, M., De Breuck, C., Sargent, M., & Daddi, E. 2015, A&A, 576, L9 (Cited on pages 4, 48, 49, 51, 52, 53, 68, 69, 70 and 87.)

Béthermin, M., Daddi, E., Magdis, G., et al. 2012, ApJ, 757, L23 (Cited on page 49.)

Biggs, A. D., Ivison, R. J., Ibar, E., et al. 2011, MNRAS, 413, 2314 (Cited on page 3.)

Billade, B., Nystrom, O., Meledin, D., et al. 2012, IEEE, 2, 208 (Cited on page 25.)

Blain, A. W. 1996, MNRAS, 283, 1340 (Cited on page 49.)

Blain, A. W., Smail, I., Ivison, R. J., Kneib, J.-P., & Frayer, D. T. 2002, Phys. Rep., 369, 111 (Cited on pages 49 and 51.)

Bothwell, M. S., Smail, I., Chapman, S. C., et al. 2013, MNRAS, 429, 3047 (Cited on pages 25, 34, 54, 71 and 88.)

Bouwens, R. 2016, in Astrophysics and Space Science Library, Vol. 423, Astrophysics and Space Science Library, ed. A. Mesinger, 111 (Cited on page 5.)

Bouwens, R. J., Aravena, M., Decarli, R., et al. 2016, ApJ, 833, 72 (Cited on page 5.)

Bradford, C. M., Aguirre, J. E., Aikin, R., et al. 2009, ApJ, 705, 112 (Cited on page 25.)

Capak, P. L., Riechers, D., Scoville, N. Z., et al. 2011, Nature, 470, 233 (Cited on page 4.)

Carilli, C. L., & Walter, F. 2013, ARA&A, 51, 105 (Cited on page 44.)

Carlstrom, J. E., Ade, P. A. R., Aird, K. A., et al. 2011, PASP, 123, 568 (Cited on pages 7 and 77.)

Casey, C. M., Narayanan, D., & Cooray, A. 2014, Phys. Rep., 541, 45 (Cited on pages 1, 8, 27, 51 and 73.)

Chabrier, G. 2003, ApJ, 586, L133 (Not cited.)

Chapman, S. C., Blain, A. W., Smail, I., & Ivison, R. J. 2005, ApJ, 622, 772 (Cited on pages 3, 4 and 52.)

Chapman, S. C., Bertoldi, F., Smail, I., et al. 2015, MNRAS, 453, 951 (Cited on page 4.)

Chary, R., & Elbaz, D. 2001, ApJ, 556, 562 (Cited on page 16.)

da Cunha, E., Groves, B., Walter, F., et al. 2013, ApJ, 766, 13 (Cited on page 49.)

da Cunha, E., Walter, F., Smail, I. R., et al. 2015, ApJ, 806, 110 (Cited on pages 4 and 71.)

Dale, D. A., & Helou, G. 2002, ApJ, 576, 159 (Cited on page 16.)

Dannerbauer, H., Lehnert, M. D., Lutz, D., et al. 2002, ApJ, 573, 473 (Cited on page 3.)

Downes, D., & Solomon, P. M. 1998, ApJ, 507, 615 (Cited on page 83.)

Draine, B. T., & Li, A. 2007, ApJ, 657, 810 (Cited on page 16.)

Engel, H., Tacconi, L. J., Davies, R. I., et al. 2010, ApJ, 724, 233 (Cited on page 50.)

Fathi, K., Gatchell, M., Hatziminaoglou, E., & Epinat, B. 2012, MNRAS, 423, L112 (Cited on page 50.)

Ferrara, A. 2010, in American Institute of Physics Conference Series, Vol. 1294, American Institute of Physics Conference Series, ed. D. J. Whalen, V. Bromm, & N. Yoshida, 148–157 (Cited on page 5.)

Frerking, M. A., Langer, W. D., & Wilson, R. W. 1982, ApJ, 262, 590 (Cited on page 81.)

González, J. E., Lacey, C. G., Baugh, C. M., & Frenk, C. S. 2011, MNRAS, 413, 749 (Cited on page 3.)

Greve, T. R., Papadopoulos, P. P., Gao, Y., & Radford, S. J. E. 2009, ApJ, 692, 1432 (Not cited.)

Greve, T. R., Vieira, J. D., Weiß, A., et al. 2012, ApJ, 756, 101 (Cited on pages 8, 27, 34, 50, 56, 70, 79 and 127.)

Gullberg, B., De Breuck, C., Vieira, J. D., et al. 2015, MNRAS, 449, 2883 (Cited on pages 21, 25, 36, 42, 54, 71, 79, 83, 84, 88, 89, 101, 102, 103 and 104.)

Harris, A. I., Baker, A. J., Frayer, D. T., et al. 2012, ApJ, 752, 152 (Cited on page 4.)

Hayward, C. C., Narayanan, D., Kereš, D., et al. 2013, MNRAS, 428, 2529 (Cited on page 49.)

Hezaveh, Y. D., & Holder, G. P. 2011, ApJ, 734, 52 (Cited on pages 49, 50 and 51.)

Hezaveh, Y. D., Marrone, D. P., Fassnacht, C. D., et al. 2013, ApJ, 767, 132 (Cited on pages 8, 9, 49 and 51.)

Hodge, J. A., Carilli, C. L., Walter, F., Daddi, E., & Riechers, D. 2013, ApJ, 776, 22 (Cited on pages 4 and 52.)

Hopkins, A. M., & Beacom, J. F. 2006, ApJ, 651, 142 (Cited on page 3.)

Hughes, D. H., Serjeant, S., Dunlop, J., et al. 1998, Nature, 394, 241 (Cited on page 2.)

Ikarashi, S., Ivison, R. J., Caputi, K. I., et al. 2015, ApJ, 810, 133 (Cited on page 50.)

Ilbert, O., McCracken, H. J., Le Fèvre, O., et al. 2013, A&A, 556, A55 (Cited on page 68.)

Ivison, R. J., Greve, T. R., Smail, I., et al. 2002, MNRAS, 337, 1 (Cited on page 3.)

Ivison, R. J., Lewis, A. J. R., Weiss, A., et al. 2016, ApJ, 832, 78 (Cited on pages 62, 63 and 74.)

Karim, A., Swinbank, A. M., Hodge, J. A., et al. 2013, MNRAS, 432, 2 (Cited on page 52.)

Kennicutt, Jr., R. C. 1998, ApJ, 498, 541 (Cited on page 13.)

Klein, T., Ciechanowicz, M., Leinz, C., et al. 2014, IEEE, 4, 588 (Cited on page 25.)

Koprowski, M. P., Dunlop, J. S., Michałowski, M. J., Cirasuolo, M., & Bowler, R. A. A. 2014, MNRAS, 444, 117 (Cited on page 4.)

Kruegel, E., & Siebenmorgen, R. 1994, A&A, 288, 929 (Cited on page 81.)

Lacey, C. G., Baugh, C. M., Frenk, C. S., et al. 2010, MNRAS, 405, 2 (Cited on page 49.)

Lagache, G., Dole, H., & Puget, J.-L. 2003, MNRAS, 338, 555 (Cited on page 16.)

Lupu, R. E., Scott, K. S., Aguirre, J. E., et al. 2012, ApJ, 757, 135 (Cited on page 4.)

Ma, J., Gonzalez, A. H., Spilker, J. S., et al. 2015, ApJ, 812, 88 (Cited on pages 11, 34 and 89.)

Madau, P., & Dickinson, M. 2014, ARA&A, 52, 415 (Cited on page 3.)

Madau, P., Ferguson, H. C., Dickinson, M. E., et al. 1996, MNRAS, 283, 1388 (Cited on page 1.)

Magnelli, B., Lutz, D., Saintonge, A., et al. 2014, A&A, 561, A86 (Cited on pages 68, 69 and 70.)

Mattsson, L. 2015, ArXiv e-prints (Cited on page 5.)

McMullin, J. P., Waters, B., Schiebel, D., Young, W., & Golap, K. 2007, in Astronomical Society of the Pacific Conference Series, Vol. 376, Astronomical Data Analysis Software and Systems XVI, ed. R. A. Shaw, F. Hill, & D. J. Bell, 127 (Cited on pages 22, 27 and 78.)

Miettinen, O., Smolčić, V., Novak, M., et al. 2015, A&A, 577, A29 (Cited on pages 4, 48 and 52.)

Mocanu, L. M., Crawford, T. M., Vieira, J. D., et al. 2013, ApJ, 779, 61 (Cited on pages 7, 27 and 79.)

Modigliani, A., Goldoni, P., Royer, F., et al. 2010, in Society of Photo-Optical Instrumentation Engineers (SPIE) Conference Series, Vol. 7737, Society of Photo-Optical Instrumentation Engineers (SPIE) Conference Series, 28 (Cited on page 26.)

Narayanan, D., & Krumholz, M. R. 2017, MNRAS, 467, 50 (Cited on page 83.)

Naylor, B. J., Ade, P. A. R., Bock, J. J., et al. 2003, in Society of Photo-Optical Instrumentation Engineers (SPIE) Conference Series, Vol. 4855, Society of Photo-Optical Instrumentation Engineers (SPIE) Conference Series, ed. T. G. Phillips & J. Zmuidzinas, 239–248 (Cited on page 25.)

Negrello, M., Perrotta, F., González-Nuevo, J., et al. 2007, MNRAS, 377, 1557 (Cited on page 49.)

Ouchi, M., Shimasaku, K., Furusawa, H., et al. 2010, ApJ, 723, 869 (Cited on page 5.)

Papadopoulos, P. P., van der Werf, P. P., Xilouris, E. M., et al. 2012, MNRAS, 426, 2601 (Cited on page 83.)

Petry, D., & CASA Development Team. 2012, in Astronomical Society of the Pacific Conference Series, Vol. 461, Astronomical Data Analysis Software and Systems XXI, ed. P. Ballester, D. Egret, & N. P. F. Lorente, 849 (Cited on pages 22 and 27.)

Pham, D. T., & Castellani, M. 2009, Proceedings of the Institution of Mechanical Engineers, Part C: Journal of Mechanical Engineering Science, 223, 12 (Cited on page 81.)

Planck Collaboration, Ade, P. A. R., Aghanim, N., et al. 2014, A&A, 571, A1 (Cited on pages 35 and 55.)

Pope, A., Scott, D., Dickinson, M., et al. 2006, MNRAS, 370, 1185 (Cited on page 3.)

Rangwala, N., Maloney, P. R., Glenn, J., et al. 2011, ApJ, 743, 94 (Cited on page 46.)

Riechers, D. A., Capak, P. L., Carilli, C. L., et al. 2010, ApJ, 720, L131 (Cited on page 4.)

Riechers, D. A., Bradford, C. M., Clements, D. L., et al. 2013, Nature, 496, 329 (Cited on pages 5, 13, 77, 82, 83 and 84.)

Rosenberg, M. J. F., van der Werf, P. P., Aalto, S., et al. 2015, ApJ, 801, 72 (Cited on page 82.)

Rujopakarn, W., Rieke, G. H., Eisenstein, D. J., & Juneau, S. 2011, ApJ, 726, 93 (Cited on page 50.)

Ryden, B. S. 2003, Introduction to cosmology, Astronomy and Astrophysics library (Addison Wesley) (Cited on page 1.)

Scoville, N. 2003, Journal of Korean Astronomical Society, 36, 167 (Cited on page 84.)

Siebenmorgen, R., & Krügel, E. 2007, A&A, 461, 445 (Cited on page 16.)

Siebenmorgen, R., Voshchinnikov, N. V., & Bagnulo, S. 2014, A&A, 561, A82 (Cited on page 16.)

Silva, L., Granato, G. L., Bressan, A., & Danese, L. 1998, ApJ, 509, 103 (Cited on pages 2 and 73.)

Simpson, J. M., Swinbank, A. M., Smail, I., et al. 2014, ApJ, 788, 125 (Cited on pages 4, 48 and 52.)

Simpson, J. M., Smail, I., Swinbank, A. M., et al. 2015, ApJ, 799, 81 (Cited on page 50.)

Siringo, G., Kreysa, E., Kovács, A., et al. 2009, A&A, 497, 945 (Cited on page 27.)

Smail, I., Ivison, R. J., & Blain, A. W. 1997, ApJ, 490, L5+ (Cited on page 2.)

Smolčić, V., Aravena, M., Navarrete, F., et al. 2012, A&A, 548, A4 (Cited on pages 4 and 52.)

Smolčić, V., Karim, A., Miettinen, O., et al. 2015, A&A, 576, A127 (Cited on page 50.)

Solomon, P. M., Downes, D., Radford, S. J. E., & Barrett, J. W. 1997, ApJ, 478, 144 (Cited on page 37.)

Spilker, J. S., Marrone, D. P., Aguirre, J. E., et al. 2014, ApJ, 785, 149 (Cited on pages 26, 37, 39, 42, 43, 44, 49 and 101.)

Spilker, J. S., Aravena, M., Marrone, D. P., et al. 2015, ApJ, 811, 124 (Cited on pages 42, 54, 81 and 88.)

Spilker, J. S., Marrone, D. P., Aravena, M., et al. 2016, ApJ, 826, 112 (Cited on pages 34, 39, 51, 71, 83 and 84.)

Stacey, G. J., Hailey-Dunsheath, S., Ferkinhoff, C. an d Nikola, T., et al. 2010, ApJ, 724, 957 (Cited on page 83.)

Staguhn, J. G., Kovács, A., Arendt, R. G., et al. 2014, ApJ, 790, 77 (Cited on page 49.)

Stahler, S. W., & Palla, F. 2004, The Formation of Stars (Wiley VCH) (Cited on page 1.)

Stark, D. P. 2016, ARA&A, 54, 761 (Cited on page 5.)

Strandet, M. L., Weiss, A., Vieira, J. D., et al. 2016, ApJ, 822, 80 (Cited on pages 34, 47, 49, 50, 51, 61, 63, 77 and 79.)

Strandet, M. L., Weiss, A., De Breuck, C., et al. 2017, ApJ, 842, L15 (Cited on pages 5, 34, 42, 47 and 77.)

Su, T., Marriage, T. A., Asboth, V., et al. 2017, MNRAS, 464, 968 (Cited on pages 61, 62 and 74.)

Tacconi, L. J., Genzel, R., Smail, I., et al. 2008, ApJ, 680, 246 (Cited on page 50.)

Thompson, T. A., Quataert, E., & Murray, N. 2005, ApJ, 630, 167 (Cited on page 84.)

van der Werf, P. P., Isaak, K. G., Meijerink, R., et al. 2010, A&A, 518, L42 (Cited on page 14.)

Venemans, B. P., McMahon, R. G., Walter, F., et al. 2012, ApJ, 751, L25 (Cited on pages 5 and 83.)

Vernet, J., Dekker, H., D'Odorico, S., et al. 2011, A&A, 536, A105 (Cited on page 26.)

Vieira, J. D., Crawford, T. M., Switzer, E. R., et al. 2010, ApJ, 719, 763 (Cited on pages 7 and 8.)

Vieira, J. D., Marrone, D. P., Chapman, S. C., et al. 2013, Nature, 495, 344 (Cited on pages 9, 49, 77 and 111.)

Walter, F., Decarli, R., Carilli, C., et al. 2012, Nature, 486, 233 (Cited on page 4.)

Wambsganss, J. 1998, Living Reviews in Relativity, 1, 12 (Cited on page 7.)

Wardlow, J. L., Smail, I., Coppin, K. E. K., et al. 2011, MNRAS, 415, 1479 (Cited on page 3.)

Weiß, A., Downes, D., Henkel, C., & Walter, F. 2005, A&A, 429, L25 (Cited on page 82.)

Weiß, A., Downes, D., Neri, R., et al. 2007, A&A, 467, 955 (Cited on pages 80, 81, 82 and 83.)

Weiß, A., Kovács, A., Güsten, R., et al. 2008, A&A, 490, 77 (Cited on page 71.)

Weiß, A., Kovács, A., Coppin, K., et al. 2009, ApJ, 707, 1201 (Cited on page 4.)

Weiß, A., De Breuck, C., Marrone, D. P., et al. 2013, ApJ, 767, 88 (Cited on pages 4, 8, 9, 19, 21, 22, 23, 24, 34, 36, 37, 42, 43, 44, 45, 47, 48, 49, 50, 51, 53, 77, 87, 101, 102, 103 and 104.)

Younger, J. D., Fazio, G. G., Huang, J.-S., et al. 2007, ApJ, 671, 1531 (Cited on page 3.)

Zavala, J. A., Aretxaga, I., & Hughes, D. H. 2014, MNRAS, 443, 2384 (Cited on page 51.)

Appendices

Appendix A

Supplementary redshift information on sources from Weiß et al. 2013

We show here the supplementary observations that resolve redshift ambiguities in the ALMA observations from Weiß et al. (2013) and go through the lines found in the ALMA 1 mm observations.

SPT0125-50: The most likely redshift option from Weiß et al. (2013) was confirmed by an H_2O absorption line from our ALMA 870 μm high resolution imaging cube for this source, presented by Spilker et al. (2014), along with a CO(10–9) detection at 232.35 GHz and H_2O emission lines from the ALMA 1 mm data. These detections identify the original ALMA lines as CO(4–3) and [C I] at redshift $z = 3.959(3)$. We only clearly see one H_2O line, as one line blends with the CO line and one is at the edge of the spectrum.

SPT0300-46: In Weiß et al. (2013), one line was detected and one tentative line feature was seen. The most likely line identification was found to be CO(4–3) and [C I] with a redshift of $z = 3.5954(7)$. This was confirmed by observations of [C II] with APEX, presented in Gullberg et al. (2015), along with the CO(10–9) line at 250.71 GHz and the $H_2O^+(1_{11} - 1_{00},\ J_{3=1/2-1/2})$ absorption line at 247.97 GHz in the ALMA 1 mm spectrum.

SPT0319-47: Weiß et al. (2013) present this source as having no lines though the ALMA 3 mm spectrum shows a wide (FWHM $\sim 1700\,\mathrm{km\,s^{-1}}$) tentative line at 104.39 GHz, with the most probable identification being CO(5–4) at $z = 4.516(4)$. The redshift was confirmed by the CO(12–11) line at 250.77 GHz in the 1 mm ALMA spectrum. In this source we have also detected [C II] with APEX/FLASH, see Figure A.1.

SPT0441-46: The redshift of this source was confirmed with APEX/FLASH [C II] observations before the publication of Weiß et al. (2013), but it was not confirmed by the submission of the targeted 1 mm redshift confirmation proposal. This source had two likely redshift options and it was therefore observed in two tunings. In the 1 mm data we see a double peaked CO(11–10) line at 231.19 GHz, a double peaked $H_2O(2_{20} - 2_{11})$ line at 224.33 GHz, and NH_3, in the form of $NH_3(2_0 - 1_0)$ at $z = 4.4771(6)$.

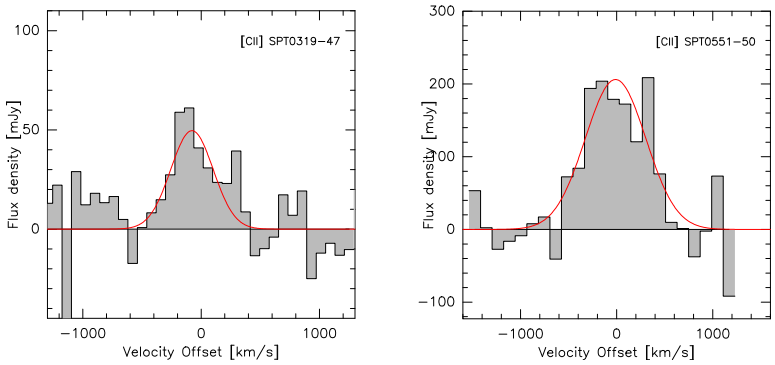

Figure A.1: APEX/FLASH observations of [C II]. The observations are described in Section **??**. *Left*: SPT0319-47, for which [C II] cements the redshift. *Right*: SPT0551-50, where the redshift was wrongly determined using optical spectroscopy but for which this [C II] line now robustly determines the redshift.

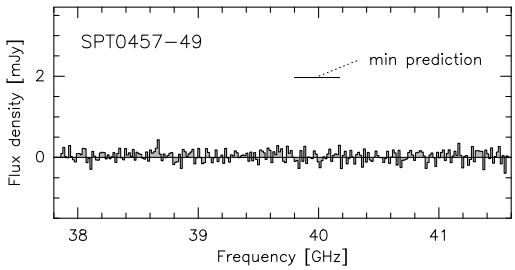

Figure A.2: An ATCA spectrum of SPT0457-49 looking for CO(1–0) at $1.77 < z < 2.0$ in the redshift desert of the 3 mm ALMA spectral scans.

SPT0457-49: Weiß et al. (2013) did not find any lines in this source and assumed it was in the redshift desert. With ATCA we have scanned the redshift range $1.77 < z < 2.05$ searching for CO(1–0) without success (see Figure A.2). We are no closer to determining the spectroscopic redshift of this source, though it is clear that its redshift cannot be assumed to lie in the redshift desert as suggested by Weiß et al. (2013) and with $z_{\rm phot} = 3.4 \pm 0.6$ it probably does not. It is a possibility that this source splits up into multiple sources at the resolution of the ALMA 3 mm map, and that the map is not deep enough to detect these components.

SPT0459-58: Weiß et al. (2013) present a single line with two almost equally likely redshift options for this source. The highest redshift option at $z = 4.856(4)$ with the line identification CO(5–4) was confirmed by the CO(11–10) line at 216.36 GHz in the 1 mm ALMA spectrum.

SPT0512-59: One line with two possible identifications is presented by Weiß et al. (2013). The most likely of these, CO(3–2) at $z = 2.2331(2)$, was confirmed by the detection of [C II] with SPIRE FTS, presented by Gullberg et al. (2015). This

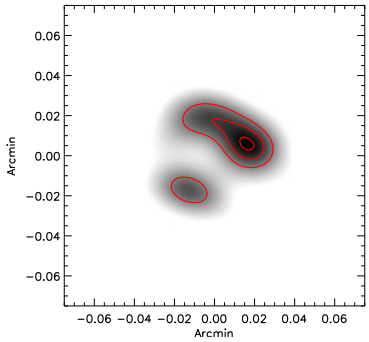

Figure A.3: The ALMA 1 mm continuum imaging of SPT0512-59. The *red* contours show 5,7 and 9 σ and indicate where the brightest component is found.

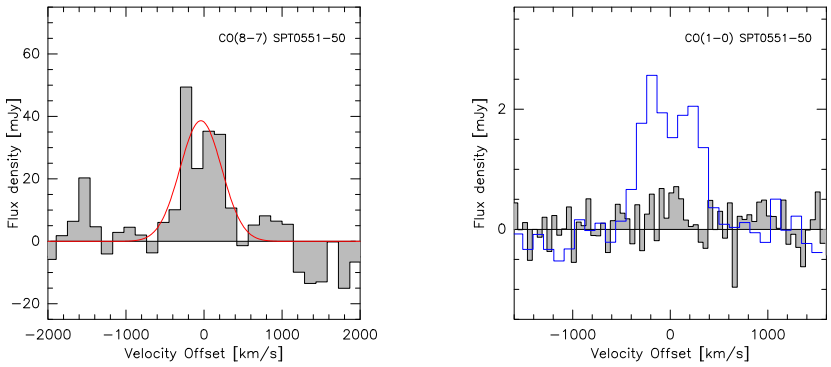

Figure A.4: The lines helping in the redshift identification of SPT0551-50. *Left*: APEX/SHeFI observation of the CO(8–7) line (See Gullberg et al. in prep.). *Right*: ATCA CO(1–0) non detection. The *blue* line shows the line from the ALMA 3 mm spectrum scaled to the expected CO(1–0) flux density.

source was also observed with ALMA at 1 mm where we detected the CO(6–5) line at 213.89 GHz and at this high resolution the source is resolved, see Figure A.3. It shows the typical structure of strong lensing with and arc towards the north-west and an unresolved counter image towards the south-east. The *red* contours mark 5,7 and 9 σ. We extracted the spectrum where we found the highest SNR.

SPT0550-53: A single line with two possible identifications was presented for this source in Weiß et al. (2013), where the most likely line identification, CO(4–3) at $z = 3.1280(7)$ was confirmed by a [C II] detection from APEX (see Gullberg et al., 2015), along with a double peaked CO(8–7) line at 223.31 GHz and a double peaked $H_2O(2_{02} - 1_{11})$ line at 239.36 GHz in the 1 mm ALMA spectrum.

SPT0551-50: This source was presented by Weiß et al. (2013) as a having a secure redshift of $z = 2.1232(2)$. This was based on a combination of a line in the ALMA 3 mm spectrum identified as CO(3–2) and a VLT CIV line. The source has

since been followed up on with several facilities: Gullberg et al. (2015) present a [C II] non-detection observed with *Herschel*/SPIRE FTS and CO(1–0) observations with ATCA also showed a non-detection (see the right panel of Figure A.4). APEX/SHeFi observations of the CO(6–5) yielded a detection though (see left panel of Figure A.4), these data will be presented by Gullberg et al. in prep. We investigated the possibility of the VLT line belonging to a foreground system and left it out of the redshift predictions following here. This opens up the option for the ALMA 3 mm CO line to be identified as CO(4–3) and the APEX/SHeFi CO line to be CO(8–7) at $z = 3.1638(3)$. The shift in frequency would be so small between the previous CO(6–5) identification and the new CO(8–7) identification that we would not be able to detect the difference with the spectral resolution of APEX/SHeFI. The photometry strongly favors the redshift $z = 3.1638(3)$ for which we find the dust temperature $T_{\rm dust} = 37 \pm 1$ K whereas the lower redshift option yields a dust temperature of $T_{\rm dust} = 27 \pm 1$ K. The photometric redshift for this source is $z_{\rm phot} = 3.1 \pm 0.6$. This redshift option was confirmed by the detection of [C II] with APEX/FLASH, see Figure A.1.

SPT2132-58: The redshift for this source was already confirmed by the time of publication of Weiß et al. (2013) through [C II] observations with APEX but it had already been included in the ALMA 1 mm follow up project, where we then detected CO(12–11) at 239.59 GHz and [N II] at 253.32 GHz.

Appendix B

Supplementary information for new sources observed at 3 mm

In this Appendix we go over each of the new sources observed at 3 mm and discuss their redshifts. We also show the [C II] spectra obtained with APEX/FLASH and present an APEX/Z-Spec spectrum that was used to find the redshift of SPT0551-48 for which we do not have ALMA observations.

SPT0002-52: We detect a single line at 103.19 GHz, which turned out to be CO(3–2) at $z = 2.3510(2)$ ($T_{\rm dust} = 42 \pm 2$ K). This was confirmed with APEX/SEPIA where we detected the CO(5–4) line at 171.97 GHz, see Figure B.2.

SPT0020-51: We detect CO(4–3) at 89.98 GHz, [C I](1–0), at 96.09 GHz and CO(5–4) at 112.50 GHz which puts this source at $z = 4.1228(8)$.

SPT0027-50: We detect CO(4–3) at 103.75 GHz and [C I](1–0) at 110.76 GHz which puts this source at $z = 3.4436(1)$.

SPT0106-64: We detect CO(5–4) at 97.51 GHz which together with the APEX/FLASH [C II] detection at 97.51 GHz puts this source at $z = 4.910(4)$.

SPT0109-47: We detect CO(4–3) at 99.92 GHz and [C I](1–0) at 106.67 GHz which puts this source at $z = 3.6137(5)$.

SPT0136-63: We detect CO(4–3) at 87.01 GHz, [C I](1–0) at 92.87 GHz and CO(5–4) at 108.76 GHz which puts this source at $z = 4.299(1)$.

SPT0147-64: We detect a single line at 99.29 GHz. Which gives the possible line identifications CO(2–1) at $z = 1.3218(1)$, CO(3–2) at $z = 2.4825(2)$, CO(4–3) at $z = 3.6432(3)$, and CO(5–4) at $z = 4.8036(3)$. The most probable of these is $z = 4.8036(3)$ with a dust temperature of $T_{\rm dust} = 38.3 \pm 1.4$ K.

SPT0150-59: We detect a single line at 91.28 GHz. Which gives the possible line identifications CO(2–1) at $z = 1.5255(2)$, CO(3–2) at $z = 2.7881(3)$, CO(4–3) at $z = 4.0506(3)$, and CO(5–4) at $z = 5.3129(4)$. The most probable of these is $z = 2.7881(3)$ with a dust temperature of $T_{\rm dust} = 34.8 \pm 1.2$ K.

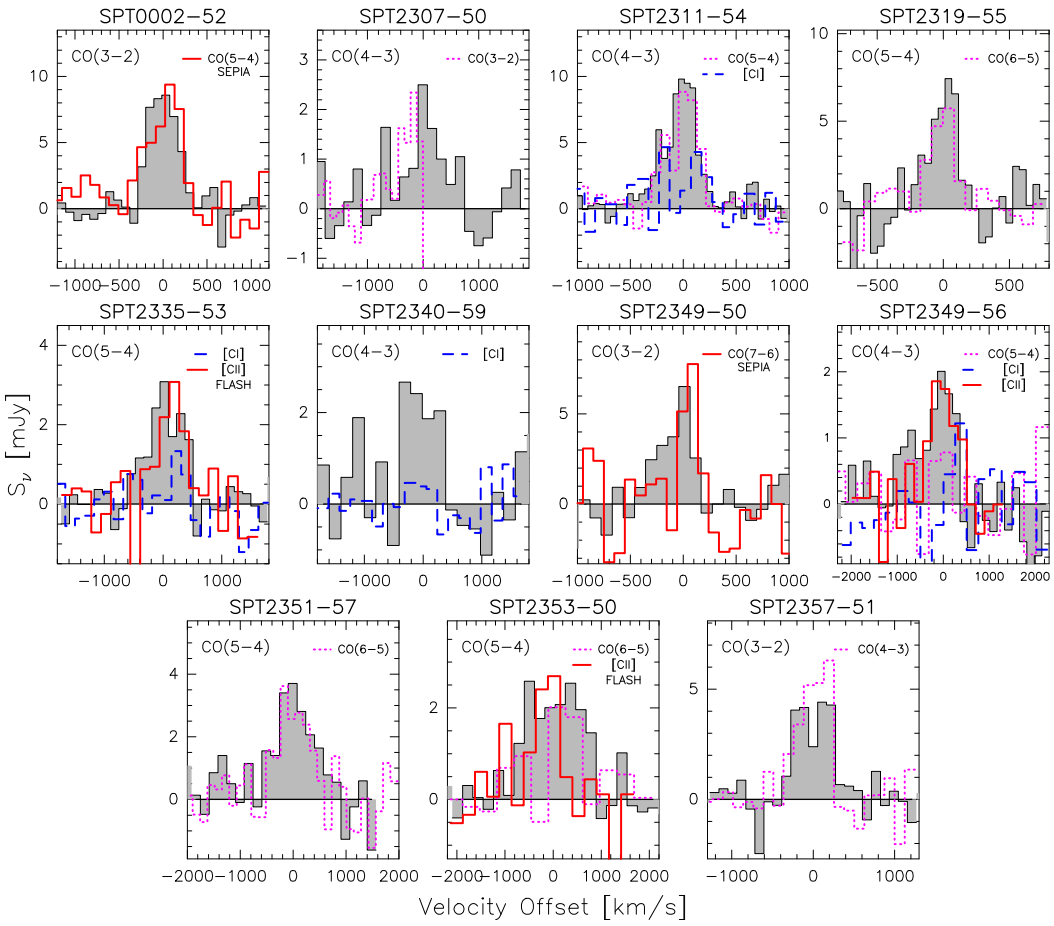

Figure B.1: Line overlays of sources showing one or more line in the Cycle 1 ALMA 3 mm spectra. In the top left corner of each plot the line shown with a *gray* histogram is given. Other CO lines are overlaid in *pink*, [C I] lines are overlaid in *blue* and lines obtained with APEX are overlaid in *red* and the instrument is given with the line name. All ALMA lines are shown at their true flux density, but the lines observed with APEX/SEPIA and APEX/FLASH have been scaled so they could be shown in the same plot. Note that both the velocity axis and the flux density axis varies over the sources as they have been adjusted to better show the lines. For SPT2307-50, the CO(3–2) line is at the edge of the spectrum, which is why it stops mid-line. Four sources (SPT2307-50, SPT2340-59, SPT2349-50, SPT2349-56) still have ambiguous redshifts and are here shown at their most probable redshift. For details on the sources, see the source description in this Appendix.

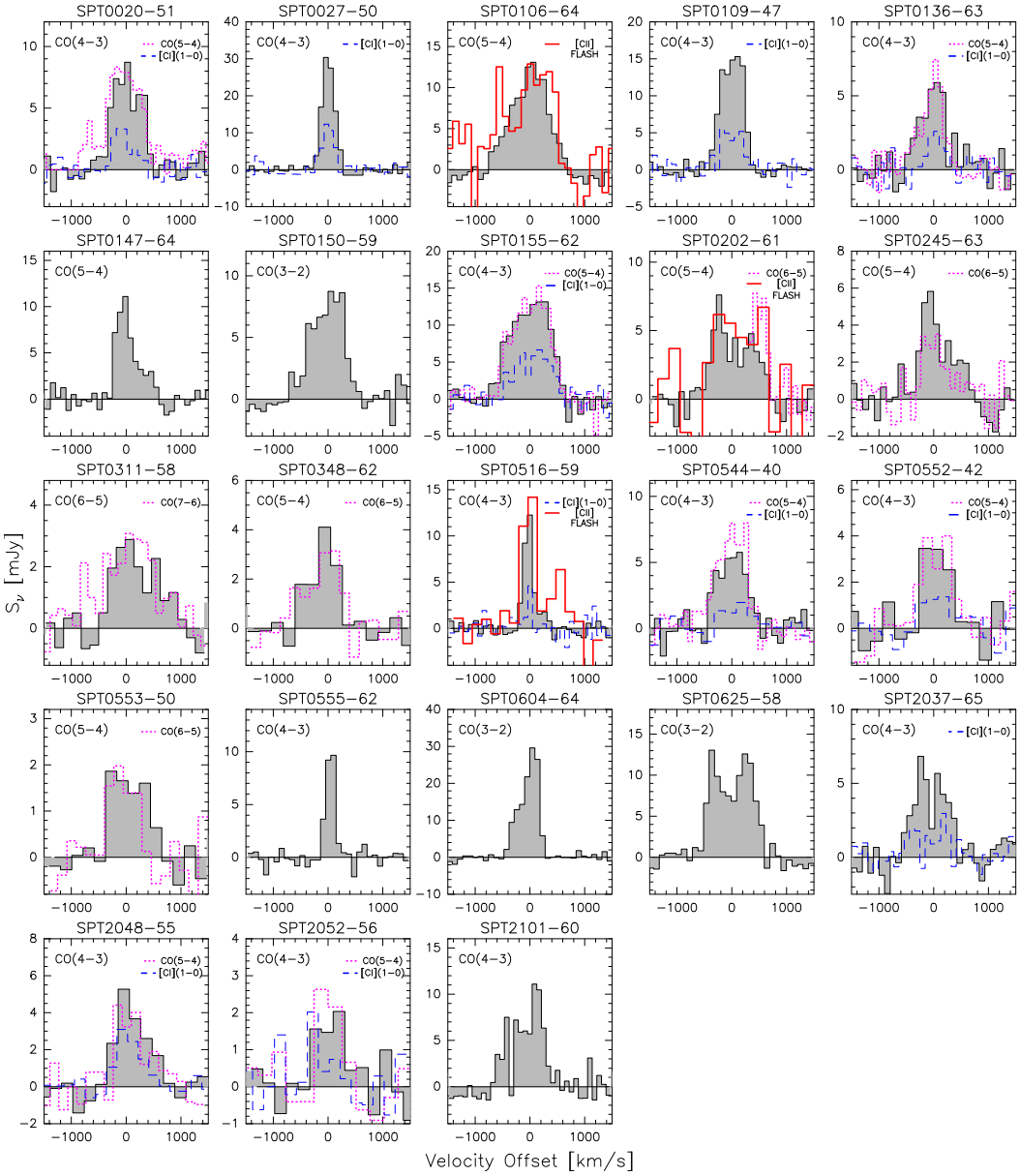

Figure B.2: Line overlays of sources showing one or more line in the Cycle 3 ALMA 3 mm spectra. In the top left corner of each plot the line shown with a *gray* histogram is given. Other CO lines are overlaid in *pink*, [C I] lines are overlaid in *blue* and lines obtained with APEX are overlaid in *red* and the instrument is given with the line name. All ALMA lines are shown at their true flux density, but the lines observed with APEX/SEPIA and APEX/FLASH have been scaled so they could be shown in the same plot. Note that both the velocity axis and the flux density axis varies over the sources as they have been adjusted to better show the lines. For SPT0202-61, the CO(6–5) line is at the edge of the spectrum, which is why it stops mid-line. Six sources (SPT0147-64, SPT0150-59, SPT0555-62, SPT0604-64, SPT0625-58, SPT2101-60) still have ambiguous redshifts and are here shown at their most probable redshift. For details on the sources, see the source description in this Appendix.

SPT0155-62: We detect CO(4–3) at 86.19 GHz, [C I](1–0) at 92.00 GHz and CO(5–4) at 107.72 GHz which puts this source at $z = 4.349(1)$.

SPT0202-61: We detect CO(5–4) at 95.76 GHz which together with the APEX/FLASH detection of [C II] puts this source at $z = 5.018(1)$.

SPT0245-63: We detect CO(5–4) at 86.97 GHz and CO(6–5) at 104.35 GHz which puts the source at $z = 5.626$.

SPT0311-58: We detect CO(6–5) at 87.51 GHz, CO(7–6) at 102.06 GHz and [C I](2–1) at 102.53 GHz which puts this source at $z = 6.900(1)$.

SPT0348-62: We detect CO(5–4) at 86.60 GHz and CO(6–5) at 103.89 GHz which puts this source at $z = 5.656(4)$.

SPT0516-59: We detect CO(4–3) at 87.50 GHz and together with the APEX/FLASH [C II] detection at 431.50 GHz puts this source at $z = 3.4045(7)$.

SPT0544-40: We detect CO(4–3) at 87.50 GHz and CO(5–4) at 105.99 GHz which puts the source at $z = 4.2692(9)$.

SPT0551-48: This source was not in the ALMA redshift search. Instead a redshift search was performed with APEX/Z-Spec, see Figure B.3 for the spectrum and Section 3.1.5 for a description of the data. In the spectrum we find at least four lines, CO(7–6), CO(8–7), [C I](2–1) and H_2O. Furthermore the CO(1–0) line was detected for this source using ATCA and improving the precision on the redshift, finding $z = 2.5833(2)$ (Aravena et al. (2016).).

SPT0552-42: We detect CO(4–3) at 84.80 GHz and CO(5–4) at 105.99 GHz which puts the source at $z = 4.4367(9)$.

SPT0553-50: We detect CO(5–4) at 91.12 GHz and CO(6–5) at 109.38 GHz which puts the source at $z = 5.323(1)$.

SPT0555-62: We detect a single line at 99.10 GHz and two line indications at 84.65 GHz and 105.82 GHz. This fits with two redshift identifications: CO(4–3) and [C I](1–0) at $z = 3.6516(9)$ and CO(5–4) and [C I](1–0) at $z = 4.815(1)$. The most probable of these is $z = 3.6516(9)$ with a dust temperature of $T_{\rm dust} = 35.1 \pm 1.4$ K.

SPT0604-64: We detect a single line at 99.35 GHz. Which gives the possible line identifications CO(2–1) at $z = 1.32054(4)$, CO(3–2) at $z = 2.48071(6)$, CO(4–3) at $z = 3.64074(8)$, and CO(5–4) at $z = 4.80060(9)$. The most probable of these is $z = 2.48071(6)$ with a dust temperature of $T_{\rm dust} = 36.9 \pm 1.2$ K.

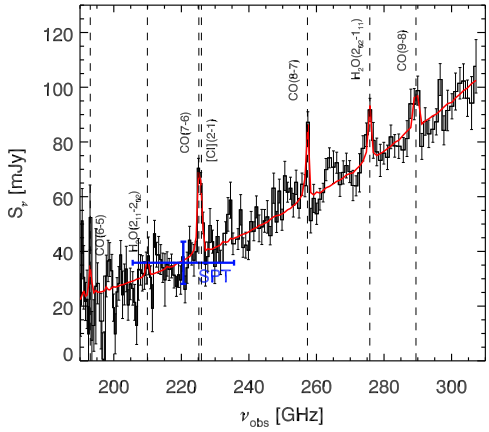

Figure B.3: APEX/Z-Spec spectrum of SPT 0551-48. Four lines, CO(7–6), CO(8–7), [C I](2–1) and $H_2O(2_{01} - 1_{11})$, secure the redshift to $z = 2.579$.

SPT0625-58: We detect a single line at 92.78 GHz. Which gives the possible line identifications CO(2–1) at $z = 1.4848(1)$, CO(3–2) at $z = 2.7270(2)$, CO(4–3) at $z = 3.9692(3)$, and CO(5–4) at $z = 5.2111(4)$. The most probable of these is $z = 2.7270(2)$ with a dust temperature of $T_{\rm dust} = 34.6 \pm 1.2$ K.

SPT2037-65: We detect CO(4–3) at 92.22 GHz and [C I](1–0) at 98.44 GHz which puts the source at $z = 4.000(5)$.

SPT2048-55: We detect CO(4–3) at 90.57 GHz, [C I](1–0) at 96.70 GHz and CO(5–4) at 113.24 GHz which puts the source at $z = 4.089(1)$.

SPT2052-56: This source splits into two components, that we have named A and B, see Figure B.4. Cycle 4 ALMA band 3 high resolution imaging shows that this sources splits into at least 7 sources forming a protocluster. We extract spectra from both components. Only component A shows lines and the redshift identification is here srtaight forward with: CO(4–3) at 87.66 GHz, [C I](1–0) at 93.60 GHz and CO(5–4) at 109.58 GHz which puts this source at $z = 4.259(2)$.

SPT2101-60: We detect a single line at 110.93 GHz. Which gives the possible line identifications CO(2–1) at $z = 1.0781(1)$, CO(3–2) at $z = 2.1171(2)$, CO(4–3) at $z = 3.1559(3)$, and CO(5–4) at $z = 4.1947(3)$. The most probable of these is $z = 3.1559(3)$ with a dust temperature of $T_{\rm dust} = 40.7 \pm 1.4$ K.

SPT2307-50: In this source we find a weak line at 112.30 GHz. We exclude the line identification CO(5–4) at $z = 4.132(4)$, as we would see CO(4–3) in the observing window. If the line is CO(4–3) at $z = 3.105(2)$, the CO(3–2) line would fall just below

the frequency range of the observing window. When the spectrum is smoothed as in Figure B.2 we do not see anything, but when investigating the edge of the spectrum unsmoothened, we find indication for the rise of a line. As less than half of the second line is observed and it is at edge channels of the spectrum, this cannot be considered a secured detection. Figure B.2 shows the possible side of the CO(3–2) line overlaid on the CO(4–3) line. Since this is not a clear detection we still consider the line identification CO(3–2) at $z = 2.079(1)$ which would have $T_{\rm dust} = 25 \pm 3\,{\rm K}$. CO(2–1) at $z = 1.052(1)$ is ruled out since the dust temperature ($T_{\rm dust} = 16 \pm 1\,{\rm K}$) would be too low. The most probable line identification based on the photometric redshift $z_{\rm phot} = 3.4 \pm 0.7$ is CO(4–3) which would then have a dust temperature of $T_{\rm dust} = 36 \pm 4\,{\rm K}$.

SPT2335-53: We detect a line at 100.12 GHz and a tentative feature at 85.51 GHz, which turns out to be CO(5–4) and [C I] at $z = 4.755(1)$. This was confirmed by a [C II] detection from APEX/FLASH, see Figure B.2. At this redshift we find a dust temperature of $T_{\rm dust} = 57 \pm 4\,{\rm K}$.

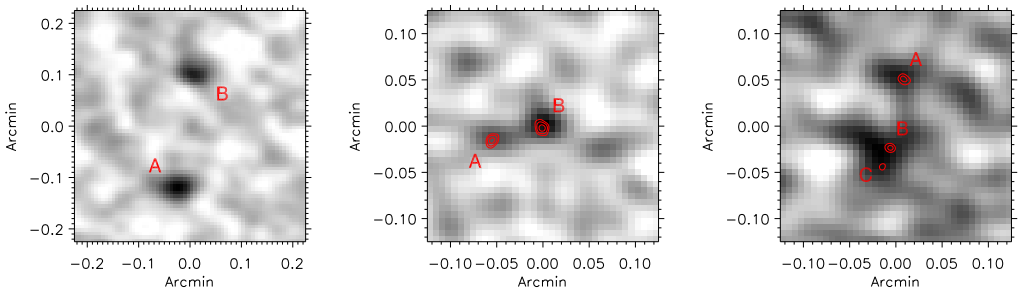

Figure B.4: 3 mm continuum imaging of the three sources that split up in to multiple components scaled by the rms (which is rms = 0.04 mJy for SPT2052-56 and rms = 0.05 mJy for SPT2340-59 and SPT2349-56). The *red* contours are high resolution 870 μm ALMA high resolution imaging, 5,10,20,30σ. *Left*: SPT2052-56 splits up into two components with the peak flux density of $S_{\rm peak} = 0.25$ mJy. As we do not have 870 μm imaging of this source there are no contours overlaid. *Middle*: SPT2340-59 which splits up in to two counterparts, with the peak flux density of $S_{\rm peak} = 0.30$ mJy. *Right*: SPT2349-56 splits into three at 870 μm, with the peak flux density of $S_{\rm peak} = 0.22$ mJy.

SPT2340-59: This source splits up into two counterparts in the ALMA 3 mm continuum image. In our 870 μm high resolution ALMA imaging, we see the same two counterparts (see Figure B.4). Counterpart B is brightest, but in the spectrum of this we do not see any lines. In counterpart A, however, we see a potential line at 94.79 GHz. If this line is real the possible line identifications are CO(3–2) at $z = 2.6480(8)$, CO(4–3) at $z = 3.864(1)$ or CO(5–4) at $z = 5.079(1)$. CO(2–1) at $z = 1.4321(5)$ is excluded as that would mean a dust temperature of $T_{\rm dust} = 17 \pm 1\,{\rm K}$, which has not been observed in any of our sources. The photometric redshift of the source is $z_{\rm phot} = 3.8 \pm 0.6$ favoring the CO(4–3) line identification. For this redshift

though, the [C I] line falls within the spectral window. With the low SNR of the CO line, it is reasonable to assume that the [C I] line is hiding within the noise.

SPT2349-50: In this source we see a single bright line at 89.21 GHz with the most probable line identification being CO(3–2) at $z = 2.8764(3)$. This was confirmed by APEX/SEPIA observations of the CO(7–6) line at 207.99 GHz.

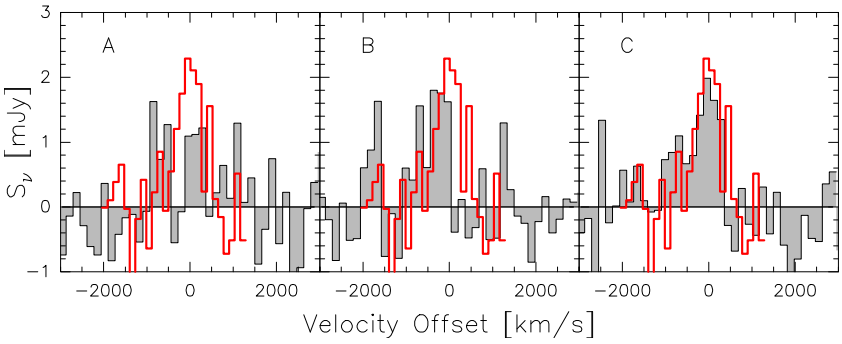

Figure B.5: The three panels shows the CO(4–3) extracted at position A, B and C, with the [C II] overlaid in *red* for SPT2349-56.

SPT2349-56: At 3 mm, this source splits into two counterparts, but in the 870 μm high resolution ALMA imaging (Vieira et al., 2013) we see three counterparts (see Figure B.4). We use the high resolution imaging to define the positions for the three counterparts and extract spectra there. We see indications of a line at $\sim$87.0GHz all positions (with the center slightly shifted at each position), with position A showing the weakest line. New Cycle 4 high-resolution ALMA imaging shows that this source splits into in total 14 components (Miller et al. submitted to Nature). When the spectra of these three positions are stacked we see a hint of a line at 108.62GHz. These two lines are consistent with the line identifications CO(4–3) and CO(5–4) at $z = 4.304(2)$ which is confirmed by APEX/FLASH [C II] observations. The [C II] only traces part of the line seen in the stack (see Figure B.2), so in Figure B.5 we show the spectra of each of the components with [C II] overlaid. It is clear from this that the [C II] traces component C.

SPT2353-50: We detect a single wide spectral feature at 87.63 GHz. We rule out the line identification CO(2–1) at $z = 1.630(2)$ and CO(3–2) at $z = 2.945(2)$ because the dust temperatures would be $T_{\rm dust} = 16 \pm 1$ K and $T_{\rm dust} = 25 \pm 2$ K respectively. The photometric redshift $z_{\rm phot} = 4.5 \pm 0.8$ favors the line identification CO(4–3) at $z = 4.261(3)$. The last possible line identification is CO(5–4) at $z = 5.576(4)$ which is not negligible with a dust temperature of $T_{\rm dust} = 46 \pm 2$ K. At this redshift, CO(6–5) falls within the spectral window, and we see a SNR $\sim$ 1.5 feature at the frequency where the line should fall. This redshift option was confirmed by the detection of [C II], see Figure B.2.

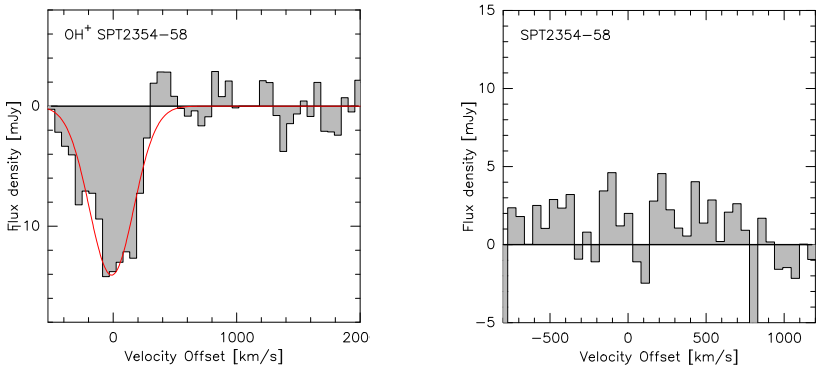

Figure B.6: These two spectra are extracted from the high resolution 870 μm data cube available for SPT2354-58. *Left*: Absorption line with OH^+ as the most likely line identification. *Right:* Where CO(5–4) would have been if the redshift is $z = 0.6431(3)$.

SPT2354-58: This is the only source where we do not find any lines in the 3 mm ALMA redshift search. For this source we have high resolution 870 μm imaging and in this data cube we found an absorption line at 338.95 GHz (see left panel of Figure B.6). We identify the line as either $OH^+(1_{22} - 0_{11})$ at $z = 1.867(1)$ or $H_2O(1_{10} - 1_{01})$ at $z = 0.6431(3)$. For other absorptions line identifications we should have seen an emission line in the 3 mm ALMA data. The first option is favored by the photometry with $T_{\rm dust} = 43 \pm 2$ K compared to $T_{\rm dust} = 27 \pm 1$ K for the second option. Furthermore we should have seen CO(5–4) at 350.77 GHz if the second option was correct and this is not the case (see right panel of Figure B.6). The most probable redshift is therefore identified as $z = 1.867(1)$.

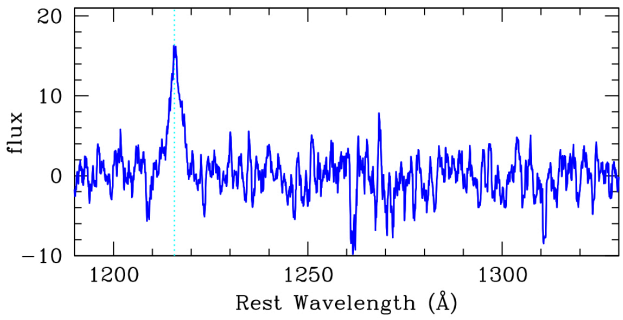

Figure B.7: UV/Optical/near-IR spectra (VLT/X-shooter) of the $z = 3.07$ identified SPT2357-51. ÊThe redshift was identified with large equivalent width Lyman-α emission in the UV, exhibiting a strong, broad emission line (FWHM = 1230 km/s) but no detectable continuum. The broad Lyα line is suggestive of an AGN, although no CIV_{1549} nor $OIII_{5007}$ are detected.

SPT2357-51: For this source optical spectroscopy with the X-shooter/VLT was performed before the ALMA observations, detecting a line. The observations are de-

scribed in Section 3.1.6 and the spectrum is shown in Figure B.7.

Appendix C

Source list of the full SPT-DSFG sample

In this Appendix we give names and positions for all sources studied in this work. For sources that split up, all positions are given.

Table C.1: Names and positions of all sources

Short name	Long name	Ra	dec	Origin of position
SPT0002-52	SPT–S J000223-5232.1	00:02:23.24	-52:31:52.5	ALMA
SPT0020-51	SPT–S J002023-5146.3	00:20:23.34	-51:46:36.5	ALMA
SPT0027-50	SPT–S J002706-5007.3	00:27:06.58	-50:07:19.5	ALMA
SPT0054-41	SPT–S J005440-4152.0	00:54:40.03	-41:51:55.9	LABOCA
SPT0103-45	SPT–S J010312-4538.8	01:03:11.50	-45:38:53.9	ALMA
SPT0106-64	SPT–S J010623-6412.9	01:06:23.86	-64:12:49.9	ALMA
SPT0109-47	SPT–S J010950-4702.1	01:09:49.66	-47:02:11.6	ALMA
SPT0112-55	SPT–S J011207-5516.2	01:12:09.92	-55:16:36.5	ALMA
SPT0113-46	SPT–S J011308-4617.7	01:13:09.01	-46:17:56.3	ALMA
SPT0114-59	SPT–S J011409-5909.2	01:14:07.80	-59:09:26.0	ALMA
SPT0125-47	SPT–S J012507-4723.8	01:25:07.08	-47:23:56.0	ALMA
SPT0125-50	SPT–S J012549-5038.3	01:25:48.45	-50:38:20.9	ALMA
SPT0128-51	SPT–S J012809-5129.8	01:28:10.19	-51:29:42.4	ALMA
SPT0136-63	SPT–S J013652-6307.3	01:36:50.28	-63:07:26.6	ALMA
SPT0147-64	SPT–S J014707-6458.9	01:47:07.14	-64:58:51.8	ALMA
SPT0150-59	SPT–S J015012-5924.0	01:50:09.47	-59:23:57.0	ALMA
SPT0155-62	SPT–S J015548-6250.8	01:55:48.10	-62:50:49.8	ALMA
SPT0202-61	SPT–S J020257-6121.1	02:02:58.81	-61:21:10.8	ALMA
SPT0226-45	SPT–S J022649-4515.9	02:26:49.52	-45:15:38.6	LABOCA
SPT0243-49	SPT–S J024308-4915.6	02:43:08.81	-49:15:35.0	ALMA
SPT0245-63	SPT–S J024542-6320.6	02:45:44.14	-63:20:38.7	ALMA
SPT0300-46	SPT–S J030004-4621.4	03:00:04.37	-46:21:24.3	ALMA
SPT0311-58	SPT–S J031132-5823.4	03:11:33.14	-58:23:33.4	ALMA
SPT0314-44	SPT–S J031428-4452.5	03:14:28.63	-44:52:21.6	LABOCA
SPT0319-47	SPT–S J031931-4724.7	03:19:31.88	-47:24:33.7	ALMA
SPT0345-47	SPT–S J034511-4725.8	03:45:10.77	-47:25:39.5	ALMA
SPT0346-52	SPT–S J034640-5205.1	03:46:41.13	-52:05:02.1	ALMA
SPT0348-62	SPT–S J034840-6220.8	03:48:42.16	-62:20:51.3	ALMA
SPT0402-45	SPT–S J040202-4553.4	04:02:02.04	-45:53:21.6	LABOCA
SPT0403-58	SPT–S J040330-5849.9	04:03:32.69	-58:50:08.8	LABOCA
SPT0404-59	SPT–S J040445-5948.9	04:04:46.30	-59:49:02.7	LABOCA
SPT0418-47	SPT–S J041840-4752.0	04:18:39.67	-47:51:52.7	ALMA
SPT0425-40	SPT–S J042518-4036.7	04:25:17.45	-40:36:58.5	LABOCA
SPT0433-59	SPT–S J043340-5909.8	04:33:41.27	-59:09:35.7	LABOCA
SPT0436-40	SPT–S J043641-4047.4	04:36:41.56	-40:47:10.6	LABOCA

continued

Table C.1: Names and positions of all sources

Short name	Long name	Ra	dec	Origin of position
SPT0441-46	SPT–S J044144-4605.5	04:41:44.08	-46:05:25.5	ALMA
SPT0452-50	SPT–S J045246-5018.3	04:52:45.83	-50:18:42.2	ALMA
SPT0457-49	SPT–S J045718-4931.8	04:57:17.52	-49:31:51.3	ALMA
SPT0459-58	SPT–S J045859-5805.1	04:58:59.80	-58:05:14.0	ALMA
SPT0459-59	SPT–S J045913-5942.4	04:59:12.34	-59:42:20.2	ALMA
SPT0509-53	SPT–S J050907-5339.2	05:09:07.28	-53:39:26.1	LABOCA
SPT0512-59	SPT–S J051259-5935.6	05:12:57.98	-59:35:41.9	ALMA
SPT0516-59	SPT–S J051639-5920.4	05:16:38.09	-59:20:32.1	ALMA
SPT0520-53	SPT–S J052039-5329.8	05:20:40.16	-53:29:48.9	LABOCA
SPT0528-53	SPT–S J052850-5300.3	05:28:49.88	-53:00:24.6	LABOCA
SPT0529-54	SPT–S J052903-5436.6	05:29:03.09	-54:36:40.0	ALMA
SPT0532-50	SPT–S J053250-5047.1	05:32:51.04	-50:47:07.5	ALMA
SPT0538-50	SPT–S J053816-5030.8	05:38:16.94	-50:30:50.7	LABOCA
SPT0541-57	SPT–S J054120-5738.3	05:41:24.10	-57:38:17.5	LABOCA
SPT0544-40	SPT–S J054401-4036.3	05:44:00.79	-40:36:31.2	ALMA
SPT0550-53	SPT–S J055002-5356.6	05:50:00.56	-53:56:41.7	ALMA
SPT0551-48	SPT–S J055156-4825.1	05:51:54.65	-48:25:01.8	LABOCA
SPT0551-50	SPT–S J055138-5058.0	05:51:39.42	-50:58:02.1	ALMA
SPT0552-42	SPT–S J055227-4244.0	05:52:26.70	-42:44:12.7	ALMA
SPT0553-50	SPT–S J055320-5007.2	05:53:20.35	-50:07:11.7	ALMA
SPT0555-62	SPT–S J055517-6218.9	05:55:16.80	-62:18:50.3	ALMA
SPT0604-64	SPT–S J060458-6447.3	06:04:57.57	-64:47:21.9	ALMA
SPT0611-55	SPT–S J061155-5514.2	06:11:57.44	-55:13:56.5	ALMA
SPT0625-58	SPT–S J062524-5835.3	06:25:22.33	-58:35:20.1	ALMA
SPT0652-55	SPT–S J065207-5516.0	06:52:07.12	-55:15:59.4	LABOCA
SPT2008-58	SPT–S J200758-5848.3	20:07:59.83	-58:48:20.2	ALMA
SPT2031-51	SPT–S J203058-5112.5	20:30:58.87	-51:12:25.4	LABOCA
SPT2037-65	SPT–S J203729-6513.3	20:37:31.98	-65:13:16.5	ALMA
SPT2048-55	SPT–S J204823-5520.5	20:48:22.87	-55:20:41.2	ALMA
SPT2052-56	SPT–S J205239-5611.6	20:52:41.47	-56:11:57.1	ALMA
		20:52:41.28	-56:11:43.5	ALMA
SPT2101-60	SPT–S J210112-6048.8	21:01:13.77	-60:48:56.1	ALMA
SPT2103-60	SPT–S J210328-6032.6	21:03:30.90	-60:32:40.3	ALMA
SPT2129-57	SPT–S J212911-5702.0	21:29:12.35	-57:01:57.3	LABOCA
SPT2132-58	SPT–S J213242-5802.9	21:32:43.23	-58:02:46.2	ALMA
SPT2134-50	SPT–S J213404-5013.2	21:34:03.34	-50:13:25.1	ALMA
SPT2146-55	SPT–S J214654-5507.8	21:46:54.02	-55:07:54.3	ALMA
SPT2147-50	SPT–S J214720-5035.9	21:47:19.05	-50:35:54.0	ALMA
SPT2152-40	SPT–S J215212-4036.6	21:52:13.01	-40:36:35.5	LABOCA
SPT2203-41	SPT–S J220317-4133.6	22:03:17.01	-41:33:28.5	LABOCA
SPT2219-42	SPT–S J221958-4206.9	22:19:59.11	-42:07:06.6	LABOCA
SPT2232-61	SPT–S J223252-6114.8	22:32:51.31	-61:14:45.8	LABOCA
SPT2307-50	SPT–S J230726-5003.8	23:07:24.71	-50:03:35.6	ALMA
SPT2311-45	SPT–S J231151-4546.7	23:11:50.82	-45:46:45.3	LABOCA
SPT2311-54	SPT–S J231125-5450.5	23:11:23.94	-54:50:30.0	ALMA
SPT2316-50	SPT–S J231657-5036.7	23:16:59.70	-50:36:33.8	LABOCA
SPT2319-55	SPT–S J231922-5557.9	23:19:21.67	-55:57:57.8	ALMA
SPT2332-53	SPT–S J233227-5358.5	23:32:26.92	-53:58:41.3	LABOCA
SPT2335-53	SPT–S J233513-5324.0	23:35:13.15	-53:24:29.9	ALMA

continued

Table C.1: Names and positions of all sources

Short name	Long name	Ra	dec	Origin of position
SPT2340-59	SPT–S J234009-5943.1	23:40:09.36	-59:43:32.8	ALMA
		23:40:08.95	-59:43:32.0	ALMA
SPT2349-50	SPT–S J234942-5053.5	23:49:42.16	-50:53:30.7	ALMA
SPT2349-52	SPT–S J234928-5246.8	23:49:29.70	-52:46:50.7	LABOCA
SPT2349-56	SPT–S J234944-5638.3	23:49:42.68	-56:38:19.4	ALMA
		23:49:42.79	-56:38:23.9	ALMA
		23:49:42.84	-56:38:25.0	ALMA
SPT2351-57	SPT–S J235149-5722.2	23:51:50.79	-57:22:18.3	ALMA
SPT2353-50	SPT–S J235339-5010.1	23:53:39.22	-50:10:08.2	ALMA
SPT2354-58	SPT–S J235434-5815.1	23:54:34.27	-58:15:08.4	ALMA
SPT2357-51	SPT–S J235718-5153.6	23:57:16.84	-51:53:52.9	ALMA

Appendix D

Photometry MAPS

For each source we have up to eight photometry maps (plus the 3 mm fluxes where we have ALMA spectra). This Appendix shows thumbnails of the available maps for all 91 sources.

The greyscale of the thumbnail is adjusted for each panel based on the flux extracted at this wavelength. SPT contours are shown in *red* at σ = 1.5,3,4,5, ... and LABOCA contours are shown in *blue* σ = 3,4,5, ...

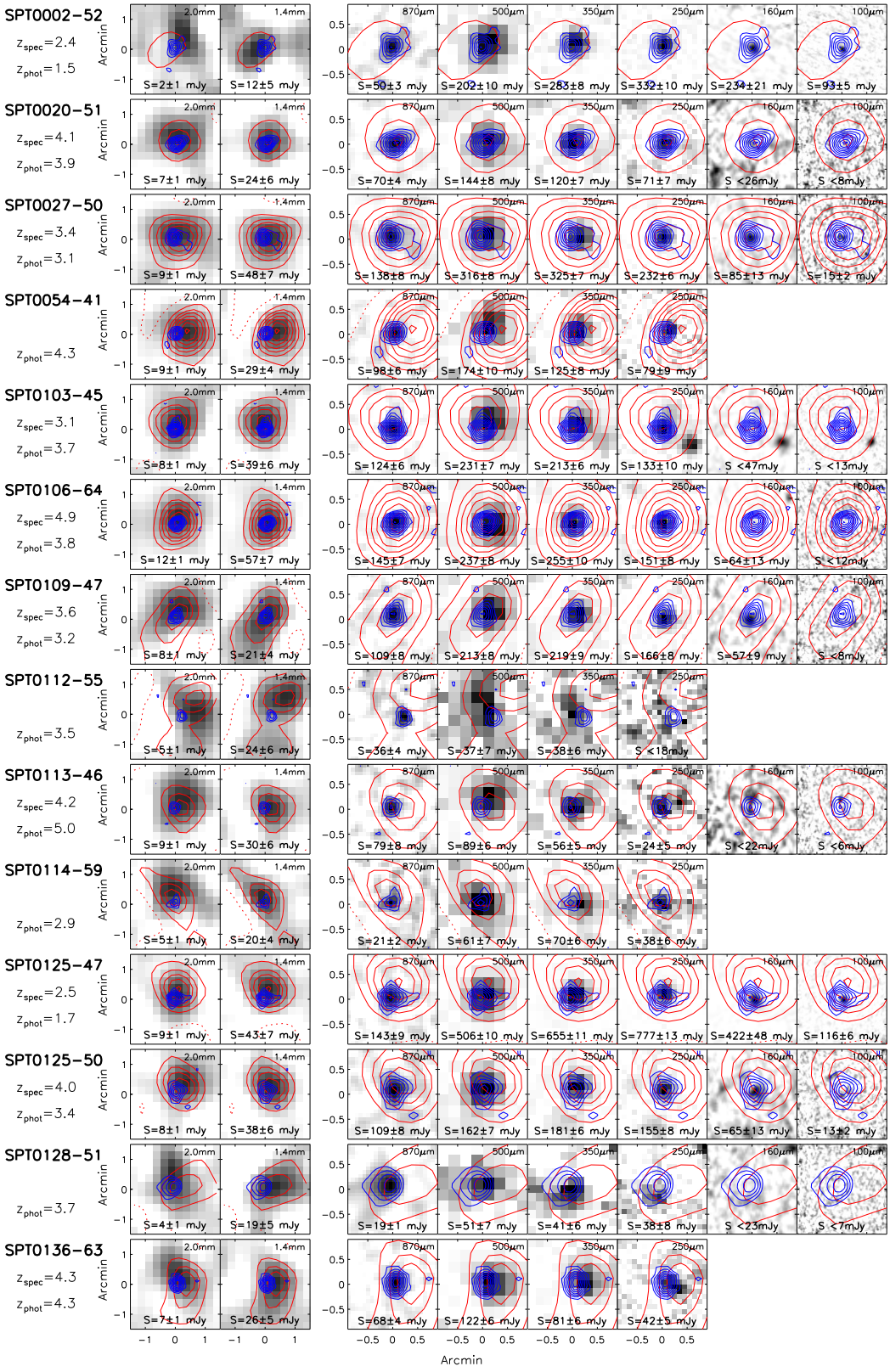
SPT0002−52
z_{spec}=2.4
z_{phot}=1.5
S=2±1 mJy
S=12±5 mJy
S=50±3 mJy
S=202±10 mJy
S=283±8 mJy
S=332±10 mJy
S=234±21 mJy
S=93±5 mJy
SPT0020−51
z_{spec}=4.1
z_{phot}=3.9
S=7±1 mJy
S=24±6 mJy
S=70±4 mJy
S=144±8 mJy
S=120±7 mJy
S=71±7 mJy
S <26mJy
S <8mJy
SPT0027−50
z_{spec}=3.4
z_{phot}=3.1
S=9±1 mJy
S=48±7 mJy
S=138±8 mJy
S=316±8 mJy
S=325±7 mJy
S=232±6 mJy
S=85±13 mJy
S=15±2 mJy
SPT0054−41
z_{phot}=4.3
S=9±1 mJy
S=29±4 mJy
S=98±6 mJy
S=174±10 mJy
S=125±8 mJy
S=79±9 mJy
SPT0103−45
z_{spec}=3.1
z_{phot}=3.7
S=8±1 mJy
S=39±6 mJy
S=124±6 mJy
S=231±7 mJy
S=213±6 mJy
S=133±10 mJy
S <47mJy
S <13mJy
SPT0106−64
z_{spec}=4.9
z_{phot}=3.8
S=12±1 mJy
S=57±7 mJy
S=145±7 mJy
S=237±8 mJy
S=255±10 mJy
S=151±8 mJy
S=64±13 mJy
S <12mJy
SPT0109−47
z_{spec}=3.6
z_{phot}=3.2
S=8±1 mJy
S=21±4 mJy
S=109±8 mJy
S=213±8 mJy
S=219±9 mJy
S=166±8 mJy
S=57±9 mJy
S <8mJy
SPT0112−55
z_{phot}=3.5
S=5±1 mJy
S=24±6 mJy
S=36±4 mJy
S=37±7 mJy
S=38±6 mJy
S <18mJy
SPT0113−46
z_{spec}=4.2
z_{phot}=5.0
S=9±1 mJy
S=30±6 mJy
S=79±8 mJy
S=89±6 mJy
S=56±5 mJy
S=24±5 mJy
S <22mJy
S <6mJy
SPT0114−59
z_{phot}=2.9
S=5±1 mJy
S=20±4 mJy
S=21±2 mJy
S=61±7 mJy
S=70±6 mJy
S=38±6 mJy
SPT0125−47
z_{spec}=2.5
z_{phot}=1.7
S=9±1 mJy
S=43±7 mJy
S=143±9 mJy
S=506±10 mJy
S=655±11 mJy
S=777±13 mJy
S=422±48 mJy
S=116±6 mJy
SPT0125−50
z_{spec}=4.0
z_{phot}=3.4
S=8±1 mJy
S=38±6 mJy
S=109±8 mJy
S=162±7 mJy
S=181±6 mJy
S=155±8 mJy
S=65±13 mJy
S=13±2 mJy
SPT0128−51
z_{phot}=3.7
S=4±1 mJy
S=19±5 mJy
S=19±1 mJy
S=51±7 mJy
S=41±6 mJy
S=38±8 mJy
S <23mJy
S <7mJy
SPT0136−63
z_{spec}=4.3
z_{phot}=4.3
S=7±1 mJy
S=26±5 mJy
S=68±4 mJy
S=122±6 mJy
S=81±6 mJy
S=42±5 mJy
2.0mm
1.4mm
870μm
500μm
350μm
250μm
160μm
100μm
Arcmin

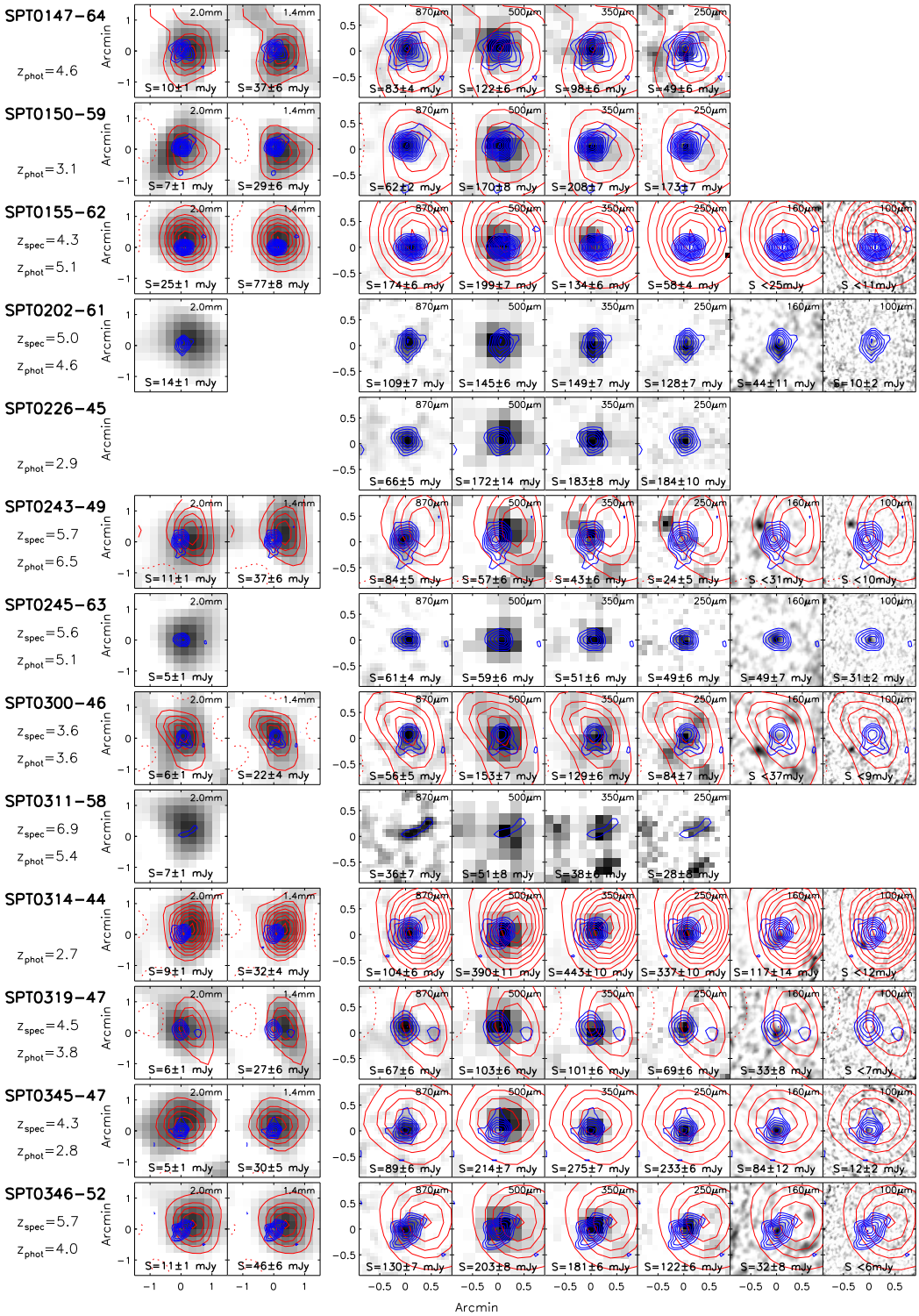
SPT0147−64
z_{phot}=4.6
S=10±1 mJy
S=37±6 mJy
S=83±4 mJy
S=122±6 mJy
S=98±6 mJy
S=49±6 mJy
SPT0150−59
z_{phot}=3.1
S=7±1 mJy
S=29±6 mJy
S=62±2 mJy
S=170±8 mJy
S=208±7 mJy
S=173±7 mJy
SPT0155−62
z_{spec}=4.3
z_{phot}=5.1
S=25±1 mJy
S=77±8 mJy
S=174±6 mJy
S=199±7 mJy
S=134±6 mJy
S=58±4 mJy
S <25mJy
S <11mJy
SPT0202−61
z_{spec}=5.0
z_{phot}=4.6
S=14±1 mJy
S=109±7 mJy
S=145±6 mJy
S=149±7 mJy
S=128±7 mJy
S=44±11 mJy
S=10±2 mJy
SPT0226−45
z_{phot}=2.9
S=66±5 mJy
S=172±14 mJy
S=183±8 mJy
S=184±10 mJy
SPT0243−49
z_{spec}=5.7
z_{phot}=6.5
S=11±1 mJy
S=37±6 mJy
S=84±5 mJy
S=57±6 mJy
S=43±6 mJy
S=24±5 mJy
S <31mJy
S <10mJy
SPT0245−63
z_{spec}=5.6
z_{phot}=5.1
S=5±1 mJy
S=61±4 mJy
S=59±6 mJy
S=51±6 mJy
S=49±6 mJy
S=49±7 mJy
S=31±2 mJy
SPT0300−46
z_{spec}=3.6
z_{phot}=3.6
S=6±1 mJy
S=22±4 mJy
S=56±5 mJy
S=153±7 mJy
S=129±6 mJy
S=84±7 mJy
S <37mJy
S <9mJy
SPT0311−58
z_{spec}=6.9
z_{phot}=5.4
S=7±1 mJy
S=36±7 mJy
S=51±8 mJy
S=38±6 mJy
S=28±8 mJy
SPT0314−44
z_{phot}=2.7
S=9±1 mJy
S=32±4 mJy
S=104±6 mJy
S=390±11 mJy
S=443±10 mJy
S=337±10 mJy
S=117±14 mJy
S <12mJy
SPT0319−47
z_{spec}=4.5
z_{phot}=3.8
S=6±1 mJy
S=27±6 mJy
S=67±6 mJy
S=103±6 mJy
S=101±6 mJy
S=69±6 mJy
S=33±8 mJy
S <7mJy
SPT0345−47
z_{spec}=4.3
z_{phot}=2.8
S=5±1 mJy
S=30±5 mJy
S=89±6 mJy
S=214±7 mJy
S=275±7 mJy
S=233±6 mJy
S=84±12 mJy
S=12±2 mJy
SPT0346−52
z_{spec}=5.7
z_{phot}=4.0
S=11±1 mJy
S=46±6 mJy
S=130±7 mJy
S=203±8 mJy
S=181±6 mJy
S=122±6 mJy
S=32±8 mJy
S <6mJy
2.0mm
1.4mm
870μm
500μm
350μm
250μm
160μm
100μm
Arcmin

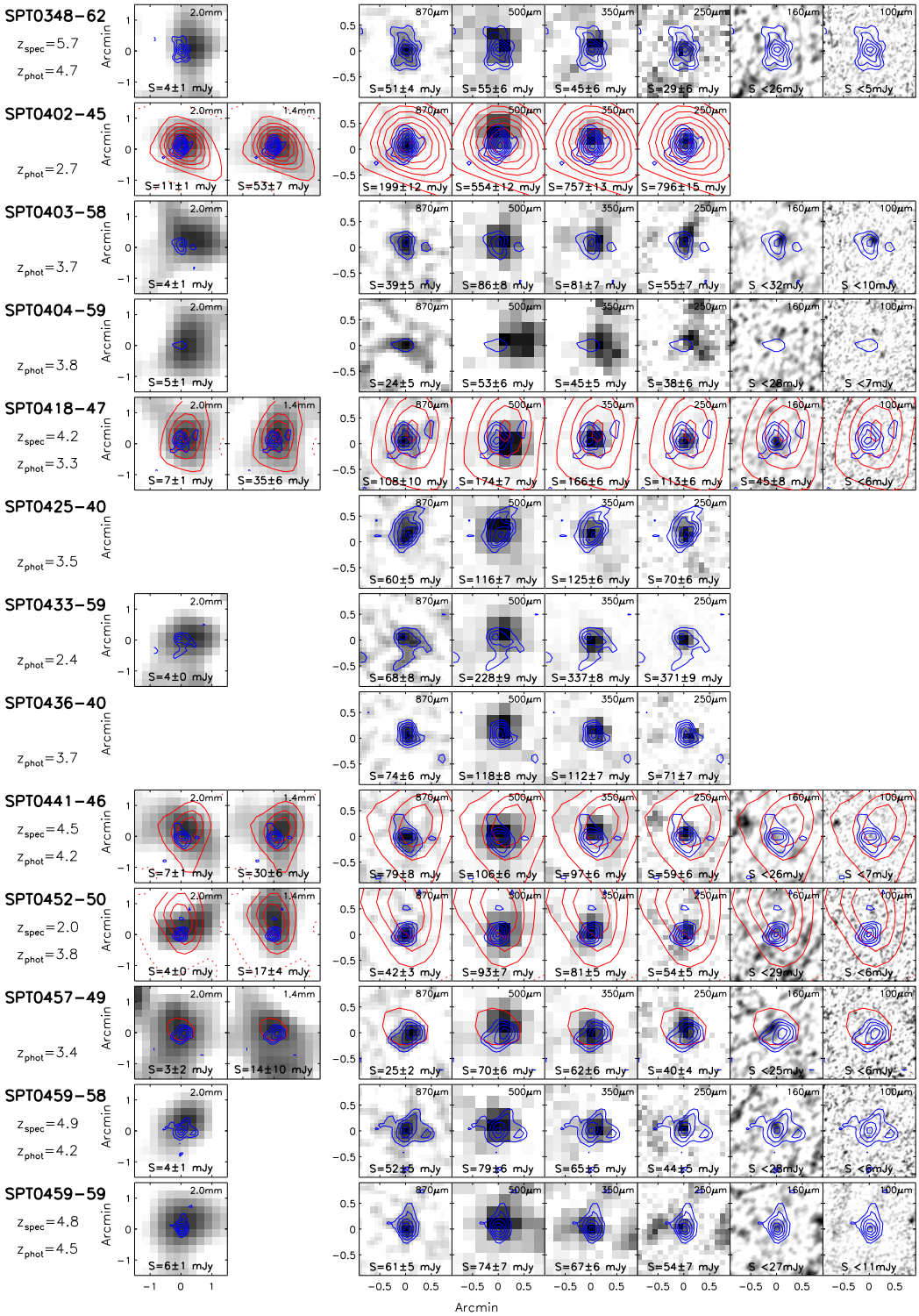
SPT0348−62
z_{spec}=5.7
z_{phot}=4.7
S=4±1 mJy
S=51±4 mJy
S=55±6 mJy
S=45±6 mJy
S=29±6 mJy
S <26mJy
S <5mJy
SPT0402−45
z_{phot}=2.7
S=11±1 mJy
S=53±7 mJy
S=199±12 mJy
S=554±12 mJy
S=757±13 mJy
S=796±15 mJy
SPT0403−58
z_{phot}=3.7
S=4±1 mJy
S=39±5 mJy
S=86±8 mJy
S=81±7 mJy
S=55±7 mJy
S <32mJy
S <10mJy
SPT0404−59
z_{phot}=3.8
S=5±1 mJy
S=24±5 mJy
S=53±6 mJy
S=45±5 mJy
S=38±6 mJy
S <28mJy
S <7mJy
SPT0418−47
z_{spec}=4.2
z_{phot}=3.3
S=7±1 mJy
S=35±6 mJy
S=108±10 mJy
S=174±7 mJy
S=166±6 mJy
S=113±6 mJy
S=45±8 mJy
S <6mJy
SPT0425−40
z_{phot}=3.5
S=60±5 mJy
S=116±7 mJy
S=125±6 mJy
S=70±6 mJy
SPT0433−59
z_{phot}=2.4
S=4±0 mJy
S=68±8 mJy
S=228±9 mJy
S=337±8 mJy
S=371±9 mJy
SPT0436−40
z_{phot}=3.7
S=74±6 mJy
S=118±8 mJy
S=112±7 mJy
S=71±7 mJy
SPT0441−46
z_{spec}=4.5
z_{phot}=4.2
S=7±1 mJy
S=30±6 mJy
S=79±8 mJy
S=106±6 mJy
S=97±6 mJy
S=59±6 mJy
S <26mJy
S <7mJy
SPT0452−50
z_{spec}=2.0
z_{phot}=3.8
S=4±0 mJy
S=17±4 mJy
S=42±3 mJy
S=93±7 mJy
S=81±5 mJy
S=54±5 mJy
S <29mJy
S <6mJy
SPT0457−49
z_{phot}=3.4
S=3±2 mJy
S=14±10 mJy
S=25±2 mJy
S=70±6 mJy
S=62±6 mJy
S=40±4 mJy
S <25mJy
S <6mJy
SPT0459−58
z_{spec}=4.9
z_{phot}=4.2
S=4±1 mJy
S=52±5 mJy
S=79±6 mJy
S=65±5 mJy
S=44±5 mJy
S <28mJy
S <6mJy
SPT0459−59
z_{spec}=4.8
z_{phot}=4.5
S=6±1 mJy
S=61±5 mJy
S=74±7 mJy
S=67±6 mJy
S=54±7 mJy
S <27mJy
S <11mJy
2.0mm
1.4mm
870μm
500μm
350μm
250μm
160μm
100μm
Arcmin

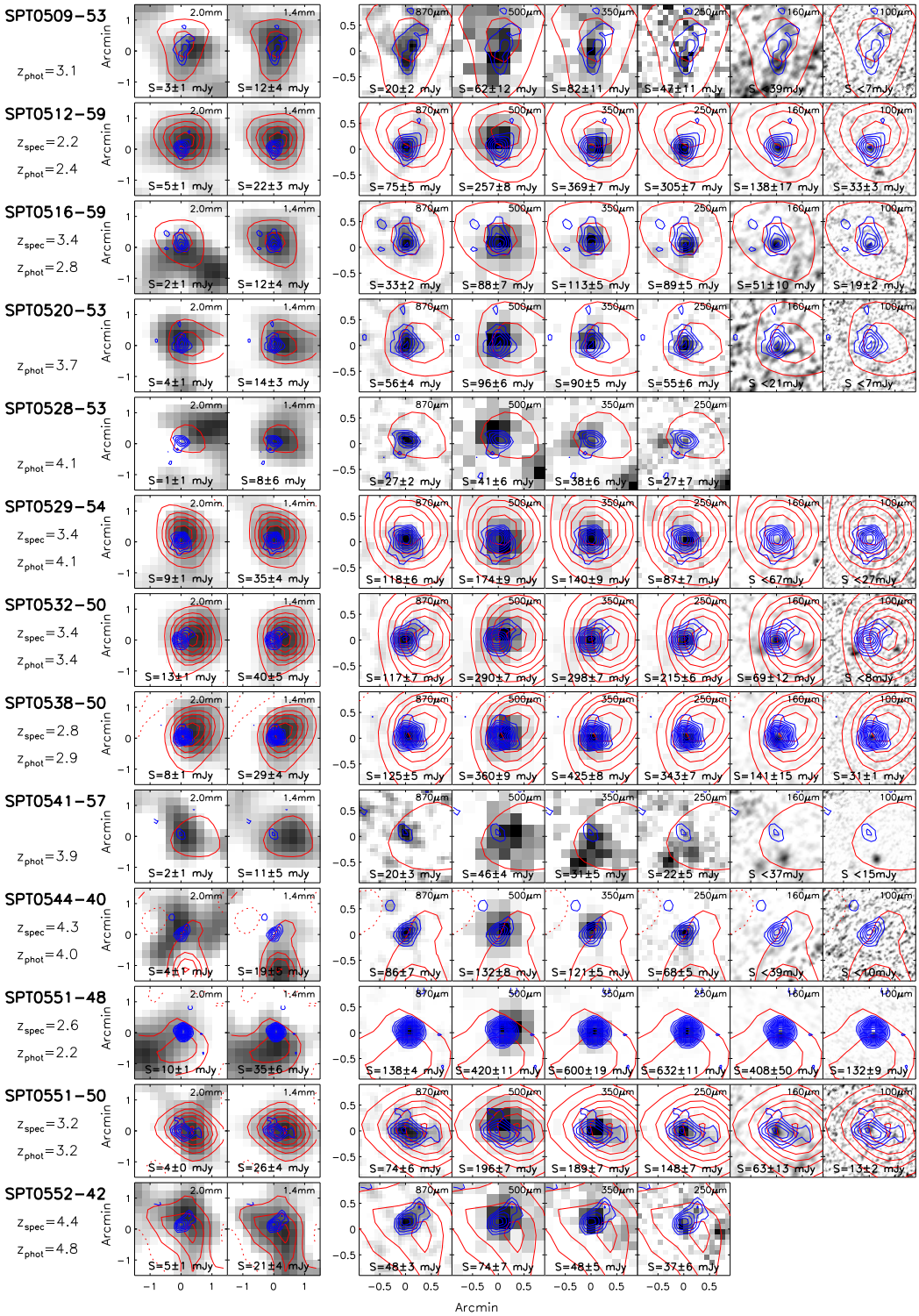
SPT0509−53
z_{phot}=3.1
S=3±1 mJy
S=12±4 mJy
S=20±2 mJy
S=62±12 mJy
S=82±11 mJy
S=47±11 mJy
S <39mJy
S <7mJy
SPT0512−59
z_{spec}=2.2
z_{phot}=2.4
S=5±1 mJy
S=22±3 mJy
S=75±5 mJy
S=257±8 mJy
S=369±7 mJy
S=305±7 mJy
S=138±17 mJy
S=33±3 mJy
SPT0516−59
z_{spec}=3.4
z_{phot}=2.8
S=2±1 mJy
S=12±4 mJy
S=33±2 mJy
S=88±7 mJy
S=113±5 mJy
S=89±5 mJy
S=51±10 mJy
S=19±2 mJy
SPT0520−53
z_{phot}=3.7
S=4±1 mJy
S=14±3 mJy
S=56±4 mJy
S=96±6 mJy
S=90±5 mJy
S=55±6 mJy
S <21mJy
S <7mJy
SPT0528−53
z_{phot}=4.1
S=1±1 mJy
S=8±6 mJy
S=27±2 mJy
S=41±6 mJy
S=38±6 mJy
S=27±7 mJy
SPT0529−54
z_{spec}=3.4
z_{phot}=4.1
S=9±1 mJy
S=35±4 mJy
S=118±6 mJy
S=174±9 mJy
S=140±9 mJy
S=87±7 mJy
S <67mJy
S <27mJy
SPT0532−50
z_{spec}=3.4
z_{phot}=3.4
S=13±1 mJy
S=40±5 mJy
S=117±7 mJy
S=290±7 mJy
S=298±7 mJy
S=215±6 mJy
S=69±12 mJy
S <8mJy
SPT0538−50
z_{spec}=2.8
z_{phot}=2.9
S=8±1 mJy
S=29±4 mJy
S=125±5 mJy
S=360±9 mJy
S=425±8 mJy
S=343±7 mJy
S=141±15 mJy
S=31±1 mJy
SPT0541−57
z_{phot}=3.9
S=2±1 mJy
S=11±5 mJy
S=20±3 mJy
S=46±4 mJy
S=31±5 mJy
S=22±5 mJy
S <37mJy
S <15mJy
SPT0544−40
z_{spec}=4.3
z_{phot}=4.0
S=4±1 mJy
S=19±5 mJy
S=86±7 mJy
S=132±8 mJy
S=121±5 mJy
S=68±5 mJy
S <39mJy
S <10mJy
SPT0551−48
z_{spec}=2.6
z_{phot}=2.2
S=10±1 mJy
S=35±6 mJy
S=138±4 mJy
S=420±11 mJy
S=600±19 mJy
S=632±11 mJy
S=408±50 mJy
S=132±9 mJy
SPT0551−50
z_{spec}=3.2
z_{phot}=3.2
S=4±0 mJy
S=26±4 mJy
S=74±6 mJy
S=196±7 mJy
S=189±7 mJy
S=148±7 mJy
S=63±13 mJy
S=13±2 mJy
SPT0552−42
z_{spec}=4.4
z_{phot}=4.8
S=5±1 mJy
S=21±4 mJy
S=48±3 mJy
S=74±7 mJy
S=48±5 mJy
S=37±6 mJy
2.0mm
1.4mm
870μm
500μm
350μm
250μm
160μm
100μm
Arcmin
Arcmin

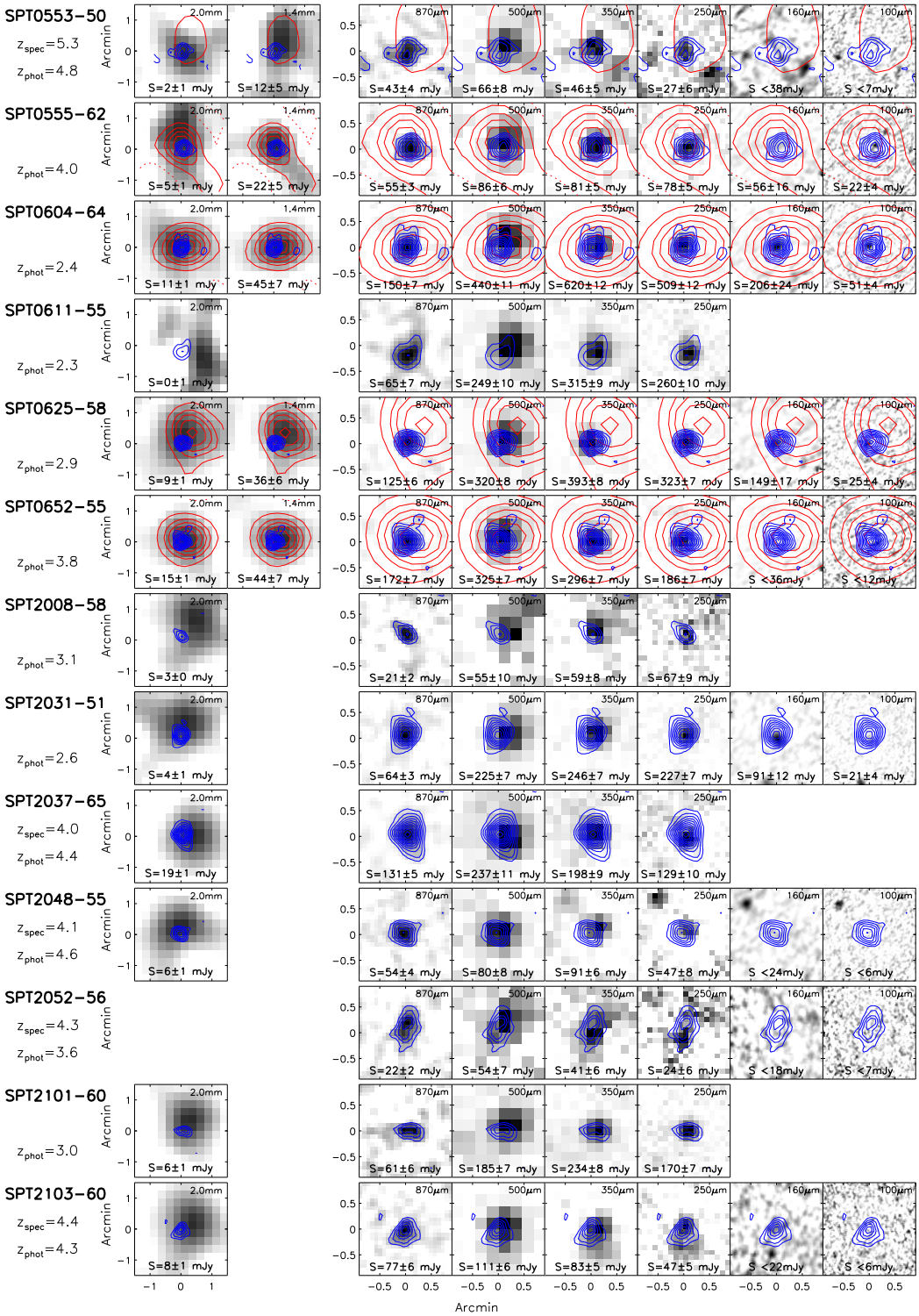
SPT0553−50
z_{spec}=5.3
z_{phot}=4.8
S=2±1 mJy
S=12±5 mJy
S=43±4 mJy
S=66±8 mJy
S=46±5 mJy
S=27±6 mJy
S <38mJy
S <7mJy
SPT0555−62
z_{phot}=4.0
S=5±1 mJy
S=22±5 mJy
S=55±3 mJy
S=86±6 mJy
S=81±5 mJy
S=78±5 mJy
S=56±16 mJy
S=22±4 mJy
SPT0604−64
z_{phot}=2.4
S=11±1 mJy
S=45±7 mJy
S=150±7 mJy
S=440±11 mJy
S=620±12 mJy
S=509±12 mJy
S=206±24 mJy
S=51±4 mJy
SPT0611−55
z_{phot}=2.3
S=0±1 mJy
S=65±7 mJy
S=249±10 mJy
S=315±9 mJy
S=260±10 mJy
SPT0625−58
z_{phot}=2.9
S=9±1 mJy
S=36±6 mJy
S=125±6 mJy
S=320±8 mJy
S=393±8 mJy
S=323±7 mJy
S=149±17 mJy
S=25±4 mJy
SPT0652−55
z_{phot}=3.8
S=15±1 mJy
S=44±7 mJy
S=172±7 mJy
S=325±7 mJy
S=296±7 mJy
S=186±7 mJy
S <36mJy
S <12mJy
SPT2008−58
z_{phot}=3.1
S=3±0 mJy
S=21±2 mJy
S=55±10 mJy
S=59±8 mJy
S=67±9 mJy
SPT2031−51
z_{phot}=2.6
S=4±1 mJy
S=64±3 mJy
S=225±7 mJy
S=246±7 mJy
S=227±7 mJy
S=91±12 mJy
S=21±4 mJy
SPT2037−65
z_{spec}=4.0
z_{phot}=4.4
S=19±1 mJy
S=131±5 mJy
S=237±11 mJy
S=198±9 mJy
S=129±10 mJy
SPT2048−55
z_{spec}=4.1
z_{phot}=4.6
S=6±1 mJy
S=54±4 mJy
S=80±8 mJy
S=91±6 mJy
S=47±8 mJy
S <24mJy
S <6mJy
SPT2052−56
z_{spec}=4.3
z_{phot}=3.6
S=22±2 mJy
S=54±7 mJy
S=41±6 mJy
S=24±6 mJy
S <18mJy
S <7mJy
SPT2101−60
z_{phot}=3.0
S=6±1 mJy
S=61±6 mJy
S=185±7 mJy
S=234±8 mJy
S=170±7 mJy
SPT2103−60
z_{spec}=4.4
z_{phot}=4.3
S=8±1 mJy
S=77±6 mJy
S=111±6 mJy
S=83±5 mJy
S=47±5 mJy
S <22mJy
S <6mJy
2.0mm
1.4mm
870μm
500μm
350μm
250μm
160μm
100μm
Arcmin

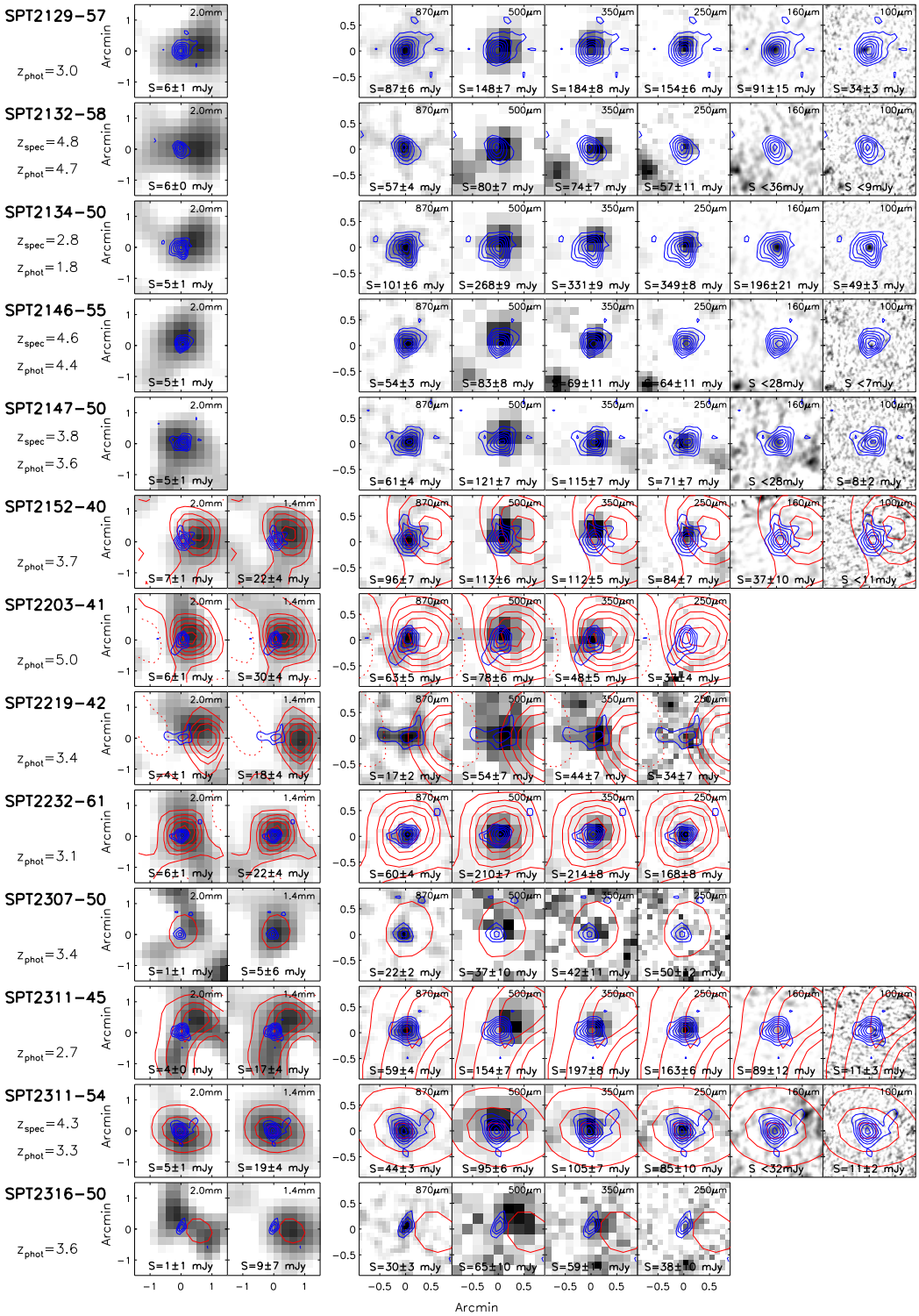
SPT2129−57
z_{phot}=3.0
S=6±1 mJy
S=87±6 mJy
S=148±7 mJy
S=184±8 mJy
S=154±6 mJy
S=91±15 mJy
S=34±3 mJy
SPT2132−58
z_{spec}=4.8
z_{phot}=4.7
S=6±0 mJy
S=57±4 mJy
S=80±7 mJy
S=74±7 mJy
S=57±11 mJy
S <36mJy
S <9mJy
SPT2134−50
z_{spec}=2.8
z_{phot}=1.8
S=5±1 mJy
S=101±6 mJy
S=268±9 mJy
S=331±9 mJy
S=349±8 mJy
S=196±21 mJy
S=49±3 mJy
SPT2146−55
z_{spec}=4.6
z_{phot}=4.4
S=5±1 mJy
S=54±3 mJy
S=83±8 mJy
S=69±11 mJy
S=64±11 mJy
S <28mJy
S <7mJy
SPT2147−50
z_{spec}=3.8
z_{phot}=3.6
S=5±1 mJy
S=61±4 mJy
S=121±7 mJy
S=115±7 mJy
S=71±7 mJy
S <28mJy
S=8±2 mJy
SPT2152−40
z_{phot}=3.7
S=7±1 mJy
S=22±4 mJy
S=96±7 mJy
S=113±6 mJy
S=112±5 mJy
S=84±7 mJy
S=37±10 mJy
S <11mJy
SPT2203−41
z_{phot}=5.0
S=6±1 mJy
S=30±4 mJy
S=63±5 mJy
S=78±6 mJy
S=48±5 mJy
SPT2219−42
z_{phot}=3.4
S=4±1 mJy
S=18±4 mJy
S=17±2 mJy
S=54±7 mJy
S=44±7 mJy
S=34±7 mJy
SPT2232−61
z_{phot}=3.1
S=6±1 mJy
S=22±4 mJy
S=60±4 mJy
S=210±7 mJy
S=214±8 mJy
S=168±8 mJy
SPT2307−50
z_{phot}=3.4
S=1±1 mJy
S=5±6 mJy
S=22±2 mJy
S=37±10 mJy
S=42±11 mJy
SPT2311−45
z_{phot}=2.7
S=4±0 mJy
S=17±4 mJy
S=59±4 mJy
S=154±7 mJy
S=197±8 mJy
S=163±6 mJy
S=89±12 mJy
S=11±3 mJy
SPT2311−54
z_{spec}=4.3
z_{phot}=3.3
S=5±1 mJy
S=19±4 mJy
S=44±3 mJy
S=95±6 mJy
S=105±7 mJy
S=85±10 mJy
S <32mJy
S=11±2 mJy
SPT2316−50
z_{phot}=3.6
S=1±1 mJy
S=9±7 mJy
S=30±3 mJy
S=65±10 mJy
S=59±7 mJy
S=38±10 mJy
2.0mm
1.4mm
870μm
500μm
350μm
250μm
160μm
100μm
Arcmin

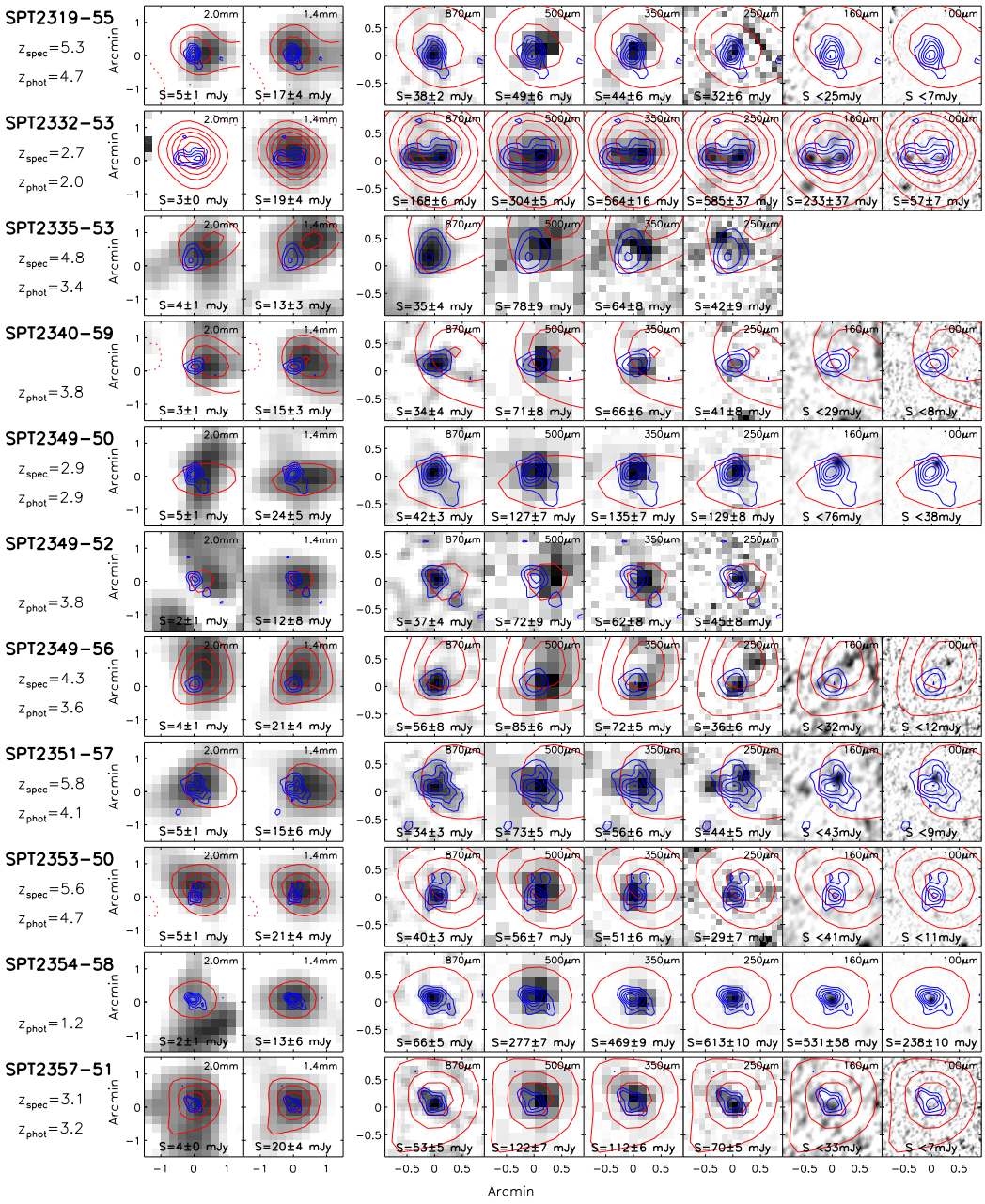
SPT2319−55
z_{spec}=5.3
z_{phot}=4.7
S=5±1 mJy
S=17±4 mJy
S=38±2 mJy
S=49±6 mJy
S=44±6 mJy
S=32±6 mJy
S <25mJy
S <7mJy
SPT2332−53
z_{spec}=2.7
z_{phot}=2.0
S=3±0 mJy
S=19±4 mJy
S=168±6 mJy
S=304±5 mJy
S=564±16 mJy
S=585±37 mJy
S=233±37 mJy
S=57±7 mJy
SPT2335−53
z_{spec}=4.8
z_{phot}=3.4
S=4±1 mJy
S=13±3 mJy
S=35±4 mJy
S=78±9 mJy
S=64±8 mJy
S=42±9 mJy
SPT2340−59
z_{phot}=3.8
S=3±1 mJy
S=15±3 mJy
S=34±4 mJy
S=71±8 mJy
S=66±6 mJy
S=41±8 mJy
S <29mJy
S <8mJy
SPT2349−50
z_{spec}=2.9
z_{phot}=2.9
S=5±1 mJy
S=24±5 mJy
S=42±3 mJy
S=127±7 mJy
S=135±7 mJy
S=129±8 mJy
S <76mJy
S <38mJy
SPT2349−52
z_{phot}=3.8
S=2±1 mJy
S=12±8 mJy
S=37±4 mJy
S=72±9 mJy
S=62±8 mJy
S=45±8 mJy
SPT2349−56
z_{spec}=4.3
z_{phot}=3.6
S=4±1 mJy
S=21±4 mJy
S=56±8 mJy
S=85±6 mJy
S=72±5 mJy
S=36±6 mJy
S <32mJy
S <12mJy
SPT2351−57
z_{spec}=5.8
z_{phot}=4.1
S=5±1 mJy
S=15±6 mJy
S=34±3 mJy
S=73±5 mJy
S=56±6 mJy
S=44±5 mJy
S <43mJy
S <9mJy
SPT2353−50
z_{spec}=5.6
z_{phot}=4.7
S=5±1 mJy
S=21±4 mJy
S=40±3 mJy
S=56±7 mJy
S=51±6 mJy
S=29±7 mJy
S <41mJy
S <11mJy
SPT2354−58
z_{phot}=1.2
S=2±1 mJy
S=13±6 mJy
S=66±5 mJy
S=277±7 mJy
S=469±9 mJy
S=613±10 mJy
S=531±58 mJy
S=238±10 mJy
SPT2357−51
z_{spec}=3.1
z_{phot}=3.2
S=4±0 mJy
S=20±4 mJy
S=53±5 mJy
S=122±7 mJy
S=112±6 mJy
S=70±5 mJy
S <33mJy
S <7mJy
2.0mm
1.4mm
870μm
500μm
350μm
250μm
160μm
100μm
Arcmin
Arcmin

Appendix E

Decomposition of SPT2332-53

SPT2332-53 is lensed by a foreground galaxy cluster and the source is not as the other sources a point source, but is spatially resolved in nearly all bands. This source was also presented by Greve et al. (2012), and we revisit it here as we now have more data and therefore can do a more thorough analysis. From Figure E.1 we identify seven components. The three components shown with *red* crosses (positions are from ATCA high resolution CO imaging, see Aravena et al., 2013) are lensed images of the SPT-DSFGs at $z = 2.7256(2)$. The four *blue* crosses show components bright in submm not associated with the DSFG. The positions of the arc components have been determined by ATCA high resolution CO observations (see Aravena et al., 2013). The positions for the components not belonging to the source has been determined in the band where it was observed with the highest SNR and where it didn't blend with other components. Because of the confusion from the surrounding sources and the not point like nature of the source we construct a decomposition of the individual. The flux extracted for each of the components are given in Table E.1 along with photometric redshifts of each components.

At the resolution of both the 100 μm and 160 μm PACS maps all components are disentangled and the flux is calculated by treating each of the arc components as point sources and adding their flux densities.

The resolution in the 250 μm SPIRE map and the 870 μm LABOCA map is similar so the flux extraction in these maps are done in the same manner. We extracted the flux in two different ways: 1) by fitting PSF's to the positions all the components and adding the flux density found for the three component belonging to the source and 2) by first fitting and removing components not belonging to the arc and using an aperture to encapsulate the three arc components. In Figure E.2 the *Herschel*/SPIRE and APEX/LABOCA maps are shown and compared to the PSF fitting of the seven components along with the residual of this. The flux densities found using the two different methods are within the uncertainties of each other. Even though there seem to be a bit of residual for the APEX/LABOCA map we estimate that the first method is more accurate and we use these fluxes for the SED fitting (and list them in Table 3.2).

At 350 μm and 500 μm it is not possible to disentangle and fit the individual components so we use method 2) described above to extract the flux density.

The resolution of the SPT map is too low to be able to disentangle the components not belonging to the source and we have therefore not corrected these flux densities.

The fluxes given in Table 3.2 and used to calculate the photometric redshifts are the combined fluxes of the three arc components, given as 'Full arc' in Table E.1.

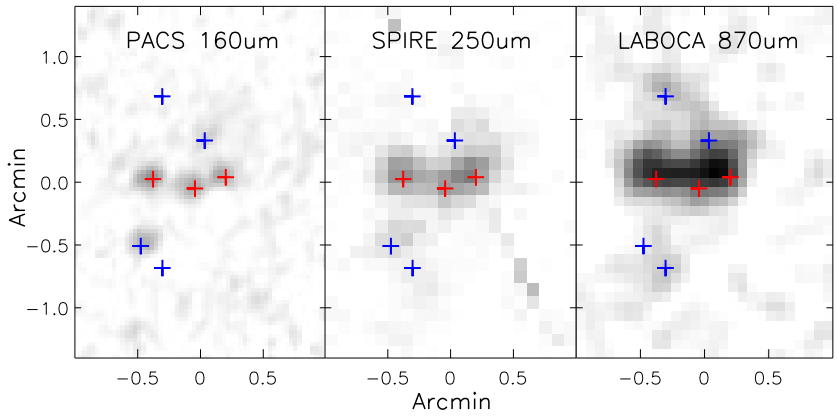

Figure E.1: From left to right: The *Herschel*/PACS 160 μm, *Herschel*/SPIRE 250 μm and APEX/LABOCA 870 μm maps for SPT2332-53. In *red* the positions of the three components of the SPT-DSFG is shown and in *blue* the positions of the components not belonging to the SPT-DSFG is shown.

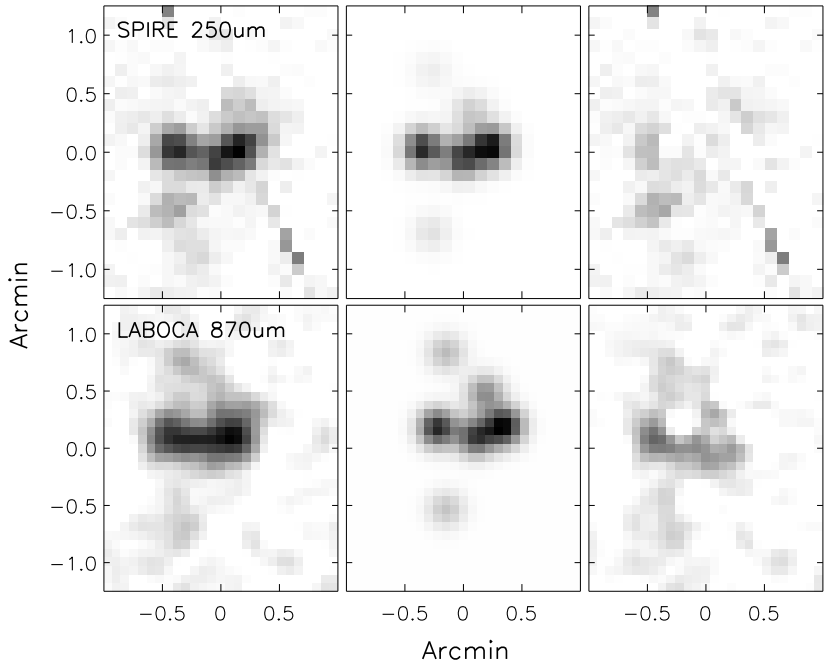

Figure E.2: SPIRE 250 μm and LABOCA 870 μm decomposition analysis. From left to right: Map, fitted PSF's, and the residual of the PSF's subtracted from the map.

Table E.1: Fluxes of all components of SPT2332-53

Component	**Ra**	**dec**	**Origin of position**	$S_{870\mu m}$ **[mJy]**	$S_{500\mu m}$ **[mJy]**	$S_{350\mu m}$ **[mJy]**	$S_{250\mu m}$ **[mJy]**	$S_{160\mu m}$ **[mJy]**	$S_{100\mu m}$ **[mJy]**	$z_{\rm phot}$
Arc 1	23:32:29.49	-53:58:39.8	ATCA	53±3			164±4	86±21	25±4	2.8±0.7
Arc 2	23:32:27.22	-53:58:44.3	ATCA	51±3			161±6	77±21	14±4	2.8±0.8
Arc 3	23:32:25.55	-53:58:38.9	ATCA	64±3			201±12	70±22	18±4	2.8±0.6
Full arc				168±6	304±5	585±37	526±14	233±37	57±7	2.0±0.5
Outlier 1	23:32:28.99	-53:58:00.3	LABOCA	20±3	55±6	23±6	<15	<63	<12	4.8±1.0
Outlier 2	23:32:26.69	-53:58:21.4	PACS 160μm	25±3			43±15	<66	<12	3.8±3.0
Outlier 3	23:32:30.16	-53:59:11.8	PACS 100μm	<12	57±6	26±5	51±6	62±21	31±4	0.9±0.5
Outlier 4	23:32:28.98	-53:59:22.3	LABOCA	15±3	43±7	34±5	23±5	<66	<12	3.9±0.8

Appendix F

Spectral Energy Distributions

We here show the the single modified black body fit for all sources in this work. On the x-axis we showed observed frequency and the data points are colored using the following scheme: ALMA 3 mm is *red*, SPT is *orange*, LABOCA is *yellow*, SPIRE is *green* and PACS is *blue*. The vertical *pink* dotted lines shows the borders for the L_{FIR} integration and the dashed *purple* vertical lines show the borders of the L_{IR} integration. The photometric redshifts obtained from the fit is printed in the plot, and if a spectroscopic redshift exists for the source, this is also printed. The fluxes plotted are given in Table 3.2 and the photometric redshifts obtained are given in Table 5.2.

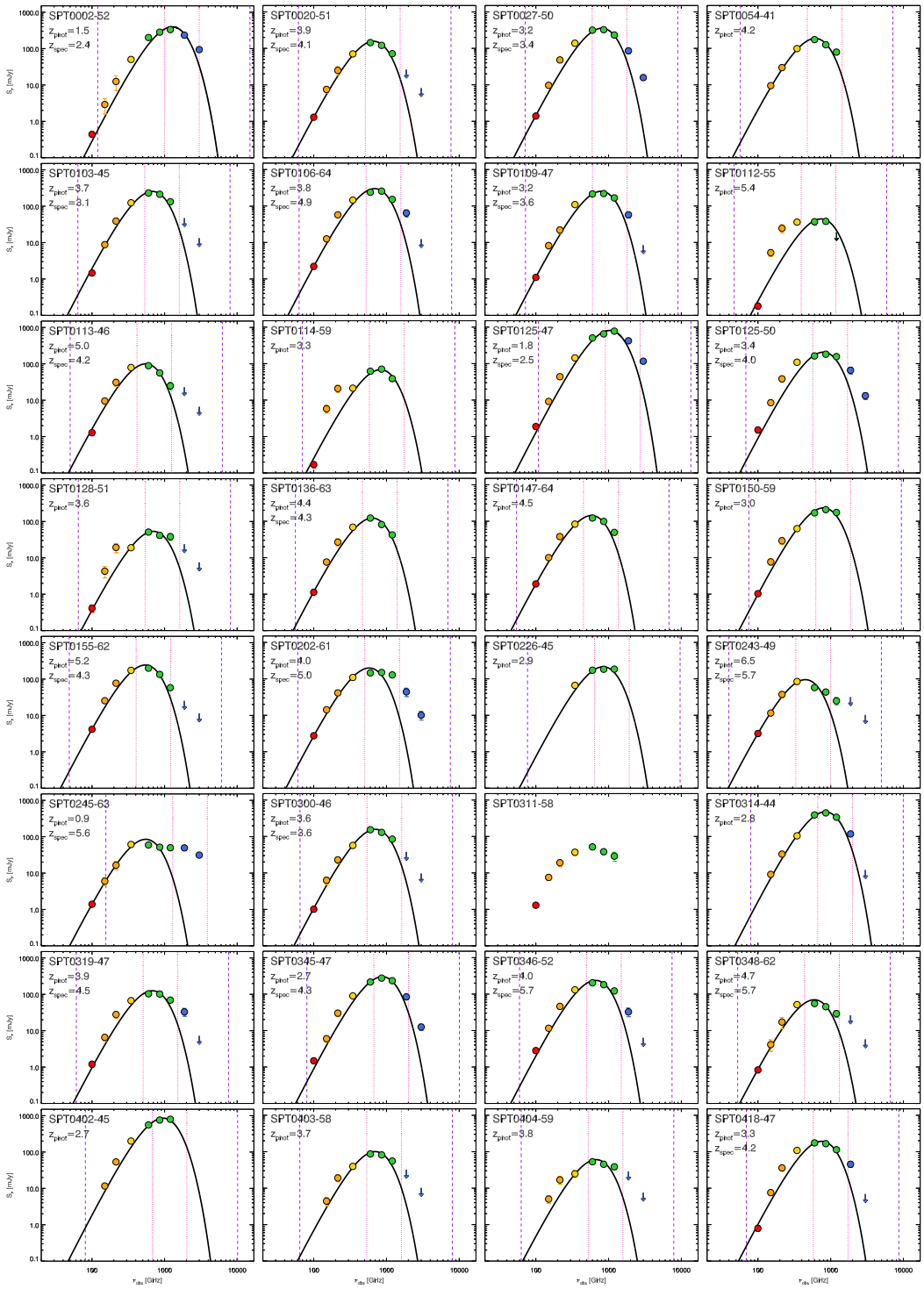

Figure F.1: SEDs of all sources investigated in this work.

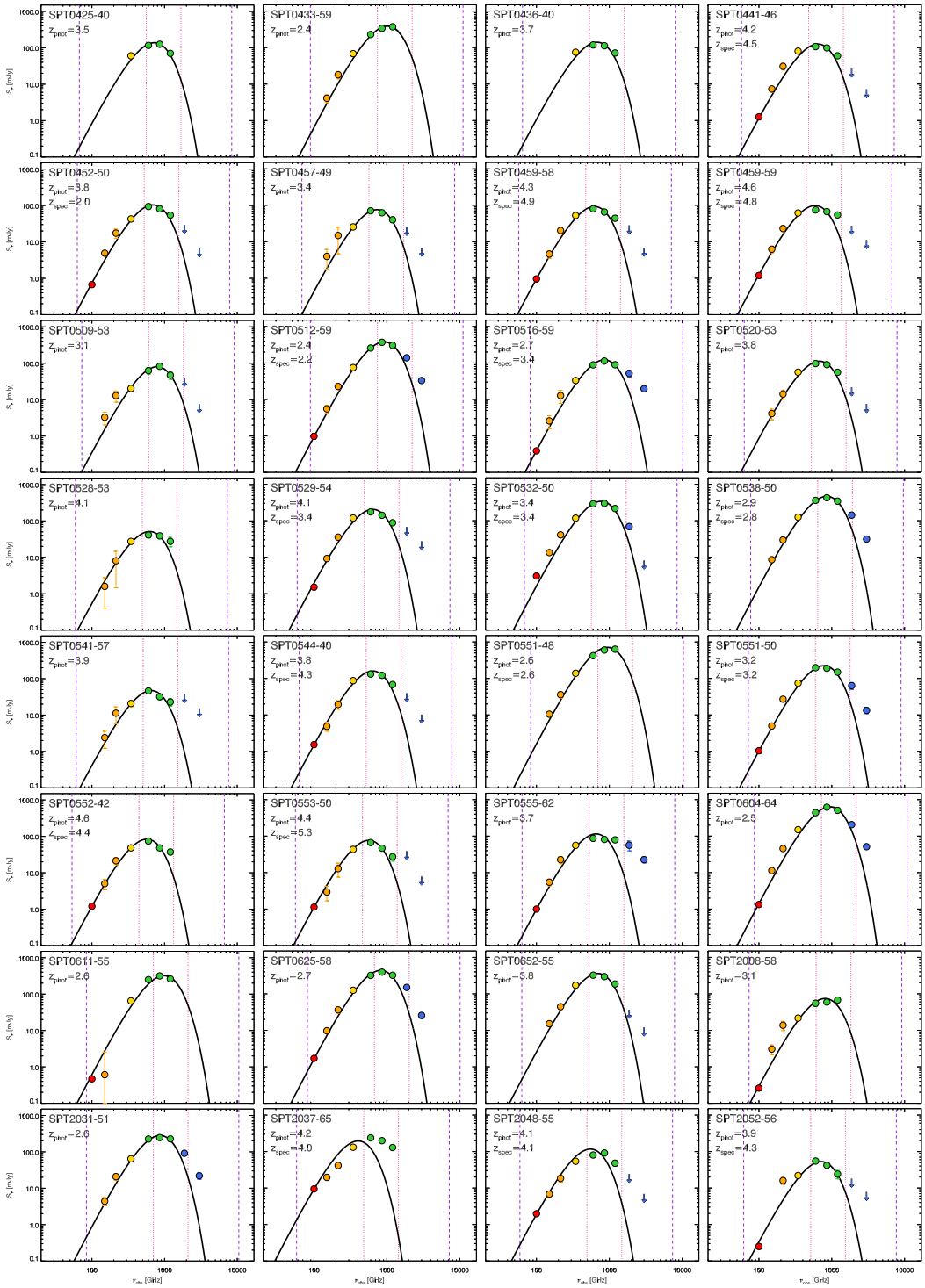

Figure F.1 continued ...

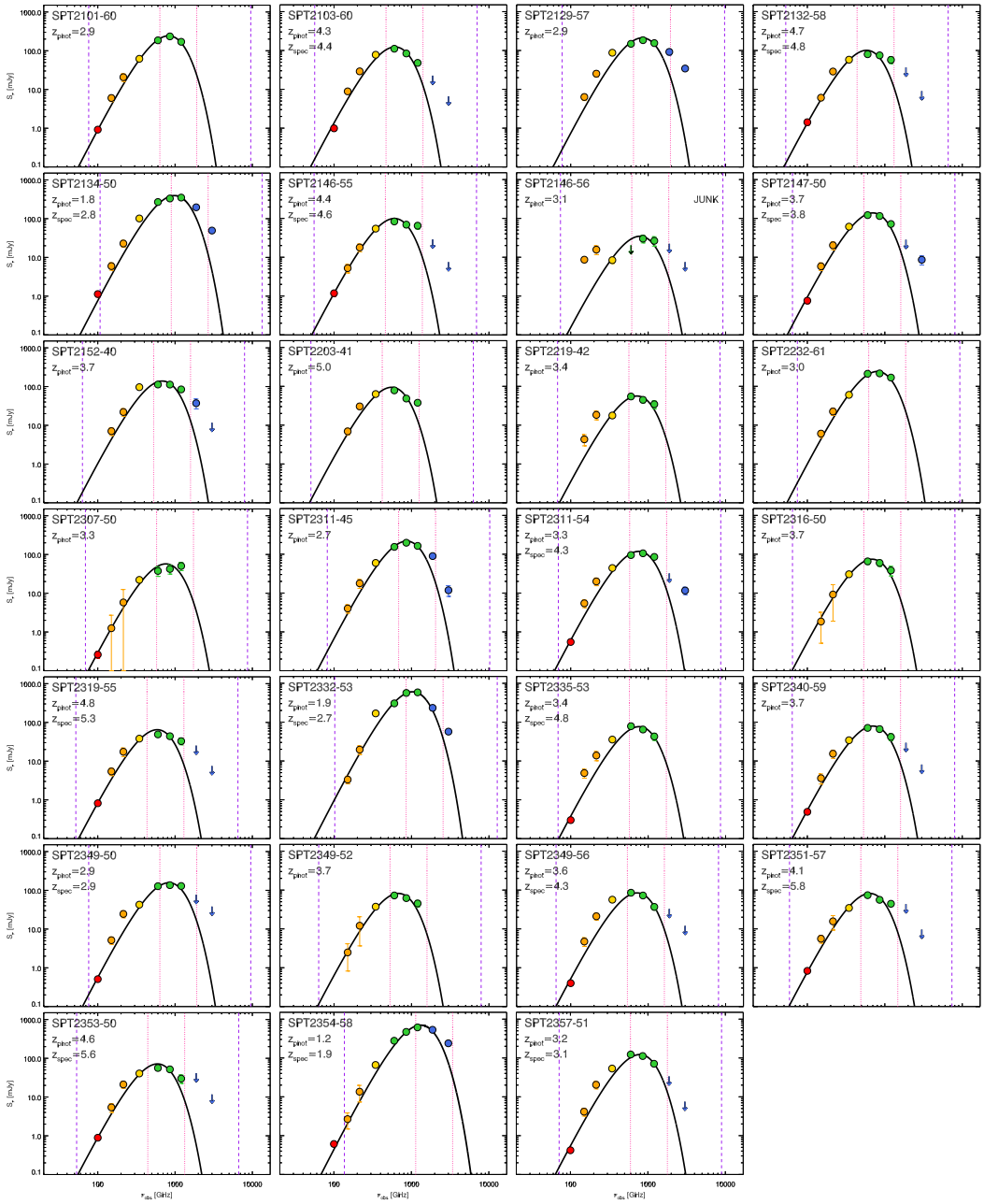

Figure F.1 continued ...

Erklärung

Ich versichere, dass ich die von mir vorgelegte Dissertation selbständig angefertigt, die benutzten Quellen und Hilfsmittel vollständig angegeben und die Stellen der Arbeit, einschließlich Tabellen und Abbildungen, die anderen Werken im Wortlaut oder dem Sinn nach entnommen sind, in jedem Einzelfall als Entlehnung kenntlich gemacht habe; dass diese Dissertation noch keiner anderen Fakultät oder Universität zur Prüfung vorgelegen hat; dass sie noch nicht veröffentlicht worden ist; sowie, dass ich eine solche Veröffentlichung vor Abschluss des Promotionsverfahrens nicht vornehmen werde. Die Bestimmungen dieser Promotionsordnung sind mir bekannt. Die von mir vorgelegte Dissertation ist von Prof. Dr. Karl M. Menten betreut worden.

Unterschift:

_____

Datum:

_____

Publications

[1] **Strandet, M. L.**; Weiß, A.; De Breuck, C.; Marrone, D. et al. 2017, ApJL, 842, 15
ISM properties of a massive dusty star-forming galaxy discovered at $z \sim 7$

[2] **Strandet, M. L.**; Weiß, A; Vieira, J. D.; De Breuck, C. et al. 2016, ApJ, 822, 80
The Redshift Distribution of Dusty Star-forming Galaxies from the SPT Survey

[3] Marrone, D. P.; et al. (32 authors including **Strandet, M.**) 2017, Accepted by Nature
The Growth of a Massive Galaxy in the Epoch of Reionisation

[4] Bothwell, M. S.; et al. (18 authors including **Strandet, M.**) 2017, MNRAS, 466, 2825
ALMA observations of atomic carbon in $z \sim 4$ dusty star-forming galaxies

[5] Jingzhe, M.; et al. (22 authors including **Strandet, M.**) 2016, ApJ, 832, 114
SPT0346-52: Negligible AGN Activity in a Compact, Hyper-starburst Galaxy at $z = 5.7$

[6] Spilker, J. S.; et al. (20 authors including **Strandet, M.**) 2016, ApJ, 826, 112
ALMA Imaging and Gravitational Lens Models of South Pole Telescope - Selected Dusty, Star-Forming Galaxies at High Redshifts

[7] Aravena, M.; et al. (20 authors including **Strandet, M.**) 2016, MNRAS, 457, 4406
A survey of the cold molecular gas in gravitationally lensed star-forming galaxies at $z > 2$

[8] Béthermin, M.; et al. (18 authors including **Strandet, M.**) 2016, A&A, 586, 7
An ALMA view of the interstellar medium of the $z = 4.77$ lensed starburst SPT-S J213242-5802.9

[9] Welikala, N.; Béthermin, M; Guery, D.; **Strandet, M.** et al. 2016, MNRAS, 455, 1629
Probing star formation in the dense environments of $z \sim 1$ lensing haloes aligned with dusty star-forming galaxies detected with the South Pole Telescope

[10] Ma, Jingzhe et al. (20 authors including **Strandet, M.**) 2015, ApJ, 812, 88.
Stellar Masses and Star Formation Rates of Lensed, Dusty, Star-forming Galaxies from the SPT Survey

[11] Spilker, J. S. et al. (22 authors including **Strandet, M.**) 2015, ApJ, 811, 124.
Sub-kiloparsec Imaging of Cool Molecular Gas in Two Strongly Lensed Dusty, Star-forming Galaxies

[12] Gullberg, B. et al. (26 authors including **Strandet, M.**) 2015, MNRAS, 449, 2883
The nature of the [CII] emission in dusty star-forming galaxies from the SPT survey

[13] Spilker, J. S. et al. (30 authors including **Strandet, M.**) 2014, ApJ, 785, 149
The Rest-frame Submillimeter Spectrum of High-redshift, Dusty, Star-forming Galaxies

[14] Bothwell, M. S. et al. (40 authors including **Strandet, M.**) 2013, ApJ, 779, 67
SPT 0538-50: Physical Conditions in the Interstellar Medium of a Strongly Lensed Dusty Star-forming Galaxy at z = 2.8

[15] Fynbo, J. P. U. et al. (14 authors including **Strandet, M.**) 2010, MNRAS, 408, 2128
Galaxy counterparts of metal-rich damped Ly-α absorbers - I. The case of the z = 2.35 DLA towards Q2222-0946